doc. numbers:
DESY, FERMILAB, IFIC, IRFU
JLAB, KEK, PNNL-SA-160884, SLAC,
and more ...

January 15, 2022

The International Linear Collider: Report to Snowmass 2021

the ILC International Development Team and the ILC community

ABSTRACT

The International Linear Collider (ILC) is on the table now as a new global energy-frontier accelerator laboratory taking data in the 2030's. The ILC addresses key questions for our current understanding of particle physics. It is based on a proven accelerator technology. Its experiments will challenge the Standard Model of particle physics and will provide a new window to look beyond it. This document brings the story of the ILC up to date, emphasizing its strong physics motivation, its readiness for construction, and the opportunity it presents to the US and the global particle physics community.

Contents

Chapter 1

Introduction

[3 pages; corresponding editor: Hitoshi Murayama (hitoshi@berkeley.edu)]

The ILC is a proposed next-generation e^+e^- collider. It starts with $\sqrt{s} = 250$ GeV as the Higgs factory, which provides typically an order of magnitude improvement in precision Higgs measurements beyond the HL-LHC. Such precision measurements will provide guidance to the next energy scale for future facilities. At the same time, it provides numerous searches for new physics with monophoton or invisible and exotic Higgs decays, for example into a light dark sector. It can host ancillary experiments with beam dump and/or near IP detectors to search for long-lived and invisible particles. It is technologically mature with a well-understood cost that is about the same as the LHC. The linear design allows for extensions to upgrade energies. The next steps would likely be the $t\bar{t}$ threshold and open $t\bar{t}$ as well as $t\bar{t}H$ production at 500–550 GeV. The site was specifically chosen to allow for an upgrade up to 1 TeV with the same technology, for the Higgs self-coupling measurement and many new physics searches. Superconducting RF cavity technology has an ample room for improvements, allowing for even a 3–4 TeV collider in the same tunnel. Future technologies such as plasma wakefield or dielectric laser accelerators may go into the tens of TeV energy range.

This report is intended to be a comprehensive sourcebook on the ILC, discussing plans for the accelerator, the experimentation, and the physics analyses and also the physics context and theoretical implications of the ILC measurements. We hope that it will be useful to those who would like to better understand or evaluate the ILC proposal. Also, since the physics programs of all proposed Higgs factories are closely aligned, most of our physics discussion will also be helpful in understanding the physics prospects for all facilities of this type.

1.1 Context for the ILC

We first describe the context for the ILC as it has evolved over half a century of development in particle physics.

The ILC stands at the end of a long history. The need for a linear collider was recognized

already in 1960's given the energy loss due to unavoidable synchrotron radiation from beams in circular colliders. To achieve power-efficient acceleration, the development of superconducting radio frequency (SCRF) cavities started in earnest in the 1980's. Over four decades, intensive research and development achieved much higher acceleration gradients and reduced the costs of SCRF by more than an order of magnitude. SCRF provides better tolerances compared to room-temperature klystron-based designs, and was chosen as the ILC technology in 2005 by the International Technology Recommendation Panel chaired by Barry Barish (2017 Nobel Laureate in Physics). The International Committee for Future Accelerators, a body created by the International Union of Pure and Applied Physics in 1976 to facilitate international collaboration in the construction and use of accelerators for high energy physics, recommended the launch of the Global Design Effort (GDE) to produce a Technical Design Report (TDR) for the ILC as an international project. The GDE successfully produced the TDR in 2013 with a purposely site-independent design [1, 2, 3, 4, 5].

There is also a long history of discussions on the scientific merit for the ILC. The energy scale of the weak interaction, which makes the Sun burn and allows the synthesis of the chemical elements, was pointed out to be around 250 GeV in 1933 by Enrico Fermi. The need to reach this energy scale has been obvious since then, though the precise target energy was not clear. Early discussions for linear colliders called for 1000 GeV as a safe choice for guaranteed science output. The GDE focused on 500 GeV for the study of the Higgs boson based on the precision electroweak data of early 2000's. It was only in 2012 that the Higgs boson was discovered at the Large Hadron Collider (LHC) at CERN. This provided a clear target energy for the ILC at 250 GeV. In the same year, the Japanese Association of High-Energy Physicists (JAHEP) issued a report expressing interest in hosting the ILC in Japan with 250 GeV center-of-momentum energy as its first phase. The European Strategy for Particle Physics updated in 2013 highlighted "*the ILC, based on superconducting technology, will provide a unique scientific opportunity at the precision frontier.*" This was followed by the report of the US Prioritization Panel for Particle Physics Projects (P5) that listed "*Use the Higgs boson as a new tool for discovery*" as the first among the science drivers for particle physics and stated "*As the physics case is extremely strong, all (funding) Scenarios include ILC support*".

Intense discussions ensued worldwide how to realize the ILC. Japanese government instituted a multitude of committees looking into the scientific and societal merit of hosting the ILC in Japan as well as its technological feasibility and costs. The US government encouraged Japan to host the ILC, with letters from the Secretary of Energy and the Deputy Secretary of State to Japanese Ministers. The 2020 update of the European Strategy for Particle Physics stated "*An electron-positron Higgs factory is the highest-priority next collider*" and added "*The timely realisation of the electron-positron International Linear Collider (ILC) in Japan would be compatible with this strategy and, in that case, the European particle physics community would wish to collaborate.*" Following this update, ICFA created the International Development Team (IDT) in August 2020 to prepare for the creation of prelab towards the realization of the ILC. The IDT is hosted by KEK, the national laboratory for high-energy accelerators in Japan.

Since its launch, IDT has collected information, worked with ICFA, interacted with the community, consulted the funding agencies, to formulate what is required of the ILC Pre-Lab. The Pre-Lab is envisioned to be a four-year process, finalizing the Engineering Design Report for the ILC in a site-specific fashion for the Kitakami mountain range in northern Japan, forging agreements among international partners, and recommending specific experiments for the ILC.

1.2 Outline

This report will update the documents prepared by ILC for the European Stategy for Particle Physics. These include a comprehensive review of the ILC up to 2019 [6] and a review of the ILC capabilities for precision measurement [7]. A comprehensive bibliography for the ILC, up to mid-2020, can be found in [8].

The outline of this report is the following: Chapter 2 will present the most important points of the physics case for the ILC. In Chapter 3, we will present the current plan and timeline for the realization of the ILC in Japan.

Chapter 4 will present the current state of the ILC accelerator design, including details of the various ILC energy stages up to a CM energy of 1 TeV. This chapter will also discuss the prospects for extension of the ILC to even higher energies and other issues for ILC accelerator R&D. It will conclude with a discussion of the opportunities and tentative plans for US contributions to the ILC accelerator.

Chapter 5 will review the basic aspects of the physics environment of the ILC—the major physics processes, the plan for stage-by-stage improvement in the energy and luminosity, and the key role played in the experimental program by electron and positron beam polarization.

Chapter 6 will describe the ILC detectors. We will begin with descriptions of the two current proposed detectors ILD and SiD, including the expected measurement capabilities and issues for which further R&D is needed. The chapter will conclude with a survey of new technologies that offer the promise of further improvements in the detector capabilities. Chapter 7 will describe the simulation framework used in studying the detector capabilites and projecting the measurement accuracy of physical observables.

Chapter 8 will describe the planned physics measurements at a CM energy of 250 GeV. These include measurements on the Higgs boson and the W boson, measurements of 2-fermion production, the ILC program in precision QCD, and descriptions of a number of relevant new particle searches.

Chapter 9 will describe the ILC program in precision electroweak measurements. This includes improvements of the precision electroweak parameters of the Z boson, both at 250 GeV through the radiative return reaction $e^+e^- \to \gamma Z$ and through a dedicated program of running at the Z resonance. It also includes high-precision measurements of the W boson mass and width and improved measurements of these properties for the Z boson.

Chapter 10 will describe the planned physics measurements at CM energies of 350 GeV and above, up to 1 TeV. The topics here include the ILC program of precision measurements of the top quark, the completion of the measurement of the Higgs boson profile, including the measurements of the Higgs self-coupling and the top quark Yukawa coupling, and the ultimate capabilities of the ILC in triple gauge boson couplings and new particle searches.

Chapter 11 will describe the fixed-target program that the intense, high-energy electron and positron beams of the ILC will make available.

Chapters 12-14 will address the interpretation of the ILC measurements. Chapter 12 will begin

with a review of the status of precision SM theory for ILC processes. It will then discuss the network of tests of the SM available at the ILC. This chapter will present a unified description of these tests using Standard Model Effective Field Theory (SMEFT), reviewing the conceptual basis of this approach and demonstrating its power in providing a unified interpretation of the full set of ILC experimental measurements. Chapter 13 will present a theoretical context for the expectation that the ILC will discover deviations from the SM predictions and the relation of such deviations to the most important question now being asked in particle physics. Chapter 14 will bring these two lines of analysis together, quantifying the ability of the ILC to overturn the SM and to provide evidence of the more correct underlying model for particle physics.

Finally, Chapter 15 will lay out some possible futures for the ILC laboratory with accelerators at still higher energies offering multi-TeV and muti-10-TeV electron, positron, and photon collisions.

Chapter 2

Outline of the ILC Physics Case

[4 pages; corresponding editor: Michael Peskin (mpeskin@slac.stanford.edu)]

The physics motivation for constructing the ILC is very strong. The flagship program of the ILC is the study of the Higgs boson at a much higher level of precision than will be possible at the LHC. The ILC will also carry out precision measurements of the other heavy and still-mysterious particle in the Standard Model (SM), the top quark. It will carry out a program of specific searches for postulated new particles in regions that are very difficult for the LHC to access. Beyond these specific targets, the ILC will greatly improve the level of our understanding of the full set of electroweak processes in the region up to its final CM energy. In the context of Standard Model Effective Field Theory (SMEFT), these measurements will work together to strongly challenge the Standard Model. In this chapter, we will introduce each of these points and prepare the ground for a more detailed discussion later in this report.

We begin with the 125 GeV Higgs boson. This particle is the centerpiece of the SM, yet still we know little about it. From the LHC experiments, we now know that the couplings of the Higgs boson agree with those predicted in the SM, at the level of 20% accuracy for the major decay modes. However, this is not nearly sufficient to distinguish the minimal SM description of the Higgs boson from those of competing models. According to SMEFT, the deviations of Higgs couplings from SM predictions are parametrically of the order of m_h^2/M^2, where M is the mass scale of additional new particles. Given the constraints from particle searches at the LHC, these deviations are expected to be at most of order 5-10%, and, to claim discovery of new physics, the deviations must be measured with high significance. This calls for a dedicated program to measure the full suite of couplings of the Higgs boson, and to push the precision of those measurements to the 1% level and below. This requires an e^+e^- collider such as the ILC.

The ILC is well-positioned to carry out this program of measuring the complete profile of the Higgs boson couplings. At 250 GeV, the ILC accesses the reaction $e^+e^- \to Zh$, producing about half a million Higgs bosons, each tagged by a recoil Z boson at the lab energy of 110 GeV. Looking in the opposite hemisphere, we will measure all of the branching ratios of the Higgs boson down to values of order 10^{-4}. These include 10 different modes of Higgs decay predicted in the SM, and also, possibly, invisible, partially-invisible, flavor changing, and other exotic modes of Higgs

decay. By counting recoil Z bosons, we will obtain an absolute measurement of the cross section for $e^+e^- \to Zh$, which can then be translated into absolute normalizations of the various partial widths.

At the second stage of the ILC at 500 GeV, the W fusion reaction $e^+e^- \to \nu\bar{\nu}h$ opens up. This reaction offers an event sample of about 1 million Higgs boson events in which the only visible signals in the event are from Higgs decay. This will not only allow new measurements to complement the 250 GeV data but also improved understanding of such issues as $h \to b\bar{b}/gg/c\bar{c}$ separation, angular distributions in $h \to WW^*$, and CP violation tests in $h \to \tau^+\tau^-$. The combination of the 250 and 500 GeV programs will give high confidence in any deviations from the SM detected in the Higgs boson data.

Running at 500 GeV and above also gives access to two important Higgs couplings that cannot be probed directly in Higgs decays, the Higgs coupling to $t\bar{t}$ and the Higgs self-coupling. Our studies of the ILC capabilities at 1 TeV predict truly archival measurements of these quantities, with errors below 2% and 10%, respectively.

Different models of new physics beyond the SM affect the various Higgs couplings differently. Since the ILC program can determine each Higgs coupling of the large set available, individually and without ambiguity, it will provide a pattern of deviations from the predictions of the SM that can distinguish different hypotheses about the underlying model.

The ILC program of experimental measurements on the Higgs boson will be described in Chapters 8 and 10 of this report, and the interpretation of these measurements will be discussed in some detail in Chapters 12 and 14.

The 500 GeV ILC will also give an excellent opportunity for the measurement of the mass and properties of the top quark. The mass of the top quark will be determined from the position of the sharp threshold in $e^+e^- \to t\bar{t}$. The threshold shape is determined by the short-distance top quark mass, so that the mass defined in this way, which is needed for high-precision predictions in and beyond the SM, is determined from the data without ambiguity. At e^+e^- colliders, the electroweak form factors of the top quark, which contain crucial information about the role of the top quark in electroweak symmetry breaking, determine the primary top quark pair production cross section. Thus, very high precision measurements of these form factors are possible. The ILC program of measurements on the top quark will be discussed in Chapter 10 of this report.

Beyond these SM particles, the ILC has the potential to access new particles predicted in models beyond the SM. The LHC experiments have given powerful access to proposed new particles with couplings to QCD, but their capability to discover particles with only electroweak couplings is limited. All LHC searches come with caveats concerning the sizes of electroweak cross sections, the expected decay patterns, the amount of missing energy, and other features. Searches at the ILC will allow these caveats to be eliminated, giving access to systems with large missing energy and other challenging features, in particular, to supersymmetry partners of the Higgs boson and to dark matter in models with compressed spectra. These issues will be described in Sections 8 and 10 of this report.

The ILC will dramatically improve the precision of our understanding of electroweak reactions.

For example, the reaction $e^+e^- \to W^+W^-$ has strong dependence on both initial- and final-state polarizations. At the ILC, we will have beam polarization in the initial state and complete reconstruction of the final state, allowing us to dissect the structure of the triple-gauge-boson coupling. The reactions $e^+e^- \to f\bar{f}$ allow searches for additional electroweak resonances that access the 10-TeV mass range and are flavor- and helicity-specific. The study of radiative-return events ($e^+e^- \to \gamma Z$) at 250 GeV will already improve the our precision knowledge of Z-fermion couplings beyond that obtained at LEP. A dedicated ILC "Giga-Z" run at the Z resonance (5×10^9 Zs) will improve the precision of most electroweak observables by more than an order of magnitude. These measurements and others are described in Chapters 8, 9, and 10.

The simplicity of hadronic final states in e^+e^- annihilation also allows not only higher precision tests of QCD but also new observables that give insight into features such as jet substructure that have come to light at the LHC. This new program of QCD measurements will be described in Chapter 8.

The ILC will also make available the most intense and highest-energy electron and positron beams for beam dump and dedicated fixed-target experiments targeting light weakly-interacting particles. This program will be described in Chapter 11.

These measurements are very powerful already when they are considered separately, but they take on increased power when they are combined to stress-test the SM in coherent way. This becomes particularly clear when the full set of SM tests is analyzed using SMEFT. In this approach, corrections to the SM are described by contributions to an effective Lagrangian from operators of dimension 6 and higher invariant under the well-tested SM gauge symmetries. There is only one Lagrangian; its higher-dimension operators generally contribute to many electroweak reactions and so receive an array of experimental constraints. We will describe this method in detail and give examples of its powerful use in Chapter 12.

There is one more important point that we should make concerning the program of measurements of the ILC. The goal of testing the SM is not simply to improve the error bars. It is widely appreciated that the Standard Model of particle physics, though it is very successful in describing the results of experiments, is not adequate as a complete theory of elementary particles. The goal of the ILC experiments must be to *prove that the SM is incomplete*, and, even more, to show the path to a better understanding of nature.

One way to prove the inadequacy of the SM is to discover a new resonance that the SM does not account for. This was the primary goal of the LHC experiments. So far, no such resonance has appeared. There is still considerable room to discover a new resonance at the HL-LHC, but that window is closing. It is important to open a new, complementary window, and this is what the ILC's capability for precision tests of the SM will make available.

It is not straightforward, though, to demonstrate a deviation from the SM through precision measurements. First, of all, the deviation must be observed with high statistical significance. Second, the possible systematic errors that could mimic the deviation must be under complete control. This calls for multiple cross-checks on the sources of error and, if possible, measurements with different sources of systematic errors that can be compared. Finally, the view provided by precision measurements cannot be one-dimensional; rather, it should be part of a collective program

that has the power to show a pattern of discrepancies. In the best case, a pattern of well-established deviations from the SM can point to a common origin and thus indicate the nature of the true underlying theory.

The experimental program of the ILC is well-equipped to address these points. The general simplicity and cleanliness of e^+e^- annihilation provides an excellent starting point in the quest for precision. This environment allows the construction of detectors with high segmentation and very low material budget, allowing collider event measurements of unprecedented quality. In the energy region of the ILC, electroweak cross sections have a large and well-understood dependence on beam polarization. With the two signs for each of the electron and positron beam polarizations, the ILC will provide four distinct event samples, each with a distinct combination of physics process. By comparing these samples, we can determine detector performance and measure important backgrounds from data. As we have noted above for the Higgs boson program, changes in the center of mass energy can also bring in new physics processes that access and cross-check the variables targetted in precision measurements. The enabling features of the ILC experimental environment will be discussed in Chapter 5. The capabilities of detectors for the ILC and strategies for further improvement will be discussed in Chapter 6. Throughout the succeeding chapters,we will show these elements at work to ensure the high quality of the ILC measurements.

The ILC thus offers a new approach to the discovery of physics beyond the SM, one of great capability and robustness. These experiments must be carried out. They have the power to lead us to a new stage in our understanding of fundamental physics.

Chapter 3

Route to the ILC

[8 pages; corresponding editor: Tatsuya Nakada, Hitoshi Murayama (hitoshi@berkeley.edu)]

(The organization, schedule, and prospects for the ILC will be explained in this chapter. These will be clearer after the ILC Pre-Lab is set up, a development expected in 2022. The current state of the ILC organization was presented by Tatsuya Nakada and others in the Monday plenary session of the LCWS 2021 workshop, https://indico.cern.ch/event/995633/ .)

3.1 International Design Team

3.2 ILC Pre-Lab

3.3 ILC Laboratory

3.4 Timeline for ILC Detectors

Chapter 4

ILC Accelerator

[general corresponding editor: Shinichiro Michizono (shinichiro.michizono@kek.jp)]

4.1 ILC accelerator design

[10 pages; corresponding editor: Benno List (benno.list@desy.de)]

The International Linear Collider (ILC) is a 250 GeV (extendable up to 1 TeV) linear e^+e^- collider, based on 1.3 GHz superconducting radio-frequency (SCRF) cavities. It is designed to achieve a luminosity of $1.35 \cdot 10^{34}$ cm^{-2}s^{-1} and provide an integrated luminosity of 400 fb^{-1} in the first four years of running. The electron beam will be polarised to 80 %, and positrons with 30 % polarization will be provided if the undulator based positron source concept is employed.

Its parameters have been set by physics requirements first outlined in 2003, updated in 2006, and thoroughly discussed over many years with the physics user community. After the discovery of the Higgs boson it was decided that an initial energy of 250 GeV provides the opportunity for a precision Standard Model and Higgs physics programme at a reduced initial cost [9]. Some relevant parameters are given in Tab. 4.1. This design evolved from two decades of R&D, described in Sec. 1, an international effort coordinated first by the GDE under ICFA mandate and since 2013 by the LCC.

The fundamental goal of the design of the ILC accelerator is a high energy-efficiency. The ILC design limits the overall power consumption of the accelerator complex during operation to 129 MW at 250 GeV and 300 MW at 1 TeV, which is comparable to the power consumption of CERN [11]. This is achieved by the use of SCRF technology for the main accelerator, which offers a high RF-to-beam efficiency through the use of superconducting cavities, operating at 1.3 GHz, where high-efficiency klystrons are commercially available. At accelerating gradients of 31.5 to 35 MV/m this technology offers high overall efficiency and reasonable investment costs, even considering the cryogenic infrastructure needed for the operation at 2 K.

The underlying TESLA technology is mature, with a broad industrial base throughout the

Quantity	Symbol	Unit	Initial	$\mathcal{L}$ Upgrade	TDR	Z pole	Upgrades	
Centre of mass energy	$\sqrt{s}$	GeV	250	250	250	91	500	1000
Luminosity	$\mathcal{L}$	$10^{34}\mathrm{cm}^{-2}\mathrm{s}^{-1}$	1.35	2.7	0.82	0.21	1.8/3.6	4.9
Polarisation for e^-/e^+	P_-/P_+	%	80/30	80/30	80/30	80/30	80/30	80/20
Repetition frequency	f_{rep}	Hz	5	5	5	3.7	5	4
Bunches per pulse	n_{bunch}	1	1312	2625	1312	1312	1312/2625	2450
Bunch population	N_{e}	10^{10}	2	2	2	2	2	1.74
Linac bunch interval	Δt_{b}	ns	554	366	554	554	554/366	366
Beam current in pulse	I_{pulse}	mA	5.8	5.8	8.8	5.8	5.8	7.6
Beam pulse duration	t_{pulse}	μs	727	961	727	727	727/961	897
Average beam power	P_{ave}	MW	5.3	10.5	10.5	xx	10.5/21	27.2
Norm. hor. emitt. at IP	$\gamma\epsilon_{\mathrm{x}}$	μm	5	5	10	xx	10	10
Norm. vert. emitt. at IP	$\gamma\epsilon_{\mathrm{y}}$	nm	35	35	35	xx	35	30
RMS hor. beam size at IP	σ^*_{x}	nm	516	516	729	xx	474	335
RMS vert. beam size at IP	σ^*_{y}	nm	7.7	7.7	7.7	xx	5.9	2.7
Luminosity in top 1 %	$\mathcal{L}_{0.01}/\mathcal{L}$		73 %	73 %	87.1 %	xx	58.3 %	44.5 %
Beamstrahlung energy loss	δ_{BS}		2.6 %	2.6 %	0.97 %	xx	4.5 %	10.5 %
Site AC power	P_{site}	MW	111	138	122	93	163	300
Site length	L_{site}	km	20.5	20.5	31	31	40	

Table 4.1: Summary table of the ILC accelerator parameters in the initial 250 GeV staged configuration (with TDR parameters at 250 GeV given for comparison) and possible upgrades. A 500 GeV machine could also be operated at 250 GeV with 10 Hz repetition rate, bringing the maximum luminosity to $5.4 \cdot 10^{34}\,\mathrm{cm}^{-2}\mathrm{s}^{-1}$ [10]. *COMPLETE NUMBERS*

world, and is in use at a number of free electron laser facilities that are in operation (E-XFEL at DESY, Hamburg), under construction (LCLS-II at SLAC, Stanford) or in preparation (SHINE in Shanghai) in the three regions Asia, Americas, and Europe that contribute to the ILC project. In preparation for the ILC, Japan and the U.S. have founded a collaboration for further cost optimisation of the TESLA technology. In recent years, new surface treatment technologies utilising nitrogen during the cavity preparation process, such as the so-called nitrogen infusion technique, have been developed at Fermilab, with the prospect of achieving higher gradients and lower loss rates with a less expensive surface preparation scheme than assumed in the TDR (see Sec. 4.3).

When the Higgs boson was discovered in 2012, the Japan Association of High Energy Physicists (JAHEP) made a proposal to host the ILC in Japan [12, 13]. Subsequently, the Japanese ILC Strategy Council conducted a survey of possible sites for the ILC in Japan, looking for suitable geological conditions for a tunnel up to 50 km in length (as required for a 1 TeV machine), and the possibility to establish a laboratory where several thousand international scientists can work and live. As a result, the candidate site in the Kitakami region in northern Japan, close to the larger cities of Sendai and Morioka, was found to be the best option. The site offers a large, uniform granite formation with no currently active faults and a geology that is well suited for tunnelling. Even in the great Tohoku earthquake in 2011, underground installations in this rock formation were essentially unaffected [14], which underlines the suitability of this candidate site.

This section starts with a short overview over the changes of the ILC design between the publication of the TDR in 2013 and today, followed by a description of the SCRF technology, and an description of the overall accelerator design and its subsystems. Thereafter, possible upgrade options are laid out, the Japanese candidate site in the Kitakami region is presented, and costs and schedule of the accelerator construction project are shown.

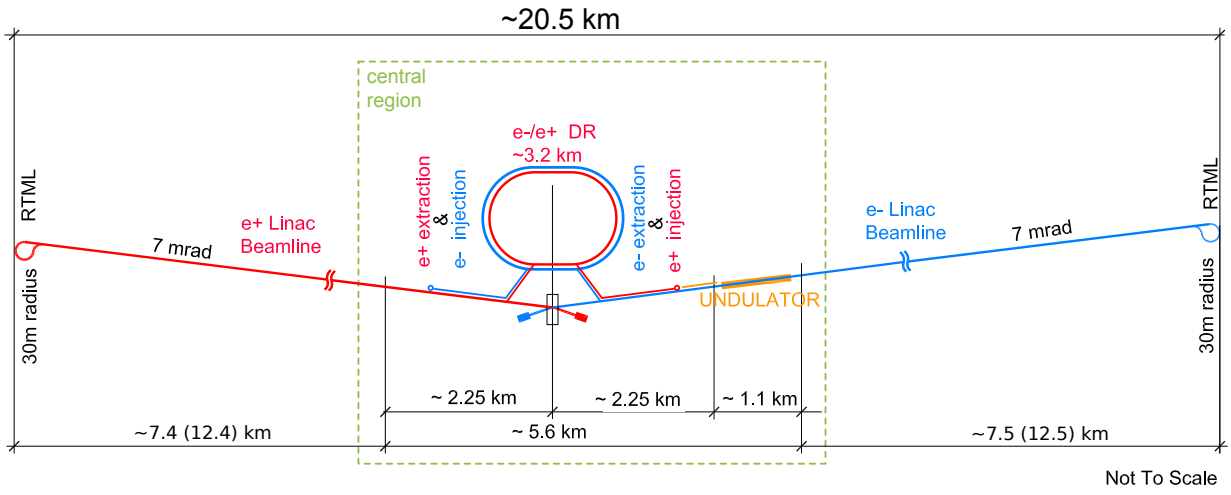

Figure 4.1: Schematic layout of the ILC in the 250 GeV staged configuration.

4.1.1 Design evolution since the TDR

Soon after the discovery of the Higgs boson, the Technical Design Report (TDR) for the ILC accelerator was published in 2013 [3, 4] after 8 years of work by the Global Design Effort (GDE). The TDR design was based on the requirements set forth by the ICFA mandated parameters committee [15]:

- a centre-of-mass energy of up to 500 GeV,
- tunability of the centre-of-mass energy between $\sqrt{s} = 200\,\text{GeV}$ and 500 GeV,
- a luminosity sufficient to collect $500\,\text{fb}^{-1}$ within four years of operation, taking into account a three-year a ramp up. This corresponds to a final luminosity of $250\,\text{fb}^{-1}$ per year and an instantaneous luminosity of $\mathcal{L} = 2 \cdot 10^{34}\,\text{cm}^{-2}\,\text{s}^{-1}$,
- an electron polarisation of at least 80 %,
- the option for a later upgrade to energies up to 1 TeV.

The accelerator design presented in the TDR met these requirements (see Tab. 4.1), at an estimated construction cost of 7,982 MILCU for a Japanese site, plus 22.9 Mh (million hours) of labour in participating institutes [4, Sec. 15.8.4]. Costs were expressed in ILC Currency Units ILCU, where 1 ILCU corresponds to 1 US$ at 2012 prices.

In the wake of the Higgs discovery, and the proposal by the Japan Association of High Energy Physicists (JAHEP) to host the ILC in Japan[12] with its recommendation to start with a 250 GeV machine [13], plans were made for a less expensive machine configuration with a centre–of–mass energy of $\sqrt{s} = 250\,\text{GeV}$, around the maximum of the Zh production cross section, half the TDR value. Various options were studied in the TDR [4, Sect. 12.5] and later [16]. This resulted in a revised proposal [9] for an accelerator with an energy of 250 GeV and a luminosity of $\mathcal{L} = 1.35 \cdot 10^{34}\,\text{cm}^{-2}\,\text{s}^{-1}$, capable of delivering about $200\,\text{fb}^{-1}$ per year, or $400\,\text{fb}^{-1}$ within the first four years of operation, taking into account the ramp-up.

Several other changes of the accelerator design have been approved by the ILC Change Management Board since 2013, in particular:

- The free space between the interaction point and the edge of the final focus quadrupoles (L^*) was unified between the ILD and SiD detectors [17], facilitating a machine layout with the best possible luminosity for both detectors.
- A vertical access shaft to the experimental cavern was foreseen [18], allowing a CMS-style assembly concept for the detectors, where large detector parts are built in an above-ground hall while the underground cavern is still being prepared.
- The shield wall thickness in the Main Linac tunnel was reduced from 3.5 to 1.5 m [19], leading to a significant cost reduction. This was made possible by dropping the requirement for personnel access during beam operation of the main linac.

- Power ratings for the main beam dumps, and intermediate beam dumps for beam aborts and machine tuning, were reduced to save costs [20].
- A revision of the expected horizontal beam emittance at the interaction point at 125 GeV beam energy, based on improved performance expectations for the damping rings and a more thorough scrutiny of beam transport effects at lower beam energies, lead to an increase of the luminosity expectation from 0.82 to $1.35 \cdot 10^{34}\,\mathrm{cm}^{-2}\,\mathrm{s}^{-1}$ [21].
- The active length of the positron source undulator has been increased from 147 to 231 m to provide sufficient intensity at 125 GeV beam energy [22].

These changes contributed to an overall cost reduction, risk mitigation, and improved performance expectation.

Several possibilities were evaluated for the length of the initial tunnel. Options that include building tunnels with the length required for a machine with $\sqrt{s} = 350\,\mathrm{GeV}$ or 500 GeV, were considered. In these scenarios, an energy upgrade would require the installation of additional cryomodules (with RF and cryogenic supplies), but little or no civil engineering activities. In order to be as cost effective as possible, the final proposal (see Figure 1), endorsed by ICFA [23], does not include these empty tunnel options.

While the length of the main linac tunnel was reduced, the beam delivery system and the main dumps are still designed to allow for an energy upgrade up to $\sqrt{s} = 1\,\mathrm{TeV}$.

Figure 4.2: A 1.3 GHz superconducting niobium nine-cell cavity.

4.1.2 Superconducting RF Technology

The heart of the ILC accelerator consists of the two superconducting Main Linacs that accelerate both beams from 5 to 125 GeV. These linacs are based on the TESLA technology: beams are accelerated in 1.3 GHz nine-cell superconducting cavities made of niobium and operated at 2 K (Fig. 4.2). These are assembled into cryomodules comprising nine cavities or eight cavities plus a quadrupole/corrector/beam position monitor unit, and all necessary cryogenic supply lines (Fig. 4.3). Pulsed klystrons supply the necessary radio frequency power (High-Level RF HLRF) to the cavities by means of a waveguide power distribution system and one input coupler per cavity.

This technology was primarily developed at DESY for the TESLA accelerator project that was proposed in 2001. Since then, the TESLA technology collaboration [24] has been improving this

technology, which is now being used in several accelerators in operation (FLASH at DESY [25, 26], E-XFEL in Hamburg [27]), under construction (LCLS-II at SLAC, Stanford, CA [28]) or planned (SHINE in Shanghai [29, 30]).

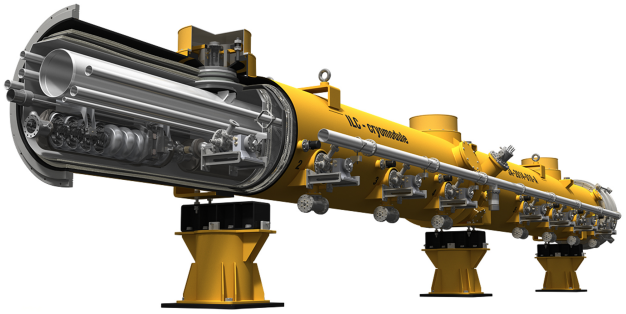

Figure 4.3: An ILC type cryomodule. ©Rey.Hori/KEK.

The quest for high gradients

The single most important parameter for the cost and performance of the ILC is the accelerating gradient g. The TDR baseline value is an average gradient $g = 31.5\,\mathrm{MV/m}$ for beam operation, with a $\pm 20\,\%$ gradient spread between individual cavities. Recent progress in R&D for high gradient cavities raises the hope to increase the gradient by $10\,\%$ to $g = 35\,\mathrm{MV/m}$, which would reduce the total cost of the 250 GeV accelerator by about $6\,\%$. To achieve the desired gradient in beam operation, the gradient achieved in the low-power vertical test (mass production acceptance test) is specified $10\,\%$ higher to allow for operational gradient overhead for low-level RF (LLRF) controls, as well as some degradation during cryomodule assembly (few MV/m). Figure 4.17 shows how the achievable gradients have evolved over the past 50 years.

Gradient impact on costs: To the extent that the cost of cavities, cryomodules and tunnel infrastructure is independent of the achievable gradient, the investment cost per GeV of beam energy is inversely proportional to the average gradient achieved. This is the reason for the enormous cost saving potential from higher gradients. This effect is partially offset by two factors: the energy stored in the electromagnetic field of the cavity, and the dynamic heat load to the cavity from the electromagnetic field. These grow quadratically with the gradient for one cavity, and therefore linearly for a given beam energy. The electromagnetic energy stored in the cavity must be replenished by the RF source during the filling time that precedes the time when the RF is used to accelerate the beam passing through the cavity; this energy is lost after each pulse and thus reduces the overall efficiency and requires more or more powerful modulators and klystrons. The overall cryogenic load is dominated by the dynamic heat load from the cavities, and thus operation at higher gradient requires larger cryogenic capacity. Cost models that parametrise these effects indicate that the minimum of the investment cost per GeV beam energy lies at 50 or more GeV,

depending on the relative costs of tunnel, SCRF infrastructure and cryo plants, and depending on the achievable Q_0 [31]. Thus, the optimal gradient is significantly higher than the value of approximately 35 MV/m that is currently realistic; this emphasises the relevance of achieving higher gradients.

It should be noted that in contrast to the initial investment, the operating costs rise when the gradient is increased, and this must be factored into the cost model.

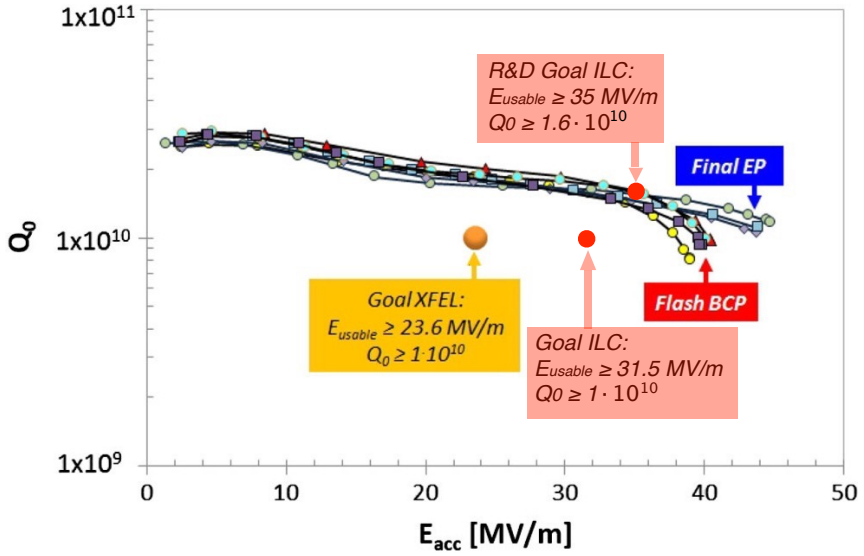

Figure 4.4: Examples of the Q_0 (E_{acc}) curves of some of the best cavities, either treated at RI using "EP final", or at EZ using "BCP flash." [32, Fig. 19]. Vendor "RI" employs a production process that closely follows the ILC specifications, with a final electropolishing step. The ILC gradient / Q_0 goals are overlaid.

Results from E-XFEL cavity production: The production and testing of 831 cavities for the E-XFEL [32, 33] provides the biggest sample of cavity production data so far. Cavities were acquired from two different vendors, RI and EZ. Vendor RI employed a production process with a final surface treatment closely following the ILC specifications, including a final electropolishing (EP) step, while the second vendor EZ used buffered chemical polishing (BCP). The E-XFEL specifications asked for a usable gradient of 23.6 MV/m with a $Q_0 \geq 1 \cdot 10^{10}$ for operation in the cryomodule; with a 10 % margin this corresponds to a target value of 26 MV/m for the performance in the vertical test stand for single cavities. Figure 4.4 shows the Q_0 data versus accelerating gradient of the best cavities received, with several cavities reaching more than 40 MV/m, significantly beyond the ILC goal, already with Q_0 values that approach the target value $1.6 \cdot 10^{10}$ that is the goal of future high-gradient R&D.

E-XFEL production data, in particular from vendor RI, provide excellent statistics for the cavity performance as received from the vendors, as shown in Fig. 4.5. For vendor RI, the yield for

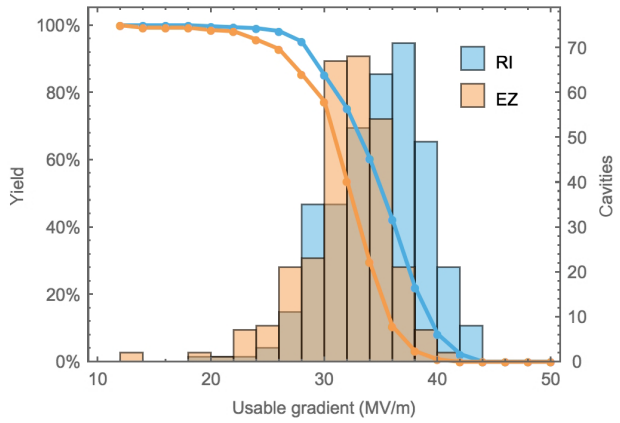

Figure 4.5: Distribution and yield of the "as received" maximum gradient of cavities produced for the E-XFEL, separated by vendor [33, Fig. 33]. Vendor RI employs a production process that closely follows the ILC specifications, with a final electro polishing step.

cavities with a maximum gradient above 28 MV/m is 85 %, with an average of 35.2 MV/m for the cavities that pass the cut.

Since the E-XFEL performance goal was substantially lower than the ILC specifications, cavities with gradient below 28 MV/m, which would not meet ILC specifications, were not generally re-treated for higher gradients, limiting our knowledge of the effectiveness of re-treatment for large gradients. Still, with some extrapolation it is possible to extract yield numbers applicable to the ILC specifications [34].

The E-XFEL data indicate that after re-treating cavities with gradients outside the ILC specification of 35 MV/m ± 20 %, *i.e.*, below 28 MV/m, a yield of 94 % for a maximum gradient above 28 MV/m can be achieved, with an average value of 35 MV/m, meeting the ILC specification. Taking into account limitations from Q_0 and the onset of field emission, the usable gradient is lower. This gives a 82 (91) % yield and an average usable gradient of 33.4 MV/m after up to one (two) re-treatments. The re-treatment and testing rate is significantly higher than assumed in the TDR, but the E-XFEL experience shows that re-treatment can mostly be limited to a simple high-pressure rinse (HPR) rather than an expensive electropolishing step.

Overall, the E-XFEL cavity production data prove that it is possible to mass-produce cavities meeting the ILC specifications as laid out in the TDR with the required performance and yield.

Basic parameters

The choice of operating frequency is a balance between the higher cost of larger, lower-frequency cavities and the increased cost at higher frequency associated with the lower sustainable gradient from the increased surface resistivity. The optimum frequency is in the region of 1.5 GHz, but during the early R&D on the technology, 1.3 GHz was chosen due to the commercial availability of

high-power klystrons at that frequency.

Cavities

The superconducting accelerating cavities for the ILC are nine-cell structures made out of high-purity niobium (Fig. 4.2), with an overall length of 1.25 m. Cavity production starts from niobium ingots which are forged and rolled into 2.8 mm thick niobium sheets that are individually checked for defects by an eddy current scan and optical inspection [3]. Cavity cells are produced by deep-drawing the sheets into half cells, 18 of which are joined by electron beam welding with two end groups to form the whole structure. This welding process is one of the most critical and cost-intensive steps of the cavity manufacturing procedure. Utmost care must be taken to avoid irregularities, impurities and inclusions in the weld itself, and deposition of molten material at the inner surface of the cavity that can lead to field emission.

After welding, the inner surface of the cavity must be prepared. The process is designed to remove material damage incurred by chemical procedures during the fabrication process, chemical residues from earlier production steps, hydrogen in the bulk niobium from earlier chemical processing, and contamination from particles. In a last step, the cavity is closed to form a hermetically sealed structure ready for transport. The treatment steps involve a series of rinses with ethanol or high pressure water, annealing in a high purity vacuum furnace at 800° C and 120° C, and electropolishing or buffered chemical polishing. The recipe for the surface preparation has been developed over a long time. Still, it remains subject to optimisation, since it is a major cost driver for the cavity production and largely determines the overall performance and yield of the cavities. In particular the electropolishing steps are complicated and costly, as they require complex infrastructure and highly toxic chemicals. One advantage of nitrogen infusion (see Sec. 4.1.2) is that the final electropolishing step is omitted.

Careful quality control during the production process is of high importance. At the E-XFEL, several quality controls were conducted by the manufacturer during production, with nonconformities reported to the institute responsible for the procurement, where a decision was made whether to accept or reject a part [32]. With this "build to print" approach, in which the manufacturer guarantees that a precise production process will be followed but does not guarantee a specific performance, procurement costs are reduced, because the manufacturer does not carry, and does not charge for, the performance risk.

Upon reception from the manufacturer, cavities are tested in a vertical cryostat ("vertical test"), where Q_0 is measured as a function of the gradient. Cavities that fall below the specified gradient goal are re-treated by an additional (expensive) electropolishing step or a comparatively simple high-pressure rinse. After retreatment, the vertical test is repeated.

Re-treatment and tests constitute a major cost driver in cavity production. For the ILC TDR, it was assumed that 25 % of the cavities would fall below the 28 MV/m gradient threshold and undergo re-treatment and a second vertical test. E-XFEL data from the vendor "RI" that followed the ILC production recipe indicate that 15 % to 37 % of the cavities fall below 28 MV/m, depending on whether the maximum or the "usable" achieved gradient is considered [34]. However, E-XFEL

experience also shows that, in most of the cases, a high-pressure rinse is sufficient as re-treatment to remove surface defects, which is a cost saving compared to the electropolishing assumed in the TDR.

After successful testing, prior to installation in the cryomodule, cavities are equipped with a magnetic shield and the frequency tuner, which exerts mechanical force on the cavity to adjust the resonant frequency to the frequency of the external RF field [4, Sect. 3.3].

Power coupler

The power coupler transfers the radio frequency (RF) power from the waveguide system to the cavity. In the ILC, a coupler with a variable coupling is employed; this is realised using a movable antenna. Another role of the coupler is to separate the cavity vacuum from the atmospheric pressure in the waveguide, and to insulate the cavity at 2 K from the surrounding room temperature. Thus, the coupler has to fulfill a number of demanding requirements: transmission of high RF power with minimal losses and no sparking, vacuum tightness and robustness against window breaking, and minimal heat conductivity. As a consequence, the coupler design is highly complex, with a large number of components and several critical high-tech manufacturing steps.

The baseline coupler design was originally developed in the 1990s for the TESLA Test Facility (TTF, now FLASH) at DESY, and has since been modified by a collaboration of LAL and DESY for use in the E-XFEL. About 840 of these couplers (depicted in Fig. 4.6) were fabricated by three different companies for the E-XFEL [35], where 800 are now in operation. A lot of experience has been gained from this production [36].

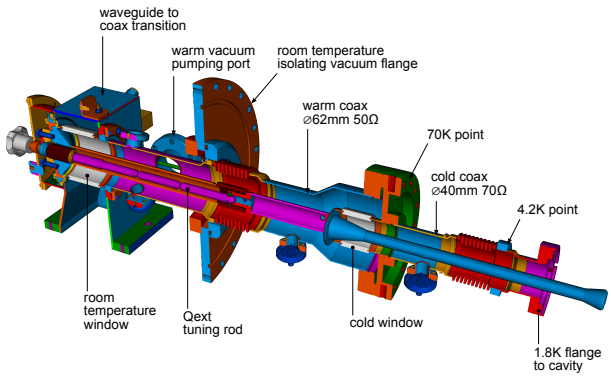

Figure 4.6: An E-XFEL type coupler.

Cryomodules

To facilitate transportation, installation and operation, 8 or 9 cavities are integrated into a 12.6 m long cryomodule (Fig. 4.3), which houses the cavities, thermal insulation, and all necessary supply tubes for liquid and gaseous helium at $2 - 80$ K temperature.

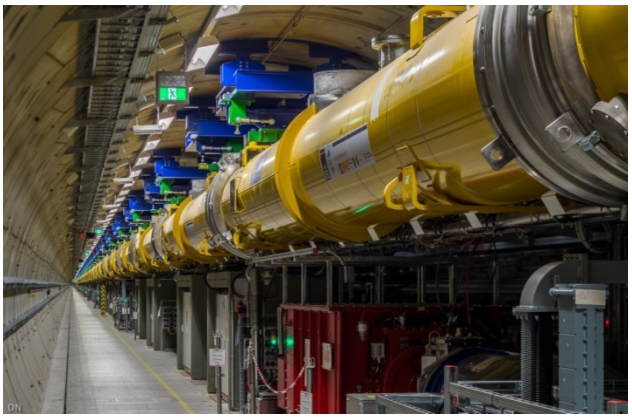

Figure 4.7: View of installed cryomodules in the tunnel of the E-XFEL [37].

Nine of these cryomodules are connected in the tunnel to form a cryostring with a common liquid helium supply. RF for one such string is provided by two klystrons. No separate helium transfer line is necessary, as all helium transport lines are integrated within the modules. A quadrupole / beam position monitor / corrector magnet unit is mounted instead of the 9th cavity in every third module. Figure 4.7 shows installed cryomodules in the tunnel of the E-XFEL [37].

Cryomodule assembly requires a dedicated facility with large clean rooms, especially trained, experienced personnel, and thorough quality control [38]. The cryomodules are certified for liquid helium pressure of up to 2 bar. Thus they must conform to the applicable pressure vessel codes, which brings with it very stringent documentation requirements for all pressure bearing parts [39].

For the E-XFEL project, 103 cryomodules were assembled in a facility built and operated by CEA [40, 38] and industrial partners, demonstrating the successful industrialization of the assembly process, with a final throughput of one cryomodule every four working days. This production rate is close to the rate envisaged for a possible European contribution of 300 cryomodules to a 250 GeV ILC in Japan.

While the design gradient for E-XFEL accelerator modules of 23.6 MV/m is significantly lower than the aim of $31.5 - 35$ MV/m for the ILC, a number of cryomodules have been built around the world that come close or reach the ILC TDR specification of 31.5 MV/m: An E-XFEL prototype module at DESY reached 30 MV/m [41], Fermilab has demonstrated cryomodule operation at the ILC specification of 31.5 MV/m [42], and KEK has reported stable pulsed operation of a cryomodule at 36 MV/m [43].

Figure 4.8 shows the average cavity gradients per cryomodule for the E-XFEL serial-production cryomodules [44]. In the tests, the gradients were limited administratively to 31 MV/m; the true maxima might be higher. For almost all of the modules, the cavity gradients are significantly above the E-XFEL specification of 23.6 MV/m.

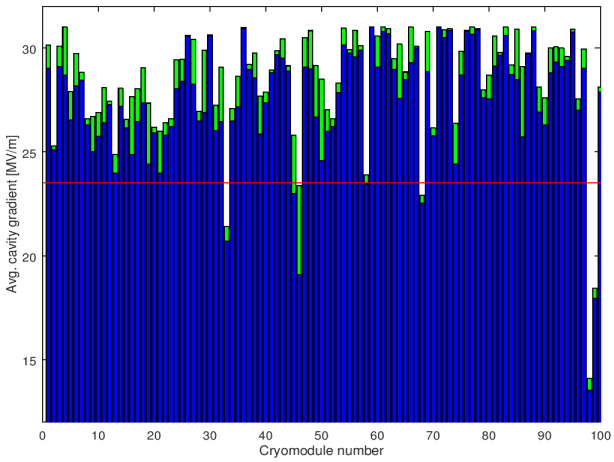

Figure 4.8: Average of the operating (blue) and maximum (green) gradient for cavities in each E-XFEL serial-production cryomodule. The specification of 23.6 MV/m is marked by a red line [44]. Modules 98 and 99 were assembled from the lowest-performing cavities.

Plug-compatible design

In order to allow various designs of sub-components from different countries and vendors to work together in the same cryomodule, a set of interface definitions has been internationally agreed upon. This "plug-compatible" design ensures that components are interchangeable between modules from different regions and thus reduces the cost risk. Corresponding interface definitions exist for the cavity, the fundamental-mode power coupler, the mechanical tuner and the helium tank. The "S1Global" project [45] has successfully built a single cryomodule from several cavities equipped with different couplers and tuners, demonstrating the viability of this concept.

High-level radio-frequency

The high-level radio-frequency (HLRF) system provides the RF power that drives the accelerating cavities. The system comprises modulators, pulsed klystrons, and a waveguide power distribution system.

Modulators: The modulators provide the short, high-power electrical pulses required by the pulsed klystrons from a continuous supply of electricity. The ILC design foresees the use of novel, solid state Marx modulators. These modulators are based on a solid-state switched capacitor network, where capacitors are charged in parallel over the long time between pulses, and discharged in series during the short pulse duration, transforming continuous low-current, low voltage electricity into short high-power pulses of the required high voltage of 120 kV at a current of 140 A, over 1.65 ms. Such Marx modulators have been developed at SLAC [46] and successfully tested at KEK [47]. However, long-term data about the required large mean time between failures (MTFB)

are not yet available.

Klystrons: The RF power to drive the accelerating cavities is provided by 10 MW L-band multi-beam klystrons. Devices meeting the ILC specifications were initially developed for the TESLA project, and later for the E-XFEL. They are now commercially available from two vendors (Thales and Toshiba), both of which provided klystrons for the E-XFEL. The ILC specifications ask for a 65 % efficiency (drive beam to output RF power), which are met by the existing devices.

Recently, the High Efficiency International Klystron Activity (HEIKA) collaboration [48, 49] has been formed that investigates novel techniques for high–efficiency klystrons. Taking advantage of modern beam dynamic tools, methods such as the Bunching, Alignment and Collecting (BAC) method [50] and the Core Oscillation Method (COM) [51] (Fig. 4.9) have been developed that promise increased efficiencies up to 90 % [52]. One advantage of these methods is that it is possible to increase the efficiency of existing klystrons by equipping them with a new electron optics, as was demonstrated retrofitting an existing tube from VDBT, Moscow. This increased the output power by almost 50 % and its efficiency from 42 % to 66 % [53].

To operate the ILC at an increased gradient of 35 MV/m would require that the maximum klystron output power is increased from 10 to 11 MW. It is assumed that this will be possible by applying the results from this R&D effort to high-efficiency klystrons.

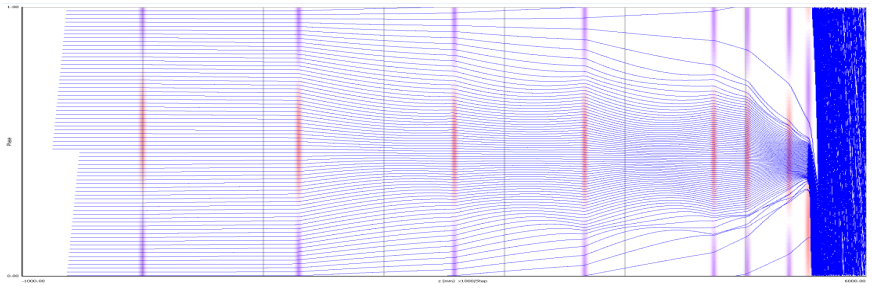

Figure 4.9: Electron phase profile of an 800 MHz klystron employing the Core Oscillation Method (COM) [51].

Local Power–Distribution System (LPDS): In the baseline design, a single RF station with one modulator and klystron supplies RF to 39 cavities, which corresponds to 4.5 cryomodules [4, Sec. 3.6.4]. Then 2 klystrons drive a 9 cryomodule cryo-string unit. The power is distributed by the LPDS, a system of waveguides, power dividers and loads. All cavities from a 9-cavity module and half of a 8–cavity module are connected in one LPDS, and three such LPDS units are connected to one klystron. This arrangement allows an easy refurbishment such that a third klystron can be added to a cryo-string, increasing the available power per cavity by 50 % for a luminosity upgrade (cf. Sec. **??**).

The LPDS design must provide a cost–effective solution for the distribution of the RF power with minimal losses, and at the same time provide the flexibility to adjust the power delivered to

each cavity by at least ±20 % to allow for the specified spread in maximum gradient. The LPDS design therefore contains remotely controlled, motor-driven Variable Power Dividers (VPD), phase shifters, and H–hybrids that can distribute the power with the required flexibility. This design allows one to optimise the power distribution during operation, based on the cavity performance in the installed cryomodule, and thus to get the optimum performance out of the system. It does not require a measurement of the individual cavity gradients after the module assembly, and is thus compatible with the ILC production scheme, where only a fraction of the cryomodules are tested. This is a notable difference from the scheme employed at the E-XFEL, where 100 % of the modules were tested, and the the power distribution for each module was tailored to the measured cavity gradients, saving investment costs for the LPDS but making the system less flexible.

Cryogenics

The operation of the large number of superconducting cryomodules for the main linacs and the linacs associated with the sources requires a large–scale supply of liquid helium. The cyomodules operate at 2 K and are cooled with superfluid helium, which at 2 K has a vapour pressure of about 32 mbar.

The accelerator is supplied with liquid helium by several cryogenic plants [4, Sec. 3.5] of a size similar to those in operation at CERN for the LHC, at Fermilab, and DESY, with a cooling capacity equivalent to about 19 kW at 4.5 K. The 2 K and 4.5 K helium refrigerators are located in an underground access hall [54] that is connected to the surface, where the helium compressors, gas tanks and further cryogenic infrastructure are located. The total helium inventory is approximately 310000 liquid litres or about 41 metric tonnes, about one third of the LHC's helium inventory. A factor 2 more helium is needed for 500 GeV operation.

Series production and industrialisation

Due to the construction of the E-XFEL, the industrial basis for the key SCRF components is broad and mature. In all three regions (Europe, America, Asia), several vendors for cavities have been qualified for ILC type cavities, and provided cost estimates in the past. RF couplers have also been successfully produced by European and American vendors for the E-XFEL and LCLS-II projects.

ILC/TESLA type cryomodules have been built in laboratories around the world (DESY, CEA in Europe, FNAL and JLAB in America, KEK in Asia). Series production has been established in America at Fermilab and JLAB for LCLS-II. The largest series production was conducted by CEA in France, again for the E-XFEL, with the assembly of 103 cryomodules in total by an industrial partner under the supervision of CEA personnel, with a final throughput of one cryomodule produced every four working days.

ILC type, pulsed 10 MW klystrons are commercially available from two vendors in Japan and Europe.

4.1.3 Accelerator design

Electron and positron sources

The electron and positron sources are designed to produce 5 GeV beam pulses with a bunch charge that is 50 % higher than the design bunch charge of 3.2 nC ($2 \cdot 10^{10}$ e), in order to have sufficient reserve to compensate any unforeseen inefficiencies in the beam transport. In the baseline design, both sources produce polarized beams with the same time structure as the main beam, *i.e.*, 1312 bunches in a 727 μs long pulse.

The electron source design [4] is based on the SLC polarized electron source, which has demonstarted that the bunch charge, polarisation and cathode lifetime parameters are feasible. The long bunch trains of the ILC do require a newly developed laser system and powerful preaccelerator structures, for which preliminary designs are available. The design calls for a Ti:sapphire laser impinging on a photocathode based on a strained GaAs/GaAsP superlattice structure, which will produce electron bunches with an expected polarisation of 85 %, sufficient for 80 % beam polarization at the interaction point, as demonstrated at SLAC [55].

The positron source poses a larger challenge.

In the baseline design, hard gamma rays are produced in a helical undulator driven by the main electron beam, which are converted to positrons in a rotating target. Positrons are captured in a flux concentrator or a quarter wave transformer, accelerated to 400 MeV in two normal conducting preaccelerators followed by a superconducting accelerator very similar to the main linac, before they are injected into the damping rings at 5 GeV. The helical undulators produce photons with circular polarisation, which is transferred to the positrons produced in the target, which are longitudinally polarised as a result. The positron polarisation thus achieved is 30 %. The E-166 experiment at SLAC has successfully demonstrated this concept [56], albeit at intensities much lower than foreseen for the ILC. Technological challenges of the undulator source concept are the target heat load, the radiation load in the flux concentrator device, and the dumping of the high intensity photon beam remnant.

As an alternative, an electron-driven positron source concept has been developed. In the electron-driven scheme, a 3 GeV electron beam from a dedicated normal conducting linac produces positrons in a rotating target. The electron drive beam, being independent from the main linac, has a completely different time structure. Positrons are produced in 20 pulses at 300 Hz with 66 bunches each. With this scheme, it takes about 67 ms to produce the positrons needed for a single Main Linac pulse with its 1312 bunches, compared to 0.8 ms for the undulator source. This different time structure spreads the heat load on the target over a longer time, allowing a target rotation speed of only 5 m/s rather than 100 m/s, which reduces the engineering complexity of the target design, in particular the vacuum seals of the rotating parts. Although not free from its own engineering challenges, such as the high beam loading in the normal conducting cavities, the electron driven design is currently considered to be a low risk design that is sure to work.

Aside from the low technical risk, the main advantage of the electron driven design is the independence of positron production and electron main linac operation, which is an advantage for

accelerator commissioning and operation in general. In particular, electron beam energies below 120 GeV for operation at the Z resonance or the WW threshold would be no problem. The undulator source, on the other hand, offers the possibility to provide beams at the maximum repetition rate of 10 Hz given by the damping time in the damping rings of 100 ms, whereas the electron driven scheme is limited to 6 Hz due to the additional 66 ms for positron production. The main difference between the concepts is the positron polarisation offered by the undulator source, which adds significantly to the physics capabilities of the machine. The physics implications of positron polarization is discussed later in the report, in Sec. 5.3.

Both concepts have been reviewed recently [22] inside the ILC community, with the result that both source concepts appear viable, with no known show stoppers, but they require some more engineering work. The decision on the choice will be taken once the project has been approved, based on the physics requirements, operational aspects, and technological maturity and risks.

Beam polarisation and spin reversal At the ILC, the electron beam and potentially the positron beam are longitudinally polarised at the source, *i.e.*, the polarisation vector is oriented parallel or antiparallel to the beam direction. Whenever a longitudinally polarised beam of energy E_{beam} is deflected by an angle θ_{bend}, the polarisation vector undergoes a precession through an angle $\theta_{\text{pol}} = \gamma a \theta_{\text{bend}}$ [57], with the Lorentz factor $\gamma = E_{\text{beam}}/m_{\text{e}}$ and the electron's anomalous magnetic moment $a = (g-2)/2$. To preserve the longitudinal beam polarisation during the long transport from the source through the damping rings to the start of the main linac, which involves many horizontal bends, the beam polarisation vector is rotated into the transverse plane, perpendicular to the damping ring plane, before the beam is transferred to the damping rings, and rotated back to a longitudinal direction by a set of spin rotators at the end of the RTML (see Sec. 4.1.3). Through the use of two rotators, it is possible to bring the polarisation vector into any desired direction, and compensate any remaining net precession between these spin rotators and the interaction point, so that any desired longitudinal or transverse polarisation at the IP can be provided.

To control systematic effects, fast helicity reversal is required. This is helicity reversal of each beam independently, on a pulse to pulse basis, which must be achieved without a change of the magnetic fields of the spin rotator magnets. For the electron beam, a fast helicity reversal is possible through a flip of the cathode laser polarisation. For the undulator-based positron source, the photon polarisation is given by the undulator field. Two parallel sets of spin rotators in front of the damping rings are used that rotate the polarisation vector either to the $+y$ or $-y$ direction. With this scheme, fast kickers can select a path through either of the two spin rotators and thus provide a fast spin reversal capability [57, 58].

Damping rings

The ILC includes two oval damping rings of 3.2 km circumference, sharing a common tunnel in the central accelerator complex. The damping rings reduce the horizontal and vertical emittance of the beams by almost six orders of magnitude[1] within a time span of only 100 ms, to provide the

[1] The vertical emittance of the positrons is reduced from $\epsilon_{\text{y}} \approx 0.8\,\mu$m to 2 pm.

low emittance beams required at the interaction point. Both damping rings operate at an energy of 5 GeV.

The damping rings' main objectives are

- to accept electron and positron beams at large emittance and produce the low-emittance beams required for high-luminosity production.
- to dampen the incoming beam jitter to provide highly stable beams.
- to delay bunches from the source and allow feed-forward systems to compensate for pulse-to-pulse variations in parameters such as the bunch charge.

Compared to today's fourth generation light sources, the target value for the normalized beam emittance (4 μm/20 nm for the normalised horizontal / vertical beam emittance) is low, but not a record value, and it is thus considered to be a realistic goal.

The main challenges for the damping ring design are to provide

- a sufficient dynamic aperture to cope with the large injected emittance of the positrons.
- a low equilibrium emittance in the horizontal plane.
- a very low emittance in the vertical plane.
- a small damping time constant.
- damping of instabilities from electron clouds (for the positron DR) and fast ions (for the electron DR).
- a small ($3.2 - 6.4$ ns) bunch spacing, requiring very fast kickers for injection and ejection.

Careful optimization has resulted in a TME (Theoretical Minimum Emittance) style lattice for the arcs that balances a low horizontal emittance with the required large dynamic aperture [4, Chap. 6]. Recently, the horizontal emittance has been reduced further by lowering the dispersion in the arcs through the use of longer dipoles [21]. The emittance in the vertical plane is minimised by careful alignment of the magnets and tuning of the closed orbit to compensate for misalignments and field errors, as demonstrated at the CESR-TA facility [59].

The required small damping time constant requires large synchrotron radiation damping, which is provided by the insertion of 54 wigglers in each ring. This results in an energy loss of up to 7.7 MV per turn and up to 3.3 MW RF power to store the positron beam at the design current of 390 mA. This actually exceeds the average beam power of the accelerated positron beam, 2.6 MW at a 250 GeV.

Electron cloud (EC) and fast ion (FI) instabilities limit the overall current in the damping rings to about $400 - 800$ mA, where the EC limit that affects the positrons is assumed to be more stringent. These instabilities arise from electrons and ions being attracted by the circulating beam

towards the beam axis. A low base vacuum pressure of 10^{-7} Pa is required to limit these effects to the required level. In addition, gaps between bunch trains of around 50 bunches are required in the DR filling pattern, which permits the use of clearing electrodes to mitigate EC formation. These techniques have been developed and tested at the CESR-TA facility [60]

In the damping rings, the bunch separation is only 6.4 ns (3.2 ns for a luminosity upgrade to 2625 bunches). Extracting individual bunches without affecting their emittance requires kickers with rise/fall times of 3 ns or less. Such systems have been tested at ATF [61].

The damping ring RF system will employ superconducting cavities operating at half the Main Linac frequency (650 MHz). Klystrons and accelerator modules can be scaled from existing 500 MHz units in operation at CESR and KEK [4, Sec. 6.6].

Low emittance beam transport: ring to Main Linac (RTML)

The Ring to Main Linac (RTML) system [4, Chap. 7] is responsible for transporting and matching the beam from the Damping Ring to the entrance of the Main Linac. Its main objectives are

- transport of the beams from the Damping Rings at the center of the accelerator complex to the upstream ends of the Main Linacs,
- collimation of the beam halo generated in the Damping Rings,
- rotation of the spin polarisation vector from the vertical to the desired angle at the IP (typically, in longitudinal direction).

The RTML consists of two arms for the positrons and the electrons. Each arm comprises a damping ring extraction line transferring the beams from the damping ring extraction into the main linac tunnel, a long low emittance transfer line (LTL), the turnaround section at the upstream end of each accelerator arm, and a spin rotation and diagnostics section.

The long transport line is the largest, most costly part of the RTML. The main challenge is to transport the low emittance beam at 5 GeV with minimal emittance increase, and in a cost-effective manner, considering that its total length is about 14 km for the 250 GeV machine.

In order to preserve the polarisation of the particles generated in the sources, their spins are rotated into a vertical direction (perpendicular to the Damping Ring plane) before injection into the Damping Rings. A set of two rotators [62] employing superconducting solenoids allows to rotate the spin into any direction required.

At the end of the RTML, after the spin rotation section and before injection into the bunch compressors (which are considered part of the Main Linac, not the RTML [63]), a diagnostics section allows measurement of the emittance and the coupling between the horizontal and vertical plane. A skew quadrupole system is included to correct for any such coupling.

A number of circular fixed-aperture and rectangular variable-aperture collimators in the RTML provide betatron collimation at the beginning of the LTL, in the turn around and before the bunch compressors.

Bunch compressors and Main Linac

Figure 4.10: Artist's rendition of the ILC Main Linac tunnel. The shield wall in the middle has been removed. ©Rey.Hori/KEK.

The heart of the ILC are the two Main Linacs, which accelerate the beams from 5 to 125 GeV. The linac tunnel, as depicted in Figs. 4.10 and 4.11, has two parts, separated by a shield wall. One side (on the right in Fig. 4.10) houses the beamline with the accelerating cryomodules as well as the RTML beamline hanging on the ceiling. The other side contains power supplies, control electronics, and the modulators and klystrons of the High-Level RF system. The concrete shield wall (indicated as a dark-grey strip in in Fig. 4.10) has a thickness of 1.5 m [19]. The shield wall allows access to the electronics, klystrons and modulators during operation of the klystrons with cold cryomodules, protecting personnel from X-ray radiation emanating from the cavities caused by dark currents. Access during beam operation, which would require a wall thickness of 3.5 m, is not possible.

The first part of the Main Linac is a two-stage bunch compressor system [4, Sec. 7.3.3.5], each consisting of an accelerating section followed by a wiggler. The first stage operates at 5 GeV, with no net acceleration, the second stage accelerates the beam to 15 GeV. The bunch compressors reduce the bunch length from 6 to 0.3 mm.

After the bunch compressors, the Main Linac continues for about 6 km with a long section consisting entirely of cryomodules, bringing the beam to 125 GeV.

RF distribution: Each cryomodule contains 9 cavities, or for every third module, 8 cavities and a package with a superconducting quadrupole, corrector magnets, and beam position monitor. Nine

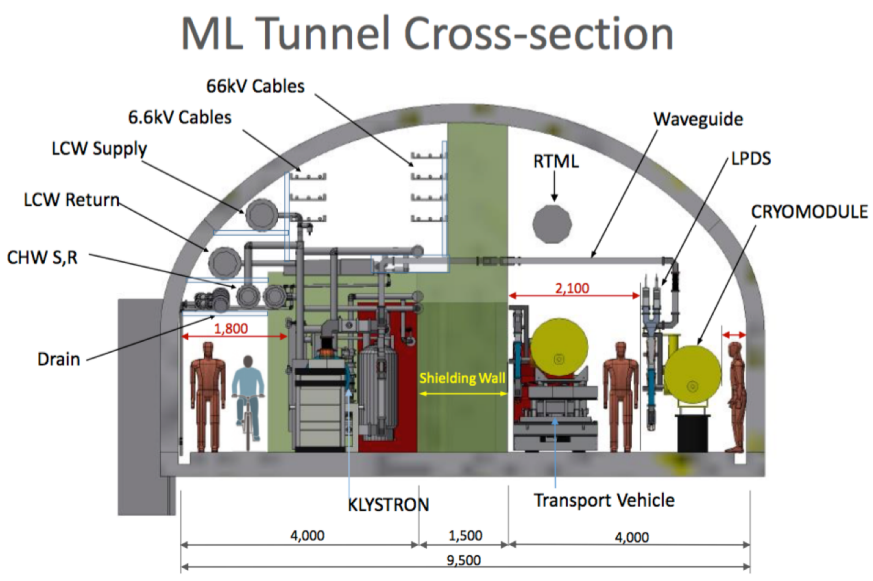

Figure 4.11: Cross section through the Main Linac tunnel.

such modules, with a total of 78 cavities, are powered by 2 klystrons and provide 2.54(2.82) GeV at a gradient of 31.5(35) MV/m. Table 4.2 gives an overview over the units that form the linacs. The waveguide distribution system allows an easy refurbishment to connect a third klystron for a luminosity upgrade. The 50 % RF power increase would allow 50 % higher current through smaller bunch separation, and longer beam pulses because of a reduced filling time, so that the number of bunches per pulse and hence the luminosity can be doubled, while the RF pulse duration of 1.65 ms stays constant.

Cryogenic supply: A 9 module unit forms a cryo string, which is connected to the helium supply line with a Joule-Thomson valve. All helium lines are part of the cryomodule, obviating the need for a separate helium transfer line. Up to 21 strings with 189 modules and 2.4 km total length can be connected to a single plant; this is limited by practical plant sizes and the gas–return header pressure drop.

Cost reduction from larger gradients: Figure 4.12 shows the layout of the cryogenic supply system for the 250 GeV machine. At the top, the situation is depicted for the gradient of 31.5 MV/m with a quality factor of $Q_0 = 1.0 \cdot 10^{10}$, as assumed in the TDR [4]. In this case, the access points PM±10 would house two cryogenic plants, each supplying up to 189 cryomodules or an equivalent cryogenic load. In this configuration 6 large plants in the access halls plus 2 smaller plants in the central region would be needed. The bottom picture shows the situation for a gradient of 35 MV/m with $Q_0 = 1.6 \cdot 10^{10}$, as could be expected from successful R&D. The increased gradient would allow reduction of the total number of cryomodules by roughly 10 % from 987 to 906. The increased quality factor would reduce the dynamic losses such that 4 cryo plants would provide

Unit	Comprises	Length	Voltage
Cavity	1.038 m active length	1.25 m	32.6 / 36.2 MV
Cryomodule	$8\,^2/_3$ cavities	12.65 m	282 / 314 MV
RF Unit	4.5 cryomodules	58.2 m	1.27 / 1.41 GV
Cryostring	2 RF units	116.4 m	2.54 / 2.82 GV
Cryounit	up to 21 cryostrings	2454 m	53.4 / 39.3 GV

Table 4.2: Units that make up the main linacs. The voltage takes into account that the beam is 5° shifted in phase ("off crest") for longitudinal stability, and is given for an average gradient of 31.5/35 MV/m. A RF unit is powered by one klystron, each cryostring is connected by a valve box to the liquid helium supply, and a cryounit is supplied by one cryogenic plant. Total lengths include additional space between components. Cryomodules comprise 9 or 8 cavities, in a 2 : 1 mixture, resulting in $8\,^2/_3$ cavities per cryomodule on average.

sufficient helium.

In general, the accelerator is designed to make good use of any anticipated performance gain from continued high gradient R&D, in the case that raising the gradient is seen to be beneficial from an economical point of view, without incurring unwanted technology risk.

Beam delivery system and machine detector interface

The Beam Delivery System (BDS) transports the e^+/e^- beams from the end of the main linacs, focuses them to the required small beam spot at the Interaction Point (IP), brings them into collision, and transports the spent beams to the main dumps [4, Chap. 8]. The main functions of the BDS are

- measuring the main linac beam parameters and matching it into the final focus.
- protecting beamline and detector from mis-steered beams [2].
- removing large amplitude (beam–halo) and off–momentum particles from the beam to minimize background in the detector.
- accurately measuring the key parameters energy and polarisation before and after the collisions.

The BDS must provide sufficient diagnostic and feedback systems to achieve these goals.

The BDS is designed such that it can be upgraded to a maximum beam energy of 500 GeV; components such as the beam dumps, that are not cost drivers for the overall project but would be cumbersome to replace later, are dimensioned for the maximum beam energy from the beginning.

[2] On the electron side, the protective fast beam abort system is actually located upstream of the positron source undulator.

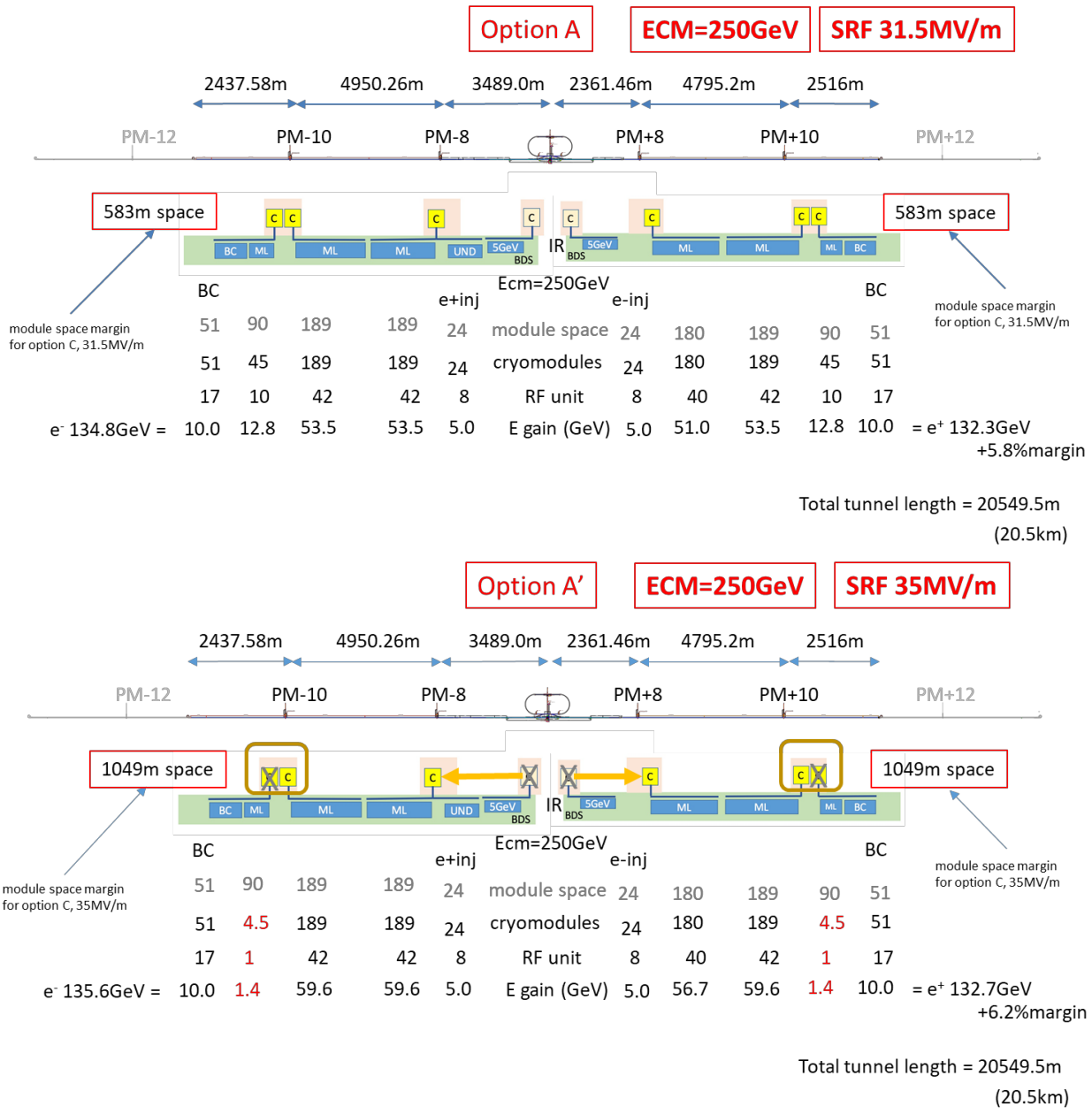

Figure 4.12: Cryogenic layout for a gradient of 31.5 MV/m (top) and 35 MV/m (bottom) [9]. "Module space" indicates how many cryomodules can be physically installed, "cryomodules" and "RF unit" indicates the number of actually installed modules and klystrons (one klystron per 4.5 cryomodules). "E gain" indicates the energy gain in GeV. "BC", "ML", "e+ inj", "e- inj" and "UND" refer to the sections with need for liquid helium: bunch compressor, main linac, 5GeV boosters in the positron and electron source, and the positron source undulator section, respectively. PM$\pm$8, 10, 12 refer to access hall locations, "C" to cryo plants; meter numbers on top indicate the length of the corresponding section.

In other places, such as the energy collimation dogleg, those components necessary for 125 GeV beam operation are installed and space for a later upgrade is reserved.

Overall, the BDS is 2254 m long from the end of the main linac (or the undulator and target bypass insert of the positron source on the electron side, respectively) to the IP.

Diagnostics and collimation section: The BDS starts with a diagnostics section, where emittance, energy and polarisation are measured and any coupling between the vertical and horizontal planes is corrected by a set of skew quadrupoles. The energy measurement is incorporated into the machine protection system and can, *e.g.*, extract off-momentum bunches caused by a klystron failure in the main linac that would otherwise damage the machine or detector. An emergency dump [20] is dimensioned such that it can absorb a full beam pulse at 500 GeV, sufficient for 1 TeV operation.

The diagnostics section is followed by a collimation system, which first removes beam halo particles (betatron collimation). Then, off-momentum particles are removed. In this energy collimation section, sufficient dispersion must be generated by bending the beam in a dogleg, while avoiding excessive synchrotron radiation generation in dispersive regions that leads to an increase of the horizontal emittance. This emittance dilution effect grows as E_{beam}^6 at constant bending radius for the normalised emittance, and determines the overall length of the energy collimation section for a maximum 500 GeV beam energy to about 400 m.

Final focus with feedback system and crab cavities: The final focus system demagnifies the beam to the required spot size of $516 \times 7.7\,\mathrm{nm}^2$ by means of a final quadrupole doublet. Even the relatively small energy spread of $\approx 0.1\,\%$ leads to a significant spread of the focal length of the doublet and requires a correction to achieve the desired beam size, which is realised by a local chromaticity correction scheme [64].

To bring the beams to collision with the neccessary nanometre accuracy requires a continuous compensation of drift and vibration effects. Along the ILC, the pulse length and bunch separation (727 μs and 554 ns, respectively) are large enough to allow corrections between pulses as well as within a bunch train (intratrain feedback). Beam-beam offsets of a fraction of the beam size lead to a measurable deflection of the outgoing beams,and these measurements are used to feed fast stripline kickers that stabilize the beam. Finally, the 3.9 GHz crab cavities close to the interaction point are incorporated that rotate the bunches to compensate for the 14 mrad beam crossing angle [4, Sect. 8.9].

Test results from ATF2: The Accelerator Test Facility 2 (ATF2) was built at KEK in 2008 as a test bench for the ILC final focus scheme [3, Sec. 3.6]. Its primary goals were to achieve a 37 nm vertical beam size at the interaction point (IP), and to demonstrate beam stabilisation at the nanometre level [65, 66]. After scaling for the different beam energies (ATF2 operates at $E_{\mathrm{beam}} = 1.3\,\mathrm{GeV}$), the 37 nm beam size corresponds to the TDR design value of $\sigma_{\mathrm{y}}^* = 5.7\,\mathrm{nm}$ at 250 GeV beam energy. As Fig. 4.13 shows, this goal has been reached within 10 % [67] by the

successive application of various correction and stabilisation techniques, validating the final focus design, in particular the local chromaticity correction [68].

The fifth generation FONT5 feedback system [69] for the ILC and CLIC has also been tested at the ATF2, where a beam stabilisation to 41 nm has been demonstrated, in excellent agreement with the predicted one given the incoming bunch jitter and bunch-to-bunch correlation [70].

Since November 2016, intensity-dependence effects on the ATF2 beam size have been studied extensively. They show a degradation of the beam size with increasing intensity that is compatible with the effect of wakefields. Simulations and experiments in ATF2 show that the effect is not important when scaled to ILC. Also, it could be mitigated by including a dedicated "wakefield knob" in the routine tuning procedure.

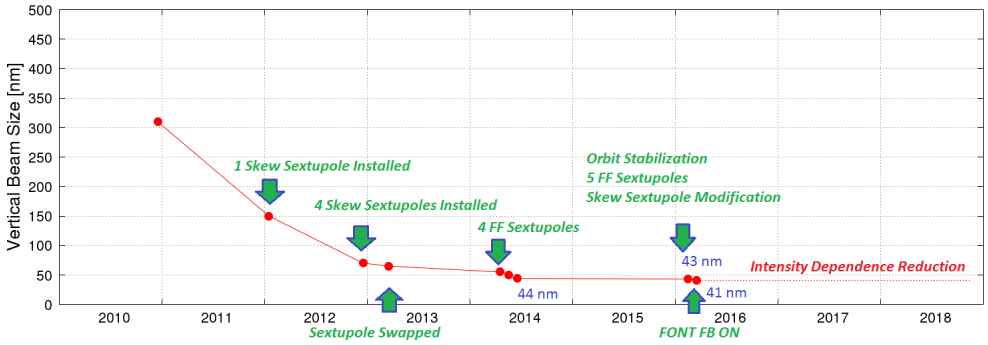

Figure 4.13: Beamsizes achieved at the Accelerator Test Facility 2 (ATF2) as a function of time [71]. The latest result (41 nm [67]) is within 10 % of the goal beam size of 37 nm.

Machine detector interface (MDI): The ILC is configured to have two detectors that share one interaction point, with one detector in data taking position at any time, in a so–called "push–pull" operation [3, Sec. 8.4]. Both detectors are mounted on movable platforms that allow an exchange of the detectors within approximately 24 hours.

In the push–pull scheme, the innermost final focus quadrupole "QD0", a slim, superconducting magnet package combined with a sextupole for local chromaticity correction, is installed within the detectors. The other part of the final focus doublet ("QF1") is located outside the detector on a bridge, and does not move with the detector. Since the TDR, the free space L^* between interaction point and the QD0 edge has been harmonised to a common value of $L^* = 4.1\,\mathrm{m}$ [17], which facilitates the design of a final focus optics that delivers optimal and equal performance to both detectors.

The detectors are located in an underground cavern. In contrast to the TDR design, it is foreseen to have a large vertical access shaft [18], which permits a CMS–style detector installation concept, in which the detectors are assembled in large modules in a surface hall and lowered into the hall by means of a gantry crane capable of lowering pieces up to 4000 t. As the CMS experience shows, this concept significantly reduces the schedule risk associated with the experimental hall, since the

cavern needs to be available for detector installation only one or two years prior to commissioning.

Main dump: The main beam dumps [4, Sect. 8.8] are rated for a maximum beam power of 17 MW [20], enough for a 1 TeV upgrade of the accelerator. The main dump design is based on the successful SLAC 2.2 MW beam dump [72]. It utilises water at 10 bar pressure (to prevent boiling) as absorber medium. The main engineering challenges lie in the safe recombination of the produced oxyhydrogen gas and in the safe containment and disposal of radioisotopes, in particular tritium and ^{7}Be produced from spallation processes. The entry window is another component that has to be carefully designed.

Measurement of beam energy, luminosity, and beam polarisation: Two energy spectrometers, one located 700 m upstream of the IP, the other 55 m downstream, provide independent and complementary measurements of the beam energy with an accuracy of 100 ppm [73].

The luminosity is measured to 10^{-3} accuracy from low angle Bhabha scattering in the so–called LumiCal (see Sect. 6.3.1) at polar angles from 30 to 90 mrad. Additional calorimeters (BeamCal) in the region 5 to 30 mrad provide a fast signal that is sensitive to the beam sizes and offsets of the colliding beam, and that can thus be used for their tuning, as part of an intra-beam feedback system (see Sec. 4.1.3).

Beam polarisation is measured with 0.25 % accuracy by means of Compton scattering: electrons that scatter off green or infrared light laser photons lose enough energy that they can be detected in a spectrometer; their momentum spectrum is used to fit the beam polarisation [74]. Two such polarimeters are located 1800 m upstream and 150 m downstream of the IP, which allows to interpolate the precise polarisation at the IP and control the systematics, including effects from precession of the polarisation vector by transverse fields and depolarising effects in the interaction, which lead to a sizeable variation of the polarisation within the bunch during the collision (see Sec. 5.3).

4.1.4 Operation at the Z-pole

TDR described the design of ILC for the energy range between 200 GeV and 500 GeV with possible upgrade to 1 TeV. The project starts with 250 GeV as the Higgs factory. However, once the ILC for 250 GeV is built, it is still possible to operate it below the lowest energy region in particular at the center-of-mass energy 91.2 GeV, i.e., at the Z-pole, although the luminosity is lower than at 250 GeV.

The first issue for the Z-pole operation is the positron production. Since the electron beam of energy 45.6 GeV cannot produce sufficient number of positrons by the undultor scheme, another electron beam (125 GeV) dedicated to positron production is necessary. In this scheme the miximum repetition frequency of collision allowed by the AC power system of ILC250 turned out to be 3.7 Hz. Thus, the machine operation cycle is as follows:

1. Create 5 GeV electron beam (1312 bunches) and store it in DR for $1/(2\times3.7\,\mathrm{Hz}) = 135$ ms.

2. Extract the electron beam from DR, accelerate it to 125 GeV in the electron main linac, let it go through the undulator, create positron beam, accelerate the positron to 5 GeV and store it in the positron DR for 135 ms.

3. Create the next 5 GeV electron beam and store it in DR for 135 ms in parallel with step 2.

4. Extract the electron/positron beams from each DR, accelerate to 45.6 GeV in the electron/positron main linacs and collide them.

This one cycle takes 2×135 ms = 270 ms = 1/3.7 Hz. The spent electron beam after the step 2 is transported to the special beam dump (designed for up to 8 MW).

In this scenario the positron main linac is operated at 3.7 Hz, whereas the electron main linac is at 7.4 Hz, one pulse accelerate electrons to 125 GeV at the full gradient (31.5 MV/m) and the next pulse to 45.6 GeV at the gradient 8.76 MV/m by adopting reduced klystron power. (For the latter pulse one might conceive of accelerating the beam to 45.6 GeV at full gradient and turn off the power in the rest of the linac. This scheme does not work because the cavities in the rest of the linac must be detuned for avoiding the beam loading but detuning by the mechanical tuner cannot be done at 3.7 Hz.)

The time for damping in DR is 135 ms, shorter than 200 ms for the standard 5 Hz operation. This is feasible because the power system of DR can accept up to 10 Hz.

There are many issues to be considered in addition to above such as

- Required wiggler strength in DR and re-evalution of the dynamic aperturte
- Beam dynamics in the low-gradient main linac under alternating gradient (31.5 and 8.76 MV/m) operation mode. (Orbit correction for colliding beam only).
- Tight horizontal collimation depth due to large geometric emittance. Momentum band-width of the BDS system (longer bunch length 0.41 mm is adopted to reduce the beam energy spread).
- The wakefield effects in BDS due to low energy and long bunch.
- Beam-beam interaction with large disruption parameter ($D_y \approx 32$)

These issues are discussed in detail in [75].

The relevant parameters are listed in Tab. 4.1. The luminosity is estimated to be $2.05 \times 10^{33}/\mathrm{cm}^2/\mathrm{s}$ with 1312 bunches per pulse and $4.1 \times 10^{33}/\mathrm{cm}^2/\mathrm{s}$ with doubled number of bunches. The expected beam polarization is the same as in250 GeV case, i.e., $> 80\%$ for electron and $\sim$30% for positron.

In the case the e-driven positron source is adopted instead of the undulator source, the simple 5 Hz operation is possible as at 250 GeV and, therefore, the luminosity is higher by a factor 5/3.7, i.e., $2.8 \times 10^{33}/\mathrm{cm}^2/\mathrm{s}$ with 1312 bunches, although the positron beam is not polarized.

4.1.5 Civil engineering and site

In 2014, the ILC Strategy Council announced the result of its candidate site evaluation for the best possible ILC site in Japan [76]. The evaluation was conducted by a number of Japanese experts from universities and industry, and reviewed by an international commitee. It considered technical as well as socio-environmental aspects, and concluded that the candidate site in the Kitakami region is best suited for the ILC.

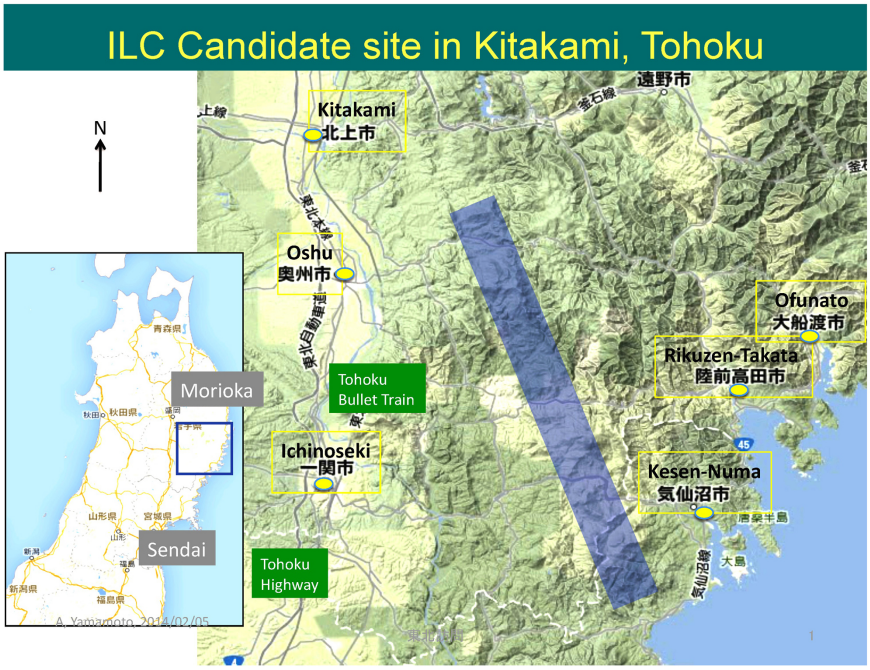

Figure 4.14: The Kitakami candidate site for the ILC [77].

The site (Fig. 4.14) is located in the Japan's northern Tohoku region, not far from Sendai with its international airport, in the prefectures of Iwate and Miyagi. The closest cities are Ichinoseki, Oshu, and Kitakami, which all offer Shinkansen (bullet train) access to Sendai and Tokyo. The closest harbour is in the city of Kesen-Numa. The coastal region in this area was severely hit by the great Tohoku earthquake in 2011. Both prefectures are supportive of the ILC project and view it as an important part of their strategy to recover from the earthquake disaster.

The Kitakami site was largely selected because of its excellent geological condition. The proposed ILC trajectory lies in two large, homogeneous granite formations, the Hitokabe granite in the north and Senmaya granite to the south. The site provides up to 50 km of space, enough for a possible 1 TeV upgrade or more, depending on the achievable accelerating gradient. Extensive geological surveys have been conducted in the area, including boring, seismic measurements, and electrical measurements [78], as shown in Fig. 4.15. The surveys show that the rock is of good quality, with no active seismic faults in the area.

Earthquakes are frequent throughout Japan, and the accelerator and detectors need proper supports that isolate them from vibrations during earthquakes and micro tremors [79]. Proven technologies exist to cope with all seismic events, including magnitude 9 earthquakes such as the great Tohoku earthquake.

Vibration measurements taken during the construction of a road tunnel show that accelerator operation would be possible during the excavation of a tunnel for an energy upgrade [80].

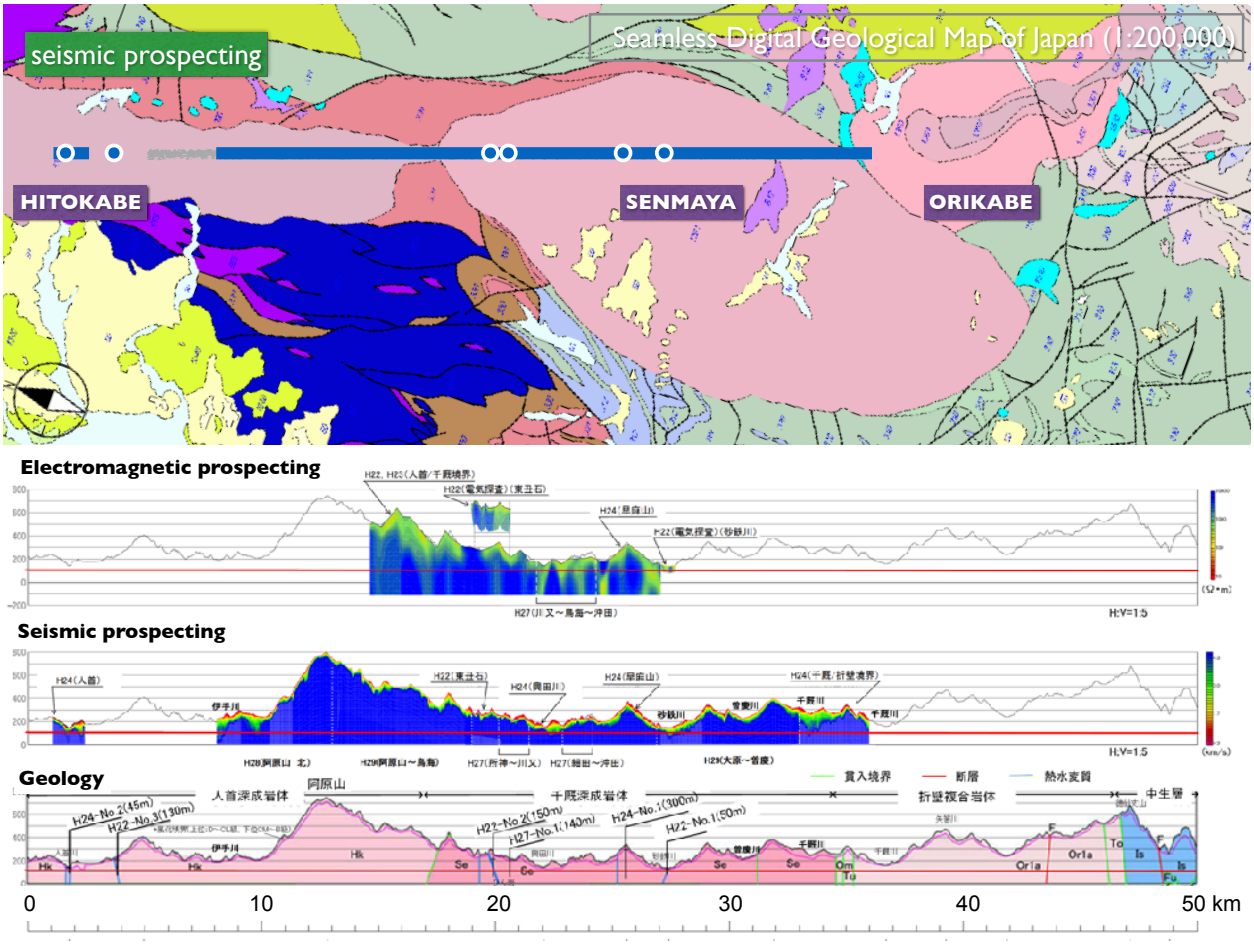

Figure 4.15: Geological situation at the Kitakami site.

4.1.6 Cost and schedule

For the Technical Design Report, the construction cost of the ILC accelerator was carefully evaluated from a detailed, bottom–up, WBS (Work Breakdown Structure)-based cost estimation [4, Sect. 15]. The TDR estimate distinguishes two cost categories: Value accounts for materials and supplies procured from industry and is given in ILCU (ILC Currency Unit, where 1 ILCU = 1 US$ in 2012 prices), and Labour accounts for work performed in the participating institutions and is

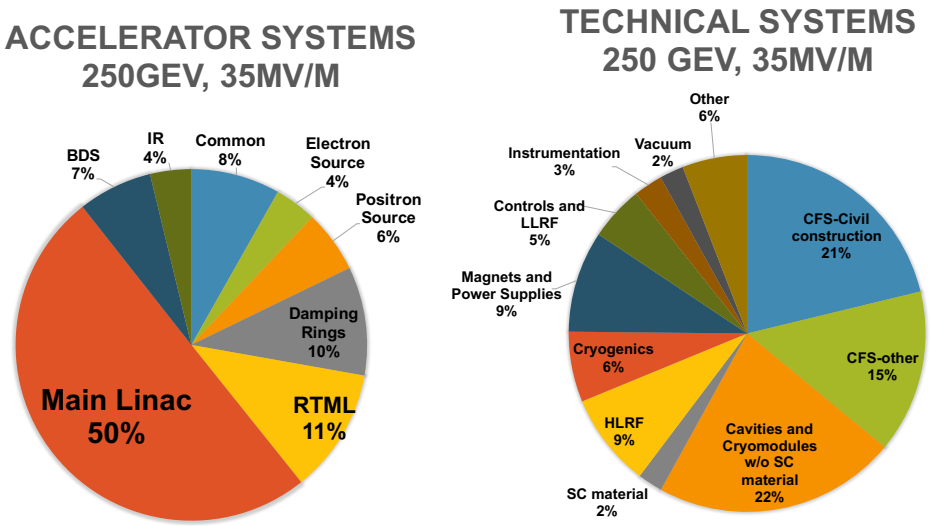

Figure 4.16: Breakdown of Value costs into accelerator systems (left) and technical systems (right) for the 250 GeV ILC accelerator, assuming that cost reduction measures are successful and a gradient of 35 MV/m can be reached.

given in person–hours or person–years[3].

The Value of acquired goods reflects its worth in the local currency of the purchasing institution. Therefore, conversion of Value between currencies is performed based on Purchasing Power Parities (PPP), which are regularly evaluated and published by the OECD [81, 82], rather than currency exchange rates. The PPP values reflect local price levels and thus depend on the type of goods and the country, but fluctuate significantly less than currency exchange rates. Therefore, conversions from ILCU to other currencies cannot not be made on the basis of exchange rates to the U.S. dollar, but on PPP values.

The TDR estimate covers the cost of the accelerator construction, assumed to last 9 years plus one year of commissioning. It includes the cost for the fabrication, procurement, testing, installation, and commissioning of the whole accelerator, its components, and the tunnels, buildings *etc.*, and the operation of a central laboratory at the site over the construction period. It does not, however, cover costs during the preparation phase preceding the start of construction work ("ground breaking"), such as design work, land acquisition, infrastructure (roads, electricity, water) for the site.

Based on the TDR cost estimate, an updated cost estimate was produced for the 250 GeV accelerator. This updated cost estimate includes the cumulative effect of the changes to the design since the TDR (see Sect. 4.1.1), and evaluates the cost for the reduced machine by applying appropriate scaling factors to the individual cost contributions of the TDR cost estimate.

The resulting Value estimate for the ILC accelerator at 250 GeV is $4,780 - 5,260$ MILCU [9]

[3]One person–year corresponds to 1700 working hours.

in 2012 prices, where the lower number assumes a cavity gradient of 35 MV/m, while the higher number is based on the TDR number of 31.5 MV/m. In addition, 17,165 kh (thousand person-hours) are required of institutional Labour.

In 2018, the ILC Advisory Panel of the Japanese Ministry of Education, Culture, Sports, Science and Technoloy (MEXT) concluded its review of the ILC [83]. For this review, costs were evaluated in Japanese Yen in 2017 prices, taking into account the local inflation for goods and construction costs. For the purpose of this estimate, also the Labour costs were converted to Yen to yield 119.8 G¥, resulting in a total range of the accelerator construction cost of $635.0 - 702.8$ G¥, where the range covers uncertainties in the civil construction costs (18 G¥) and of the gradient (49.8 G¥). For the this estimate, conversion rates of 1 US$ = 100 JP¥ and 1 € = 1.15 US$ were assumed.

Operation costs of the accelerator and the central laboratory are estimated to be $36.6 - 39.2$ G¥ (about $318 - 341$ M€) per year.

4.2 ILC staging up to 1 TeV

[6 pages; corresponding editor: Alex Aryshev (alar@post.kek.jp)]

[this section should include a table of accelerator parameters at the various stages for easy reference]

4.2.1 Introduction

The requirements for ILC physical characteristics [84] define a continuous range of center-of-mass energy from 92 GeV (Z-pole [75]) to 500 GeV with the possibility of additional upgrading to a center-of-mass energy of 1 TeV. The GDE has focused on providing a reliable design and cost estimation for the $200 - 500$ GeV base machine. The design is a price-performance optimized solution for a given energy range. The center-of-mass energy of 250 GeV can be realized with a straight machine 20 km long, and the energy of 500 GeV can be achieved if it is expanded to 30 km. To be as cost-effective as possible, the final ILC proposal approved by ICFA [85] does not include empty tunnel options for future upgrades. Despite the fact that the length of the main tunnel of the linear accelerator has been reduced, the beam delivery system and main dumps are designed to allow for an energy upgrade up to 1 TeV.

The development of accelerator structures with higher acceleration gradients can lead to a significant increase in energy while maintaining a compact infrastructure. To date, significant progress has been made in the development of structures with a gradient well above the 31.5 MV/m required for the ILC, and even above the 45 MV/m as required for the 1 TeV ILC [86, 87]. In the longer term, structures with an alternative shape or with a thin-film Nb_3Sn coating or multilayer coating can significantly improve the performance of linear particle accelerators [88, 89]. Newer acceleration schemes can achieve even higher gradients as discussed in Sect. 4.3 ILC Scope Beyond 1 TeV. Finally, the emergence of acceleration schemes based on plasma wake field acceleration or other advanced concept could open up the ILC energy regime up to 30 TeV. Thus, the ILC

laboratory has the potential to turn into higher energies electron-positron collider. The ability to increase energy levels makes the Linear Collider a very flexible tool, allowing to respond for a new discoveries at the LHC. There are several options for upgrading the ILC in terms of energy, luminosity and beam polarization.

The level of developments detail of the staging and upgrade scenarios is significantly less mature than the baseline. In particular, the TeV upgrade parameters and associated conceptual design represent a relatively simple and straightforward scaling of the base machine based on straight assumptions about higher achievable operating parameters for SCRF technology with an average acceleration gradient of 45 mV/m with $Q_0 = 2 \times 10^{10}$. Achieving these values requires further research and development beyond the basic technology. It is anticipated that this R&D will continue in parallel with both construction and operation of the base machine, so that the expansion of the core linear accelerators required to increase particle energy will benefit from improved technology. In addition, accelerator research and development should continue to dramatically increase particle collision energy in preparation for future experimental efforts that may indicate the existence of new particles and new phenomena on a higher energy scale.

Both luminosity enhancement and low-energy staging are based on existing technology and do not require additional research and development. For upgrades to TeV energies, a design approach that has minimal impact on the operation of the ILC should also be discussed. The presented two sets of parameters for upgrading to TeV (the so-called low and high beamstrahlung) were obtained after careful consideration of the physical impact.

It should be emphasized that the flexibility in the choice of beam parameters remains one of the key advantages of the ILC. It can be adjusted whenever new ideas and discoveries either from (HL-) LHC or from the ILC itself set new requirements. In particular, the center-of-mass energy of the ILC can always be reduced from the nominal maximum energy without loss of efficiency, as long as the electron beam energy remains high enough to produce positrons.

4.2.2 Parameters

Table 4.1 shows the main ILC parameters for center-of-mass energy of 250 GeV, an increased luminosity of 500 GeV and two possible sets of parameters for the energy 1 TeV. The parameters for the first stage of the 250 GeV machine are identical to the baseline parameters set for this energy.

4.2.3 Luminosity upgrade

The ILC luminosity can be improved by increasing the luminosity per bunch (or by the charge of the bunch) or by increasing the number of bunches per second [90]. Increasing the brightness per bunch requires a smaller vertical beam size, which can be achieved by tighter focusing and / or lower beam emittance. However, this approach invariably involves high perturbation of the beam, resulting in the risk of luminosity loss due to improper beam steering. Thus, a very accurate feedback system is required. The ILC design also allows the number of bunches to collide per second to be increased

by doubling the number of bunches per pulse and possibly increasing the pulse repetition rate. Doubling the number of bunches per pulse from the base number of 1312 to 2625 will require a decrease in the time separation between bunches from 554 ns to 366 ns, which will lead to an increase in the beam current from 5.8 mA to 8.8 mA, which will require installation of 50% more klystrons and modulators. Since the RF pulse duration of 1.65 ms will not change, the cryogenic load will also not change. The beam pulse duration increases from 714 μs to 961 μs. The choice of the distance between bunches is consistent with both the harmonic number of the damping ring and the duration of the RF pulse of the main linear accelerator. Doubling the number of bunches would double the beam current in the damping rings. For a positron ring, this may exceed the limitations associated with the electron cloud instability. To reduce this risk, the damping ring tunnel is large enough to accommodate a third damping ring so that the positron current can be distributed over the two rings. The pulse repetition rate (5 Hz in the base configuration) is limited by the available cryogenic power, the damping time in the rings, and the target heat load in the positron source target. The rings are rated for the time for damping of 100 ms and thus can have a repetition rate of up to 10 Hz, which is double the nominal. Operation at an increased repetition rate will be possible if, after upgrading the energy, the machine is operated at energies below the maximum or if additional cryogenic power is installed. Basic schematics for electron and positron sources are specified to produce more bunches needed for upgrades. RTML, and in particular the SCRF RF linear accelerator sections for beam compressors - are already compatible with a large number of bunches.

The invasive nature of the additional cryogenic power installation requires a shutdown, during which all additional RF power supply must be installed. This will also include additional water cooling and the required AC power, although pipe sizes are already specified for the additional baseline load and do not need upgrades. In particular, the 25% increase in cryogenic load (mainly due to high power coupler losses and HOM losses due to higher current) is within the base specification. All beam position monitors (and other instruments) are compatible with shorter beam spacing. Beam dynamics problems (multi-bunch effects) are also acceptable, and high power couplers and HOM couplers/absorbers are specified in the baseline for higher beam currents.

4.2.4 Energy upgrade

An obvious advantage of a linear collider is the possibility of its energy upgrade. In principle, the main linear accelerator can be expanded at a constant cost for the added beam energy with some additional costs of moving the turnarounds and compressors. Additional costs arise when the beam delivery system (BDS), including the beam dumps has to be expanded to cope with the increased beam energy. The current ILC BDS is designed to be easily modified to operate at center-of-mass energies up to 1 TeV at minimal cost. Depending on the actual gradient achieved during the construction of the ILC, maximum 162 cryomodules can be installed in addition to those required to reach 250 GeV, which will increase the center of mass energy by approximately 50 GeV to about 300 GeV, and two additional cryogenic plants may need to be installed. Further increases in energy will require the expansion of the tunnel. As noted above, accelerator with a total length of at least 50 km can be placed on the Kitakami site, which is more than enough for center-of-mass energy of 1 TeV. Any expansion of the accelerator system can be accomplished by adding new cryomodules

at the low energy (upstream) ends of the accelerator without the need to move already installed modules.

The upgrade can take place in two phases: a preparation phase, when the accelerator is still running and producing data, and an installation phase, when the accelerator stops. During the preparation phase, the necessary components will be purchased and manufactured, in particular cryomodules, klystrons and modulators. At the same time, civil engineering will continue to excavate new access tunnels, underground halls and the main tunnel. Recent research shows that the level of vibration caused by tunneling will bring new tunnels closer to existing ones before machine operation is impacted [91], minimizing the required shutdown time. During the installation phase, the newly built tunnels will be connected to the existing ones, the beam lines at the turnarounds and wiggler sections of the bunch compressors will be dismantled, and new cryomodules and a new turnaround and bunch compressors will be installed. In doing so, any necessary changes can be made to the positron source and the final focus of the machine. Since the cryomodules are ready for installation at the beginning of the shutdown period, it is anticipated that the shutdown could be limited to about a year for an energy upgrade

The choice of beam parameters and luminosity increase for the TeV upgrade is also based on direct scaling from a set of base parameters, but more limited by additional considerations related to higher energy and average beam power:

1. the total AC power required for the modified machine must be below some realistic limit (assumed to be 300 MW);
2. the beam current and pulse duration must be compatible with injectors, damping rings and the main linear accelerator of the basic design;
3. energy losses due to beamstrahlung should be acceptable, and the maximum pair-production angle should be limited at the maximum luminosity per bunch crossing.

Limiting the total AC power requires reducing the repetition rate from 5 Hz to 4 Hz, while the need to maintain the RF pulse length in the original main linear accelerator at approximately 1.6 ms and the choice of the damping ring harmonic number limits the number of bunches to 2450. The limits of beamstrahlung, depend on physics, therefore, for the study of physical and detector groups, two sets of parameters were proposed: a set of parameters for low beamstrahlung with $\delta_{BS} \sim 5\%$ and a luminosity of 3.02×10^{34} cm^{-2}s^{-1}, equal to the increased luminosity value for the 500 GeV baseline and the second set with high beamstrahlung radiation with $\delta_{BS} \sim 10\%$ and, accordingly, a higher luminosity 5.11×10^{34} cm^{-2}s^{-1}. Both of these parameter sets are based on the reduced charge of one bunch (1.7×10^{10}), shorter bunch length (250μm and 225μm for low and high δ_{BS}, respectively), and increased horizontal beam size for controlling beamstrahlung and pair-production angle, while the vertical beta function at the interaction point (IP) is further reduced to increase the luminosity per bunch crossing [92]. The bunch lengths and IP beta functions are within the range of bunch compressor and final focusing systems. It is relatively easy to adjust the machine parameters between these beamstrahlung parameter sets.

Increasing the beam energy will require the expansion of the main SCRF linear accelerators to provide an additional 250 GeV per beam. The beam current for the TeV upgrade (7.6 mA) is

higher than the baseline (5.8 mA) but less than that for luminosity upgrade (8.8 mA), suggesting some level of modification. Assuming the luminosity upgrade is the first to occur; the injectors (sources and damping rings) will be reused unchanged. Compressor sections along with the RTML will be moved to the beginning of the extended linear accelerators. It is also necessary to lengthen the 5 GeV long-transfer line from the damping ring to the turn-around. The beam delivery system will require the installation of additional dipoles to provide the required higher integrated field strength. The cost and schedule of the upgrade is entirely dependent on the expansion of the main linear accelerators. One of the key cost considerations is the choice of an accelerating gradient. Ongoing R&D for high gradient SCRF is expected to continue in parallel with the construction and operation of the base machine. With this in mind, it is assumed that when the linear accelerator technology is upgraded, a higher gradient and quality factor is incorporated. The actual choice of these options will clearly depend on the state-of-the-art at the time of the upgrade. However, for the purposes of this discussion, an average acceleration gradient of 45 MV/m with $Q_0 = 2\times10^{10}$ will be assumed. Using the existing baseline linear accelerator in this way has three key consequences for the upgrade:

1. The beam current and pulse length must be compatible with the existing RF installation and cryogenic refrigeration capacity.

2. The existing linear accelerator lattice, which was originally designed to transfer beam energies from 15 to 250 GeV, should now transfer beam energies from 265 to 500 GeV. This will require replacing the first 10 GeV of the original linear accelerator, since these quadrupoles will not be able to transport a higher energy beam (from 265 to 500 GeV, not 15 to 250 GeV).

3. The rest of the original linear accelerator will use the *FoFoDoDo* lattice as opposed to the basic *FoDo* lattice, which will result in weaker focusing and larger beta function values. Simulation of the beam dynamics showed that the growth of the vertical emittance can be kept within acceptable limits.

4.2.5 Positron source

The undulator-based positron source must be compatible with the initial energy of the electron beam of 500 GeV. The solution is to replace the baseline helical undulator with a shorter one, with a longer period and a smaller field. The upgraded undulator will provide a photon beam similar to the baseline so that the same target and capture device can be used without modification [93]. One of the important considerations is the opening angle of photons, which is doubled for higher beam energy; this makes collimating photons for polarization more challenging. Currently, a conservative estimate of 20% polarization is considered acceptable, but higher values may be possible, provided that a suitable solution is found for collimating photons with a smaller aperture [94].The baseline design geometry of the target-bypass dogleg for the high-energy electron beam already accommodates the 500 GeV beam transport with a few percent horizontal emittance growth [95], although additional dipole magnets will need to be installed.

4.2.6 RTML

The two-stage compressor system will need to be "relocated" to a new location upstream. This scenario assumes that a new two-stage compressor will be installed, as well as a new turnaround and an extended transport line. Also, during the shutdown for the final installation of the warm wiggler base sections and cryomodules, the most upstream sections of the main linear accelerator will be updated as discussed in the "Energy upgrade" subsection. The original turnaround will be disconnected and bypassed by a new long transport line. It is likely that the space between the original and the upgraded linac will also be used for additional diagnostic and dump systems, including an emergency extraction dump to protect the machine, similar to the one found at the linac exit (BDS entrance).

4.2.7 Beam Delivery System (BDS)

The BDS geometry (length and average bend radius) is already compatible with the transport of a 500 GeV beam with an acceptable increase in the emittance generated by synchrotron radiation [93]. Additional dipoles are required (as well as appropriate power supplies and cooling) to be installed in drift spaces provided in the base grid. The main high power dumps have already been designed for higher average beam powers to avoid the need to replace them during modernization (dumps will become radioactive after several years of operation).

4.2.8 Polarization upgrade

It is assumed that at center-of-mass energies up to 500 GeV, ILC beams will have at least 80% of the electron polarization at IP in combination with a positron polarization of 30% for an undulator positron source. At 1 TeV, the positron polarization will reach at least 20%. As an upgrade option, the positron polarization can be increased to 60% for a center-of-mass energy of about 500 GeV, as discussed in Sec. 4.5.2 Electron and Positron Sources. The design of the accelerator includes sets of spin rotators, which, in principle, make it possible to form any desired direction of the polarization vectors at the IP. However, in the detailed scenarios, we only take into account the longitudinal polarization. At a beam energy above 125 GeV, the flux of undulator photons increases rapidly. Photon polarization is maximal at zero angle of radiation emission; it reduces and even inverts at large angles. Thus, collimation of the excess photon flux at large radiation angles increases the net polarization. Present research studies show that 60% polarization of positrons at IP can be possible at a center-of-mass energy of 500 GeV with the addition of a photon collimator.

4.2.9 Summary

These chapters examined incremental upgrade and upgrade options other than the 500 GeV baseline scheme and demonstrates the greater design flexibility and capabilities of the ILC installation. The basic design already contains minimal support to simply increase luminosity by doubling the average beam power (50% increase in average RF power). The parameters and scope of future upgrades

to center-of-mass energy of 1 TeV were presented, based on the expansion of the main linear accelerators with minimal impact on the existing (baseline) machine. The construction of the extended machine, in principle, could proceed in parallel with the physical launch, with minimal interruption for connecting the baseline and modernized linear accelerators and the subsequent commissioning of the machine. The physical parameters (luminosity) for retrofitting to TeV energies represent a compromise between the physical requirements of the beam-beam (limiting bremsstrahlung and pair-production angle) and the desire to limit the total required AC power to about 300 MW.

4.3 R&D program on superconducting RF

[5 pages; corresponding editor: Hasan Padamsee (hsp3@cornell.edu)]

In Section 4.1.2, we have described the evolution of superconducting RF technology up to the present and explained the robustness of the ILC plan for operation at a nominal gradient of 31.5 MeV/m. However, superconducting RF technology continues to move forward. To reduce the cost of the 250 GeV ILC, to reduce the cost of the upgrade to 500 GeV, and to propose affordable designs for the ILC at 1 TeV and beyond, it is important to continue to improve this technology to achieve gradients as high as possible in cavities that can be produced reliably by industry. In this section, we will describe the R&D program to improve the gradient of superconducting RF cavities. The improvements that we describe here go beyond the baseline ILC design, but we expect that they will be brought into play as the ILC evolves to higher energy. The far-future application of extremely high-gradient superconducting RF to take the ILC beyond 1 TeV will be described in Sec. 15.1.

4.3.1 Gradient status for the ILC baseline 250 GeV

Figure 4.17 shows the steady progress in single and multicell cavity gradients [96] over the last 3+ decades coming from high purity, high RRR Nb, electropolishing, 800 C furnace treatment for H removal, 100 atm. high pressure water rinsing for removal of field emission particulates, and final baking at 120 C for removal of the high field Q-slope. These procedures establish a standard ILC cavity preparation and treatment recipe from which cavity gradients of 35 MV/m are expected, as observed from the EXFEL production run. More than 40 "best" cavities from the EXFEL production run showed 40–45 MV/m [97], as shown in Fig. 4.18. At DESY, two large grain 9-cell cavities reached 45 MV/m [98].

Key areas of further development over the last 5 years have been for higher Q values at medium gradients (16–22 MV/m) for CW operation with the invention of new techniques of Nitrogen doping [99, 100]. Nitrogen doping for high Q has already been applied to the construction of a large (4–8 GeV) new accelerator, LCLS-II, and its high energy upgrade LCLS-II-HE. For LCLS-II-HE, ten 1.3 GHz 9-cell N-doped cavities have reached average 3.5×10^{10} at 25.7 MV/m.

Further improvements can be expected from exciting developments [101] that show $Q = 5 \times 10^{10}$ at 30 MV/m by baking at 300 C (mid-T baking) to dissolve the natural oxide (and other surface layers) into the bulk, but not exposing the cavity to air or water before RF measurements. It is

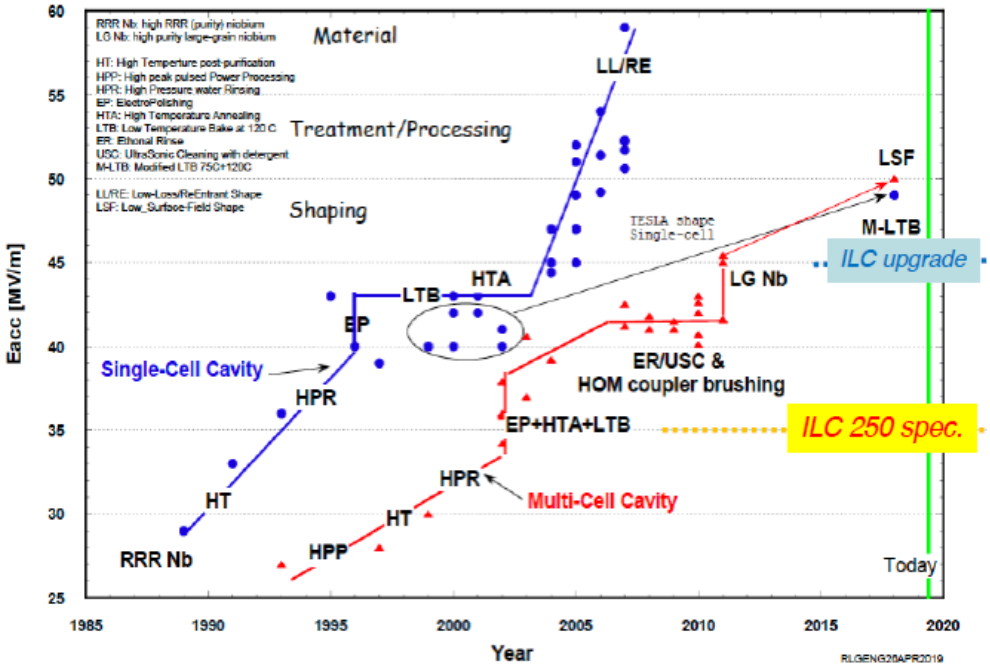

Figure 4.17: Steady progress in single and multi-cell cavity gradients over 3+ decades [96].

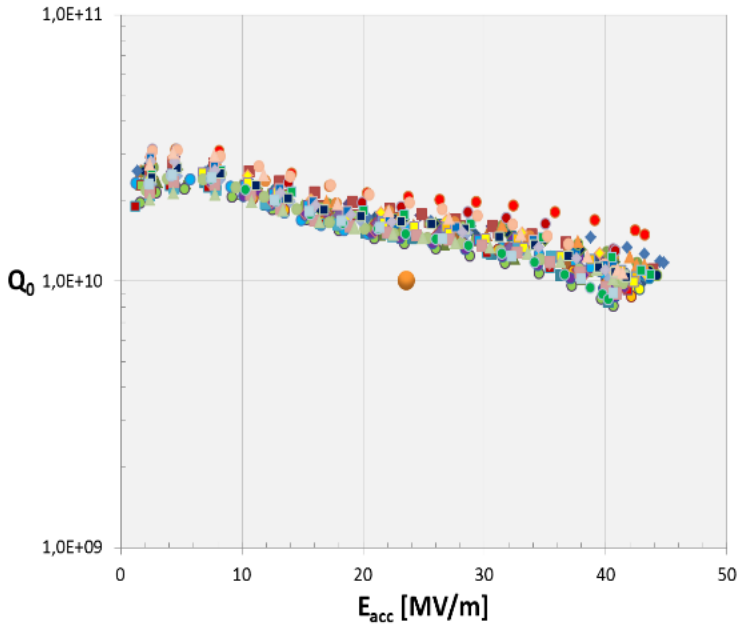

Figure 4.18: 9-cell test results from DESY on $>$ 40 cavities produced and treated by Research Instruments (RI) [97].

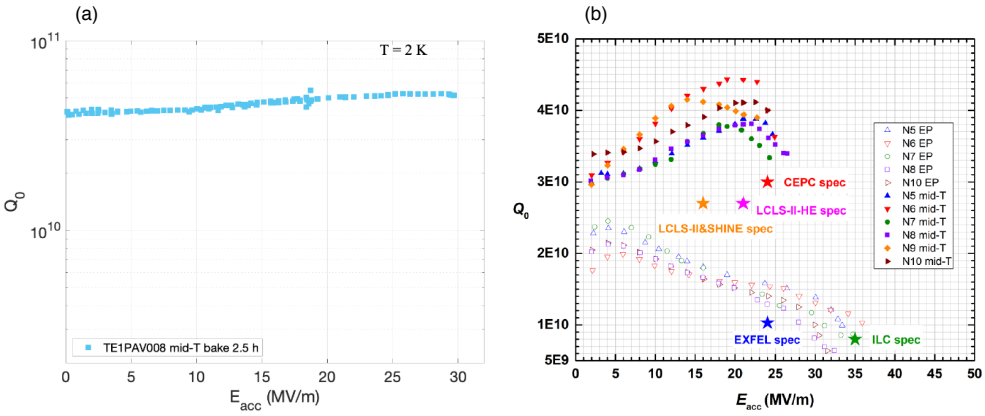

Figure 4.19: (a) Q = 5×10^{10} at 30 MV/m by baking at 300 C to dissolve the natural oxide (and other surface layers) into the bulk, but not exposing the cavity to air or water before RF measurements. (b) IHEP (China) results on mid-T baking for 9-cell cavities compared to results on the same cavities with the standard ILC treatment [102].

interesting to note how the Q rises with field, as seen for N-doping (Fig. 4.19(a)).. After exposure to air, followed by HPR, the Q dropped to 2×10^{10} at 30 MV/m. Surface analysis of similarly treated samples show a Nitrogen peak at a few nm below the surface, suggesting that N is present at the surface and has diffused into the Nb to give the doping effect. IHEP in China followed up on these encouraging results with several 9-cell TESLA cavities with exciting results [102], as shown in Fig. 4.19(b). After mid-T (300 C) furnace bake, and HPR, all the 9-cell cavities demonstrate high Q in the range of 3.5–4.4 $\times 10^{10}$ at the gradient between 16–24 MV/m, as shown in Fig. 4.19(b). These cavities have all exceeded the specification of LCLS-II HE (2.7×10^{10} at 21MV/m). KEK is also pursuing the mid-T baking option. Although in its early stages, the mid-T baking procedure shows the potential of Nb for high gradients with high Qs.

4.3.2 High Gradient (45 MV/m) SRF for Upgrade Paths to 1 TeV

Section 4.2 discusses ILC energy upgrade paths from 250 GeV to 380 GeV (Top Factory), 500 GeV and 1000 GeV. For the 1000 GeV upgrade (Scenario B), the 2013 ILC TDR uses a gradient of 45 MV/m with $Q_0 = 2 \times 10^{10}$ for the additional linac from 500 GeV to 1000 GeV. The SRF parameters are chosen on the forward-looking assumptions of advances in SRF technology derived from R&D which will continue in parallel to both construction and operation of ILC 250 GeV to 1000 GeV. Such extrapolations in SRF performance are reasonably based on expectations from proof-of-principle results already in hand. As discussed further below, single cell cavities with improved treatment reach 49 MV/m, and single cell cavities with improved shapes that reach 52–59 MV/m.

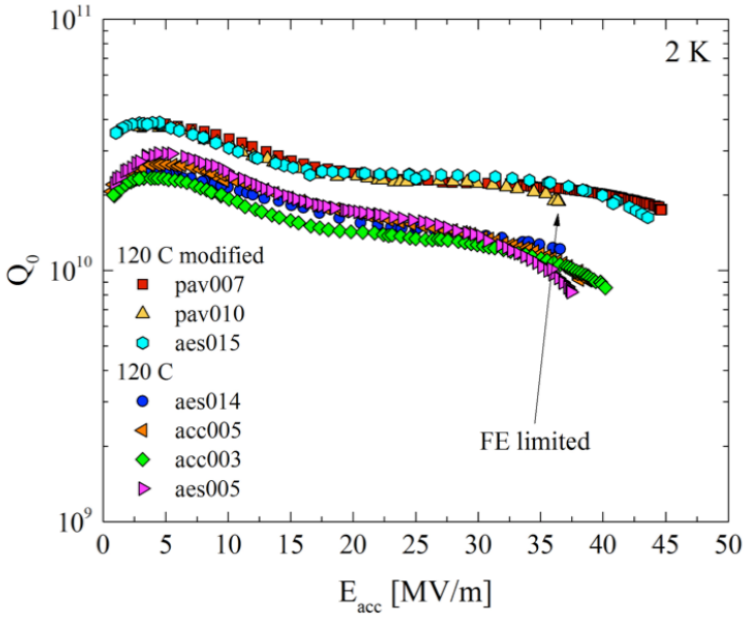

Figure 4.20: Comparison of the performance of several 1-cell cavities from N-infusion with cavities prepared by the standard ILC recipe of EP and 120 C baking.

Nitrogen Infusion

On the high gradient frontier (with higher Q's), the invention of Nitrogen infusion [87], stemming from Nitrogen-doping, demonstrates gradients of 40–45 MV/m as shown in Fig. 4.20, and compared to the performance of cavities prepared with the standard ILC recipe. JLAB has shown success with infusion[103], but KEK [104] and DESY [105] have found the technique to be sensitive to the quality of the infusion furnace, and difficult to implement.

Two-Step Baking and Cold Electropolishing

In another new development, extraordinarily high quench fields for 1.3 GHz niobium TESLA-shaped SRF cavities, some near 50 MV/m have been achieved with the 75/120 C bake surface treatment developed at FNAL, as shown in Fig. 4.21(a). Two-Step baking with Cold Electropolishing [86] show gradients in the range of 40–50 MV/m (average 45 MV/m), as depicted in Fig. 4.21(b). Note that 3 cavities that quench below 28 MV/m were found to have physical defects that likely limited the performance.

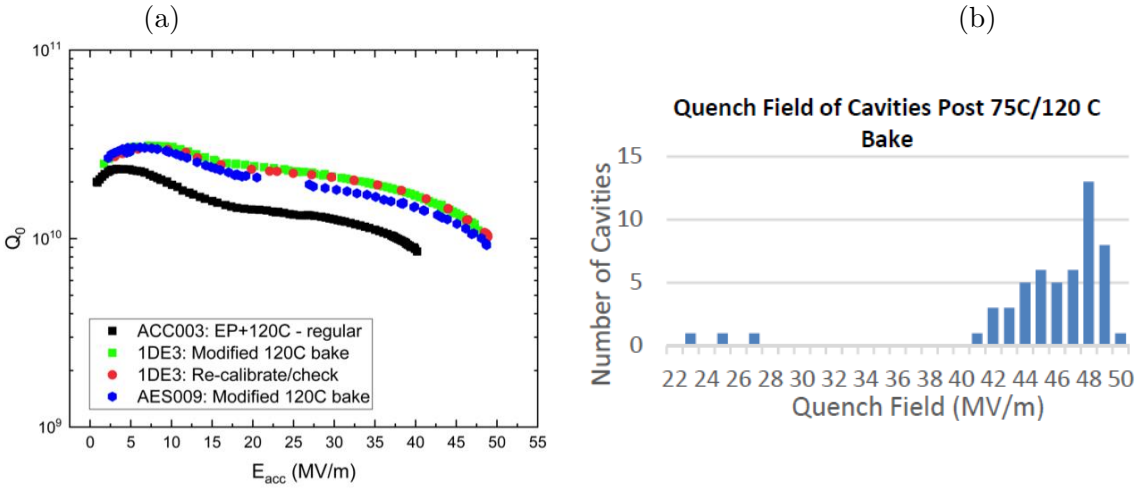

Figure 4.21: (a): Q vs. E curve of 1-cell cavity reaching 49 MV/m from Cold EP/optimized baking (75/120 C) compared to the curve of a cavity prepared by the standard ILC recipe. (b) Histogram of gradients of a large number of single cell cavities prepared by Cold EP/optimized baking (75/120 C).

4.3.3 Toward 60 MV/m - Advanced Shape Cavities

Continuing along the gradient frontier, multicell cavities of Re-entrant [106, 107], Low-Loss [108] and ICHIRO [109] shapes (Fig. 4.22(b)) have been introduced to lower H_{pk}/E_{acc} 10 - 20% by rounding the equator to expand the surface area of the high magnetic field region, and by allowing E_{pk}/E_{acc} to rise by about 20%. The Re-entrant shape has an Ω-like profile with H_{pk}/E_{acc} = Oe/35.4/(MV/m), E_{pk}/E_{acc} = 2.28 (for 60 mm aperture) as compared to 42.6 Oe/(MV/m) and E_{pk}/E_{acc} = 2.0 for the standard TESLA shape (70 mm aperture). The GR/Q value for the re-entrant shape is about 34% higher than the TESLA shape, which reduces cryogenic losses. The 20% increase in E_{pk} makes cavities with the new shapes more susceptible to field emission, but we can expect progress in field emission reduction with cleaner surface preparation developments over the coming decades.

The motivation in trying the new shape was that quench, governed by H_{pk}, is a hard limit, whereas field emission, governed by E_{pk}, can be improved by better engineering. The Low-Loss shape with 60 mm aperture has H_{pk}/E_{acc} = 36.1 Oe/(MV/m), and E_{pk}/E_{acc} = 2.36, and a 23% higher GR/Q than the TESLA shape. The ICHIRO shape is a variant of the Low-Loss shape. A relative newcomer to the advanced shape effort is the LSF shape [110] which obtains H_{pk}/E_{acc} = 37.1 Oe/(MV/m) without raising E_{pk}/E_{acc} (= 1.98). It has a small refinement of the Low-Loss shape.

Many single cell cavities with the advanced shapes were built, prepared with the standard ILC recipe, and tested to demonstrate gradients of 50 – 54 MV/m with Q0 values above 10^{10} [111, 112], as shown in Fig. 4.22(a). A record field of 54 MV/m at Q about 10^{10} was set by a single cell Re-entrant cavity with 60 mm aperture, and 59 MV/m at Q about 3×10^9 (see Fig. 4.22(c) [113])

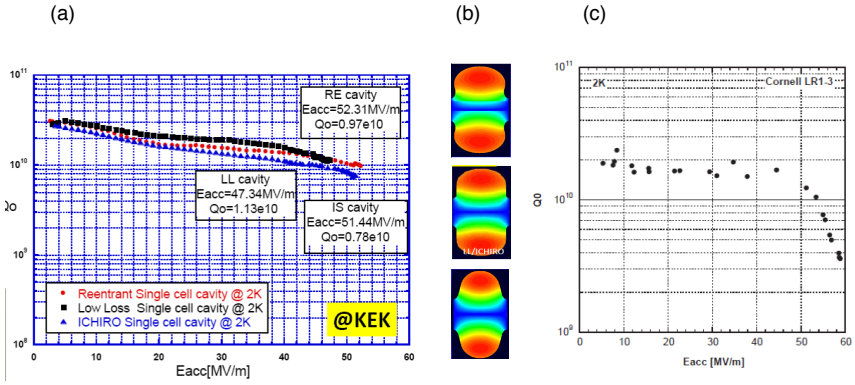

Figure 4.22: (a) Gradients greater than 50 MV/m demonstrated in single cell cavities of various improved shapes. (b) Comparison of Reentrant-top, Low Loss/Ichiro-middle and TESLA-bottom cavity cell shapes, color is magnetic field intensity, red highest, blue lowest. (c) Record gradient near 59 MV/m demonstrated with the re-entrant shape (60 mm aperture).

for the same cavity. However, the best multi-cell cavities of the new shapes have only reached 42 MV/m [114], mostly due to the dominance of field emission. A 5-cell cavity of the LSF shape recently tested at JLAB showed 50 MV/m gradient in three of the five cells [115] by exciting several modes of the fundamental pass-band.

As we have seen earlier, the newly developed, two-step bake procedure has demonstrated a gradient of 49 MV/m in TESLA shape 1-cell cavities. Combining the two-step bake with one of the advanced shape cavities has the potential of improving the gradients toward 60 MV/m. For example, the Low-Loss shape has the potential for 18% improvement from 49 to 58 MV/m. But no laboratory has attempted such combined efforts as yet.

Cost reduction efforts

The energy upgrades would also benefit from cost saving measures under exploration, such as niobium material cost reduction (15-25%) for sheet production directly from ingots (with large grains), and/or from seamless cavity manufacturing from tubes using hydroforming, or spinning, instead of the expensive machining and electron beam welding procedures now in practice. Cost-reducing avenues for cryomodules [116] are to connect cryomodules in continuous, long strings similar to cryostats for long strings of superconducting magnets, saving the cost for the expensive ends. The elimination of the external cryogenic transfer line by placing all cryogenic supply and return services in the cryomodule also reduce costs, not only directly for the cryogenic components, but also by reducing tunnel space required. Additional cost reductions and efficiency improvements (not included in the TDR 1 TeV estimate) can be also be expected from improved klystron and modulator technology. In Sec. 15.1, we discuss the ILC upgrade path from 1 TeV to 2 TeV based on gradients/Q of 55 MV/m/2×10^{10} obtained by the best new treatments, such as the two-step bake/Cold EP, applied to advanced shape structures, such as the Low-Loss structure, built from

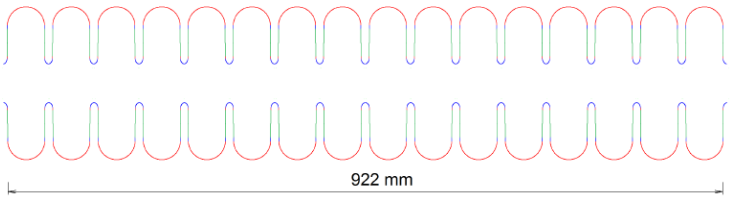

Figure 4.23: A segment of a one-meter TW structure.

Niobium. This section also provides tables summarizing the main parameters of the 2 TeV ILC upgrade path to be compared to CLIC 1.5 TeV and the 70–80 MV/m SRF upgrade paths to 3 TeV As discussed in Sec. 15.1, we consider the ILC upgrade path from 1 TeV to 3 TeV based on very high gradient SRF opened by R&D underway on two fronts:

1. Optimized travelling wave (TW) superconducting structures [117, 118, 119] with effective gradients up to 70 MV/m, along with 100% increase in R/Q - which reduces the dynamic heat load by 100%, and
2. 80 MV/m/1 $\times$ 10^{10} gradient/Q potential for Nb_3Sn [119] at 4.2 K, based on extrapolations from high power pulsed measurements on single cell Nb3Sn cavities.

Travelling wave structures

Travelling wave (TW) structures offer several main advantages compared to standing wave (SW) structures: substantially lower peak magnetic (H_{pk}/E_{acc}), lower peak electric field (Epk/E_{acc}) ratios, together with substantially higher R/Q (for lower cryogenic losses). The emphasis for future design is to lower H_{pk}/E_{acc}, as much as possible, since Hpk presents a hard ultimate limit to the performance of Nb cavities via the critical superheating field. But, as Fig 4.23 shows, the TW structure requires twice the number of cells per meter as for the SW structure in order to provide the proper phase advance (about 105 degrees), as well as a feedback waveguide for redirecting power from the end of the structure back to the front end of accelerating structure, which avoids high peak surface fields in the accelerating cells. The feedback requires careful tuning to compensate reflections along the TW ring to obtain a pure traveling wave regime at the desired frequency.

As discussed in Sec. 15.1, to obtain a luminosity comparable to CLIC 3 TeV, the beam bunch charge for the 3 TeV upgrade can be 3 x lower than the bunch charge for 0.5 TeV. Hence it is possible to lower the cavity aperture (from 70 mm to 50 mm) without severe penalty in wake-fields to obtain an overall 48% reduction in H_{pk}/E_{acc}, and factor of 2 gain in R/Q over the TESLA standing wave structure. Accordingly, we examine the impact of 70 MV/m for the 3 TeV ILC upgrade to obtain a luminosity comparable to CLIC 3 TeV. Section 15.1 provides tables summarizing the main parameters of the 70 MV/m ILC upgrade path as compared to CLIC 3 TeV, including capital costs, AC powers, energy spreads and backgrounds at the IP. Modelling and optimization calculations are underway for TW structure optimization [119]. Table 4.3 shows one set of optimized parameters for optimized cell shape, phase advance, and 50 mm aperture that yield H_{pk}/E_{acc} = 28.8 Oe/(MV/m)

Optimization	
Phase advance θ, deg	
A, mm	
B, mm	
a, mm	
b, mm	
E_{pk}/E_{acc}	
B_{pk}/E_{acc}, mT/(MV/m)	
R_{sh}/Q, Ohm/m	
α, degrees	
l, mm	
R_{eq}, mm	
v_{gr}/c	
E^*_{acc}, MV/m	
$E^*_{acc} \cdot 2L$, MV	

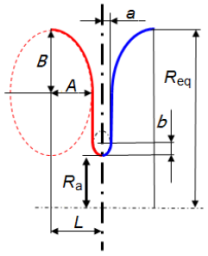

Table 4.3: Parameters of optimized cells with limiting surface fields: E_{pk} = 120 MV/m and B_{pk} = 200 mT, aperture radius R_a = 25 mm. Eacc is the accelerating rate when the limiting surface fields are achieved. 2L is the cell length = 57.55 mm. An 18-cell structure (1.036 m) will have the nearly same active length as the TESLA structure (1.061 m). (from [107], Table 5, column 2).

with E_{pk}/E_{acc} = 1.73. Since Hpk/Eacc is 42.6 Oe/MV/m and E_{pk}/E_{acc} = 2 for the TESLA structure, the TW structure has reduced the critical parameter H_{pk}/E_{acc} by 48%! The geometrical parameters for the cell shape are defined in the inset figure accompanying Table 4.3. If results for the best single cell TESLA shape cavities prepared today (E_{acc} = 49 MV/m, H_{pk} = 209 Oe) can be reached in such a TW structure it will be possible to reach E_{acc} = 72.5 MV/m. The 100% R/Q increase lowers the dynamic heat load and cryogenic power needed for high gradients.

The high group velocity in the TW mode also increases the cell-to-cell coupling from 1.8% for the TESLA structure to 2.3%. Thus TW structures have less sensitivity to cavity detuning errors, making tuning easier, despite the larger number of cells. Studies [119] show that the cell shape can be fine tuned to avoid multipacting, without increasing H_{pk} more than 1%. HOM damping is under study. Preliminary results show that the first 10 monopole modes up to 7 GHz show no trapping.

Many significant challenges must still be addressed along the TW development path. High circulating power in the feedback waveguide must be demonstrated. Cavity fabrication and surface processing procedures and fixtures must deal with (roughly) double the number of cells per structure.

First structure fabrication and testing efforts have started for TW cavity development [117, 118]. With the relatively easier BCP treatment only, the first single cell TW cavity (Fig. 4.24(a)) with recirculating waveguide achieved 26 MV/m accelerating gradient, limited by the high field Q-slope, as expected for BCP. This result is very encouraging for a first attempt. A 3-cell Nb TW structure with recirculating waveguide (Fig. 4.24(b))was designed and fabricated but has not yet been tested.

In Sec. 15.1, we consider the ILC upgrade path from 1 TeV to 3 TeV based on 70 MV/m TW Nb cavities to be compared to CLIC 3 TeV. The Section provides tables summarizing the main

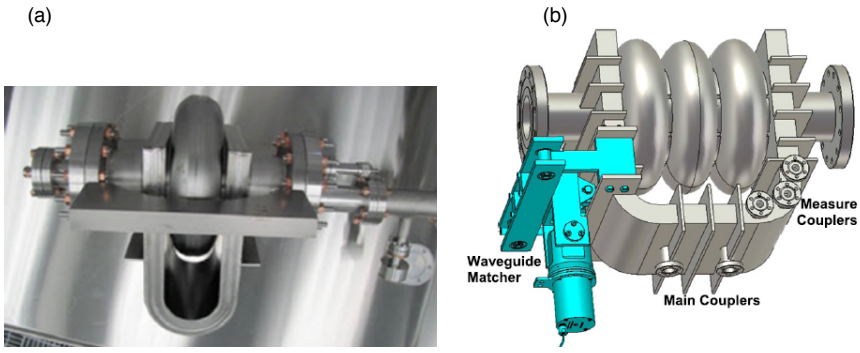

Figure 4.24: (a) 1-cell TW Niobium structure with return waveguide, treated by BCP and tested to reach 26 MV/m. (b) 3-cell TW structure built but not yet tested.

parameters of the 3 TeV ILC with CLIC 3 TeV.

4.3.4 Nb_3Sn

A15 compounds are intermetallic and brittle in the bulk form, so SRF structures are produced as a thin layer on the inner surface of an already formed structure. Nb_3Sn is the most explored compound with the best results [120, 121, 122], but does not as yet give as good performance as with Nb cavities. The A15 phase is in the composition range of 18–25 at% Sn. The superconducting properties T_c, Δ, and H_c, depend strongly on the Sn content [123]. Perfect ordering in the stoichiometric phase is achieved close to stoichiometry (at 24.5 at%) where H_{sh} is 0.42 mT as compared to Nb's H_{sh} of 0.22 mT at 0 K. Accordingly, we can expect the upper limit of the gradient to be 400 mT or near 95 MV/m.

A few microns thick Nb_3Sn films can be deposited on the inner surface of Nb cavities exposed to Sn vapor (10^{-3} mbar) in an UHV furnace at temperatures between 1050 C and 1250 C. In general, the Nb_3Sn films produced exhibit good material quality with Sn content of about 25%, Tc from 16 to 18 K, Δ from 2.7 to 3.2 meV [124]. Coating results are typically reproducible for the same Nb cavity substrate, but have been seen to vary between different cavities.

Some of the limitations of Nb_3Sn arise from the sensitivity of the thermodynamic critical field Hc (and therefore the superheating field) to the exact Sn concentration. For example, a Sn depletion of 3% reduces Hc by 75%. Other difficulties are the high surface roughness at Nb_3Sn grain boundaries possibly causing local field enhancement. Somewhat thinner (1 um) layers give smoother surfaces and best results (Fig. 4.25).

Most practitioners of Nb_3Sn have encountered a Q-slope problem and with gradient limits. Progress has continued. The best case of a flat Q vs E curve out to 23 MV/m has been achieved at Fermilab [120, 121, 122] The performance at 4.2 K is also very attractive showing $Q_0 > 10^{10}$ at gradient of 18 MV/m. Latest films have smaller surface roughness (by a factor of 2), smaller thickness (1 μm vs 2–3 μm) and smaller grain size (0.7 μm vs 1.2 μm). Careful material science

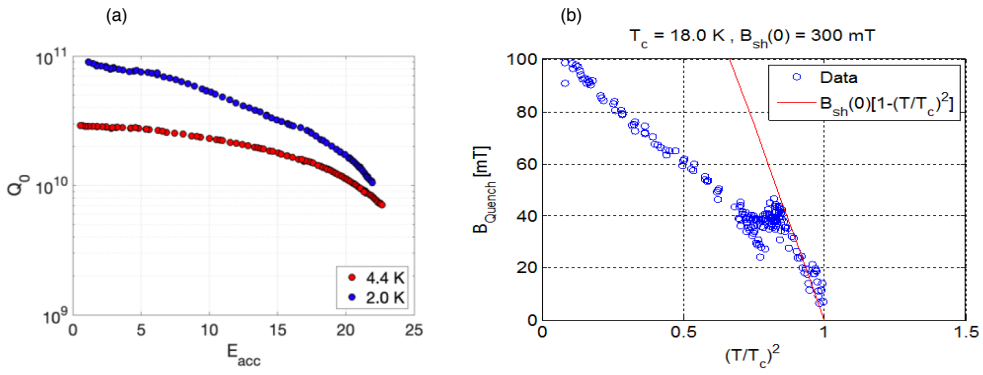

Figure 4.25: (a) Record CW behavior for Nb_3Sn coated at Fermilab showed E_{acc} = 23 MV/m. (b) Measurements of the critical RF field of Nb_3Sn using high power pulsed RF. The high temperature results extrapolate to a maximum surface magnetic field of 300 mT, which would translate to E_{acc} = 85 MV/m for a Low-Loss shape cavity.

is yet required to understand and confidently control the Nb_3Sn crystal growth dynamics so as to produce low-loss surfaces.

High power pulsed RF measurements (Fig. 4.25(b)) at Cornell on a Nb_3Sn cavity show encouraging trends for very high gradients [120]. At high temperature ($T > 15$ K), the results track the high superheating field, extrapolating to 300 mT ($E_{acc} \approx 80$ MV/m) at zero temperature. But at lower temperature, thermal limitations take over to limit the highest field to about 100 mT (24MV/m) which is close to the CW result of 22 MV/m.

In Sec. 15.1 ILC upgrade beyond TDR, we consider the ILC upgrade path from 1 TeV to 3 TeV based on Nb_3Sn cavities with gradients/Q of 80 MV/m/1 $\times 10^{10}$. The Section provides Tables summarizing the main parameters of the 3 TeV ILC to be compared to CLIC 3 TeV, and also discusses the potential benefits from 80 MV/m Nb_3Sn.

4.4 ILC Accelerator technical preparation plan

[5 pages; corresponding editor: Shinichiro Michizono (shinichiro.michizono@kek.jp)]

Although much work has already been done to establish the ILC design and technical readiness, a number of issues remain to the studied to prepare the final design of the ILC. The techical basis for the ILC was fully documented ten years ago in the ILC Technical Design Report and its Addendum [3, 4]. Still, three sets of issues need to be studied anew. First, it is necessary to revisit all of the items to understand whether any updates are called based on more recent R&D results (including the past ten years of SRF cost reduction R&D) and consistency with the ILC staging plan [9]. Second, because the TDR work was done without a specific site in view. issues related to the site must be addressed again for the specific candidate site in the Tohoku region of Japan. Finally, the MEXT advisory panel and the Science Council of Japan have called attention to some

Figure 4.26: Summary of the Work Packages for the technical preparations that will be carried out during the ILC Pre-Lab period.

remaining technical issues that need to be resolved during the ILC preparation period [125, 126].

The International Development Team (IDT) was established by the International Committee for the Future Accelerators in August 2020 to prepare for establishing the ILC Pre-lab as the first step toward the construction of the ILC in Japan. IDT-WG2 is now identifying the accelerator-related activities for the ILC Pre-lab necessary before starting the construction of the ILC. The ILC Pre-lab activities is expected to continue about 4 years and the principal accelerator activities of the ILC Pre-lab are technical preparations and engineering design and documentation. The deliverables of the Pre-lab accelerator activities, both technical preparations and engineering design and documentation, will be provided as in-kind contributions by member laboratories of the Pre-lab. Overall management of worldwide Pre-lab accelerator activities will be provided by the Associate Director for Accelerators, assisted by the Central Technical Office. Similarly, each technical preparation and engineering design work package will be led by a manager drawn from one of the member laboratories, guided by the domain and common technology managers. The detailed organization chart for Pre-lab accelerator activities will be defined by the Pre-lab Directorate. The ILC Machine Advisory Committee (ILCMAC), in its advisory role to the Associate Director for Accelerators, will monitor technical progress and review the engineering design and documentation. A full description of technical preparation is given in the document "Technical Preparation and Work Packages (WPs) during ILC Pre-lab" [127]. In this section, we will briefly review this plan.

The Work Packages (WPs) for the technical preparation activities include:

- **Main Linac (ML) and SRF production**: Cavity and Cryomodule (CM) global production readiness will be demonstrated through the fabrication of roughly 40 cavities in each of the 3

regions, the requirement of RF performance achieved with $\geq 90\%$ success demonstrated with sufficient statistics by using a part (about a half) of the 40 cavities in each region, and the fabrication of 2 CMs in each of the three regions using 40% of the cavities fabricated.

- **ML global integration**: The program of global CM transfer will be conducted to demonstrate the the CM production satisfies satisfies high-pressure gas safety (HPGS) regulations, safe transport across oceans, and the qualification of the CM performance after shipping from Europe and the Americas to Japan across the oceans. One of the two CMs in each region wil be used for this purpose. We plan to accomplish this goal with two steps. In the first step, if transport-test CMs (fully constructed but not suitable for use in the linac) are available from LCLS-II and/or European XFEL, those will be used to test simple transportation and to gather important information about stress, acceleration, *etc.*, excluding the HPGS regulation process. In the second step, the ILC prototype CM developed during the ILC Pre-lab phase will be shipped to Japan, including the HPGS regulation process and the full CM quality assurance program within the ILC Pre-lab phase period.

- **Positron source** : The final design will be selected from either the an undulator-driven or the electron-driven option and its technology readiness will be demonstrated.

- **Damping Ring (DR) and Beam Delivery System (BDS)**: Readiness of the nanobeam technology for the DR, based on work at the ATF3 and related facilities, and the BDS systems will be demonstrated, particularly including the fast kicker and feedback controls.

- **Beam dump**: A system design will be established, including beam window handling, cooling water circulation, and safety assurance.

A total of 18 WPs (3 ML&SRF, 8 Sources, 3 DR, 2 BDS, and 2 Dumps) are proposed as illustrated in Fig. 4.26 and summarized in an extended list below. The classification of some items should be clarified. The crab cavity (WP-3) will be installed in the BDS area, but is classified as ML&SRF since the crab cavity uses SRF technology. The photon dump (WP-18) will be used for the undulator positron source. However, this WP-18 is classified as dump due to its specialty. The target replacement (WP-11) is a common WP for undulator and e-driven positron sources. These relationships are also shown in Fig. 4.26.

The explicit tasks of the WPs are as follows:

- **WP-1 (ML&SRF)**: Cavity Industrial Production Readiness (3×40 Cavities)
  - Cavity industrial production readiness to be demonstrated, including cavities with He tank + magnetic shield for cavity, high-pressure-gas regulation, surface-preparation/heat treatment (HT)/Clean-room work, partly including the 2nd pass, vertical test (VT)
  - Plug compatibility, Nb material, and recipe for surface treatment to be reconfirmed/decided
  - Cavity Production Success yield to be confirmed (before He tank jacketing)
  - Tuner baseline design to be established

  Note: Infrastructure for surface treatment, HT, VT, pre-tuning, *etc.*, is the responsibility of each region.

- **WP-2 (ML&SRF)**: Cryomodule (CM) Assembly, Global Transfer and Performance Assurance (3×2 CMs)
  - Coupler production readiness to be demonstrated, including preparation/RF processing (3×20 Couplers)
  - Tuner production readiness to be demonstrated, including reliability verification (3×20 Tuners)
  - Superconducting Magnet (SCM: Q+D combined) production readiness to be demonstrated (3×3 SCMs, 1 prototype + 2 in each region)
  - CM production readiness to be demonstrated including high-pressure-gas, vacuum vessel (VV), cold-mass, and assembly (cavity-string, coupler, tuner, SCM, *etc.*)
  - CM test including degradation mitigation (in 2-CM joint work, etc.) at assembly site before ready for CM transportation
  - CM Transportation cage and shock damper to be established
  - Ground transportation practice, using mockup-CM
  - Ground transportation test, using production-CM longer than Eu-XFEL
  - Global transport of CM by sea shipment (requiring longer container)
  - Performance assurance test after CM global transport (at KEK)
  - Returning transport of CM back to home country (by sea shipment)

  Note: Infrastructure for coupler conditioning: klystron, baking furnace, and associated environment is the responsibility of each region. Also, hub-lab infrastructure for the CM production, assembly, and test is the responsibility of each region.

- **WP-3 (ML&SRF)**: Crab Cavity (CC) for BDS (2 CCs + 1 for SRF validation)
  - Decision of installation location with cryogenics/RF location accelerator tunnel
  - Confirmation of the complete CC system specifications
  - Development of CC cavity/coupler/tuner integrated design (ahead of Preliminary CC technology Down-selection)
  - Preliminary CC technology down-selection (2 cavity options)
  - CC Model-work and Prototype production and high-power validation of CC cavity/coupler/tuner integrated system for two primary candidates (ahead of final CC technology Down-selection)
  - Harmonized operation of the two prototype cavities in a vertical test to verify ILC synchronization performance (cryo insert development and commercial optical RF synchronization system)
  - Final CC technology down-selection
  - Preliminary Crab CM design – confirming dressed cavity integration and compliance with beam-line specification
  - Final CM engineering design prior to production

  - Infrastructure for CC development and test in each region

- Additional ML&SRF tasks beyond the Pre-Lab (1 CM)
  - Cavity (incl He tank) production (incl couplers and tuner), magnetic shield for CM, high-pressure gas regulation, EP/HT/Clean work, including VT
  - Input coupler production including preparation/RF processing readiness (excluding klystron, baking furnace, clean room)
  - Prototype CM production including High-pressure gas, vacuum vessel, cold-mass, and assembly (cavity-string, coupler/tuner, SCM and tooling, *etc.*)
  - Prototype CM test including harmonized operation with two cavities
  - Prototype CC-CM transport cage and shock damper design and manufacture
  - Prototype CC-CM transport tests
  - Infrastructure for CM development and testing in each region
- **WP-4 (Sources)**: Electron Source
  - Drive laser system
  - HV Photogun
  - GaAs/GaAsP Photocathodes
- **WP-5 (Sources)**: Undulator Positron Source
  - Simulation (field errors, masks, alignment)
- **WP-6 (Sources)**: Undulator Positron Source rotating target
  - Design finalization, partial laboratory test, mock-up design
  - Magnetic bearings: performance, specification, test
  - Full wheel validation, mock-up
- **WP-7 (Sources)**: Undulator Positron Source magnetic focusing system
  - OMD design finalization with yield calculation
  - OMD with fully assembled wheel
- **WP-8 (Sources)**: Electron-Driven Positron Source rotating target
  - Target stress calculation with FEM
  - Vacuum seal
  - Target module prototyping
- **WP-9 (Sources)**: Electron-Driven Positron Source rotating target
  - Target stress calculation with FEM

  - Vacuum seal
  - Target module prototyping

- **WP-10 (Sources)**: Electron-Driven Positron Source capture system
  - APS cavity for the capture linac
  - Capture linac beam loading compensation and tuning method
  - Capture linac operation and commissioning
  - Power unit prototyping
  - Solenoid prototyping
  - Capture linac unit prototyping

- **WP-11 (Sources)**: Positron Source target maintenance
  - Target Maintenance (a common issue for the undulator and electron-driven sources)

- **WP-12 (Damping Rings)**: System Design
  - Optics optimization, simulation of the dynamic aperture with magnet model
  - Magnet design : Normal conducting magnet and SC wiggler
  - Magnet design : Permanent magnet
  - Prototyping of permanent magnet

- **WP-13 (Damping Rings)**: Evaluation of collective effects in the ILC damping ring
  - Simulation : Electron cloud instability
  - Simulation : Ion-trapping instability
  - Simulation : Fast ion instability (FII)
  - System design : Fast FB for FII
  - Beam test : Fast FB for FII

- **WP-14 (Damping Rings)**: System design of ILC DR injection/extraction kickers
  - Fast kicker: System design of DR and LTR/RTL optics optimization
  - Fast kicker: Hardware preparation of drift fast step recovery diode pulser
  - Fast kicker: System design and prototyping of induction kicker
  - Fast kicker: Long-term stability test at ATF
  - E-driven kicker: System design,including induction kicker development

- **WP-15 (BDS)**: System design of ILC final focus beamline
  - ILC-FFS system design: Hardware optimization
  - ILC-FFS system design: Realistic beam line driven / IP design

  - ILC-FFS beam tests: Long-Term stability
  - ILC-FFS beam tests: High-order aberrations
  - ILC-FFS beam tests: R&D complementary studies

- **WP-16 (BDS)**: Final doublet design optimization
  - Re-optimization of TDR FF design considering new coil winding technology and IR design advances
  - Assembly of QD0 prototype, connection to Service Cryostat and measurement of warm/cold vibration stability with a sensitivity of a few nanometers

- **WP-17 (Beam Dump)**: System design of the main beam dump
  - Engineering design of water flow system
  - Engineering design and prototyping of components; vortex flow in the dump vessel, heat exchanger, hydrogen recombiner
  - Engineering design and prototyping of window sealing and remote exchange
  - Design of the countermeasure for failures / safety system

- **WP-18 (Beam Dump)**: System design of the photon dump for the undulator positron source
  - System design and component test of an open-window water dump
  - System design and component test of a graphite dump

The cost and required human resources required for the WPs are estimated in [127]. The values given are are initial estimates. The actual numbers will depend on the laboratories that will take the responsibility for the deliverables, so these estimates will be re-evaluated later. Infrastructure associated with the series of items mentioned above will need to be newly prepared and/or improved with each region taking responsibility for implementation and financial support. The technical readiness scoped in each WP needs to be verified through periodical reviews conducted by the ILC Pre-Lab. The ILC technical design will need to be updated reflecting the progress on the WPs, and these updates will be implemented/added to the engineering documents. Stability and tuning issues in some WPs will also need to be coordinated with the start-to-end accelerator design that will be done as part of the "engineering design and documentation" activities of the Pre-Lab. These linkages will be carried out as a part of the ILC Pre-Lab responsibility.

We expect the these activities can be completed within a four-year preparation period. We divide the timeline into two categories: "Technical Preparation and Readiness" and "Engineering documentation". Here is a plan showing how the WP activities fit into the timeline, using the SRF and Positron Source work as examples:

Year	Technical preparation	Engineering documentation
1	Continue cost-reduction R&D for SRF cavities Start pre-series production of SRF cavities in cooperation with industry Continue e^+ source development	Start review and update of TDR cost estimates by an international team
2	Complete cost-reduction R&D Determine production yield Start assembling cavities into cryomodules Review e^+ source designs	Conduct a review on the progress for technical work and cost estimation by an internal panel
3	Demonstrate overseas shipment of cryomodules taking all the safety and legal aspects into account Select e^+ source design and start prototyping and cost issues of critical items, *e.g.*, the e^+ target	Complete cost estimate and conduct internal and external review Complete risk analysis for the technical and cost issues Complete a draft of the Engineering Design Report
4	Evaluate cryomodules after shipment and demonstrate the quality assurance procedure Establish regional organization for the ILC component production Continue prototype work for critical components of the e^+ source, *e.g.*, the e^+ target	Complete and publish the Engineering Design Report Start producing specification documents and drawings of large items for tendering

Progress in technical preparation activities will be monitored and evaluated through periodic reviews. The activities will be also synchronized with the engineering documentation.

4.5 Opportunities for US contributions

[8 pages; corresponding editor: Sam Posen (sposen@fnal.gov)]

US laboratories host world-class infrastructure and expertise in technology that is relevant for particle accelerators. This presents a number of opportunities for the US to make important contributions to the ILC accelerator that leverage existing capabilities. These contributions would help the project to go forward and position the US well for strong participation in ILC-based experiments.

4.5.1 Superconducting Linac

The superconducting linear accelerator that drives the ILC requires 1000 cryomodules to reach a center of mass energy of 250 GeV. Each cryomodule (see Fig. 4.27) contains 8 ∼1 meter long superconducting radiofrequency (SRF) cavities, which generate large amplitude electric fields to accelerate the beam. They also contain liquid-helium-based cryogenics to keep the cavities at 2 K, magnets, RF power couplers, frequency tuners, vacuum valves, and instrumentation. US labs have substantial experience with these sophisticated components from US-based accelerator projects

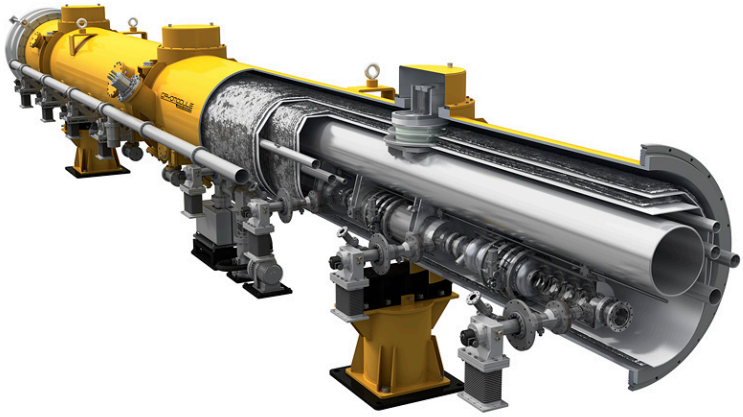

Figure 4.27: Cutaway view of an ILC cryomodule. (Image by Rey Hori [128].)

including CEBAF, SNS, LCLS-II, and PIP-II. Large scale production facilities exist at Fermilab and at Jefferson Lab for assembling SRF cryomodules (see Fig. 4.28). These facilities include large cleanrooms for making vacuum connections between cavities while minimizing the risk of generating particulates that can cause field emission, large fixtures for connecting cavity strings to cold masses and inserting cold masses into cryomodules, and equipment for welding, RF diagnostics, and coupler assembly. Fermilab and JLab also have existing cryomodule test facilities, which require 2 K refrigerators, dedicated radiation areas, and RF systems. These facilities have very recently been used for the mass production of cryomodules for LCLS-II, for which the cryomodule design was largely based on ILC. As such the production facilities have already been recently tested with a very relevant system, though ILC would require approximately 5 times as many modules to be produced as the entire production of LCLS-II and its high energy upgrade LCLS-II-HE combined. However, the Fermilab and JLab and the teams would take on the larger production with enthusiasm and experience. The vast majority of the infrastructure is already in place, with some modifications required for the higher throughput required to meet the 1 cryomodule per week target for the Americas region at peak production.

In addition to Fermilab and JLab, there are also SRF facilities at Argonne, Cornell, and FRIB, which are less specialized towards production of ILC-like cryomodules, but could be leveraged for example for cavity treatment. SLAC's expertise in high power RF sources could be leveraged for driving the cavities as well as RF distribution. SLAC is also planning a relevant cryomodule test facility that could be used. Berkeley's expertise in low level RF could be leveraged for cavity control, particularly for resonance control at high accelerating gradients.

Fig. 4.28: View of some of the cryomodule assembly facilities at Fermilab (left) and Jefferson Lab (right).

US expertise can also contribute to advanced performance for ILC cryomodules. Since the 2012 TDR, significant progress has been made in SRF R&D, including new procedures developed by researchers from US labs for reaching high gradients. Some of these developments could be implemented in ILC cryomodules to push performance by 10%, either resulting in fewer cryomodules

Figure 4.28: View of some of the cryomodule assembly facilities at Fermilab (left) and Jefferson Lab (right).

required to reach the design center of mass energy, or else as a safety margin on top of the nominal energy and beginning towards first energy upgrades. The relevant new technologies include cold electropolishing [129] and the two step bake [86].

Advances from US labs can also contribute to some of the auxiliary systems of the cryomodules. The tuner used in LCLS-II was an evolution of previous designs and is well suited to the short beamtubes of the ILC, while maintaining minimal backlash [130]. The quadrupole magnet used in LCLS-II is also an evolution of previous designs, with conduction cooling and a split design to allow it to be assembled outside of the cleanroom [131]. A system and procedure for plasma processing of SRF cavities was developed at ORNL [132] and later adapted to 9-cell cavities by FNAL [133], which may be useful for reducing effects such as field emission in some cases.

US labs are expected to also play a leading role in developing technologies for energy upgrades to the ILC to reach the 380 GeV-1 TeV energy range beyond the baseline ILC and the multi-TeV energy range in the future. This includes SRF R&D, such as development of advanced superconductors including Nb3Sn for cavities [134], advanced geometries [118], and a plasma accelerator that leverage the SRF-based ILC baseline system. For more details on these upgrades, see Sec. 15.

4.5.2 Electron and Positron Sources

Many US labs have capabilities in sources from their own facilities. The plan for ILC has a polarized positron source, which can be accomplished in different ways. One of these employs superconducting undulators, the other targets, and both subjects have expertise at a number of US labs.

4.5.3 Damping Ring, Beam Delivery System, and Beam Dump

US accelerator scientists have extensive experience also in the technologies needed for the damping ring, beam delivery system, and beam dump.

The damping ring is expected to be similar to multiple US facilities, such as the APS upgrade at Argonne, CESR at Cornell, and NSLS-II at Brookhaven.

For beam dynamics and lattice development, researchers at nearly all US labs with accelerators have substantial relevant experience as well as specialized tools and codes such as ACE3P, ELEGANT, and BLAST.

Expertise in superconducting magnets at labs such as FNAL, Berkeley, and BNL can be applied to the magnets needed for the final focus at the interaction point. A similar task is ongoing at US labs for production of magnets for the high luminosity upgrade of the LHC.

For research and development related to plasma-accelerator-based multi-TeV upgrades to ILC, US labs host multiple accelerator facilities that could be used for relevant R&D including AWA at Argonne, FACET at SLAC, ATF at BNL, BELLA at LBL, and FAST at Fermilab.

4.5.4 Summary

The US National Laboratories are anticipating a wide range of contributions to the ILC accelerator. These contributions are synergistic, both from past programs—*i.e.*, they leverage existing infrastructure and expertise in US labs—and for developments for the future—*i.e.*, much of the needed R&D for the US contribution to ILC has application to other accelerator projects that the laboratories are involved in.

By virtue of this, there is a broad interest among all of the US National Laboratories invested in accelerator physics in participating in ILC. In addition to synergies with US labs, there is also synergy with US industry. A substantial part of the US funds for ILC construction will be put towards procurements from US companies for high-tech components that will be used in cryomodules and other accelerator elements.

Chapter 5

General Aspects of the ILC Physics Environment

[5 pages; corresponding editors: Daniel Jeans (daniel.jeans@kek.jp), Jenny List (jenny.list@desy.de), Michael Peskin (mpeskin@slac.stanford.edu)]

This chapter gives a general orientation to the physics of the ILC. We will describe the major physics processes that the ILC will allow us to study, and the reactions that appear as backgrounds in the analyses discussed in Chapters 8–10.

We will also call attention to the effects of beam polarization. Beam polarization is not an important parameter for proton-proton collisions, first, because it is difficult to prepare highly polarized proton beams and, second, because the spin of a proton is divided among the quarks and gluons in a complex way. For electrons, the story is different. Because the electron is an elementary particle, its polarization is transferred directly into any reaction. Longitudinal polarization is maintained in linear acceleration, so that a highly polarized source of electrons or positrons produces a comparable effect of polarization in collisions. Further, in the SM, highly relativistic left- and right-handed polarized electrons are essentially different species, with different electroweak quantum numbers. Thus, measurements with different beam polarization measure different reactions, and the comparison of these reaction rates can give direct insight into the physics.

5.1 Key Standard Model Processes

The major reactions at e^+e^- colliders in the energy range of 100 GeV to 1 TeV are shown in Fig. 5.1. The typical size of a cross section in e^+e^- annihilation is the point cross section

$$1\ \mathrm{R} = \frac{4\pi\alpha^2}{3E_{CM}^2} = 1.4\ \mathrm{pb}\cdot\left(\frac{250\ \mathrm{GeV}}{E_{CM}}\right)^2, \tag{5.1}$$

corresponding to several million events in a data set of 2 ab^{-1} at 250 GeV. This is a much smaller number of events than is typically collected by a hadron collider experiment. However, these

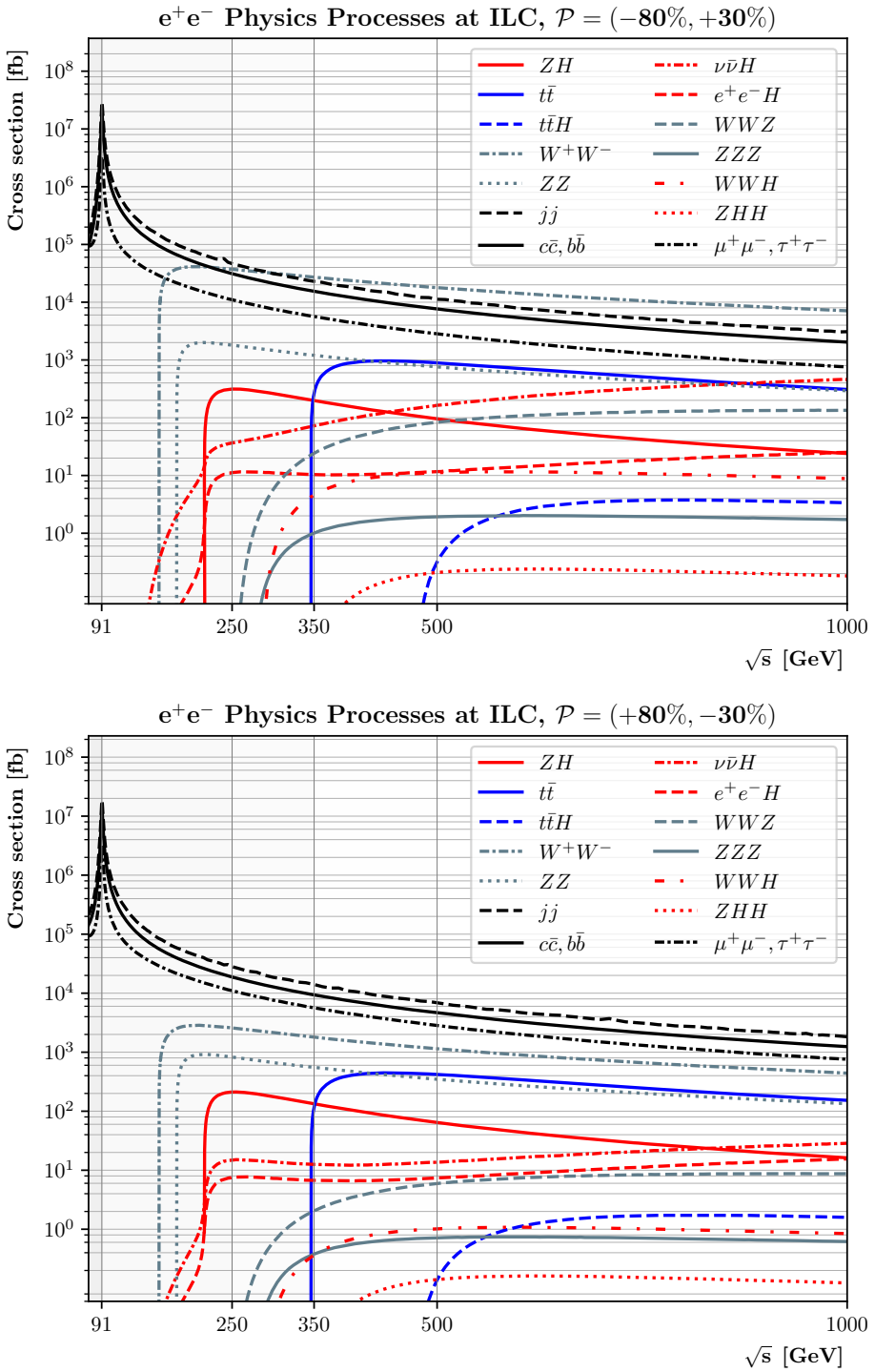

Figure 5.1: Cross sections of the most important Standard Model processes in e^+e^- annihilation in the energy range of the ILC. Initial state radiation is included, and cross section are plotted for reactions in which the annihilation retains $> 90\%$ of the nominal CM energy. The cross sections are shown for predominantly left-handed beam polarization (-80% /+30% for e^-/e^+) (top) and for predominantly right-handed beam polarization (+80% /-30%) (bottom). It is instructive to compare the two plots, which have subtle and not-so-subtle differences.

events appear individually in e^+e^- bunch collisions, are essentially free of extra tracks and debris associated with the beams, and are reconstructable with high efficiency over an angular region that extends to within milliradians of the beam directions. The simplicity of typical events allows the use of detector technologies with high degrees of discrimination and precision, as will be discussed in the next chapter.

Since the electron is an elementary particle, the basic parameters of the ILC beams are very well understood. Though the beams contain a distribution of electron and positron energies due to initial state photon radiation and radiation of photons in the beam-beam interaction ("beamstrahlung"), these are minor and computable effects. There is no analogue of the nonperturbative parton distributions needed for the interpretation of cross sections at hadron colliders. Similarly, the beam polarizations can be measured both by dedicated detectors and through SM processes with large cross sections. Thus, the ILC can carry out precision measurements of absolute cross sections in addition to asymmetries and distributions.

Each of the reactions shown in the figure has its own individual role in the program of the ILC. Each reaction gives access to its own set of precision tests of the Standard Model and searches for the effects of new physics. It is important to understand the hierarchy of reactions to understand the important sources of background that enter the various analyses. At an e^+e^- collider, backgrounds from simple QED and QCD processes are readily eliminated. The major backgrounds to processes with the production of heavy particles—within the SM, W, Z, Higgs, and top—are other reactions with heavy SM particles in the final state.

Each reaction also has its own characteristic dependence on beam polarization, as is shown in the figure. This will be an important theme of the discussion in this Chapter.

The simplest reaction in e^+e^- annihilation is that of $e^+e^- \to f\bar{f}$, where f can be a quark or a lepton. Even for the hadronic reactions, the final state is typically two narrow jets and is easily discriminated from reactions of electroweak bosons. At the tree level in the SM, the differential cross section is very simple. For example, for 100% left-handed polarized beams and $s \gg m_Z^2$, the differential cross sections are

$$\frac{d\sigma}{d\cos\theta} = \frac{\pi\alpha^2}{2s}\left[(\frac{1}{2}I^3_{fL} + \frac{1}{2}Y_{fL})^2)(1+\cos\theta)^2 + (\frac{1}{2}Y_{fR})^2(1-\cos\theta)^2\right] , \tag{5.2}$$

where (I^3_{fL}, Y_{fL}) are the electroweak quantum numbers of f_L and $(0, Y_{fR})$ are the electroweak quantum numbers of f_R. Note that the production of the two helicity states of f separates into the two hemispheres. Thus, with two different values for the beam polarization and separate measurment of the forward and backward cross sections, it is possible to probe all four individual helicity amplitudes contributing to this reaction. This provides a powerful and specific probe for new physics, as we will discuss in Sec. 10.4. Bhabha scattering ($e^+e^- \to e^+e^-$) has a more complex differential cross section, but this reaction is extremely well understood within the SM, leading to its own set of new physics tests.

The reaction $e^+e^- \to$ hadrons is also an exceptionally clean setting for studies of jets and the measurement of fragmentation functions. The potential ILC contributions to QCD, including new observables sensitive to jet substructure, are described in Sec. 8.4.

The annihilation reaction with the largest cross section in this energy region is $e^+e^- \to W^+W^-$. This reaction is forward-peaked, due to the contribution from a diagram with t-channel neutrino exchange. The reaction can be reconstructed in all W decay modes, with the most complex final states having 4 jets. This reaction obtains contributions from diagrams with the triple gauge couplings $WW\gamma$ and WWZ. Because of a cancellation among the SM diagrams required by the unitarity of that theory, the angular distributions and polarization effects in this reaction are exceptionally sensitive to new physics contributions to the triple gauge couplings. These effects are most pronounced in the central and backward W^+W^- production. We will discuss the measurement of these effects in Secs. 8.3 and 10.3. In contrast, the forward production is essentially model-independent. Because the neutrino exchange diagram requires left-handed electrons and right-handed positrons, the forward production has a large polarization asymmetry and so provides a very useful *in situ* measurement of beam polarization.

The other vector boson pair production reactions, $e^+e^- \to \gamma\gamma, Z\gamma, ZZ$, do not involve triple gauge couplings in the Standard Model. It can be shown that the new physics corrections to these reactions are also suppressed in the description of new physics by Effective Field Theory. Thus, these reactions can provide fundamental test of the Effective Field Theory framework, and, in some cases, tests of general positivity theorems of Quantum Field Theory. We will discuss these issues in Sec. 12.9.

The reaction $e^+e^- \to \gamma Z$ with γs almost collinear to the beam direction provides a large source of Z bosons that can be used to probe the Z properties even at CM energies well above the Z resonance. In the ILC run at 250 GeV, we expect to study about 90 million Z bosons in this "radiative return" reaction, leading to an improvement of a factor of 10 in the precision of $\sin^2\theta_w$ even without running at the Z resonance. The study of this reaction will be discussed in Sec. 9.2.

At 250 GeV, the dominant reaction for production of the Higgs boson is $e^+e^- \to ZH$. This process is expected to produce about half a million Higgs bosons in the 250 GeV run of the ILC, with each Higgs boson tagged by a recoiling Z boson. This will give an excellent setting for the measurement of SM and non-Standard Higgs boson decays. That study will be described in Secs. 8.1 and 8.2.

The ILC also expects a number of reactions with photons in the initial state. The photons arise as virtual photons from initial-state radiation and as real beamstrahlung photons emitted in the beam-beam interaction. For the ILC accelerator parameter sets, these two sources contribute roughly equally to the spectrum of initial photons. Important reactions due to initial-state photons are single W production ($e\gamma \to W\nu$) and single Z production ($e\gamma \to Ze$). Reactions with two photons in the initial state include photon annihilation to lepton pairs, quark pairs, and W^+W^-. The single boson production reactions have a role in the precision determination of the W and Z masses, as will be described in Sec. 9.4. All of these processes appear as the major backgrounds to new particle searches involving missing energy, as discussed particularly in Secs. 10.5 and 10.6.

The cross sections for $\gamma\gamma$ production at large angle decrease as $1/s(\gamma\gamma)$. The converse of this statement is that there is a large cross section for $\gamma\gamma$ annihilation to quarks and leptons at the lowest possible CM energies. This leads to an "underlying event" giving a few tracks in each e^+e^- bunch crossing. We find that this background has a negligible effect on our analyses.

At energies above 250 GeV, the initial electrons and positrons can radiate W and Z bosons and these can interact to produce SM and, possibly, new particles by vector boson fusion. The cross sections for these processes rise as $\log(s/m_W^2)$ and so above 500 GeV they become the dominant modes of heavy particle production. The coupling of the electron to the Z is rather small, so the ratio of the ZZ to WW luminosities is

$$\left[\frac{(\frac{1}{2}-\sin^2\theta_w)^2+(\sin^2\theta_w)^2}{\cos^2\theta_w}/\frac{1}{2}\right]^2 = 1\% \tag{5.3}$$

for unpolarized beams, and even smaller for polarized beams enhanced in the $e_L^- e_R^+$ initial state. Thus, WW fusion plays the dominant role. The most important processes here are WW fusion to a single Z ($e^+e^- \to \nu\bar{\nu}Z$) and to a single Higgs boson ($e^+e^- \to \nu\bar{\nu}H$).

The process $e^+e^- \to \nu\bar{\nu}H$ begins to dominate the $e^+e^- \to ZH$ process at about 400 GeV. Above this energy, the WW fusion process provides a second, independent data set for the study of Higgs boson couplings. In the WW fusion events, the Higgs boson appears as a heavy, centrally-produced particle with no other visible activity in the event. The fact that the Higgs boson can be produced in two distinct ways at e^+e^- colliders allows cross-checks of any anomalies with the same experimental program. This is another of the special benefits of studying the Higgs boson through e^+e^- annihilation. The study of the Higgs boson in WW fusion will be discussed in detail in Sec. 10.2.1.

The threshold for top quark pair production $e^+e^- \to t\bar{t}$, occurs in the region around of CM energy of 340–345 GeV. At and above this energy, the ILC can study the couplings of the top quark with a high precision. Of special interest are the electroweak couplings of the top quark, which have secondary importance at hadron colliders but provide the primary pair production mechanism at e^+e^- colliders. These couplings can be especially sensitive to new physics corrections, especially in models in which the Higgs boson is composite. Also, because the top quark theshold is a very narrow feature, the measurement of the threshold shape can give a very direct and accurate measurement of the top quark mass. We will discuss all of these issues in Sec. 10.1.

At the highest ILC energies, it is also possible to access multi-Higgs boson production processes. The most important of these are the reactions $e^+e^- \to ZHH$ and $e^+e^- \to \nu\bar{\nu}HH$, which depend directly on the Higgs boson self-coupling, and $e^+e^- \to t\bar{t}H$, which directly measures the Higgs boson coupling to the top quark. We will discuss these analyses in Sec. 10.2.

Thus, each separate ILC reaction has a role to play in challenging the predictions of the SM. But, even further, we do not need to interpret the individual processes in isolation from one another. By interpreting the SM and its possible corrections using Effective Field Theory, the contributions from the different reactions can be brought together and applied in a unified way. The whole set of ILC measurements is then more powerful than the simple sum of its parts. We will discuss this strategy of interpretating the ILC measurements in some detail in Chapter 12.

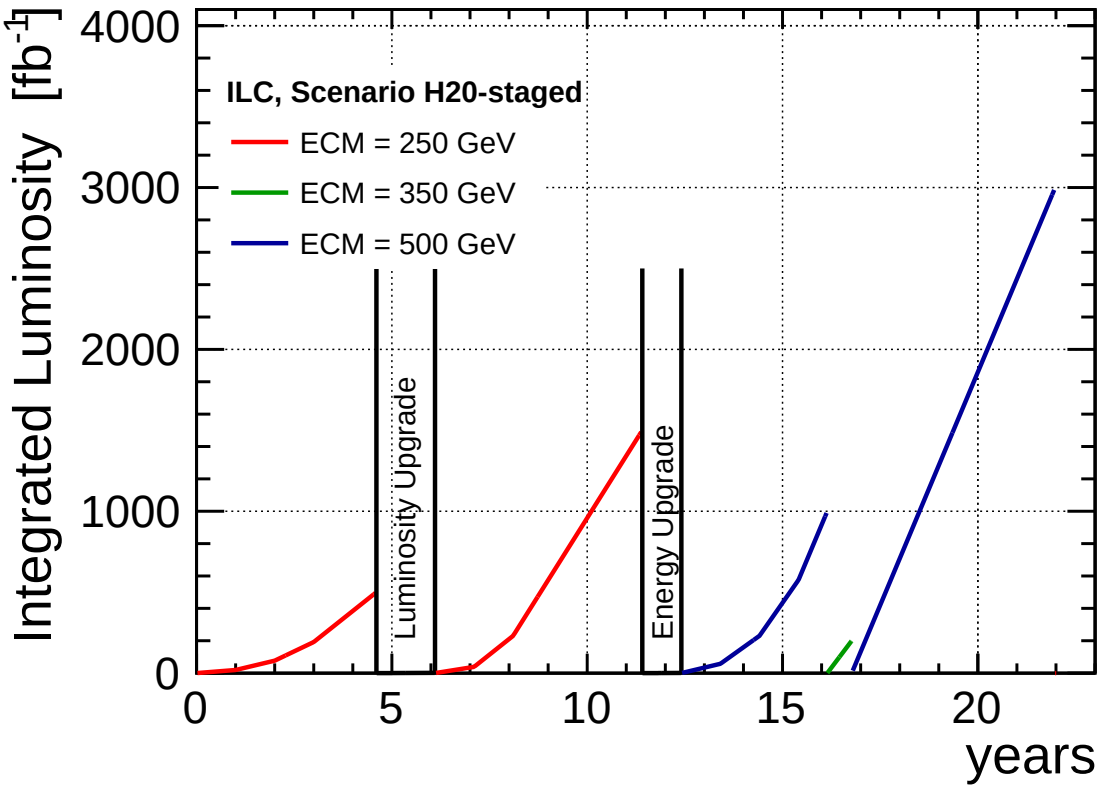

Figure 5.2: Plan for the operation of the ILC through its various stages from 250 GeV to 500 GeV. The details of this program most relevant for physics studies are shown in Table 5.1. The detailed accelerator parameters for each stage are given in Table 4.1. The total length of the program is 22 years. Additional stages at the Z boson resonance and at 1 TeV could be added to this plan. Parameters for these programs are also presented in Table 5.1.

	91 GeV	250 GeV	350 GeV	500 GeV	1000 GeV
$\int \mathcal{L}$ (ab^{-1})	0.1	2	0.2	4	8
duration (yr)	1.5	11	0.75	9	10
beam polarization (e^-/e^+; %)	80/30	80/30	80/30	80/30	80/20
(LL, LR, RL, RR) (%)	(10,40,40,10)	(5,45,45,5)	(5,68,22,5)	(10,40,40,10)	(10,40,40,10)
δ_{ISR} (%)	10.8	11.7	12.0	12.4	13.0
δ_{BS} (%)		2.6		4.5	10.5

Table 5.1: Parameters of the successive ILC stages most relevant for physics studies. The values given here are those actually used for the results to be quoted in this report. The fourth line gives the fraction of the total running time spent in each of the four possible beam polarization orientations. The fifth and sixth lines give the average energy loss to initial state radiation and beamstrahlung, respectively.

Figure 5.3: Luminosity spectra for e^+e^-, $e\gamma$, and $\gamma\gamma$ annihilation reactions for each of the designs in Table 5.1. The x axis in each graph is the effective CM energy as a fraction of the nominal CM energy.

5.2 Energy and Luminosity

As we have discussed already in Sec. 4.2, the ILC is designed to be upgraded, in stages, in energy and luminosity. Our current plan for the energy and luminosity evolution of the ILC is shown in Fig. 5.2. The parameters of the successive stages that are most important for understanding the physics studies are shown in Table 5.1.

The last lines of the table show the average fractional energy loss to initial state radiation and beamstrahlung. The e^+e^-, $e\gamma$, and $\gamma\gamma$ luminosity spectra for the various stages are shown in Fig. 5.3.

The ILC will begin with collisions at 250 GeV and a modest luminosity of 1.35×10^{34} $cm^{-2}sec^{-1}$. This luminosity would then be doubled by doubling the number of accelerated bunches per RF pulse, an upgrade that only requires the addition of RF power. In about 11 years, the ILC will have accumulated a total integrated luminosity of 2 ab^{-1}. This will be followed by an energy upgrade, which entails lengthening the linear accelerators to double their energy. We assume the current ILC accelerator parameters for this upgrade, but this will be less costly if higher-gradient superconducting RF cavities are available at that time. The 500 GeV stage will accumulate 4 ab^{-1} of integrated luminosity at 500 GeV, with also 200 fb^{-1} of luminosity near 350 GeV to measure the top quark mass to the level of the theoretical systematic errors.

Two additional runs could be added to this plan. The first is a run at the Z boson resonance, accumulating about 5×10^9 Z bosons. The accelerator parameters for this "Giga-Z" program have been discussed in Sec. [need this section in the acc. chapter]. If this run is done after the installation of RF for the 250 GeV luminosity upgrade, the Z program would take about 1.5 years. The second

is a run at 1 TeV, requiring a second lengthening of the linear accelerators. Since the luminosity of a linear collider naturally increases roughly linearly with the center of mass energy, we expect that the 1 TeV operator will accumulate 8 ab^{-1} if integrated luminosity in a 10-year program.

All of this data-taking will benefit from the expected high degree of polarization of the electron beam and the planned polarization of the positron beam. At 1 TeV, where the main object of study will be the WW fusion reactions, this benefit can be enhanced by chosing to operate predominantly with $e^-_L e^+_R$-polarized beams.

This plan for the evolution of the ILC is based on a detailed optimization study based on the physics goals, carried out in 2015 [135]. Of course, the plan is can be revised according to new developments in particle physics and superconducting RF technology.

5.3 Beam Polarization

The ILC design includes beam polarization for both electron and positrons. Beam polarization can be used in experiments in a number of different ways. In this section, we will summarize these and provide the polarization measures appropriate to each case. More details can be found in the individual analysis described below.

The ILC design calls for electron polarization of 80% and positron polarization of 30%. Both signs of the polarization will be available in each run. It is important that the polarization be flipped as often as possible to cancel systematic errors from drifts of detector parameters. For both beams, the polarization can be flipped pseudo-randomly bunch train by bunch train. For the electron beam, this is done at the source by controlling the polarization of the laser used to stimulate electron emission from the cathode. This is similar to the scheme used in the SLD experiment [136]. For the positron beam, the polarization is flipped by spin rotators placed downstream of the helical undulator [58].

The polarization of a beam containing N_L left- and N_R right-handed particles is given by

$$P = \frac{N_L - N_R}{N_L + N_R} \tag{5.4}$$

Since typically cross sections for left-handed electrons are larger, we will take left-handed polarizations to give positive P in this discussion. Then a beam of polarization P contains the fractions of particles of each helicity

$$f_L = \frac{1+P}{2} \qquad f_L = \frac{1-P}{2} \tag{5.5}$$

For the ILC polarizations, the e^-_L and e^+_L beams have the content

$$f_R(e^-_L) = 90\% \qquad f_L(e^-_L) = 10\% \qquad f_R(e^+_L) = 65\% \qquad f_L(e^+_L) = 35\% \tag{5.6}$$

Since the e^-_R and e^-_L have different $SU(2) \times U(1)$ quantum numbers, each of the four polarization settings is effectively a different scattering experiment. The results of the four experiments can be combined in various ways for different purposes. We describe four of these here.

Cross section asymmetries: Because of helicity conservation in vector boson couplings, e^+e^- annihilation reactions proceed only from the $e^-_Le^+_R$ and $e^-_Re^+_L$ helicity combinations. Typically, in annihilation to fermions, these two cross sections differ by a factor of 2. (Specifically for $e^+e^- \to ZH$, the cross sections differ by a factor 1.4.). If we write the two cross sections for 100% polarized initial states as

$$\sigma = \sigma_0(1 \pm \mathcal{A}) \tag{5.7}$$

with + for pure $e^-_Le^+_R$ and − for pure $e^-_Re^+_L$, then the cross section for electron and positron polarizations P_e and P_p is

$$\begin{aligned} \sigma(P_e, P_p) &= f_L(e)f_R(p)\ \sigma_0(1+\mathcal{A}) + f_R(e)f_L(p)\ \sigma_0(1-\mathcal{A}) \\ &= \left(\frac{1-P_eP_p}{2}\right)\sigma_0 + \left(\frac{P_e-P_p}{2}\right)\sigma_0\mathcal{A}\ . \end{aligned} \tag{5.8}$$

The asymmetry A between the cross sections with LR and RL polarized beams is then

$$A = P_{eff}\mathcal{A}\ , \qquad \text{with} \qquad P_{eff} = \frac{P_e - P_p}{1 - P_eP_p} = 89\% \tag{5.9}$$

for 80%/30% beam polarizations at the ILC. For this measurement of the intrinsic polarization asymmetry, many sources of systematic error cancel out, including the absolute luminosity and the absolute detector acceptance. It is necessary that the deetector performance be the same for left- and right- handed beams, which is insured if the polarization is flipped rapidly, and that the detector acceptance be very accurately forward-backward symmetric. The measurement of $\mathcal{A}$ does depend strongly on the absolute knowledge of the polarization. At the ILC, we plan to use multiple methods to bring the relative systematic error on the polarization down to 5×10^{-4}. [ref to where this is described in the report]

It is clear already from eq. (5.2) that the polarization asymmetric $\mathcal{A}$ gives direct information on the quantum numbers of the particles participating in an e^+e^- annihilation reaction. As we will see in Sec. 12.4, the polarization asymmetry in the reaction $e^+e^- \to ZH$ also plays an outsize role in the global analysis using Effective Field Theory that determines the Higgs boson couplings. It is then remarkable that this quantity can be obtained so precisely using polarized beams.

Cross section enhancements: Another result of eq. (5.8) is that, if the physics of a process very much favors the $e^-_Le^+_R$ helicity state, beam polarization gives an enhancement of the effective luminosity. For WW fusion reactions, which appear only from the $e^-_Le^+_R$ initial state, the effective luminosity for $e^-(L)e^+(R)$ polarized beams is enhanced from that for unpolarized beams by the factor

$$\mathcal{L}_{eff}/\mathcal{L} = (1+P_e)(1-P_p) = 2.3 \tag{5.10}$$

for 80%/30% beam polarizations at the ILC.

In practice, one should not try to achieve the full promised luminosity enhancement. Each physics process has its own dependence on polarization, and it is also important to reserve some of the luminosity for data on the modes with smaller production cross sections. This is reflected in our choice of the division of polarization modes in line 4 of Table 5.1. The run at the top quark threshold has a quite specific goal, and running with mainly $e^-(L)e^+(R)$ polarized beams is optimal

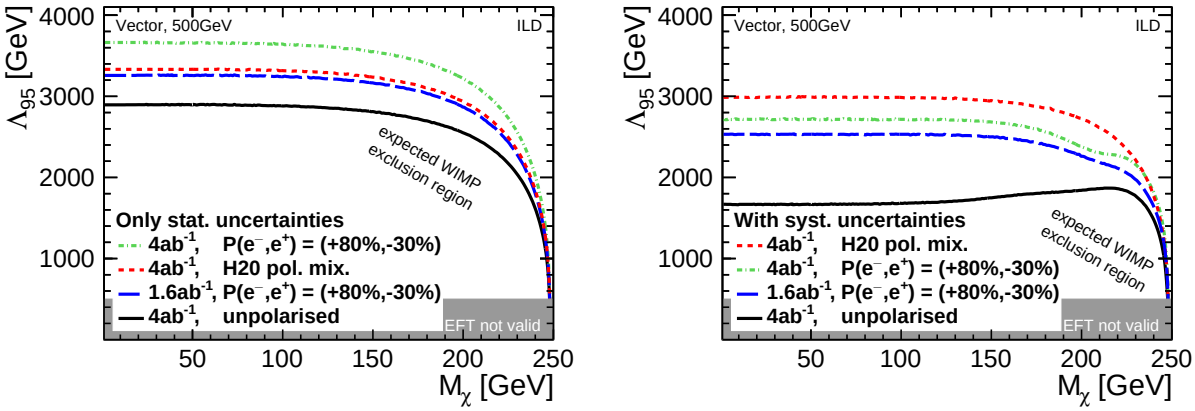

Figure 5.4: Limits on an Effective Field Theory mass scale associated with dark matter particle pair production in e^+e^- annihilation from a search simulation at 500 GeV, showing the dependence of the results on beam polarization, from [137]. Higher limits are better. In both figures, the black curve is an analysis for unpolarized beams, the red (short-dash) curve corresponds to the mixture of polarization states in Table 5.1. Left: analysis with statistical errors only; Right: analysis including both statistical and systematic errors.

for this. At other energies, where the physics program is more general, the fraction of polarizations used should be optimized taking into account the uses in the next two sections.

Background reduction: Especially for reactions that include neutrinos or other sources of missing energy, the process $e^+e^- \to W^+W^-$ is a the dominant source of background. It is therefore important that the cross section for $e^+e^- \to W^+W^-$ is dramatically reduced in the $e^-_R e^+_L$ initial state. Backgrounds from photon-induced processes such as $\gamma\gamma \to \ell^+\ell^-$ and single W production are still present in the $e^-_L e^+_L$ and $e^-_R e^+_R$ samples, while the annihilation reactions cannot appear. This ability to reduce some relevant backgrounds and to directly measure others can be crucial in measuring the rates of these processes precisely or, in the case of particle searches, establishing strong limits.

This is illustrated for a search for dark matter pair production that will be described in Sec. 10.5. Fig. 5.4 shows the results of a simulated search for dark matter pair production $e^+e^- \to \chi\chi$ at 500 GeV [137]. The analysis assumes no signal and puts a lower limit on an Effective Field Theory mass scale Λ. What concerns us now is the left-hand plot, which includes statistical errors only. The red (short-dash) curve shows the limit from the mixture of polarization states in Table 5.1. The figure shows that almost all of the exclusion comes from the 40% of the run that is collected with the $e^-(R)e^+(L)$ beam configuration. However, there is a second half to this story, which is explained below.

Control of systematic errors: With its four configurations for the polarization of the electron and positron beams, the ILC will be carrying out four different experiments simultaneously. These four data samples have very different mixes of physics processes, with e^+e^- annihilation reactions

essentially missing from the $e^-(L)e^+(L)$ and $e^-(R)e^+(R)$ samples while non-annihilation processes remain. However, with rapid polarization flipping, the experiments will be done in the same detector. This allows nuisance parameters associated with detector acceptance and energy response to measured by comparison the different samples. The potential systematic errors associated with these parameters can thus be greatly reduced.

As an example of an application of this strategy, look now at the right-hand plot in Fig. 5.4. Nominally, uncertainties from knowledge of the detector would weaken the observed limits, and this effect is visible in the black curve giving the result for unpolarized beams and in the curves for individual polarization states. However, the use of a mix of polarization states, including the nominally unproductive helicity-violating configurations, can be used to evaluate these uncertain detector parameters and retain most of the power of the analysis that included only statistical errors.

In processes subject to smaller systematic errors, it is more difficult to quantitatively express the advantage of positron polarization. A small advantage from the enhancement of cross sections is be compensated by the loss of productive luminosity in measuring the samples with helicity-violating polarization configurations. However, the use of positron polarization leads to double the number of individual data sets, adding redundancy and cross-checks. The goal of the ILC is to discover that the physics of e^+e^- annihilation differs from the predictions of the Standard Model. These checks could prove essential in making that case.

Chapter 6

ILC Detectors

[general corresponding editors: James Brau (jimbrau@uoregon.edu), Jan Strube (jan.strube@pnnl.gov), Maxim Titov (maxim.titov@cea.fr), Andrew White (awhite@uta.edu)]

6.1 Detector Requirements for the Physics Program

The ILC accelerator design allows for one interaction region, equipped for two experiments. The two experiments are swapped into the Interaction Point within the so-called "push-pull" scheme. The experiments have been designed to allow fast move-in and move-out from the interaction region, on a timescale of a few hours to a day. In 2008 a call for letters of intent was issued to the community. Following a detailed review by an international detector advisory group, two experiments were selected in 2009 and invited to prepare more detailed proposals. These are the SiD detector and the ILD detector described in this section. Both prepared detailed and costed proposals which were scrutinised by the international advisory group and included in the 2013 ILC Technical Design Report [5]. These specific detector designs have been critical input to the design of the ILC itself. A future process is expected in which detector designs will be reconsidered, with optimisations of these two designs and alternative designs which are proposed. In this chapter the two TDR detector proposals are described.

The ILC detectors have been designed to make precision measurements on the Higgs boson, W, Z, t, and other particles. They are able to meet the requirements for such measurements, first, because the experimental conditions are naturally very much more benign than those at the LHC, and second, because the detector collaborations have developed technologies specifically to take advantage of these more forgiving conditions.

An e^+e^- collider gives much lower collision rates and events of much lower complexity than a hadron collider, and detectors can be adapted to take advantage of this. The radiation levels at the ILC will be modest compared with the LHC, except for the special forward calorimters very close to the beamline, where radiation exposure will be an issue. This allows the consideration of a wide range of materials and technologies for the tracking and calorimeter systems. The generally

low radiation levels allow the innermost vertex detector elements to be located at very small radii, significantly enhancing the efficiency for short-lived particle identification. More generally, the relatively benign ILC experiment environment permits the design of tracking detectors with minimal material budget. This allows the detectors to meet the stringent requirement on the track momentum resolution which is driven by the need to precisely reconstruct the Z mass in the Higgs recoil analysis. This requirement translates into a momentum resolution nearly an order of magnitude better than achieved in the LHC experiments.

At the same time, although they are studying electroweak particle production, it is essential that the ILC detectors have excellent performance for jets. At an e^+e^- collider, W and Z bosons are readily observed in their hadronic decay modes, and the study of these modes plays a major role in most analyses. To meet the requirements of precision measurements, the ILC detectors are optimized from the beginning to enable jet reconstruction and measurement using the particle-flow algorithm (PFA). This drives the goal of 3% jet mass resolution at energies above 100 GeV, a resolution about twice as good as has been achieved in the LHC experiments.

Finally, while the LHC detectors depend crucially on multi-level triggers that filter out only a small fraction of events for analysis, the rate of interactions at the ILC is sufficiently low to allow running without a trigger. The ILC accelerator design is based on trains of electron and positron bunches, with a repetition rate of 5 Hz, and with 1312 bunches (and bunch collisions) per train. The 199 ms interval between bunch trains provides ample time for a full readout of data from the previous train. While there are background processes arising from beam-beam interactions, the detector occupancies arising from these have been shown to be manageable.

The combination of extremely precise tracking, excellent jet mass resolution, and triggerless running gives the ILC, at 250 GeV and at higher energies, a superb potential for discovery.

To meet these goals an ambitious R&D program has been pursued for more than a decade to develop and demonstrate the needed technologies. The results of this program are described in some detail in Ref. [138]. The two experiments proposed for the ILC, SiD and ILD, utilise and rely on the results from these R&D efforts.

Since the goals of SiD and ILD in terms of material budget, tracking performance, heavy-flavor tagging, and jet mass resolution are very demanding, it important to provide information about the level of detailed input that enters our performance estimates. These are best discussed together with the event reconstruction and analysis framework that we will present in Chapter 7. In that section, we will present estimates of detector performance as illustrations at the successive stages of event analysis.

6.2 The ILD Detector

The International Large Detector, ILD, is a detector proposal for the International Linear Collider, ILC. The ILD concept is supported by a broad and international community of scientists, and has been subjected to a numbe r of international reviews.

A central role in ILD plays the concept of particle flow, an idea to reconstruct complex events at

a collider with unprecedented precision. ILD decided early on to adopt particle flow as the central guiding principle for its detector concept, and developed the ILD design around this paradigm. For a review on particle flow, see e.g. [139].

The ILD concept has been documented in a number of documents. The basic concept and its validation were first discussed in the ILD detector baseline document in 2013 [5]. Recently ILD published an update of this document, the Interim Design Report, IDR [**?**].

The ILD detector design: requirements

The science which will be done at the ILC has been summarised earlier in this document. It is strongly dominated by the quest for ultimate precision in measurements of the properties of key particles like the Higgs boson, the weak gauge bosons, and, once the center-of-mass energy is beyond its production threshold, the top quark (see for example [140] or [141] for recent summaries).

The anticipated precision physics program drives the requirements for the detector. Many final states which will be analysed are hadronic final states, with many jets. Thus a precise reconstruction of jets is essential, which translates into an excellent jet energy resolution. Several studies that investigated the reconstruction of W and Z bosons suggest that a jet energy resolution of about 3% is needed to fully exploit the power of the collider. Such a resolution is almost two times more precise than the ATLAS and CMS detectors at the LHC have achieved. The concept of particle flow is currently believed to be the only practical approach through which this level of precision can be reached. Particle flow requires the reconstruction of charged and neutral particles with excellent efficiency over a large solid angle. A tracker with outstanding efficiency is a essential ingredient, combined with a calorimeter capable of reconstructing neutral particles with high efficiency. For ILD the choice has been made to combine a large volume hybrid tracking system, with an excellent silicon detector part and a large gaseous tracker - which promises excellent efficiency combined with low material - and a highly granular calorimeter both in the electromagnetic and the hadronic sections. To ease linking between the tracker and the calorimeter, the calorimeter should be inside the coil.

A number of highly relevant physics processes require the precise reconstruction of exclusive final states containing heavy flavour quarks. This translates into the need for very precise reconstruction of the decay vertices of long lived particles, and thus implies a high resolution vertexing system close to the interaction region.

The excellent performance of the detector system depends critically on the amount of material in the inner part of the ILD detector. The total material budget in front of the calorimeter should be below 10% of a radiation length, for the barrel part of the detector acceptance.

The whole detector should be operated without a hardware trigger, to maximise the sensitivity to new physics signals. This in turn put stringent requirements on the readout electronics, in terms of speed and power consumption. The integration of ILD is faced with the additional complexity to allow for a rapid movement of the detector in and out of the interaction region, the so-called push-pull scheme. This scheme will allow the operation of two separate and complementary experiments in one interaction region at the ILC.

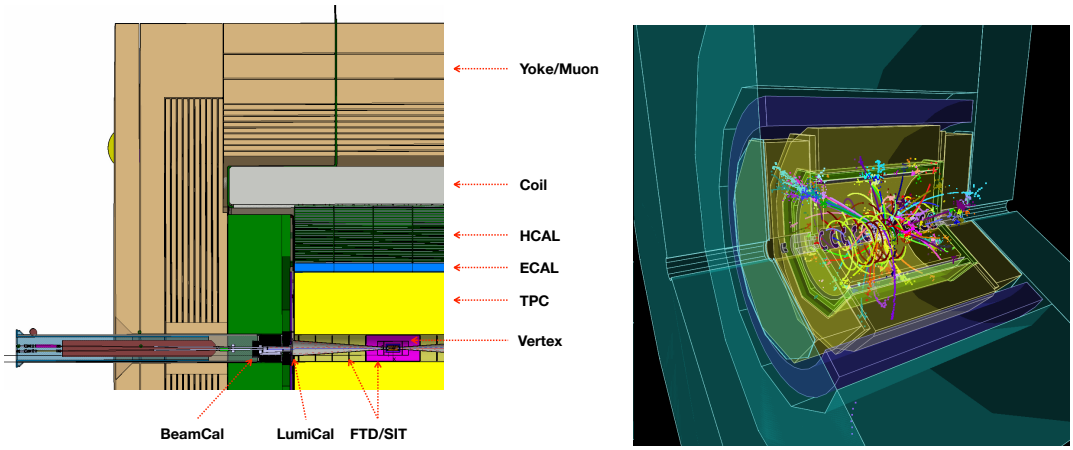

Figure 6.1: Left: Single quadrant view of the ILD detector. Right: Event display of a simulated hadronic decay of a $t\bar{t}$ event in ILD. The colouring of the tracks show the results of the reconstruction, each colour corresponding to a reconstructed particle.

The design drivers of the ILD detector can thus be summarized by the following requirements:

- **Impact parameter resolution:** An impact parameter resolution of $5\ \mu\text{m} \oplus 10\ \mu\text{m}/[p\ (\text{GeV}/c) \sin^{3/2}\theta]$ has been defined as a goal, where θ is the angle between the particle and the beamline.
- **Momentum resolution:** An inverse momentum resolution of $\Delta(1/p) = 2\times10^{-5}\ (\text{GeV/c}^{-1}/)$ asymptotically at high momenta should be reached with the combined silicon - TPC tracker. Maintaining excellent tracking efficiency and very good momentum resolution at lower momenta will be achieved by an aggressive design to minimise the detector's material budget.
- **Jet energy resolution:** Using the paradigm of particle flow a jet energy resolution $\Delta E/E = 3\%$ for light flavour jets should be reached. The resolution is defined in reference to light-quark jets, as the R.M.S. of the inner 90% of the energy distribution.
- **Readout:** The detector readout will not use a hardware trigger, ensuring full efficiency for all possible event topologies.
- **Powering** To allow a continuous readout, and, at the same time, minimize the amount of dead material in the detector, the power of major systems will be cycled between bunch trains.

Implementation of the ILD detector

The ambitious requirements of the ILC detectors sparked a world-wide R&D program to develop and demonstrate the different technologies needed [142]. The R&D was mostly coordinated and executed within so-called R&D collaborations, which concentrated on particular technologies and

sub-detector systems. These collaborations operated outside the ILD concept group, serving, in many cases, several detector concept groups. The ILD concept group from its beginning has collaborated very closely with these R&D groups, and has organised the needed R&D work through and with the R&D collaborations.

The ILD detector as it has been documented in the **??** has been the result of a decade-long effort. A three-dimensional rendering of the detector model is shown in figure **??**. A quadrant view of the large detector model is shown in figure 6.1 (left), together with an event display in this detector of a top event figure 6.1 (right).

The ILD concept from its inception has been open to new technologies. No final decision on subdetector technologies has been taken at this time, and in many cases several options are currently under consideration. ILD is actively inviting new groups to join the effort and propose new ideas or improvements to the current concept.

The main parameters of the ILD detector are summarised in table 6.1, together with the different technological options under consideration.

In the following paragraphs, the different components of the ILD concept are introduced and discussed.

Vertexing system

The system closest to the interaction region is a pixel detector designed to reconstruct decay vertices of short lived particles with great precision. ILD has chosen a system consisting of three double layers of pixel detectors. The innermost layer is only half as long as the others to reduce the exposure to background hits. Each layer will provide a spatial resolution around 4 μm at a pitch of about 22 μm, and a timing resolution per layer of around 2–4 μs. R&D is directed towards improving this even further, to a point which would allow hits from individual bunch crossings to be resolved.

Over the last 10 years the CMOS pixel technology has matured close to a point where all the requirements (material budget, readout speed, granularity) needed for an ILC detector can be met. The technology has seen a first large scale use in the STAR vertex detector [143], and more recently in the upgrade of the ALICE vertex detector. To minimize the material in the system, sensors are routinely thinned to 50 μm.

Other technologies under consideration for ILD are DEPFET, which is also currently being deployed in the Belle II vertex detector [144], fine pitch CCDs [145], and also less mature technologies such as SOI (Silicon-on-insulator) and Chronopix [142]. Very light weight support structures have been developed, which bring the goal of 0.15% of a radiation length per layer within reach. Such structures are now used in the Belle II vertex detector.

In figure 6.2 the purity of the flavour identification in ILD is shown as a function of its efficiency. The performance for b-jet identification is excellent, and charm-jet identification is also good, providing a purity of about 70% at an efficiency of 60%. The system also allows the accurate determination of the charge of displaced vertices, and contributes strongly to the low-momentum

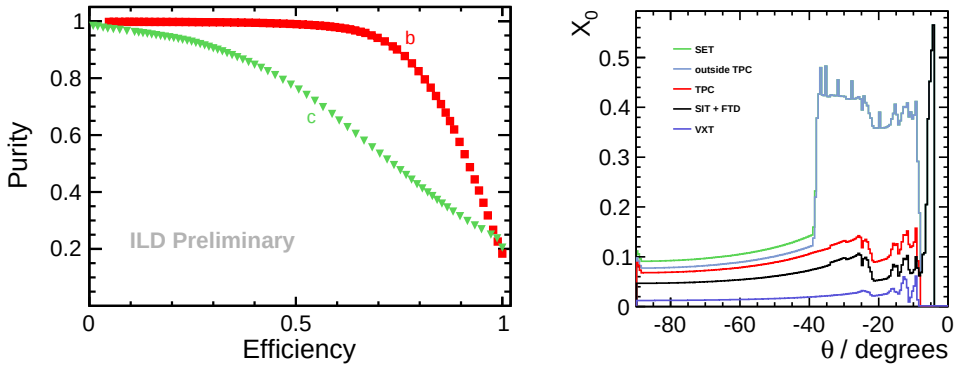

Figure 6.2: Left: Purity of the flavour tag as a function of the efficiency, for different flavours tagged. Right: Cumulative material budget in ILD up to the calorimeter, in fraction of a radiation length (figures from [146]).

tracking capabilities of the overall system, down to a few 10s of MeV. An important aspect of the system leading to superb flavour tagging is the small amount of material in the tracker. This is shown in figure 6.2 (right).

Tracking System

ILD has decided to approach the problem of charged particle tracking with a hybrid solution, which combines a high resolution time-projection chamber (TPC) with a few layers of strategically placed strip or pixel detectors before and after the TPC. The time-projection chamber will fill a large volume about 4.6 m in length, spanning radii from 33 to 180 cm. In this volume the TPC provides up to 220 three dimensional points for continuous tracking with a single-hit resolution of better than 100 μm in $r\phi$, and about 1 mm in z. This high number of points allows a reconstruction of the charged particle component of the event with high accuracy, including the reconstruction of secondaries, long lived particles, kinks, etc.. For momenta above 100 MeV, and within the acceptance of the TPC, greater than 99.9% tracking efficiency has been found in events simulated realistically with full backgrounds. At the same time the complete TPC system will introduce only about 10% of a radiation length into the detector [147].

Inside and outside of the TPC volume a few layers of silicon detectors provide high resolution points, at a point resolution of 10μm. Combined with the TPC track, this will result in an asymptotic momentum resolution of $\delta p_t/p_t^2 = 2 \times 10^{-5}$ ((GeV/c)$^{-1}$) for the complete system. Since the material in the system is very low, a significantly better resolution at low momenta can be achieved

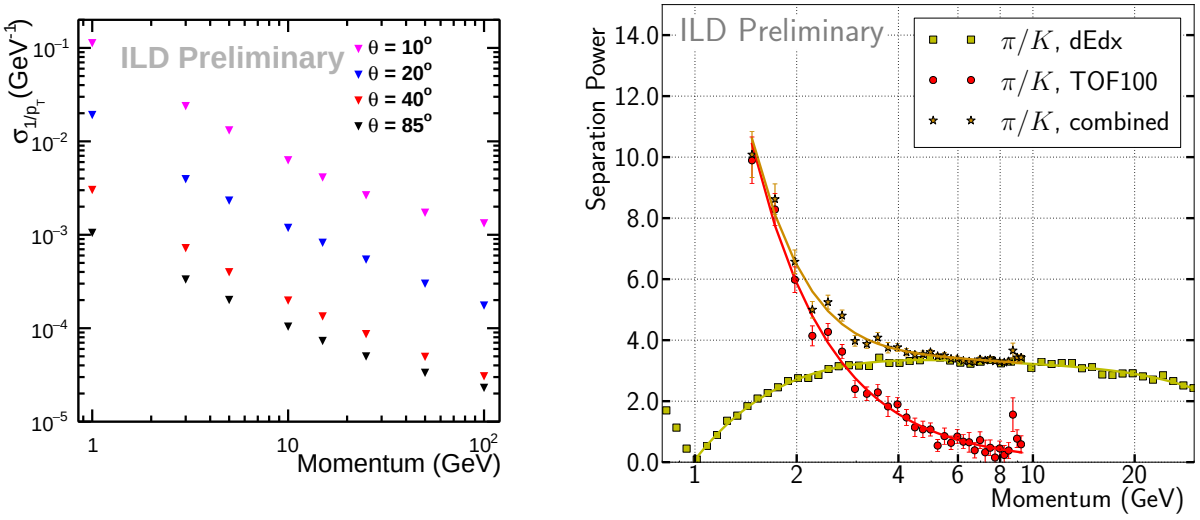

Figure 6.3: Left: Simulated resolution in $1/p_t$ as a function of the momentum for single muons. The different curves correspond to different polar angles. Right: Simulated separation power (probability for a pion to be reconstructed as a kaon) between pions and kaons, from dE/dx and from timing, assuming a 100 ps timing resolution of the first ECAL layer (figures from [146]).

than is possible with a silicon-only tracker. The achievable resolution is illustrated in figure 6.3, where the $1/p_t$-resolution is shown as a function of the momentum of the charged particle. In the forward direction, extending the coverage down to the beam-pipe, a system of two pixel disks (point resolution 5μm) and five strip disks (resolution 10μm outside of the TPC, and 5μm inside the TPC) provide tracking coverage down to the beam-pipe.

The time-projection chamber also enables the identification of the particle type by the measurement of the specific energy loss, dE/dx, for tracks at intermediate momenta [148]. The achievable performance is shown in figure 6.3 (right). If the inner and/or outer silicon layers can in addition provide timing with 100 ps resolution, time of flight measurements can provide additional information, which is particularly effective in the momentum regime which is problematic for dE/dx, as it is shown in figure 6.3 (right).

The design and performance of the TPC has been the subject of intense R&D over the last 15 years. A TPC based on the readout with micro-pattern gas detectors has been developed, and tested in several technological prototypes. The fundamental performance has been demonstrated, and solutions to construct a TPC with the required low mass have been developed. Most recently the performance of the specific energy loss, dE/dx, has been validated in test beam data. Based on these results, the TPC technology is sufficiently mature for use in the ILD detector, and can deliver the required performance (see e.g. [149, 150]).

Calorimeter System

A very powerful calorimeter system is essential to the performance of a detector designed for particle flow reconstruction. Particle flow stresses the ability to separate the individual particles in a jet, both charged and neutral. This puts the imaging capabilities of the system at a premium, and pushes the calorimeter development in the direction of a system with very high granularity in all parts of the system. A highly granular sampling calorimeter is the chosen solution to this challenge [151]. The conceptual and technological development of the particle flow calorimeter have been largely done by the CALICE collaboration (for a review of recent CALICE results see e.g. [152]).

ILD has chosen a sampling calorimeter readout with silicon diodes as one option for the electromagnetic calorimeter. Diodes with pads of about (5×5) mm^2 are used, to sample a shower up to 30 times in the electromagnetic section. In 2018 a test beam experiment demonstrated the large scale feasibility of this technology, by showing not only that the anticipated resolution can be reached. A very similar system has been adopted by the CMS experiment for the upgrade of the endcap calorimeter, and will deliver invaluable information on the scalability and engineering details of such a system.

As an alternative to the silicon based system, sensitive layers made from thin scintillator strips are also investigated. Orienting the strips perpendicular to each other has the potential to realize an effective cell size of 5×5mm^2, with the number of read-out channels reduced by an order of magnitude compared to the all silicon case.

For the hadronic part of the calorimeter of the ILD detector, two technologies are studied, based on either silicon photo diode (SiPM) on scintillator tile technology [153] or resistive plate chambers [154]. The SiPM-on-tile option has a moderate granularity, with 3×3 cm^2 tiles, and provides an analogue readout of the signal in each tile (AHCAL). The RPC technology has a better granularity, of 1×1 cm^2, but provides only 2-bit amplitude information (SDHCAL). For both technologies, significant prototypes have been built and operated. Both follow the engineering design anticipated for the final detector, and demonstrate thus not only the performance, but also the scalability of the technology to a large detector. As for the ECAL the SiPm-on-tile technology has been selected as baseline for part of the upgrade of tge CMS hadronic end-cap calorimeter, and will thus see a major application in the near future.

The simulated particle flow performance is shown in figure 6.4 (right).

The iron return yoke of the detector, located outside of the coil, is instrumented to act as a tail catcher and as a muon identification system. Several technologies are possible for the instrumented layers. Both RPC chambers and scintillator strips readout with SiPMs have been investigated. Up to 14 active layers, located mostly in the inner half of the iron yoke (see table 6.1 and figure 6.1 for more details) could be instrumented.

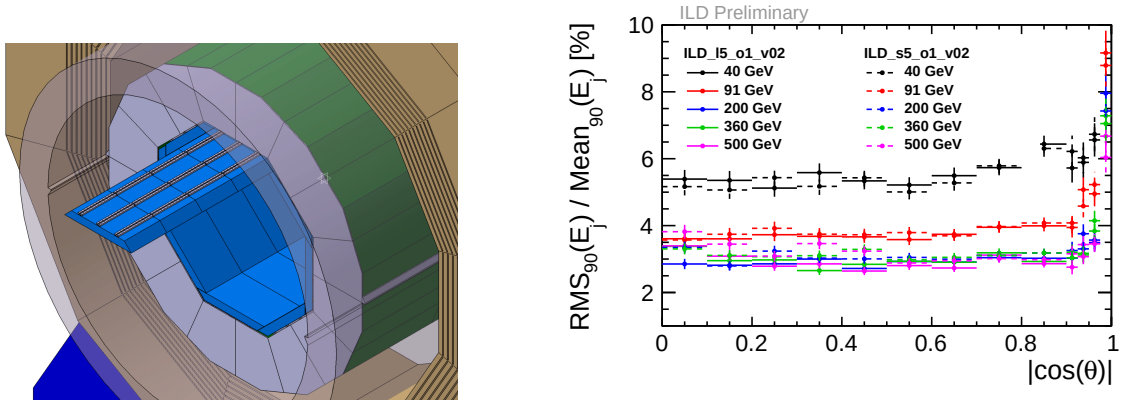

Figure 6.4: Left: Three-dimensional rendering of the barrel calorimeter system, with one ECAL module partially extracted. Right: Particle flow performance, measured as the energy resolution in two-jet light flavour events, for different jet energies as a function of $\cos(\theta)$. The resolution is defined as the rms of the distribution truncated so that 90% of the total jet energy is contained inside the distribution. The data are shown for the large (L) and the small (S) version of the ILD detector. (figures taken from [146])

The Forward System

Three rather specific calorimeter systems are foreseen for the very forward region of the ILD detector [155]. LumiCal is a high precision fine sampling silicon tungsten calorimeter primarily designed to measure electrons from Bhabha scattering, and to precisely determine the integrated luminosity [156]. The LHCAL (Luminosity Hadronic CALorimeter) just outside the LumiCal extends the reach of the endcap calorimeter system to smaller angles relative to the beam, and closes the gap between the inner edge of the ECAL endcap and the luminosity calorimeter, LumiCal. Below the LumiCal acceptance, where background from beamstrahlung rises sharply, BeamCal, placed further downstream from the interaction point, provides added coverage and is used to provide a fast feedback on the beam position at the interaction region. As the systems move close to the beam-pipe, the requirements on radiation hardness and on speed become more and more challenging. Indeed this very forward region in ILD is the only region where radiation hardness of the systems is a key requirement.

Detector Integration and Costing

One of the major goals of the ILD concept group was from the beginning to develop the detector concept from a collection of technological ideas to a real detector that can actually be built, commissioned, and operated within given engineering and site-dependent constraints. The effort, driven by dedicated working groups, resulted in an engineering model of ILD that describes the mechanical setup of the detector structures themselves as well as the detector services such as cabling, cooling, gas systems, and cryogenics. The technical description of ILD is based on Interface Control Documents and is documented on the ILC-EDMS system with a web-based front-end [157].

A detailed CAD model of ILD exists and can be accessed at the same location.

The main mechanical structure of the ILD detector is the iron yoke that consists of three barrel rings and two endcaps. The yoke provides the required shielding for radiation and magnetic fields to allow access to the outside of the detector during data taking. The central yoke ring supports the cryostat for the detector solenoid and the barrel detectors, calorimeters and tracking system. The yoke endcaps carry the detectors in the forward direction and can be opened to allow access to the inner detector. The mechanical concept of ILD has been designed and tested in simulations for seismic conditions that can be expected at the foreseen ILC site in northern Japan.

A common concept for the detector services such as cables, cooling, gases and cryogenics has been developed. The requirements are in many cases based on engineering prototypes of the ILD sub-systems.

The main detector solenoid is based on CMS experience and can deliver magnetic fields up to 4 T. A correction system for the compensation of the crossing angle of the ILC beam, the Detector Integrated Dipole, has been designed and can be integrated into the main magnet cryostat.

The cost of the ILD detector has been estimated at the time of the ILD detailed baseline report and confirmed for the IDR. The total detector cost is about 390 Million ILCU in 2012 costs. One ILCU has been defined to be approximately equal to 1 Dollar or 0.97 Euros in 2013. The cost of the detector is strongly dominated by the cost of the calorimeter system and the yoke, which together account for about 60% of the total cost. The total cost of ILD scales weakly with the overall size of the detector.

6.2.1 Science with ILD

ILD has been designed to operate with electron-positron collisions between 90 GeV and 1 TeV. The science goals of the ILC have been described in detail in [141], and will not be repeated here. It should be pointed out that the analyses which have been performed within the ILD concept group are based on fully simulated events, using a realistic detector model and advanced reconstruction software, and in many cases includes estimates of key systematic effects. This is particularly important when estimating the reach the ILC and ILD will have for specific measurements. Determining, for example, the branching ratios of the Higgs at the percent level depends critically on the detector performance, and thus on the quality of the event simulation and reconstruction.

In many cases the performance used in the physics analyses has been tested against prototype experiments. The key performance numbers for the vertexing, tracking and calorimeter systems are all based on results from test beam experiments. The particle flow performance, a key aspect of the ILD physics reach, could in the absence of a large scale demonstration experiment not be fully verified, but key aspects have been shown in experiments. This includes the single particle resolution for neutral and charged particles, the particle separation in jets, the linking power between tracking and calorimetry, and key aspects of detailed shower analyses important for particle flow.

While the physics case studies are based on the version of the ILD detector presented in the detector volume of the ILC DBD [158], ILD has recently initiated a systematic benchmarking

effort to study the performance of the ILD concept, and to determine in particular the correlations between science objectives and detector performance. The list of benchmark analyses which are under study is given in table 6.2. Even if the ILC will start operation at a center-of-mass energy of 250 GeV, the ILD detector is being designed to meet the more challenging requirements of higher center-of-mass energies, since major parts of the detector, e.g. the coil, the yoke and the main calorimeters will not be replaced when upgrading the accelerator. Therefore, most of the detector benchmark analyses are performed at a center-of-mass energy of 500 GeV, and one benchmark even at 1 TeV. The assumed integrated luminosities and beam polarisation settings follow the canonical running scenario [135]. In addition to the well-established performance aspects of the ILD detector, the potential of new features not yet incorporated in the existing detector prototypes, e.g. time-of-flight information, is being evaluated.

The results of these studies are expected to become available in 2019 and will be published in the ILD Design Report [159]. They will form the basis for the definition of a new ILD baseline detector model, which will then be used for a new physics-oriented Monte-Carlo production for 250 GeV. Such a production is planned with the most recent beam parameters of the accelerator [9] and significantly improved reconstruction algorithms, and is expected to lead to further improvements of the expected results of the precision physics program of the ILC [141].

6.2.2 Integration of ILD into the experimental environment

ILD is designed to be able to work in a push-pull arrangement with another detector at a common ILC interaction region. In this scheme ILD sits on a movable platform in the underground experimental hall. This platform allows for a roll-in of ILD from the parking position into the beam and vice versa within a few hours. The detector can be fully opened and maintained in the parking position.

The current mechanical design of ILD assumes an initial assembly of the detector on the surface, similar to the construction of CMS at the LHC. A vertical shaft from the surface into the underground experimental cavern allows ILD to be lowered in five large segments, corresponding to the five yoke rings.

ILD is designed to fully cope with the ILC beam conditions. The expected levels of beam induced backgrounds have been simulated and are seen to be at tolerable levels, e.g. for the vertex detectors. Judiciously placed shielding keep scattered backgrounds under control. The design of the interaction region and the collimation system of the collider has been defined so as to keep the external background sources at levels below the detector requirements.

ILD is self-shielding with respect to radiation and magnetic fields to enable the operation and maintenance of equipment surrounding the detector, e.g. cryogenics. Of paramount importance is the possibility to operate and maintain the second ILC push-pull detector in the underground cavern during ILC operation.

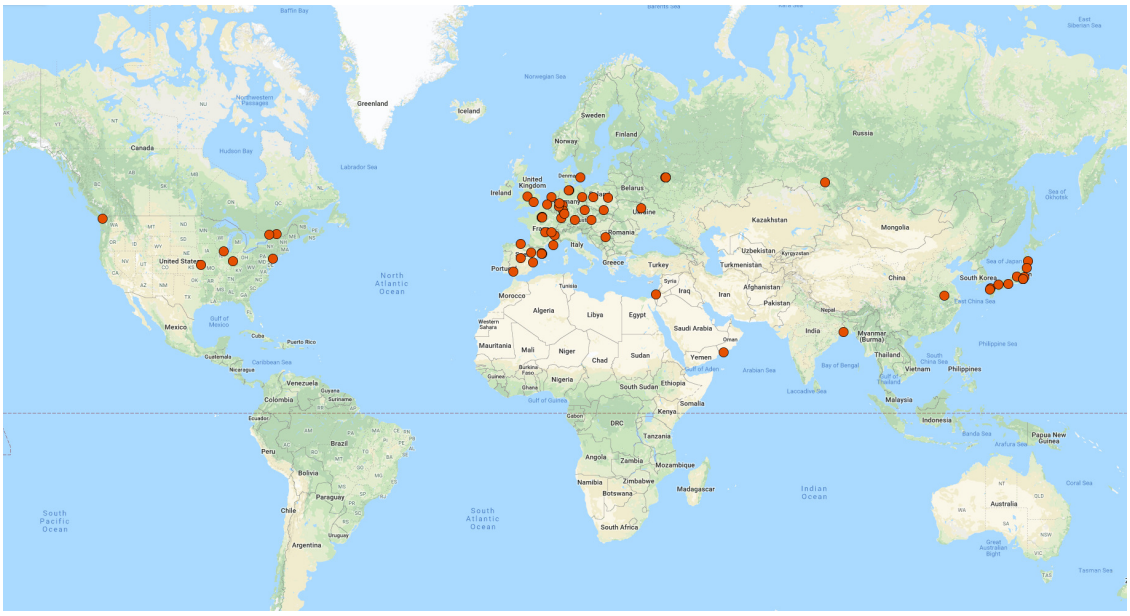

Figure 6.5: Map with the location of the ILD member institutes indicated.

6.2.3 The ILD Concept Group

As described above, the ILD collaboration initially started out as a fairly loosely organised group of scientists interested to explore the design of a detector for a linear collider like the ILC. With the delivery of the DBD in 2013, the group re-organised itself more along the lines of a traditional collaboration. The group gave itself a set of by-laws, which governs the function of the group, and defines rules for the membership in ILD. Groups who want to be members of ILD must sign a memorandum of participation, a first step towards an eventual memorandum of understanding to construct ILD, as soon as the ILC has been approved.

In total 65 groups from 30 countries signed the letter of participation in 2015. In 2018 the list of groups had grown to 72. A map indicating the location of the ILD member institutes is shown in figure 6.5.

6.2.4 Conclusion and Outlook

The ILD detector concept is a well developed integrated detector optimised for use at the electron-positron collider ILC. It is based on advanced detector technology, and driven by the science requirements at the ILC. Most of its major components have been fully demonstrated through prototyping and test beam experiments. The physics performance of ILD has been validated using detailed simulation systems. A community interested in building and operating ILD has formed over the last few years. It is already sizeable, encompassing 72 institutes from around the world. The community is ready to move forward once the ILC project receives approval.

[8 pages; corresponding editor: Ties Behnke (ties.behnke@desy.de)]

6.3 The SiD Detector

[8 pages; corresponding editor: Andrew White (awhite@uta.edu)]

6.3.1 Detector description and capabilities

The SiD detector concept is a general-purpose experiment designed to perform precision measurements at the ILC. It satisfies the challenging detector requirements resulting from the full range of ILC physics processes. SiD is based on the paradigm of particle flow, an algorithm by which the reconstruction of both charged and neutral particles is accomplished by an optimised combination of tracking and calorimetry. The net result is a significantly more precise jet energy measurement than that achieved via conventional methods and which results in a di-jet mass resolution good enough to distinguish between Ws and Zs. The SiD detector (Fig. 6.6) is a compact detector based on a powerful silicon pixel vertex detector, silicon tracking, silicon-tungsten electromagnetic calorimetry, and highly segmented hadronic calorimetry. SiD also incorporates a high-field solenoid, iron flux return, and a muon identification system. The use of silicon sensors in the vertex, tracking, and calorimetry enables a unique integrated tracking system ideally suited to particle flow.

The choice of silicon detectors for tracking and vertexing ensures that SiD is robust with respect to beam backgrounds or beam loss, provides superior charged particle momentum resolution, and eliminates out-of-time tracks and backgrounds. The main tracking detector and calorimeters are "live" only during a single bunch crossing, so beam-related backgrounds and low-pT backgrounds from $\gamma\gamma$ processes will be reduced to the minimum possible levels. The SiD calorimetry is optimised for excellent jet energy measurement using the particle flow technique. The complete tracking and calorimeter systems are contained within a superconducting solenoid, which has a 5 T field strength, enabling the overall compact design. The coil is located within a layered iron structure that returns the magnetic flux and is instrumented to allow the identification of muons. All aspects of SiD are the result of intensive and leading-edge research aimed at achieving performance at unprecedented levels. At the same time, the design represents a balance between cost and physics performance. Nevertheless, given advances in technologies it is now appropriate to consider updates to the SiD design as discussed below. First, we describe the baseline SiD design for which the key parameters are listed in Table 6.3.

Silicon-based tracking

The tracking system (Fig. 6.7) is a key element of the SiD detector concept. The particle flow algorithm requires excellent tracking with superb efficiency and two-particle separation. The requirements for precision measurements, in particular in the Higgs sector, place high demands on the momentum resolution at the level of $\delta(1/p_T) \sim 2 - 5 \times 10^{-5}/\mathrm{GeV}/c$.

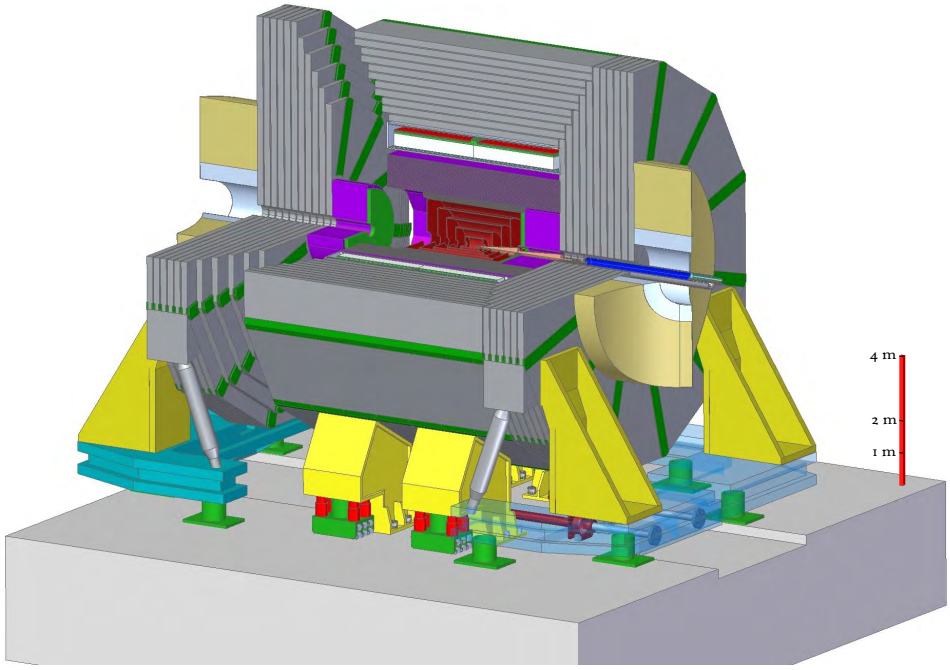

Figure 6.6: The SiD detector concept.

Highly efficient charged particle tracking is achieved using the pixel detector and main tracker to recognise and measure prompt tracks, in conjunction with the ECAL, which can identify short track stubs in its first few layers to catch tracks arising from secondary decays of long-lived particles. With the choice of a 5 T solenoidal magnetic field, in part chosen to control the e^+e^--pair background, the design allows for a compact tracker design.

Vertex detector

To unravel the underlying physics mechanisms of new observed processes, the identification of heavy flavours will play a critical role. One of the main tools for heavy flavour identification is the vertex detector. The physics goals dictate an unprecedented spatial three-dimensional point resolution and a very low material budget to minimise multiple Coulomb scattering. The running conditions at the ILC impose the readout speed and radiation tolerance. These requirements are normally in tension. High granularity and fast readout compete with each other and tend to increase the power dissipation. Increased power dissipation in turn leads to an increased material budget. The challenges on the vertex detector are considerable and significant R&D is being carried out on both the development of the sensors and the mechanical support. The SiD vertex detector uses a barrel and disk layout. The barrel section consists of five silicon pixel layers with a pixel size of 20 $\times$ 20 μm^2. The forward and backward regions each have four silicon pixel disks. In addition, there are three silicon pixel disks at a larger distance from the interaction point to provide uniform coverage for the transition region between the vertex detector and the outer tracker. This

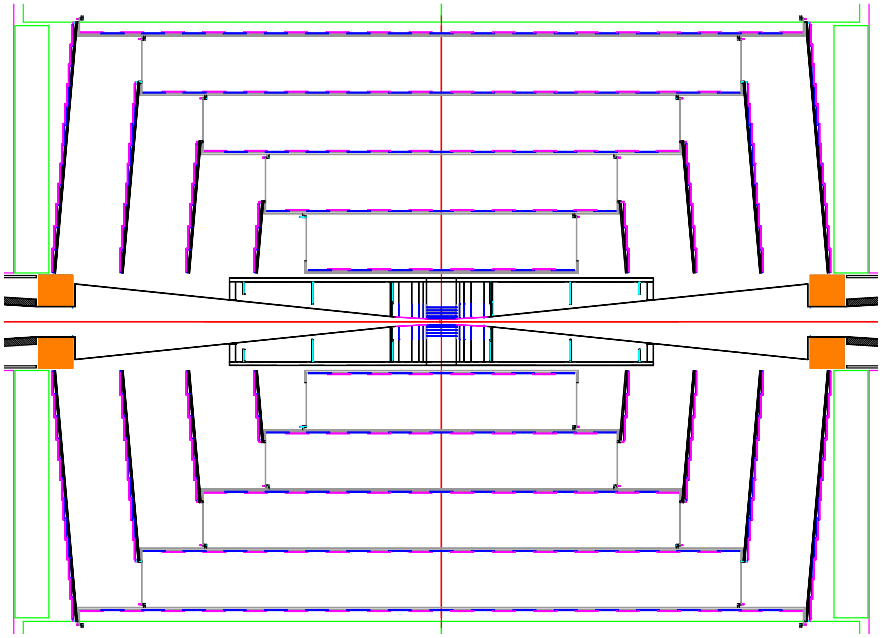

Figure 6.7: r-z view of vertex detector and outer tracker.

configuration provides for very good hermeticity with uniform coverage and guarantees excellent charged-track pattern recognition capability and impact parameter resolution over the full solid angle. This enhances the capability of the integrated tracking system and, in conjunction with the high magnetic field, makes for a very compact system, thereby minimising the size and costs of the calorimetry.

To provide for a very robust track-finding performance the baseline choice for the vertex detector has a sensor technology that provides time-stamping of each hit with sufficient precision to assign it to a particular bunch crossing. This significantly suppresses backgrounds.

Several vertex detector sensor technologies are being developed. One of these is a monolithic CMOS pixel detector with time-stamping capability (Chronopixel [160]), being developed in collaboration with SRI International. The pixel size is about 10 $\times$ 10 μm^2 with a design goal of 99% charged-particle efficiency. The time-stamping feature of the design means each hit is accompanied by a time tag with sufficient precision to assign it to a particular bunch crossing of the ILC – henc the name Chronopixel. This reduces the occupancy to negligible levels, even in the innermost vertex detector layer, yielding a robust vertex detector which operates at background levels significantly in excess of those currently foreseen for the ILC. Chronopixel differs from the similar detectors developed by other groups by its capability to record time stamps for two hits in each pixel while using standard CMOS processing for manufacturing. Following a series of prototypes, the Chronopixel has been proven to be a feasible concept for the ILC. The three prototype versions were fabricated in 2008, in 2012, and in 2014. The main goal of the third prototype was to test possible solutions for a high capacitance problem discovered in prototype 2. The problem was traced to the TSMC 90 nm technology design rules, which led to an unacceptably large value

of the sensor diode capacitance. Six different layouts for the prototype 3 sensor diode were tested, and the tests demonstrated that the high capacitance problem was solved.

With prototype 3 proving that a Chronopixel sensor can be successful with all known problems solved, optimal sensor design would be the focus of future tests. The charge collection efficiency for different sensor diode options needs to be measured to determine the option with the best signal-to-noise ratio. Also, sensor efficiency for charged particles with sufficient energy to penetrate the sensor thickness and ceramic package, along with a trigger telescope measurement, needs to be determined. Beyond these fundamental measurements, a prototype of a few cm^2 with a final readout scheme would test the longer trace readout resistance, capacitance, and crosstalk.

A more challenging approach is the 3D vertical integrated silicon technology, for which a full demonstration is also close.

Minimising the support material is critical to the development of a high-performance vertex detector. An array of low-mass materials such as reticulated foams and silicon-carbide materials are under consideration. An alternative approach that is being pursued very actively is the embedding of thinned, active sensors in ultra low-mass media. This line of R&D explores thinning active silicon devices to such a thickness that the silicon becomes flexible. The devices can then be embedded in, for example, Kapton structures, providing extreme versatility in designing and constructing a vertex detector.

Power delivery must be accomplished without exceeding the material budget and overheating the detector. The vertex detector design relies on power pulsing during bunch trains to minimise heating and uses forced air for cooling.

Main tracker

The main tracker technology of choice is silicon strip sensors arrayed in five nested cylinders in the central region and four disks following a conical surface with an angle of 5 degrees with respect to the normal to the beamline in each of the end regions. The geometry of the endcaps minimises the material budget to enhance forward tracking. The detectors are single-sided silicon sensors, approximately 10×10 cm^2 with a readout pitch of 50 μm. The endcaps utilise two sensors bonded back-to-back for small angle stereo measurements. With an outer cylinder radius of 1.25 m and a 5 T field, the charged track momentum resolution will be better than $\delta(1/p_T) = 5 \times 10^{-5}/(\mathrm{GeV}/c)$ for high momentum tracks with coverage down to polar angles of 10 degrees. A plot of the material budget as a function of polar angle is shown in Fig. 6.8.

The all-silicon tracking approach has been extensively tested using full Monte-Carlo simulations including full beam backgrounds. Besides having an excellent momentum resolution it provides robust pattern recognition even in the presence of backgrounds and has a real safety margin, if the machine backgrounds will be worse than expected.

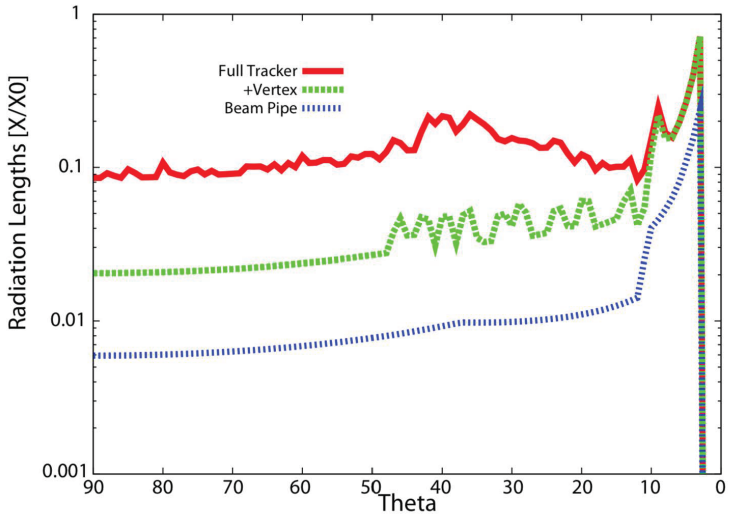

Figure 6.8: Material in the SiD detector, in terms of fractions of a radiation length, as a function of the polar angle.

Main calorimeters

The SiD baseline design incorporates the elements needed to successfully implement the PFA approach. This imposes a number of basic requirements on the calorimetry. The central calorimeter system must be contained within the solenoid in order to reliably associate tracks to energy deposits. The electromagnetic and hadronic sections must have imaging capabilities that allow both efficient track-following and correct assignment of energy clusters to tracks. These requirements imply that the calorimeters must be finely segmented both longitudinally and transversely. In order to ensure that no significant amount of energy can escape detection, the calorimetry must extend down to small angles with respect to the beampipe and must be sufficiently deep to prevent significant energy leakage. Since the average penetration depth of a hadronic shower grows with its energy, the calorimeter system must be designed for the highest-energy collisions envisaged.

In order to ease detector construction the calorimeter mechanical design consists of a series of modules of manageable size and weight. The boundaries between modules are kept as small as possible to prevent significant non-instrumented regions. The detectors are designed to have excellent long-term stability and reliability, since access during the data-taking period will be extremely limited, if not impossible.

The combined ECAL and HCAL systems consist of a central barrel part and two endcaps, nested inside the barrel. The entire barrel system is contained within the volume of the cylindrical superconducting solenoid.

SiD's reliance on particle flow calorimetry to obtain a jet energy resolution of $\sim$3% demands a highly segmented (longitudinally and laterally) electromagnetic calorimeter. It also calls for a minimized lateral electromagnetic shower size, by minimizing the Moliere radius to efficiently

separate photons, electrons and charged hadrons [**?**].

The SiD ECal design employs thirty longitudinal layers, the first twenty each with 2.50 mm tungsten alloy thickness and 1.25 mm readout gaps, and the last ten with 5.00 mm tungsten alloy. The total depth is 26 radiation lengths, providing good containment of electromagnetic showers.

Simulations have shown the energy resolution for electrons or photons to be well described by $0.17 \ / \ \sqrt{E} \oplus 0.009$, degrading a bit at higher energies due to changes in sampling fraction and a small leakage.

The baseline design employs tiled, large, commercially produced silicon sensors (currently assuming 15 cm wafers). The sensors are segmented into pixels that are individually read out over the full range of charge depositions. The complete electronics for the pixels is contained in a single chip, the KPiX ASIC [161], which is bump bonded to the wafer. The low beam-crossing duty cycle (10^{-3}) allows reducing the heat load using power pulsing, thus allowing passive thermal management within the ECal modules.

Bench tests of the KPiX bonded sensor with a cosmic ray telescope trigger yielded a Landau distribution with a peak of the signal at about 4 fC is consistent with our expectation for minimum-ionizing particles (MIP) passing through the fully-depleted 320 μm thick sensors. Crosstalk between channels has been managed and the noise distribution shows an RMS of 0.2 fC, well below the 4 fC MIP signal, and exceeding the ECal requirement.

The overall mechanical structure of the ECal barrel has been designed for minimal uninstrumented gaps. Input power and signals are delivered with Kapton flex cables. The KPiX chip has an average power less than 20 mW, resulting in a total heat load that is managed with a cold plate and water pipes routed into the calorimeter.

A first SiD ECal prototype stack of nine (of thirty) layers has been constructed and was exposed to a 12.1 GeV electron beam at the SLAC End Station Test Beam Facility. This data collection demonstrated good measurements of multiple particle overlap and reconstruction of overlapping showers [162]. Comparison of the deposited energy distribution in each of the nine layers also agrees well with simulations. An algorithm developed to count the number of incident electrons in each event was used to assess the ability of the calorimeter to separate two showers as a function of the separation of the showers, achieving 100% for separations of >10 mm.

The hadronic calorimeter has a depth of 4.5 nuclear interaction lengths, consisting of alternating steel plates and active layers. The baseline choice for the active layers is scintillator tiles read out via silicon photomultipliers. For this approach SiD is closely following the analog hadron calorimeter developments within the CALICE collaboration. In this context, the simulated HCAL energy resolution has been shown to reproduce well the results from the CALICE AHCAL prototype module exposed to pion beams.

Forward calorimeters

Two special calorimeters are foreseen in the very forward region: LumiCal for a precise luminosity measurement, and BeamCal for the fast estimation of the collision parameters and tagging

of forward-scattered beam particles. LumiCal and BeamCal are both compact cylindrical electromagnetic calorimeters centered on the outgoing beam, making use of semiconductor-tungsten technology. BeamCal is placed just in front of the final focus quadrupole and LumiCal is aligned with the electromagnetic calorimeter endcap.

LumiCal makes use of conventional silicon diode sensor readout. It is a precision device with challenging requirements on the mechanics and position control, and must achieve a small Moliere radius to reach its precision targets. Substantial work has been done to thin the silicon sensor readout planes within the silicon-tungsten assembly. Dedicated electronics with an appropriately large dynamic range is under development.

BeamCal is exposed to a large flux of low-energy electron-positron pairs originating from beamstrahlung. These depositions, useful for a bunch-by-bunch luminosity estimate and the determination of beam parameters, require radiation hard sensors. The BeamCal has to cope with 100% occupancies, requiring dedicated front-end electronics. A challenge for BeamCal is to identify sensors that will tolerate over one MGy of ionizing radiation per year. Sensor technologies under consideration include polycrystalline chemical vapor deposition (CVD) diamond (too expensive to be used for the full coverage), GaAs, SiC, Sapphire, and conventional silicon diode sensors. The radiation tolerance of all of these sensor technologies has been studied in a high-intensity electron beam.

For SiD, the main activities are the study of these radiation-hard sensors, development of the first version of the so-called Bean readout chip, and the simulation of BeamCal tagging for physics studies. SiD coordinates these activities through its participation in the FCAL R&D Collaboration.

Magnet coil

The SiD superconducting solenoid is based on the CMS solenoid design philosophy and construction techniques, using a slightly modified CMS conductor as its baseline design. Superconducting strand count in the coextruded Rutherford cable was increased from 32 to 40 to accommodate the higher 5 T central field.

Many iron flux return configurations have been simulated in two dimensions so as to reduce the fringe field. An Opera 3D calculation with the Detector Integrated Dipole (DID) coil has been completed. Calculations of magnetic field with a 3D ANSYS program are in progress. These will have the capability to calculate forces and stress on the DID as well as run transient cases to check the viability of using the DID as a quench propagator for the solenoid. Field and force calculations with an iron endcap HCAL were studied. The field homogeneity improvement was found to be insufficient to pursue this option.

Conceptual DID construction and assembly methods have been studied. The solenoid electrical power system, including a water-cooled dump resistor and grounding, was established. Significant work has been expended on examining different conductor stabiliser options and conductor fabrication methods. This work is pursued as a cost- and time-saving effort for solenoid construction.

Muon system

The flux-return yoke is instrumented with position sensitive detectors to serve as both a muon filter and a tail catcher. The total area to be instrumented is very significant – several thousand square meters. Technologies that lend themselves to low-cost large-area detectors are therefore under investigation. Particles arriving at the muon system have seen large amounts of material in the calorimeters and encounter significant multiple scattering inside the iron. Spatial resolution of a few centimetres is therefore sufficient. Occupancies are low, so strip detectors are possible. The SiD baseline design uses scintillator technology, with RPCs as an alternative. The scintillator technology uses extruded scintillator readout with wavelength shifting fibre and SiPMs, and has been successfully demonstrated. Simulation studies have shown that nine or more layers of sensitive detectors yield adequate energy measurements and good muon detection efficiency and purity. The flux-return yoke itself has been optimised with respect to the uniformity of the central solenoidal field, the external fringe field, and ease of the iron assembly. This was achieved by separating the barrel and end sections of the yoke along a 30 degree line.

The machine-detector interface

A time-efficient implementation of the push-pull model of operation sets specific requirements and challenges for many detector and machine systems, in particular the interaction region (IR) magnets, the cryogenics, the alignment system, the beamline shielding, the detector design and the overall integration. The minimal functional requirements and interface specifications for the push-pull IR have been successfully developed and published [163, 164]. All further IR design work on both the detectors and machine sides are constrained by these specifications.

6.3.2 R&D issues for the SiD design

Monolithic Active Pixel Sensors

MAPS technology is being actively studied for the SiD tracking and electromagnetic calorimeter systems, with initial prototyping underway. For larger-scale objects like a full tracker or an ECAL sensor, larger structures than the usual full-reticle size (roughly $2.5 \times 2.5\text{cm}^2$) units are required. Reticles would be stitched together with balcony circuitry on one or two (opposing) edges.

In terms of general MAPS R&D required for SiD, mastering of the stitching technology is required, as for such large areas - O($\sim$100m^2) for the tracker and O($\sim$1000m^2) for the ECAL - yield becomes an issue. The distribution of power and data over such a large area sensor will be a challenge as well and dedicated R&D is needed.

Given the timescales involved for the construction of an ILC detector like SiD, with the mainstay of construction happening at the end of decade, investment into new processes are needed, as the presently available processes will most likely not be available anymore. The most probable technology for a next-generation MAPS process are the $\sim$65nm CMOS processes that are just becoming available to the community. As CMOS processes use larger wafers (ten or twelve inch

wafers) as well as taking advantage of a fully industrial process, the move to MAPS also has clear advantages in terms of a cost reduction for both the tracker and the ECAL.

Simulation studies of electromagnetic showers have demonstrated that the ILC TDR level resolutions, and even better, can be achieved with a digital hit/no-hit threshold MAPS ECAL. [165] The pixel structure of 25 µm x 100 µm is chosen to optimize tracking and ECAL applications.

Hadron Calorimeter

Extensions to and optimization of the hadron calorimeter design will also address the following:

- inclusion of timing layers to assist the particle flow algorithm in separating the delayed shower components from slow neutrons from the prompt components.
- potential cost saving by making some of the outer layers thicker if there is no significant degradation in energy resolution.
- optimization of the boundary region between the ECAL and the HCAL and optimization of the first layers of the HCAL to best assist with the measurement of electromagnetic shower leakage into the HCAL.
- reconsideration of the effects of projective cracks between modules. There is some indication from earlier studies that projective cracks have no negative effect on energy resolution, but this needs further verification.
- exploration of alternative layouts for HCAL sectors in the end-caps.
- optimization of the boundary between the HCAL barrel and end-caps.

Muon system

- Optimization of number of instrumented layers, barrel and end-caps.
- Optimization of strip lengths, mainly for barrel system.
- Design for muon endcaps - twelve-fold geometry.
- Occupancies at inner radius of muon end-caps versus strip widths.
- Role of muon system as tail-catcher for HCAL. Consideration and implications of CALICE ECAL + HCAL + Tail-catcher test beam results.
- Potential for use of muon system in search for long-lived particles; timing and pointing capabilities.

Forward Calorimeters

Tasks remaining for the forward calorimeters, with participation in the FCAL R&D Collaboration, include:

- LumiCal: complete development of large dynamic range readout electronics.
- LumiCal: develop and demonstrate the ability to position and maintain the position of the calorimeter, particularly at the inner radius, in view of the steep dependence of the rate of Bhabha events on polar angle.
- BeamCal: continue the search for and testing of suitable sensor technology(s) capable of sustained performance in the very high radiation environment.
- BeamCal: continue the study of recognizing single electron shower patterns for tagging for physics studies in the face of high radiation background.

6.4 New Technologies for ILC Detectors

(We hope that any group developing a new technology potentially useful at ILC will contribute to the appropriate subsection below. Please send a summary of your work (hopefully citing a Snowmass contributed paper) to the corresponding editors of this chapter.)

[10 pages]

6.4.1 Introduction

Marcel Vos (help from others is welcome), ECFA detector R&D report

The global particle-physics community continues to develop new ideas for improved sensors and detector systems. In this section, several promising new developments are briefly discussed. Some of these are new technologies that can be integrated in the existing detector concepts, others represent alternatives to the baseline choices made by ILD and SiD. The

As funding for detector R&D is scarce, it is important that the global program covers the essential R&D for the ILC. In Europe, CERN [166] and the ECFA detector R&D panel [167] have published road maps for the effort in instrumentation. A large EU Horizon 2020 project, AIDA Innova [168], unites the effort of seven European national laboratories, 30 universities and institutes and eight industrial partners. In the US, important directions for detector R&D are outlined in the report of the Office of Science Workshop on Basic Research Needs for HEP Detector Research and Development [169]. The "instrumentation frontier group" in the Snowmass process will draft a road map for detector R&D in the US [**?**].

Especially important is the synergy with detector construction projects on intermediate time scale. These projects can validate promising new ideas, with sufficient resources for complete engi-

neering designs and extensive prototyping. The construction phase provides valuable lessons about their practicality in a large-scale production. We envisage that projects such as the upgrades of the LHC experiments, and the construction of specialized experiments such as Mu3e and experiments at FAIR and the EIC can act as "stepping stones" in the development of the optimal solution for the ILC experiments.

6.4.2 Low Gain Avalanche Detectors

Ivan Vila, Salvador Hidalgo 1-2 pages

6.4.3 Silicon sensors with integrated support and cooling

contributed by Corrado Gargiulo, Marcel Vos and Paulo Petagna (obo AIDAinnova-WP10) and Paula Collins

The very strict performance requirements of the silicon tracking systems and vertex detectors has pushed the field to develop active and monolithic silicon sensors that can be thinned to 50 μm or less. To build a superb transparent tracking system this innovation in silicon sensors must be accompanied by important advances in the support structures and cooling systems that make a very important contribution to the material of today's state-of-the-art detector systems. Integrated support and cooling solutions are required to meet the very challenging material budget of the ILC experiments.

An important step towards the integration of support structures was made by the DEPFET collaboration [170], with the development of the all-silicon ladder concept [171]. In this ladder design, all on-detector electronics and power and signal lines are integrated on the silicon sensor itself. A robust and stiff mechanical structure is obtained by selective etching of the handle wafer, such that an integrated "support frame" surrounds the thin sensor. Similar self-supporting all-silicon structures can be produced for CMOS active pixel sensors by stitching multiple reticles and etching []. The all-silicon ladder concept was proven in the Belle 2 vertex detector [172] and the development of the CMOS multi-chip ladder is part of the R&D for the upgrade of vertex detector envisaged in 2025.

The ALICE upgrade of the Inner Tracking System [173] envisage CMOS sensors thinned to approximately 50 μm. Innovative solutions to the support structures are being pursued, including a study of large, stitched sensors that are thinned and bent to form cylindrical structures around the beam pipe.

The cooling of these ultra-low-mass detector systems represents an important challenge. Cooling by a loosely guided gas flow has been demonstrated by the heavy flavour tagger in the STAR experiment [174]. Gas-based cooling is also used to complement a traditional bi-phase cooling system in the Belle 2 pixel detector. The heat generated by the pixel sensors is effectively removed by a gas flow at several meters per second. Tests of the mechanical stability of prototypes in gas flows have been performed at CERN by ALICE and CLIC, at DESY by Belle 2 [] and . A facility is available for users at the University of Oxford under AIDA innova funding. The magnitude of

vibrations induced by the gas flow in realistic prototypes can be kept at the level of a few μm.

Micro-channel cooling promises to bring down the material involved in traditional liquid or bi-phase cooling systems. The use of active silicon cooling plates has been pioneered by the NA62 experiment [175] that has operated the GigaTracker successfully for several years. Micro-channel cooling with evaporative CO_2 at pressures up to 60 bar is part of the Vertex Locator upgrade of the LHCb experiment. The production of VELO modules based on hybrid pixel detectors glued onto silicon micro-channel cooling plates produced at CEA-LETI was successfully completed in 2021 [176]. Installation in the LHCb experiment was still ongoing at the time of writing.

Integration of micro-channels directly in the active sensor wafer [177, 178] offers the best possible cooling contact, with thermal figure-of-merit close to 1 K/W

6.4.4 Dual read-out calorimetry

contributed by Franco Bedeschi (INFN Pisa)

The 20-year-long *R&D* program on Dual-Readout Calorimetry (DR, DRC) of the DREAM/RD52 collaboration [179, 180, 181, 182, 183, 184, 185, 186] has shown that the effects of the fluctuations in the EM fraction of hadronic showers can be canceled by the independent readout of scintillation (S) and Čerenkov (C) light. The DR fibre-sampling approach achieves a high sampling frequency leading to a competitive EM energy resolution $\sim 10\%/\sqrt{E}$. Application of the DR procedure gives a stochastic term of the hadronic resolution close to or even below $30\%/\sqrt{E}$ with a small constant term. Test beam results also show excellent particle-ID performance.

The advancements in solid-state light sensors such as SiPMs have opened the way for highly granular fibre-sampling detectors with the capability to resolve the shower angular position at the mrad level or even better. In the present design 1-mm diameter fibres are placed at a distance of 1.5-2 mm (center to center) in a metal absorber. Brass, copper, iron and lead are currently under study. The lateral segmentation could then reach the mm level, largely enhancing the resolving power for close-by showers with a significant impact on π^0 and τ reconstruction quality. In addition the high Photon Detection Efficiency of SiPMs provide high light yields, thus reducing the effect of photon statistics. Readout ASICs providing time information with $\sim$ 100 ps resolution may allow the reconstruction of the shower position with $\sim$ 5 cm of longitudinal resolution.

The large number and density of channels call for an innovative readout architecture for efficient information extraction. Both charge-integrating and waveform-sampling ASICs are available on the market and candidates for tests have been identified: the Weeroc Citiroc 1A charge integrator and the Nalu Scientific system-on-chip digitisers. A first implementation of a scalable readout system has been tested with a calorimeter prototype on particle beams. Looking further ahead, digital SiPMs (dSiPMs) could provide significant simplification of the readout architecture, but the technology is still in an early *R&D* phase.

The performance of a 4π DR calorimeter for an FCC-ee experiment has been studied with full GEANT4 simulation with good results on key physics processes. This is now the baseline choice for the IDEA [187] detector concept. Significant performance improvements have also been

shown using deep-learning algorithms. Studies of the potential addition of a dual-readout crystal calorimeter in front find superb EM resolution, while maintaining the hadronic performance and even improving it by applying simple particle flow algorithms [188]. A more detailed description is found in Ref. [189].

6.4.5 Liquid Argon calorimetry

Noble-liquid calorimeters have been successfully used in many high-energy collider experiments, such as ATLAS, D0 or H1. They feature high energy resolution, excellent linearity, uniformity, stability, and radiation hardness. These properties make a noble-liquid calorimeter an appealing candidate for an experiment at the next-generation Higgs factories, especially in the case of a program of high precision physics at the Z pole where an excellent control of the systematic uncertainties is required to match statistical precisions as low as 10^{-5}.

A design of a highly granular sampling noble liquid calorimeter was first proposed in the context of a FCC-hh experiment [190], and is now being revisited and optimised for a Higgs factory machine. In the central region, it consists of a cylindrical stack of 1536 lead absorbers (2mm thick), readout electrodes (1.2mm thick) and liquid argon active gaps, arranged radially but azimuthally inclined by $\sim 50^o$ with respect to the radial direction. This design allows for reading out the signals without creating any gaps in the acceptance, high sampling frequency, uniformity in ϕ, and can be build with very good mechanical precision to minimise the constant term of the energy resolution. The use of liquid krypton as active material and of tungsten absorbers is being studied as it could result in a more compact design with better shower separation.

The use of readout electrodes allows to optimise the granularity of each of the 11 longitudinal compartments for the needs of particle-flow reconstruction and particle-ID. A total number of a few million cells can be achieved by using seven-layer PCBs, where the outermost layers provide the high voltage field in the noble-liquid gap, and next layers are signal pads, connected to the central layer where traces bring the signals to the outer edges of the electrodes. The trade-offs between granularity, noise and cross-talk in the design of the PCBs are being studied.

The expected noise levels assuming readout electronics outside the cryostat should allow the tracking of single particles and yield a total noise of about 50 MeV for an electromagnetic cluster. The alternative of using cold readout electronics placed inside the cryostat is also studied as it would achieve a much lower noise, and could simplify the design of the feedthroughs. R&D on high-density feedthroughs is indeed ongoing to allow the analogue readout of millions of channels without any performance degradation. A reduction of the amount of dead material in front of the calorimeter can be achieved thanks to the progress on 'transparent' cryostats using carbon or sandwiches of materials.

Better estimates of the expected performance (using the calorimeter alone and with particle-flow reconstruction), and answers on the feasibility of the designs of the PCBs, the readout electronics and the feedthroughs, will be available in the next months and years.

6.4.6 Vertex Detector

6.4.7 Forward Detectors

6.4.8 Muon System

Technology	**Detector**	**Start (mm)**	**Stop (mm)**	**Comment**
pixel detectors	Vertex	$r_{in} = 16$	$r_{out} = 58$	3 double layer pixels
	Forward tracking	$z_{in} = 220$	$z_{out} = 371$	2 Pixel disks
	SIT	$r_{in} = 153$	$r_{out} = 303$	2 double layer els
Silicon strip	Forward tracking	$z_{in} = 645$	$z_{out} = 2212$	5 layers of Si
	SET	$r_{in} = 1773$	$r_{out} = 1776$	1 double la strips
Gaseous tracking	TPC	$r_{in} = 329$	$r_{out} = 1770$	MPGD reac points along
Silicon tungsten calorimeter	ECAL option	$r_{in} = 1805$	$r_{out} = 2028$	30 layers of 5 pixels
	ECAL EC option	$z_{in} = 2411$	$z_{out} = 2635$	30 layers of 5 pixels
	Luminosity calorimeter	$r_{in} = 83$ $z_{in} = 2412$	$r_{out} = 194$ $z_{out} = 2541$	30 layers
Diamond tungsten or GaAs calorimeter	Beam calorimeter	$r_{in} = 18$ $z_{in} = 3115$	$r_{out} = 140$ $z_{out} = 3315$	30 layers
SiPM-on-Tile	ECAL alternative	$r_{in} = 1805$	$r_{out} = 2028$	30 layers, 5 crossed
	ECAL EC alternative	$z_{in} = 2411$	$z_{out} = 2635$	30 layers, 5 crossed
	HCAL option	$r_{in} = 2058$	$r_{out} = 3345$	48 layers, 3 × els
	HCAL EC option	$z_{in} = 2650$	$z_{out} = 3937$	48 layers, 3 × els
RPC	HCAL option	$r_{in} = 2058$	$r_{out} = 3234$	48 layers, 1 × els
	HCAL EC option	$z_{in} = 2650$	$z_{out} = 3937$	48 layers, 1 × els
SiPM on scintillator bar	Muon	$r_{in} = 4450$	$r_{out} = 7755$	14 layers
	Muon EC	$z_{in} = 4072$	$z_{out} = 6712$	up to 12 laye

Table 6.1: Key parameters of the ILD detector. All numbers from [5]. "Star" and "Stop" refer to the minimum and maxiumum extent of subdetectors in radius and/or z-value .

Measurement	**Main physics question**	**main issue addressed**
Higgs mass in $H \to b\bar{b}$	Precision Higgs mass determination	Flavour tag, jet energy resolution, lepton momentum resolution
Branching ratio $H \to \mu^+\mu^-$	Rare decay, Higgs Yukawa coupling to muons	High-momentum p_t resolution, μ identification
Limit on $H \to$ invisible	Hidden sector / Higgs portal	Jet energy resolution, Z or recoil mass resolution, hermeticity
Coupling between Z and left-handed τ	Contact interactions, new physics related to 3rd generation	Highly boosted topologies, τ reconstruction, π^0 reconstruction
WW production, W mass	Anomalous triple gauge couplings, W mass	Jet energy resolution, leptons in forward direction
Cross section of $e^+e^- \to \nu\nu qqqq$	Vector Bosons Scattering, test validity of SM at high energies	W/Z separation, jet energy resolution, hermeticity
Left-Right asymmetry in $e^+e^- \to \gamma Z$	Full six-dimensional EFT interpretation of Higgs measurements	Jet energy scale calibration, lepton and photon reconstruction
Hadronic branching ratios for $H \to b\bar{b}$ and $c\bar{c}$	New physics modifying the Higgs couplings	Flavour tag, jet energy resolution
A_{FB}, A_{LR} from $e^+e^- \to b\bar{b}$ and $t\bar{t} \to b\bar{b}qqqq/b\bar{b}qql\nu$	Form factors, electroweak coupling	Flavour tag, PID, (multi-)jet final states with jet and vertex charge
Discovery range for low ΔM Higgsinos	Testing SUSY in an area inaccessible for the LHC	Tracks with very low p_t, ISR photon identification, finding multiple vertices
Discovery range for WIMPs in mono-photon channel	Invisible particles, Dark sector	Photon detection at all angles, tagging power in the very forward calorimeters
Discovery range for extra Higgs bosons in $e^+e^- \to Zh$	Additional scalars with reduced couplings to the Z	Isolated muon finding, ISR photon identification.

Table 6.2: Table of benchmark reactions which are used by ILD to optimize the detector performance. The analyses are mostly conducted at 500 GeV center-of-mass energy, to optimally study the detector sensitivty. The channel, the physics motivation, and the main detector performance parameters are given.

SiDBarrel	Technology	In rad	Out rad	z extent
Vtx detector	Silicon pixels	1.4	6.0	± 6.25
Tracker	Silicon strips	21.7	122.1	± 152.2
ECAL	Silicon pixels-W	126.5	140.9	± 176.5
HCAL	Scint-steel	141.7	249.3	± 301.8
Solenoid	5 Tesla SC	259.1	339.2	± 298.3
Flux return	Scint-steel	340.2	604.2	± 303.3
SiDEndcap	Technology	In z	Out z	Out rad
Vtx detector	Silicon pixels	7.3	83.4	16.6
Tracker	Silicon strips	77.0	164.3	125.5
ECAL	Silicon pixel-W	165.7	180.0	125.0
HCAL	Scint-steel	180.5	302.8	140.2
Flux return	Scint/steel	303.3	567.3	604.2
LumiCal	Silicon-W	155.7	170.0	20.0
BeamCal	Semicond-W	277.5	300.7	13.5

Table 6.3: Key parameters of the baseline SiD design. (All dimension are given in cm).

Chapter 7

ILC Detector Simulation

[5 pages; corresponding editor: Frank Gaede (frank.gaede@desy.de)]

7.1 ILC Fast Simulation Frameworks

As a first step to get started with ILC physics one can use fast simulation tools that can be used to quickly generate substantial samples of simulated and reconstructed events. Situations where this is desirable include detector optimisation and new physics searches. In these cases, similar processes need to be simulated and reconstructed at a, possibly very large, number of different conditions. In the first case, one needs to modify various aspects of the detector in steps, in the latter, one needs to explore the entire allowed parameter space of a theory for new physics. In addition to these cases, fast simulation is also an asset for simulating high cross section SM processes, such as $\gamma\gamma$ processes, where the investment in processor power and intermediate storage might be prohibitively large to attain the goal that simulation statistics should be a negligible source of systematic uncertainty. The ILC community uses two tools for fast simulation that are described in the following:

7.1.1 DELPHES for ILC

DELPHES [191] is a fast, parameterized simulation framework for generic collider detectors, developed originally for phenomenological studies at hadron colliders like the LHC. In its recent incarnation the DELPHES framework has been modularized and an attempt has been made to roughly emulate a particle-flow reconstruction philosophy [192] a feature that is crucial for its applicability to the ILC. DELPHES also integrates the FastJet [193] package allowing to directly run the most common jet clustering algorithms in use for the ILC. A specific collider detector is mimicked in DELPHES via the specification of efficiencies and resolutions for the long lived final state particles, based on their charge, momentum, polar angle[1] and type (charged/neutral hadron, photon, electron or muon). A dedicated DELPHES card: *delphes_card_ILCgen.tcl* with parameterizations for a

[1] DELPHES uses pseudo-rapidity *eta* instead of polar angle

generic ILC detector has been created [194] and is shipped with the DELPHES source code [195]. The parameterization of the detector and reconstruction performance is based on the latest results of the ILD-IDR [196], where due to the nature of the rather coarse simulation accuracy of the DELPHES approach any potential differences to the SiD detector performance can be neglected for studies carried out with DELPHES . Fig. 7.1a shows a comparison of the transverse momentum resolution for charged particles at different angles as simulated with DELPHES compared to a full simulation and reconstruction for the ILD detector as well as the jet energy resolution for di-jet events of different quark flavors (Fig. 7.1b). DELPHES can read many standard generator formats

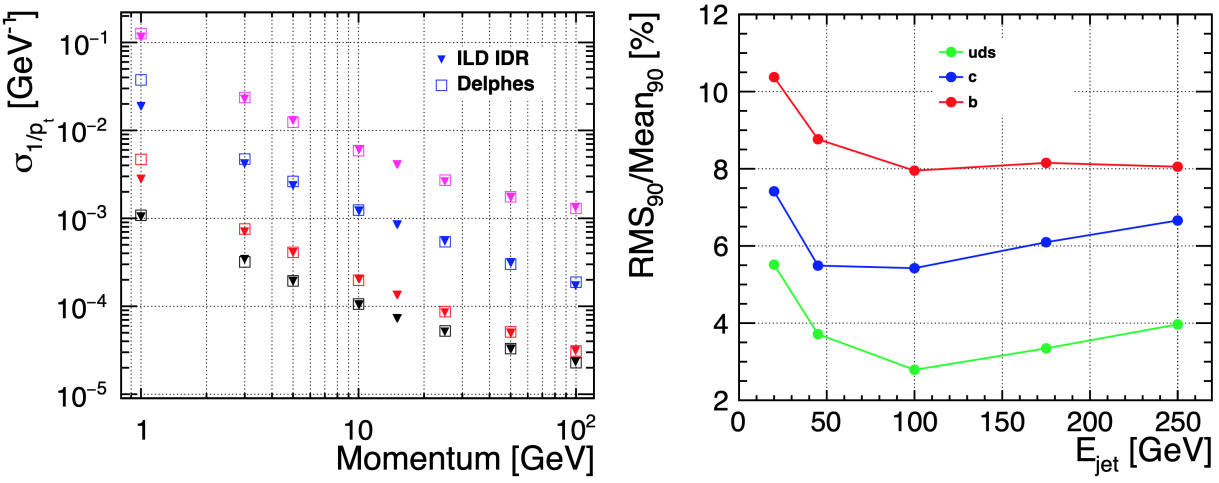

(a) (b)

Figure 7.1: (a): transverse momentum resolution for different polar angles for the ILD full simulation and for the ILCgen DELPHES parameterization. (b): jet energy resolution for the ILCgen simulation

such as *stdhep* and produces ROOT [197] output files by default. With the *delphes2lcio* [198] tool standard LCIO miniDST can be created (see section 7.3.3).

7.1.2 SGV

The SGV program[199] used at ILC has a more sophisticated way of simulating the response to charged particles than the Delphes program described above. The time to simulate and reconstruct an event is similar to the time it takes to generate it ($\sim 1 - 10$ ms). The response of the detector is as far as possible calculated from the detector design (so there is no need to parameterize pre-existing full simulation results). SGV has been shown to compare well both with full simulation and with real data [200].

The program uses a simplified "*cylinders-and-discs*" description of the detector, which is used to calculate the Kalman-filtered track-helix covariance matrix of each generated charged particle. By Cholesky decomposition of the covariance matrix, the track-parameters are simulated in a way such that all correlations are respected. The calorimetric response is calculated from the

expected single-particle performance of the different components of the calorimetric system, for each particle impinging on it. Optionally, the effects of shower-confusion can be included. To reduce the needed storage for a Giga-event size sample, event filtering can be applied at different steps of the processing, directly after generation, after the detector response is known, or after higher-level event analysis is done. Events passing all filters are output in LCIO DST-format, and can seamlessly be further analyzed within the Marlin framework.

7.2 ILCSoft Framework

Accurate and detailed modeling of the physics interactions as well as the detector response are crucial for making realistic predictions about the expected physics and detector performance. The ILC software for detector simulation, reconstruction and analysis is entirely based on the common linear collider software ecosystem called *iLCSoft* [201]. The main core software tools in iLCSoft are the common event data model and persistency tool LCIO [202], the C++ application framework Marlin [203] and the generic detector description toolkit DD4hep [204, 205]. DD4hep provides a single source of information for describing the detector geometry, its materials and the readout properties of individual sub detectors. Various components of DD4hep provide different functionalities. Here we use DDG4, the interface to full simulations with Geant4 [206] and DDRec the specialized view into the geometry needed for reconstruction. In the following we briefly describe the main features of the full simulation and reconstruction tools in use for ILC and SiD, more details can be found in the corresponding chapters of [196] and [6].

7.2.1 Simulation Models

Both ILC detector concept groups have developed detailed and realistic simulation models with realistic geometrical dimensions, material budgets, imperfections and cables and services. Wherever possible, realistic simulations and parameterizations for the individual sub detectors have been implemented based on available test beam results for the proposed technology. Great care has been taken to include realistic material estimates, established by the detector R&D groups, in particular in the tracking region where the material budget has a direct impact on the detector performance. Examples of the inner tracking regions as implemented in the realistic simulation models for SiD and ILD are shown in Fig 7.2a ,7.2b

7.2.2 Event Reconstruction

For the reconstruction of simulated events in the ILC detectors is done with a number of dedicated algorithms implemented in Marlin. For the digitization of tracking detectors and calorimeters dedicated modules exist that provide a parameterization of the expected resolutions as established by the R&D collaborations taking into account effects like cross talk, electronic noise and signal collecting efficiencies. The reconstruction of charged particle tracks is performed with a variety of pattern recognition algorithms implemented in the MarlinTrk [207] package. This is followed

by sophisticated clustering and particle flow algorithms from PandoraSDK [208] that delivers a complete collection of reconstructed particles or so called *particle flow objects*. Additional high level reconstruction algorithms, like jet clustering with FastJet [193], vertexing and flavor tagging with LCFIPlus [209], particle identification using dE/dx-information and time-of-flight measurements complete the event reconstruction for final physics analyses.

7.3 ILC SM Background Samples

7.3.1 Event generation

ILC physics sample generation is typically done with the Whizard [210] event generator providing crucial features like correct treatment of ISR and FSR via creation of photons as individual final state particles. Whizard uses tree-level matrix elements and loop corrections to generate events with the final state partons and leptons based on a realistic beam energy spectrum, the so called *hard sub-process*. The hadronization into the visible final state is performed with Pythia [211] tuned to describe the LEP data. The correct beam energy input spectrum for a given collision energy and set of accelerator parameters is created with Guinea-Pig [212], a dedicated simulation program for computing beam-beam interactions at linear colliders.

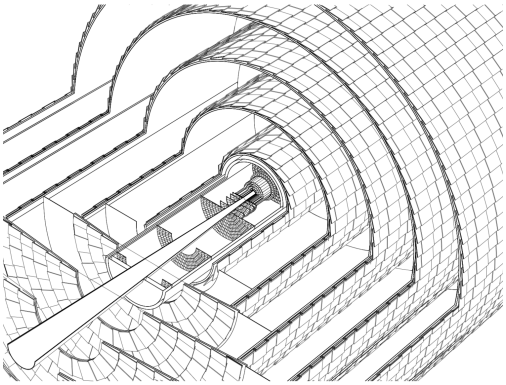

(a)

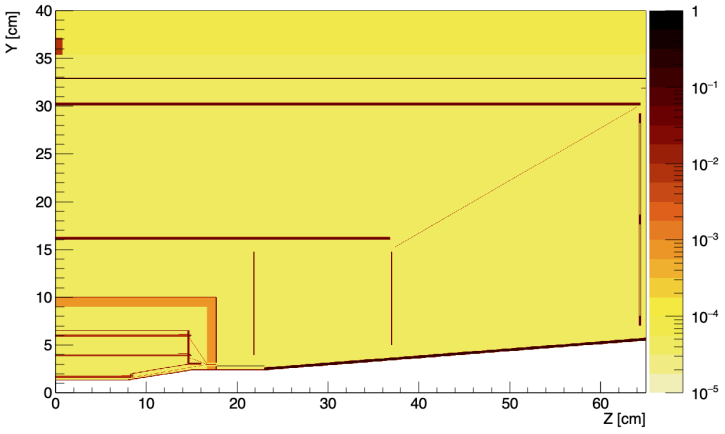

(b)

Figure 7.2: (a): cut-away view of the tracking system as implemented in the *SIDLOI3* simulation model (from [5]). (b): Material scan in inner tracking region of the ILD simulation model showing detector components of the VTX, SIT and FTD as well as dead material from the beam pipe, support structures, cables and services. Plotted is the local material budget per bin in units of X0 with an arbitrary scaling factor applied.)

7.3.2 Beam induced background

The strong beam-beam interactions lead to two distinct sources of backgrounds:

- the creation of incoherent e^+e^--pairs that are the source of the dominating background at the ILC. These electrons and positrons are predominantly created in a forward cone as shown in Fig 7.3 for the ILD detector. It is this cone that restricts the minimal allowed radius of the innermost layer of the vertex detector of any linear collider detector as can be seen in Fig. 7.3.

- creation of $\gamma\gamma \to hadrons$ events, due to the interaction of beamstrahlung photons. These type of events are generated for $\gamma\gamma$ cms-energies from 300 MeV to 2 GeV with a dedicated generator based on [213], whereas for higher energies Pythia is used.

For realistic physics analyses and detector studies for the ILC it is important to take this backgrounds into account. This is typically done through event overlay techniques in the iLCSoft based full simulation and reconstruction chains of ILD and SiD.

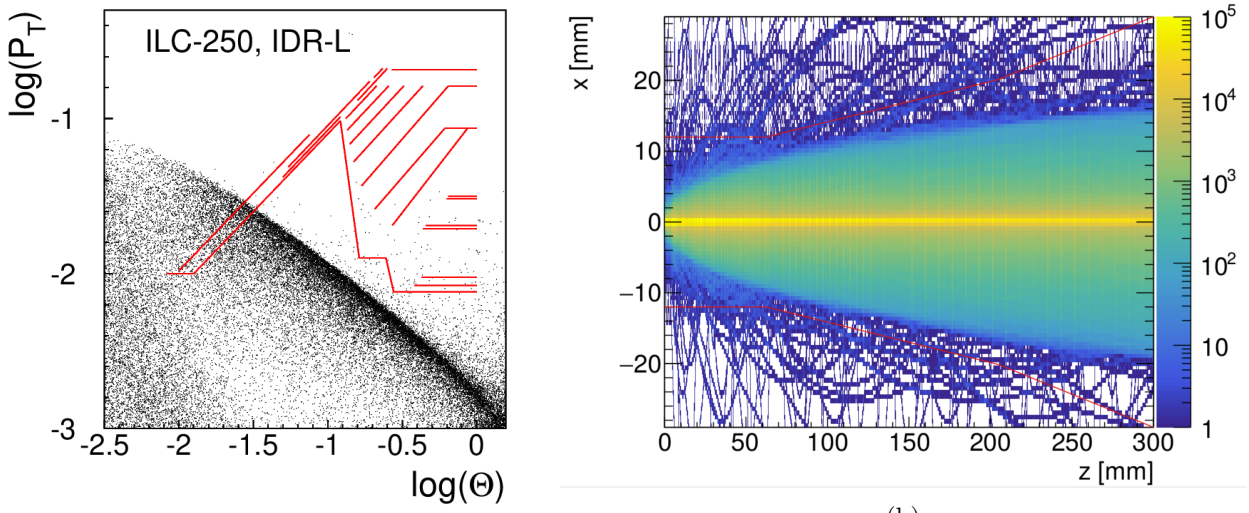

(a) (b)

Figure 7.3: (a): Cones of incoherent e^+e^--pairs in the ILD detector for $E_{cms} = 250\ GeV$ as created with GuineaPig. Shown is $\log p_t$ of the particles (radius of the helical trajectory) as a function of $\log\theta$. Also shown are the inner detector elements of the ILD detector (horizontal lines represent barrel elements and diagonal lines represent end-cap elements). (b): Cone of background from incoherent e^+e^--pairs, generated with Guinea-Pig and simulated in the 5 T B-field of the SiD detector (from [214]).

7.3.3 Event Samples and data formats

Large sets of SM samples for the ILC have been generated for $E_{cms} = 250, 350, 500, 1000\ GeV$ are available at [215]. Data sets with miniDSTs created with DELPHES and SGV of these generated samples are also available at this web site. Access to more realistic fully simulated and reconstructed event samples from ILD or SiD is possible via a lightweight guest membership. The web-site [215] provides additional information on ILC simulation resources and tools.

All ILC fast and full simulation and reconstruction tools can provide the common data format LCIO as output. The LCIO event data model (see Fig. 7.4a) is the de facto standard for ILC physics and detector studies. Recently a particularly lightweight set of output collections for ILC event data has been defined, the *miniDST*-format. By starting out with developing an analysis with DELPHES or SGV based on *miniDST*s one can later easily move to a more realistic analysis based on full simulation using the same format with only minor modifications as shown in Fig. 7.4b.

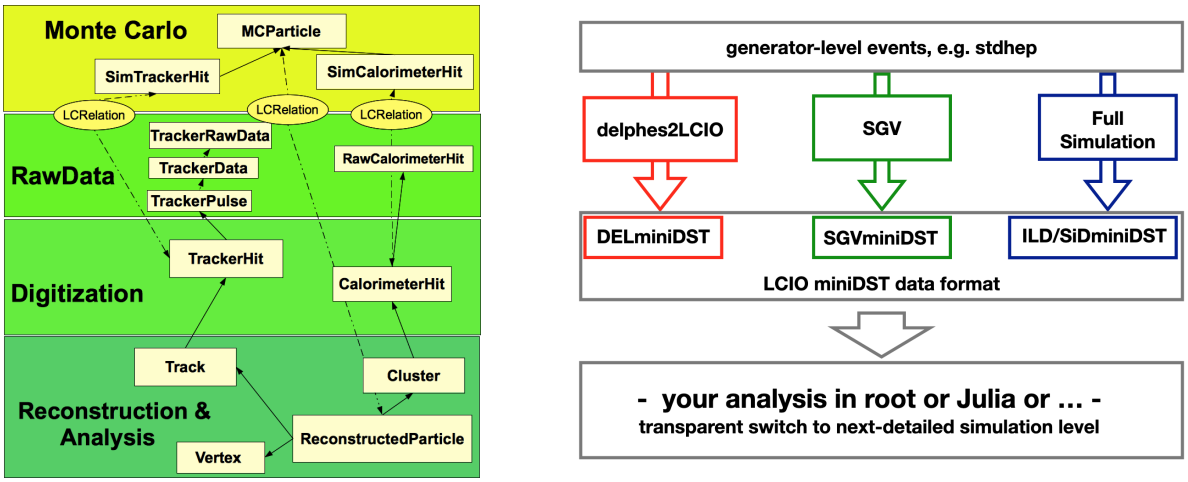

(a) (b)

Figure 7.4: (a): Schematic view of the hierarchical event data model of LCIO. (b): Using the miniDST format a common analysis code can be developed that works with all simulation and reconstruction tools presented above.

Chapter 8

ILC Physics Measurements at 250 GeV

[15 pages; general corresponding editors: Daniel Jeans (daniel.jeans@kek.jp), Jenny List (jenny.list@desy.de), Michael Peskin (mpeskin@slac.stanford.edu)]

(This chapter will review experimental studies of the various ILC reactions available at 250 GeV. The ILD group is now preparing a new high-statistics sample of 250 GeV events. Thus, we expect new analyses of many of these processes to be ready for Snowmass, in particular, a new analysis of $e^+e^- \to W^+W^-$ at 250 GeV.)

The first stage of the ILC will be at a CM energy of 250 GeV. In this chapter, we will describe aspects of the ILC experimental program that are specific to 250 GeV, in particular, the study of the Higgs boson in the process $e^+e^- \to ZH$. We will also discuss precision SM tests that are available this energy—in particular, the measurement of the triple gauge couplings through $e^+e^- \to W^+W^-$ and tests of QCD in $e^+e^- \to$ jets. Aspects of the ILC program that benefit from higher energy—in particular, searches for new particles in pair-production and fermion-fermion scattering, will be discussed over the whole ILC program in Chapter 10.

8.1 Higgs – Conventional Decays

[corresponding editor: Daniel Jeans (daniel.jeans@kek.jp)]

The precise measurement of "conventional" Higgs decay branching ratios is key to probing virtual effects of new physics in the Higgs sector. Many models of new physics lead to variations in Higgs couplings, typically leading to few-% variations of Standard Model Higgs couplings for new physics at the TeV scale. The measurement of these couplings to %-level precision or better is one of the major aims of the Higgs program at high energy electron–positron colliders such as the ILC.

Higgs production in electon–positron collisions at 250 GeV is dominated by the associated production of Higgs and Z bosons ("Higgs-strahlung"), as shown in fig 8.1 [216]. Because electron-

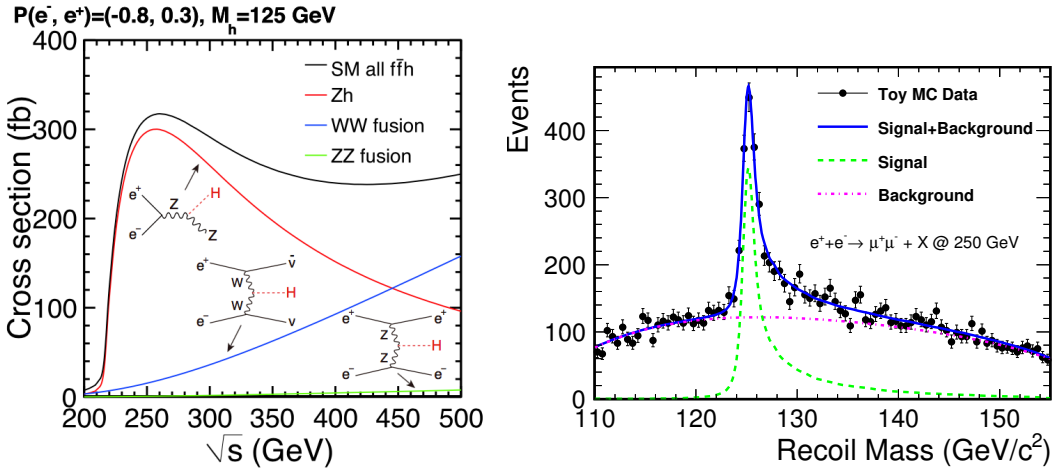

Figure 8.1: Left: Cross sections for the three major Higgs production processes as a function of center of mass energy [2]. The Zh "Higgs-strahlung" process dominates at 250 GeV. Right: Recoil mass spectrum against $Z \to \mu^+\mu^-$ for signal $e^+e^- \to Zh$ and SM background at 250 GeV [217].

positron collisions provide an initial state with well-defined four-momentum, this process allows the identification of Higgs bosons by considering the mass recoiling against an identified Z boson, without any reference to the decay products of the Higgs. A typical reconstructed recoil mass distribution is shown in fig 8.1.

Higgs-strahlung events at ILC250 in which the Z decays to hadrons or charged leptons will provide the experimenter a sample of around half a million Higgs bosons that is almost completely unbiased with respect to the Higgs decay mode. Such a sample is very useful for making precise and unbiased measurements of the Higgs boson's properties, for example the partial cross-sections to different Higgs decay modes $\sigma_{ZH} \times BR(H \to X)$.

In addition to the Higgs decay branching ratios, the total Higgs-strahlung production cross-section in the different ILC beam polarisation setups will provide important constraints on the coupling of the Higgs to the Z boson. The mass of the Higgs boson is another key parameter to be extracted, particularly because it has a significant effect on the branching ratio to WW^* and ZZ^*, in which the final state includes an off-shell boson. A precise prediction of these decay branching ratios requires a precise knowledge of the Higgs mass. ILC also presents an opportunity to probe the Higgs boson's CP properties, a key to understanding the potential for baryogenesis at the electro-weak scale, in its interaction both with tau leptons and massive vector bosons.

Projections for the experimental precisions attainable at the ILC are based on full simulation studies which take into account experimental conditions such as beam energy spread and beam background processes, as well as detailed simulation of the experimental apparatus and realistic data analysis techniques.

The Higgs coupling precisions which result from a global EFT fit combining expected ILC measurements with those from HL-LHC are shown in fig. 8.2.

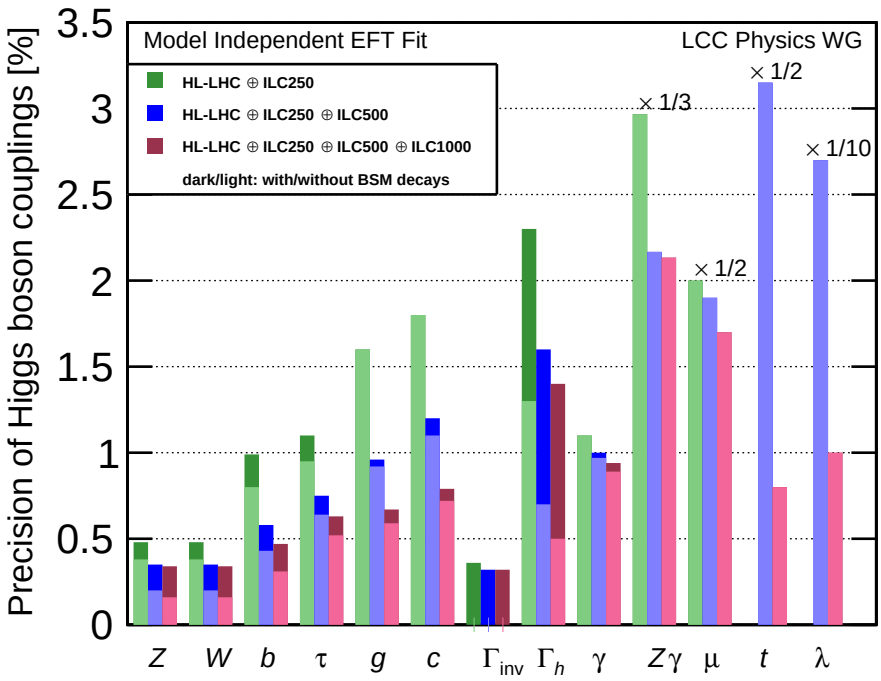

Figure 8.2: Projected Higgs boson coupling uncertainties for ILC250, ILC500, and ILC1000, also incorporating results expected from the HL-LHC, based on a SMEFT analysis. The darker bars show the results allowing invisible and exotic Higgs decay channels; the lighter bars assume that these BSM decays are not present. The column λ refers to the HHH coupling. In the last four columns, all bars are rescaled by the indicated factor. From [218].

8.1.1 Zh cross-section and Higgs mass

The recoil mass distribution shown in fig. 8.1 can be used to extract the total Zh production cross-section and the Higgs boson mass, by consideration respectively of the area and position of the signal peak [217]. The cross-section will be measured in all ILC beam polarisation combinations, switching between dominantly left- and right-handed electrons and positrons. The cross-section in the two major polarisation combinations will be measured with a precision of around 1-2 %. The asymmetry between these measurements in different polarisations offers an important additional input to the global understanding of Higgs couplings. The precision on the Higgs mass is expected to reach 14 MeV using the recoil mass method at ILC-250 [217].

The Higgs mass can also be directly reconstructed from its decay products, providing complementary measurements. A demonstration in the case of the dominant Higgs decay to $b\bar{b}$ can be found in [219], while rare Higgs decays to final states which can be very precisely measured, such as two or four muons and/or electrons, can also provide very competitive precision despite the limited number of events [220].

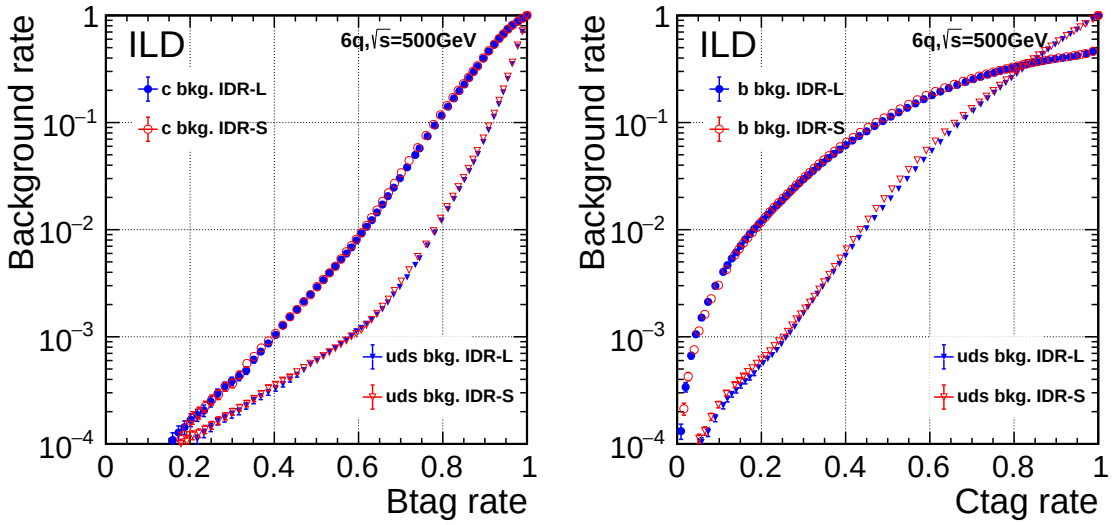

Figure 8.3: B-tag (left) and c-tag (right) performance in full-simulation studies of two variants of the ILD concept, IDR-L and IDR-S (figure from [221]).

8.1.2 Hadronic decays

The majority of Higgs bosons will decay into hadronic final states; within the SM we expect dominant contributions from b-quarks, c-quarks, and gluons. The experimental separation of these hadronic contributions relies on jet flavor tagging. The keys to distinguishing jet flavor are the identification of displaced vertices produced in the decay of meta-stable particles, of leptons within hadronic jets originating from massive hadron decays, and particle identification, in particular the ability to identify kaons.

The reconstruction of displaced vertices is aided by the tiny ILC interaction region and the vertex detector, with its few-micron hit position resolution and first layer placed only $\sim$ 15 mm from the IP. Figure 8.3 shows the excellent b- and c-tagging performance achieved by the LCFIplus algorithm in full simulation studies of the ILD concept at ILC.

Applying the LCFIplus algorithm to hadronically decaying Higgs bosons produced at ILC250, assuming the nominal 2 ab^{-1} total integrated luminosity, the partial cross–section $\sigma_{Zh} \times BR(H \to bb)$ can be measured to better than 1% precision, and $\sigma_{Zh} \times BR(H \to cc, gg)$ to several % precision [222].

The identification of $H \to s\bar{s}$ decays presents a significant experimental challenge due both to its subtle experimental signature and its small expected branching ratio. Studies are in progress to understand how the identification of hadron species, particularly kaons, can contribute to this measurement [223]. Potentially useful experimental techniques include the measurement of the specific energy loss dE/dx of charged particles, the identification of decaying K-short mesons, and of particle identification by time-of-flight.

8.1.3 Leptonic decays

The measurement of Higgs decays to tau leptons and muons are feasible at ILC supposing that the branching fractions are SM-like. The decay branching ration to tau leptons is relatively large in the SM, which, together with the suitability of the ILC experimental conditions to the identification of tau lepton decays with high precision, results in a precision at ILC250 of 3.2% in the measurement of the partial cross–section $\sigma_{Zh} \times BR(H \to \tau\tau$ [224].

The small branching ratio to muons limits the statistics available at ILC. The predicted precision on $BR(H \to \mu\mu)$ at ILC250 is 23%, which can be improved to 17% after the ILC run at 500 GeV [225].

Direct observation of the Higgs coupling to electrons is essentially impossible at ILC if the branching fraction is that predicted by the SM. The final state can in principle be well reconstructed, so if this channel is very significantly enhanced with respect to the SM, for example to a similar level as the decay to muons, it can be observed at ILC.

8.1.4 EW-boson decays

The measurement of the Higgs branching ratios to WW* and ZZ* play an important role in the global probing of the Higgs sector, since these same couplings are involved in Higgs production via WW-fusion and Higgs-strahlung, respectively. These therefore allow direct extraction of the total Higgs decay width $\Gamma_h = \Gamma_{WW/ZZ}/BR_{WW/ZZ}$.

The large number of different final states make for a complex analysis. A recent example of the measurement of ZZ decays can be found in [226], in which a precision of 5-6% on $\sigma_{Zh} \times BR(H \to ZZ)$ in the different polarisation stages of ILC-250, considering a variety of Z and h decays modes. At ILC-250, overall precisions of at least 4.6% [18%] on $\sigma_{Zh} \times BR(H \to WW[ZZ])$ are expected.

Rare loop-induced Higgs decays to $\gamma\gamma$ and γZ can also be searched for at ILC-250, although the small SM branching ratios will severely restrict the statistical precision of these measurements. In the case of $\gamma\gamma$, a precision of 34% on the partial cross-section is expected at ILC250.

The $h\gamma Z$ coupling can also be probed via the $e^+e^- \to \gamma h$ process, whose cross-section is also maximal around 250 GeV. The cross-sections in the SM are rather small, for example 0.20 fb for beam polarization $P(e^-, e^+) = (-0.8, +0.3)$. Upper limits at 95% on the production cross-sections in the different polarisation scenarios can be set at 1.8 fb for the same beam polarisation [227].

8.1.5 CP properties

CP properties of the Higgs boson can be probed in its decays to tau leptons [228], or in its coupling to the EW bosons W and Z [229].

In the tau decay channel, the tau decay products act as polarimeters, providing an estimate of the spin orientation. The correlation between the two taus' polarimeter components perpendicular to the tau momentum direction is sensitive to their CP state. The clean experimental environment

at ILC and the high precision detectors being developed are conductive to accurate reconstruction of tau lepton decays, allowing good reconsturction of tau polarimeter information. Mixing between odd and even CP components of the tau pair can be probed with a precision of 75 mrad at ILC250 [228].

The coupling of the Higgs to WW or ZZ, either in decay or production, also provides a sensitive probe of CP violation effects. Anomalous CP-violating couplings can affect angular correlations between vector boson decay planes. Limits of order (BLAH BLAH) on CP violating terms in the HVV coupling can be achieved at ILC250, and further improved at higher ILC energies [229, 230].

8.2 Higgs – Exotic Decays

[corresponding editor: Zhen Liu (zliuphys@umn.edu)]

Higgs exotic decays provide unique opportunities probe to a broad class of new physics models [231]. Studying the Higgs exotic decay precision would help reveal new physics, especially hidden sector dynamics through this generic Higgs portal. The physics we can learn from the Higgs exotic decay program is also complementary to the Higgs coupling precision measurements. An survey of lepton collider sensitivities to Higgs exotic decays into final states that are challenging at hadron colliders has been initially carried out in Ref. [232], showing the promising sensitivities at lepton colliders.

As a first attempt, let us focus on two-body Higgs decays into BSM particles, dubbed as X_i, $h \to X_1 X_2$, which are allowed to decay further, up to four-body final states. The cascade decay modes are classified into four cases, schematically shown in Fig. 8.4. These processes are motivated by a large class of BSM physics, such as singlet extensions, two-Higgs-doublet-models, SUSY models, Higgs portals, gauge extensions of the SM [231, 233, 232].

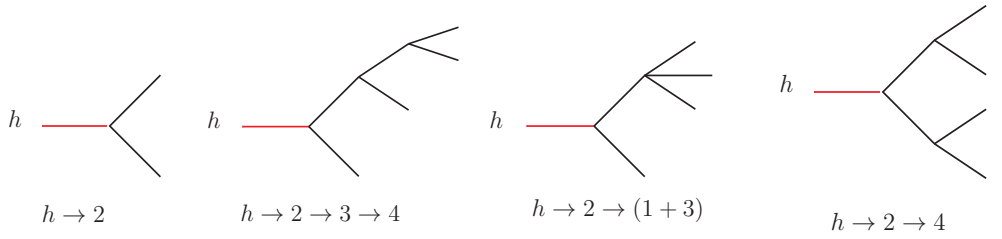

Figure 8.4: Representative topologies of the Higgs exotic decays.

For ILC running at the center of mass energy 250 GeV, the essential Higgs production mechanism is Z-Higgs associated production $e^+e^- \to Z^* \to Zh$. The Z boson with visible decays enables Higgs tagging using the "recoil mass" technique. A cut around the peak of the recoil mass spectrum would remove the majority of the SM background. To demonstrate a typical Higgs exotic search at ILC, we show benchmark processes from our analysis, $h \to jj + \not{E}_T$. In the last part of this section, we present the summary for Higgs exotic decay physics potential at ILC for an integrated luminosity of 2 ab^{-1} and provide an outlook for future studies and improvements.

For numerical analyses, we generate both the signal and the background events for a 240 GeV electron-positron collider with `MadGraph5` at parton level [234] We describe our parameter choices for the detector effects and our pre-selection cuts that are universal for the analyses for all Higgs exotic decay modes. All of the visible particles in the final state are required to have $|\cos\theta| < 0.98$, or equivalently $|\eta| < 2.3$. The final state particles are required to be well-separated with $y_{ij} \equiv 2\min\left(E_i^2, E_j^2\right)(1-\cos\theta_{ij})/E_{vis}^2 \geq 0.001$. We only study the case where the Z boson decays into $\ell^+\ell^-$ where $\ell^\pm = e^\pm, \mu^\pm$. The signal events are required to contain at least a pair of opposite-sign, same-flavor charged leptons with an opening angle greater than 80°, and satisfy $E_\ell > 5$ GeV and $|m_{\ell\ell} - m_Z| < 10\ rmGeV$, where $m_{\ell\ell}$ is the invariant mass of the di-lepton system. The recoil mass is defined as $m^2_{\rm recoil} \equiv s - 2\sqrt{s}E_{\ell\ell} + m^2_{\ell\ell}$ where $E_{\ell\ell} = E_{\ell^+} + E_{\ell^-}$. The recoil mass is required to satisfy $|m_{\rm recoil} - m_h| < 5$ GeV. To suppress the ISR contribution to the backgrounds[1], for Higgs exotic decay modes without missing energy, we require the events to have the total visible energy $E_{vis} > 225$ GeV. We mimic the detector resolution effect by adding Gaussian smearing effects on the four-momentum of the particles, detailed in Ref. [232].

$h \to jj + \not{E}_T$

The SM-like Higgs boson decays into X_2X_1 with $X_2 \to X_1jj$ through an off-shell intermediate state gives rise to this exotic decay mode. Beyond the pre-selection cut and the recoil mass cut, we require that there are two additional jets that satisfy $E_j > 10$ GeV and $|\cos\theta_j| < 0.98$. The dominant background after the recoil mass cut will be the Higgsstrahlung process with $h \to ZZ^* \to q\bar{q}\nu\bar{\nu}$.

We use the likelihood function of the m_{jj}-$\not{E}_T$ distribution to derive the exclusive limit. The results are shown in Fig. 8.5 in the plane of X_1, mass m_1, and the mass splitting between X_2 and X_1, $m_2 - m_1$ for $h \to jj + \not{E}_T$. The exclusion limits on the branching fraction in the bulk region of the parameter space reach $3 \times 10^{-4} \sim 8 \times 10^{-4}$ for $h \to jj + \not{E}_T$. We can see that when the mass splitting $m_2 - m_1$ is around 80 GeV, the future lepton colliders have the strongest sensitivities on these Higgs exotic channels, reaching around 4.3×10^{-4} for $h \to jj + \not{E}_T$. When X_1 is light and $m_2 - m_1$ is large, the energy is shared by the two jets and the X_1. Consequently, when the mass splitting $m_2 - m_1$ is around 80 GeV, the dijet invariant mass will be around 40∼60 GeV, falling in the "valley" of low SM background as shown in the left panel of Fig. 8.5. For heavier X_1, the MET will be lower due to less momentum available for the LSP.

Summary and outlook

We summarize the set of Higgs exotic decays in Fig. 8.6 for ILC with 2 ab^{-1} integrated luminosity. We also include projected LHC sensitivity in gray bars. We use the up-to-date projected sensitivities for the LHC constraints, but many do not exist or are very conservative. We emphasize that LHC does provide complementary sensitivities in many channels that involve electroweak states, such as photons and charged leptons.

[1] Corrections from beamstrahlung effect [235] and ISR effect [236] need to be carefully taken into account for certain processes relying a precise reconstruction of the recoil mass.

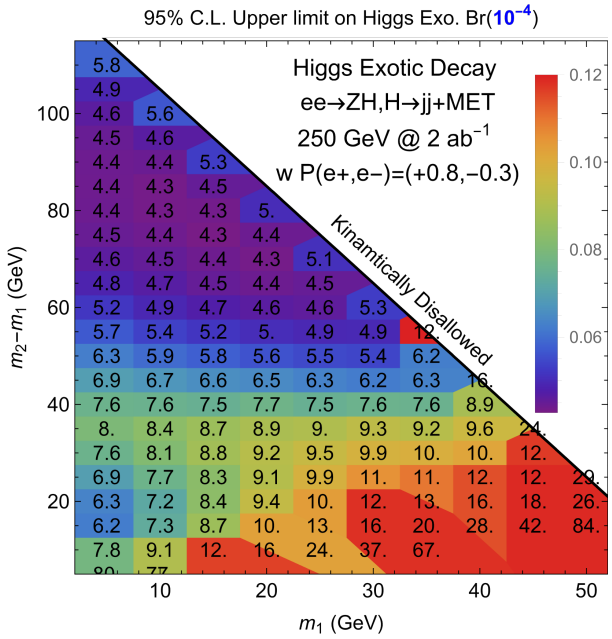

Figure 8.5: The 95% C.L. upper limit on the Higgs exotic decay branching fractions into $jj+\not{E}_T$ for various lightest detector-stable particle mass m_1 and mass splittings $m_2 - m_1$.

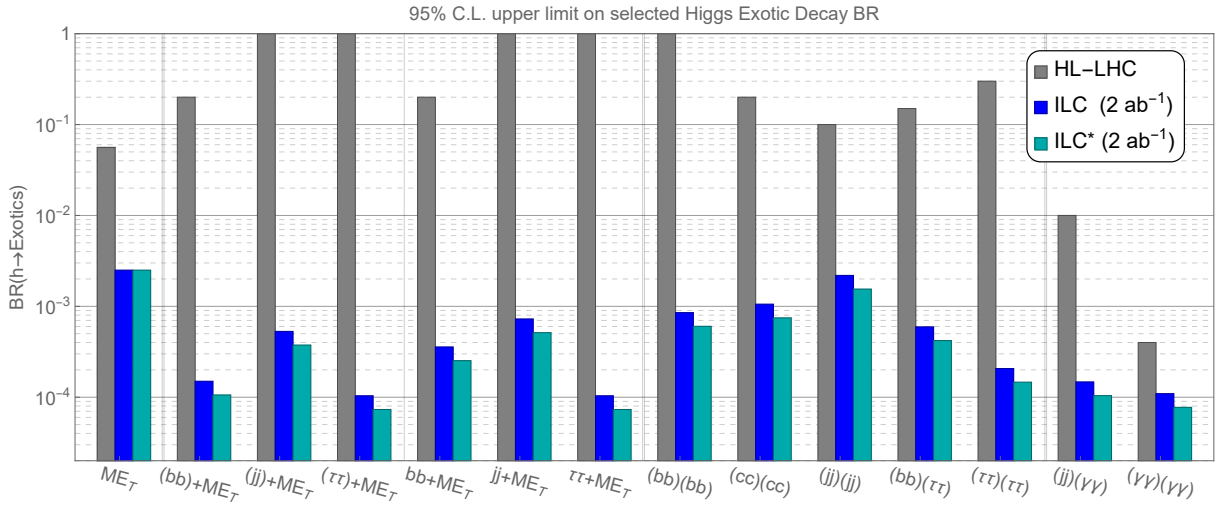

Figure 8.6: The 95% C.L. upper limit on selected Higgs exotic decay branching fractions at HL-LHC and ILC, based on Ref [232]. The ILC curves are derived using results from Ref [232] with leptonic decaying Z boson in the $e^-e^+ \to ZH$ process. The ILC* scenario further utilizes the hadronically decaying Z boson and includes an estimated (indicative) improvement of 40%. We put several vertical lines in this figure to divide different types of Higgs exotic decays.

In the summary Fig. 8.6, the exotic Higgs decay channels are selected such that they are hard to be constrained at the LHC. The improvements on the limits of the Higgs exotic decay branching fractions vary from one to four orders of magnitude for these channels. This great advantage benefits a lot from low QCD background and the Higgs tagging from the recoil mass technique at future lepton colliders. As for the Higgs exotic decays without missing energy, the improvement varies between two to three orders of magnitude, except for the one order of magnitude improvement for the $(\gamma\gamma)(\gamma\gamma)$ channel. Reconstructing the Higgs mass from the final state particles at the LHC provides additional signal-background discrimination power. Hence, the improvement from ILC on Higgs exotic decays without missing energy is less impressive than for those with missing energy. Furthermore, as discussed earlier, leptons and photons are relatively clean objects at the LHC, and the sensitivity at the LHC on these channels will be very good. ILC complements the HL-LHC for hadronic channels and channels with missing energy.

Many new and interesting channels remain open for assessment. Higgs exotic decays of $H \to XX \to 4f$ where the intermediate resonant particle X mass is below 10 GeV is one of such channels. This scenario is particularly motivated by recent discussion about Higgs exotic decay connections to strongly first order electroweak phase transition [237, 238]. In this region, the particle X can also be easily long-lived, we can consider to extend the study into long-lived particle regime [239] Another example is the Higgs decay into dark shower, where the showered hidden mensons[2] can either decay promptly or long-lived, and their decay channel back to the SM can be either hadronic or leptonic. The phenomenological study for this class of models are basically widely open due to the challenges of trigger and background at the LHC. The process is motivated by generic considerations of hidden sector strong dynamics. A more familiar example is the discussion of neutral naturalness [241], but on the other hand, the current studies have been focusing on the Higgs decays into a pair of twin glueballs [242, 243, 239, 244], which is only a subclass of the generic Higgs decays into these final states. Furthermore, this dark shower channel is also motivated by variance of the class of models with large number of light scalar embedded [245], e.g., NNaturalness [246], EW scale as a trigger [247], electroweak symmetry delayed- or non-restoration [248, 249, 250, 251], etc.

8.3 Triple Gauge Couplings

[corresponding editor: Jenny List (jenny.list@desy.de)]

This section will discuss the studies of triple gauge boson vertices involving two W bosons and a photon or a Z boson from single and pairwise production of W bosons at $\sqrt{s} = 250\,\text{GeV}$. The impact of higher center-of-mass energies on these observables will be described in Section **??**. Measurements of other important properties of the W boson, like its mass, width and decay branching fractions, will be addressed in Chapter 9.

[Is a more general physics introduction needed here?]

At LEP, a minimal set of the three couplings g_1^Z, κ_Z and λ_γ (the so-called LEP parametrisation) has been constrained a the level of a few 10^{-2}. These three "LEP parameters" are a linear

[2] It can also be fermions, for instance, composite neutrinos [240].

combination of the SMEFT parameters c_W, c_B and c_{WWW}, as described in [252]. Limits have been derived in fits of individual parameters, fixing the other two to their SM values [253], as well as in two- and three-parameter fits, which allowed two or all three couplings to vary simultaneously [254, 255, 256, 257]. The same three parameters are studied at the LHC, currently [258] reaching precisions between 6 and 8×10^{-3} in single-parameter fits and between 7 and 12×10^{-3} in two-parameter fits. Thereby g_1^Z and κ_Z show a strong, almost 100% correlation. For the HL-LHC, generator-level projections of three-parameter fits have been performed based on NLO cross-sections and assumptions on efficiencies derived from the corresponding 8 TeV ATLAS and CMS analyses [259]. This study projects precisions between 2 and 5×10^{-3}, with the same strong correlation between g_1^Z and κ_Z. This study also evaluated the effect of non-SM Z-fermion couplings (in particular the q-$\bar{q}$-Z couplings) by letting them float in the fit within 2σ bounds from fits to LEP data. This has a huge impact on the to ability extract g_1^Z and κ_Z: Their constraints weaken to the level of 1-2 $\times 10^{-2}$. This highlights an important area of ILC-LHC interplay: the couplings of the Z boson to fermions will be measured to unprecedented precision both at the Z pole and – more relevant here – at higher energies, as discussed in sections 9.2, 9.3, **??** and **??** of this report.

Most studies of the capability of future e^+e^- linear colliders to constrain triple gauge vertices have been performed at a center-of-mass energy of 500 GeV. These range from studies based on full, Geant4-based simulations of the ILD detector concept focusing on the $WW \to \mu\nu qq$ and $WW \to e\nu qq$ channels and the determination of the three LEP couplings [260] to theory-level studies showing that with polarised beams, all 28 real parameters of the most general possible Lagrangian for triple gauge interactions can be determined [261, 262, 263]. The results of the full simulation studies, which included only a subset of channels and observables, as will be discussed in section **??**, have been extrapolated to $\sqrt{s} = 250$ GeV in Sec. 2.3.3.2 of [264], with rather conservative assumptions on the change of the impact of detector effects with center-of-mass energy. This extrapolation yields precisions between 8 and 10×10^{-4}. Notably it also shows that the correlations between g_1^Z and κ_Z in e^+e^- collisions depends on the center-of-mass energy and the beam polarisations, and can even change sign. Thus runs with different energies and polarisations can eliminate any blind direction.

Finally, the expected impact of including all channels and using an unbinned log-likelihood fit to all observables (instead of binned fit to a reduced set of observables) improves the projections for ILC250 to the level of $4 - 6 \times 10^{-4}$ — nearly a full order of magnitude better than the previously discussed HL-LHC expectations, even when fixing Z-fermion couplings for the HL-LHC. A comparison with the higher energy stages of the ILC is shown in Fig 10.6.

However the TGC story does not end with an isolated look into W^+W^- production. Triple gauge vertices also occur in single-W production $e^+e^- \to e^\pm W^\mp \nu_e(\bar{\nu}_e)$. Also, both single and pair production of W bosons serve as standard candles to gauge the luminosity-weighted and long-term averaged beam polarisation values, raising the question whether effects of anomalous couplings and beam polarisation can be reliably disentangled, and whether beam polarisations introduce an additional uncertainty. Furthermore, there is the question of possible impact from the other involved vertices, namely the $e-\nu-W$ vertex in all t-channel contributions and the $e-e-Z$ vertex in s-channel WW and t-channel single-W production. In order to address these questions, a fit to a variety of binned generator-level $e^+e^- \to f\bar{f}$, $e^+e^- \to W^+W^-$ and single-W distributions has been pioneered in [264] and further developed in [265, 266, 267]. The results of a fit to differential

(a) (b)

Figure 8.7: (a) Expected precisions at $\sqrt{s} = 250$ GeV on charged TGCs for different assumptions on the beam polarisations and the integrated luminosity. Note that these appear more pessimistic than in Fig. 10.6 since here only the $\mu\nu qq$ channel is used in a binned three-angle analysis (b) Effect of floating the left-right asymmetry for WW production. Since the simultaneous the effect on the polarisation uncertainty, i.e. on the t-channel contribution is negligible (c.f. Fig. **??**), the large loss in TGC precision can be attributed to the left-right asymmetry of the the $Z - e - e$ coupling, underlining a) the importance a precise knowledge of this quantity — not only on the Z pole, but also its effective value at a 250 GeV — and b) the increased robustness due to beam polarisation, which reduces the dependency on the left-right asymmetry considerably. Both from [266, 267].

distributions from $e^+e^- \to \mu^+\mu^-$ and $e^+e^- \to \mu\nu qq$, which treats not only the three triple gauge couplings, but also (unpolarised) total cross-sections, left-right asymmetries, the angular acceptance and the beam polarisations as free parameters, is displayed in Fig **??** for various assumptions on the integrated luminosity and beam polarisations at an e^+e^- collider with $\sqrt{s} = 250$ GeV. For the ILC-like configuration (orange bars), the triple gauge couplings are determined at the level of 10 to 15 $\times 10^{-4}$ in this much more general fit from the muon final state only, corresponding to 7 to 11 $\times 10^{-4}$ when including $WW \to e\nu qq$. Within the uncertainty of the extrapolation and the different number of observables and free parameters, this compares very well with the 8 to 10×10^{-4} from the extrapolation of the full simulation analysis and shows that the ILC measurements will be extremely robust against consideration of additional free parameters.

The beam polarisation thereby plays an important role. Since the effect of anomalous TGCs on the differential cross-sections differs between $e^-_L e^+_R$ and $e^-_R e^+_L$, the ability to take data in different polarisation configurations adds qualitatively new information. This leads to increased uncertainties by 40%, 30% and 20% for g_1^Z, κ_γ and λ_γ, respectively, in the absence of beam polarisation. Thus, the additional information provided by the polarised beams is equivalent to a factor 1.5 to 2 more luminosity. However there is a second important aspect, concerning the robustness against finite knowledge of other SM parameters, e.g. the dependence on the left-right asymmetry of the $Z-e-e$ coupling discussed above. When the left-right asymmetry is set free in the fit, the uncertainties on g_1^Z and κ_γ for the unpolarised case are a factor of two larger than in the polarised case, which shows that the additional information from the polarisation reduces the dependency on residual parametric and theoretical uncertainties on the effective left-right asymmetry in WW production at 250 GeV.

8.4 Precision QCD

[corresponding editor: Ian Moult (ian.moult@yale.edu)]

The theory of Quantum Chromodynamics is one of the central elements of the Standard Model, and plays a dominant role in understanding a wide range of collider experiments. Due to their QCD

neutral initial state, e^+e^- colliders are the simplest setting in which to study the dynamics of energy flow in QCD, enabling precision measurements well beyond what is possible in hadron colliders. While e^+e^- colliders such as the ILC allow the precision measurement of QCD parameters, such as α_s, their legacy is much larger due to the notions of factorization and universality, which allow detailed measurements of QCD final states to be applied in the search for new physics in hadronic colliders.

To emphasize the immense impact that the ILC would have on studies of QCD, it is worth recalling the impact that LEP has had, as well as emphasizing some of its shortcomings that the ILC would be able to fill. While a wide variety of event shapes were measured at LEP, since LEP ran at the Z-pole, these were primarily dijet event shapes measured on quark jets. This data has had a profound impact on the study of jets at the LHC in the fact that quark jets are extremely well modelled in parton shower Monte Carlo programs, since their non-perturbative effects can be tuned against this rich dataset. On the other hand, gluon jets, which were not produced that often at LEP, but are copiously produced at the LHC, are poorly modeled. The precision measurement of event shapes have also enabled precision extractions of the strong coupling constant, α_s.

In the time since LEP there has been massive theoretical progress, driven by a renewed interest in studying the dynamics of jets in jet substructure at the LHC. The high energies and remarkable angular resolution of the LHC have enabled the detailed structure of energy within jets to be measured, requiring new calculational techniques to be developed. This was originally driven by the fact that the energy pattern within jets can be used to distinguish jets initiated by a light quark or gluon from jets initiated by an electroweak scale boson. The techniques developed with this initial motivation in mind have enabled a variety of new ways of understanding the dynamics of QCD with increasing sophistication. This includes both qualitative advances in the design of observables for probing specific features of QCD, as well as advances in theoretical techniques for event shape calculations. It is therefore worth asking what one could do with a fresh slate if one had a new e^+e^- machine for understanding QCD. This section provides a brief overview of some such possibilities, as well as more detailed references for the interested reader, emphasizing that the higher energies and better resolution calorimeters of the ILC would be transformative for QCD.

Energy Flow Observables in QCD

Measurements of the flow of radiation in collider events provide one of the most interesting tests of our understanding of QCD. High energy collisions are particularly interesting, since they provide a probe of the dynamics of QCD from asymptotically free quarks and gluons, through the confining phase transition to free hadrons at asymptotic infinity. Energy flow in colliders can be studied either using event shapes, which can be thought of as resolution variables about an underlying S-matrix element of quarks and gluons, or using correlation functions, which measure statistical properties of the radiation. Both approaches have seen significant progress driven by jet substructure at the LHC, giving rise to many interesting new observables that could be measured at the ILC, providing a significantly extended understanding of energy flow in quantum field theory.

New Event Shape Observables

Event shape observables, which constrain radiation about a particular S-matrix element are particularly useful at the LHC for identifying boosted electroweak scale bosons decaying into jets. There has therefore been significant progress in their understanding, and many new observables have been proposed. In particular, one of the most important outputs of the jet substructure program is the ability to design event shape observables with specific properties. Such observables were simply not available in the LEP era, and would therefore be extremely interesting to measure at the ILC.

While there are endless examples of such observables, here we content ourself with describing one particular class of observables, namely "groomed" observables. One of the insights of the jet substructure program has been the introduction of grooming algorithms that systematically remove low energy soft radiation. Such low energy soft radiation generically contributes the leading hadronization corrections, and therefore grooming can significantly reduce non-perturbative effects. For a generic infrared and collinear safe observable, one can then measure its "groomed" counterpart, which will also be IRC safe. Although these observables are theoretically cumbersome, due to the fact that they reduce non-perturbative corrections they can be practically useful, for example for measurements of α_s.

These "groomed" observables have received significant theoretical attention due to their use in jet substructure. However, since they were introduced post-LEP, they have not been measured in an e^+e^- environment. An example of a theoretical prediction for a groomed observable is shown in Fig. 8.8. Measurements of these observables are useful for fundamental studies of QCD, and also would provide insights into their behavior at the LHC, but in a simpler context.

Characterizing QCD with Correlation Functions

Since the LEP era there has been a significant improvement in our understanding of energy flow in collider experiments, driven quite interestingly, by purely formal developments. While the observables in the previous section were so called "jet shape" observables, if the goal is to understand the structure of the underlying theory, one may be curious why one does not proceed in the standard manner taken for other physical systems, namely measuring correlation functions. Unlike for condensed matter systems where one typically characterizes systems by correlation functions of local operators, building up from low point correlators, in collider experiments one cannot measure correlation functions of local operators. However, instead, one can measure certain non-local lightray operators called energy flow operators, defined as integrals of the stress tensor along null infinity in a direction characterized by a unit vector $\vec{n}$

$$\mathcal{E}(\vec{n}) = \lim_{r\to\infty} \int_0^\infty dt\; r^2 n^i T_{0i}(t, r\vec{n})\,. \tag{8.1}$$

One can then characterize the system by measuring correlation functions of $\langle \mathcal{E}(\vec{n}_1)\mathcal{E}(\vec{n}_2)\cdots\mathcal{E}(\vec{n}_k)\rangle$ of these operators. These objects are particularly simple theoretically, since they exhibit symmetry properties similar to standard correlation functions of local operators, and are also governed by

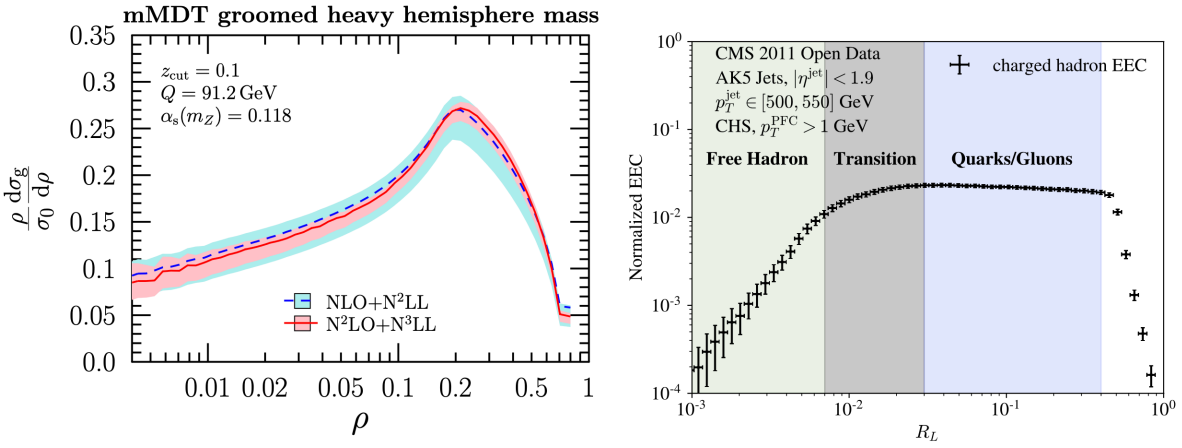

Figure 8.8: (a) The groomed mass observable in e^+e^- (b) A precision measurement of the two-point correlator in the collinear limit at the LHC. Both of these new observables provide interesting probes of α_s

an operator product expansion. This enables one to discuss jet phenomenon in the language of correlation functions. Furthermore, they exhibit simple structures in perturbation theory. One can show that jet shape observables are infinite sums over these correlation functions, and hence they lose many of these desirable theoretical properties.

Although the two-point correlator was measured at LEP, it was not studied in detail in the OPE limit to look for scaling behavior, and higher point correlators, which probe more interesting features of the theory, such as spin correlations, were never measured. A measurement of the two-point correlator using Open Data from the CMS experiment is shown in Fig. 8.8, illustrating beautiful scaling behavior of weakly coupled quarks and gluons, and a transition to the scaling of free hadrons. Measurements of this quality in the ILC environment would provide remarkable insights into the dynamics of QCD jets, and the hadronization transition.

The ILC would provide a beautiful environment where one can rethink how jets are studied and measure in detail the structure of multi-point correlators in QCD. These are of significant interest for understanding QCD, but also provide insight into the behavior of perturbative nearly conformal theories more general, and have been the focus of much recent interest of the theoretical community. Precision measurements of these correlators would build a bridge between the QCD phenomenology and formal theory communities which would result in significant progress.

Precision Extractions of α_s with Old and New Observables

One of the key parameters of interest in QCD is the value of the strong coupling constant, α_s. Since this is an arbitrary parameter of the theory, it can only be obtained by comparison precision theoretical predictions with experimental measurements. While there are many different possible observables that can be used to constrain the value of α_s, measurements of the distribution of

energy in e^+e^- have proven to be competitive. However, there is currently an unresolved tension between extractions of α_s from event shape extractions at LEP as compared with lattice based extractions. Resolving this tension is important to illustrate a consistent understanding of QCD at the percent level.

The most precise extractions of α_s from event shapes are based on thrust and the C-parameter, which are closely related double logarithmic observables. To understand any possible issues in these extractions, it is crucial to have measurements based on other observables. Two observables that can be computed to high accuracy that exhibit significant differences from thrust/ C-parameter are the groomed thrust event shape, and the energy-energy correlators.

One of the complexities in extractions of α_s from event shapes is that one has to incorporate non-perturbative power corrections. These power corrections cannot be computed from first principles, and therefore must be simultaneously fit for along with the value of α_s. One approach to reducing this potential uncertainty is to use grooming algorithms, inspired by the study of jet substructure at the LHC, to reduce non-perturbative corrections from low energy soft radiation. This makes the groomed thrust a potentially appealing observable for extractions of α_s. Much like the thrust observable, its resummation is governed by the cusp and collinear anomalous dimensions, but grooming reduces it to a single logarithmic observable, and reduces the non-perturbative corrections. Due to this differing theoretical structure, an extraction of α_s from the groomed thrust would provide a relatively independent measurement of the value of α_s. The groomed thrust can be computed to high perturbative accuracy, using a factorization formula. This is shown in Fig. 8.8. Furthermore, non-perturbative corrections to the groomed thrust distribution have been studied in [].

While the groomed thrust provides many complementary features to the standard thrust based extraction of α_s, it is ultimately based on the same event shape paradigm, and therefore similar assumptions enter in the treatment of non-perturbative effects. Another interesting complementary measurement would be to perform a measurement of the two-point energy correlator in the collinear limit. The collinear limit is described by completely different physics (fixed spin DGLAP) than the Sudakov region, and furthermore, since the energy correlators are not event shape observables, they have a different structure for their non-perturbative effects. However, despite being an old observable that was measured at LEP, extractions of α_s from the collinear limit were never performed at LEP. We believe that this is partially due to the angular resolution of the calorimeters. Comparing the measurement of the two-point correlator at LEP vs. using the modern calorimetry of the LHC shows a completely different understanding of the collinear limit. Achieving a similarly precise measurement in the clean e^+e^- environment of the ILC would be extremely valuable for precision measurements of α_s, and would hopefully resolve the longstanding tensions in its extracted values.

Gluons from the Higgs

As compared with LEP, a particular advantage of the ILC for the study of QCD is pure samples of gluon jets through the interaction $e^+e^- \to ZH \to l^+l^-gg$. This would be a unique feature of the ILC, since this is not possible at LEP, and at the LHC, one of the primary issues in understanding precision jet substructure is the difficulty in disentangling quark and gluon jets. As such the study

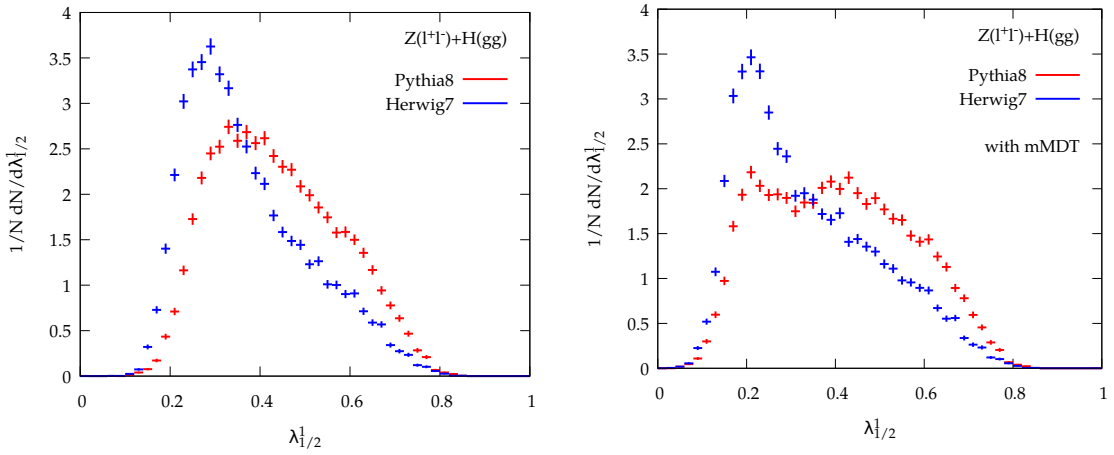

Figure 8.9: Generalized angularities (a), and groomed angularities (b) measured on gluon jets with different event generators. Large discrepancies are observed due to a lack of tuning data.

of properties of gluon jets in QCD is extremely poor, and this is reflected in large discrepancies in different parton shower simulations, see Fig. 8.9. This lack of understanding of gluon jets, and in particular their non-perturbative properties, is a major issue and a leading uncertainty in many new physics searches at the LHC. One of the promises of jet substructure is that it offers the potential of discriminating quark vs. gluon jets to identify new physics signals. However, this requires a detailed understanding of both quark and gluon jets. Currently, quark vs. gluon tagging has not fulfilled its promise due to large uncertainties in the modelling of gluon jets. Having pure samples of gluon jets in QCD would significantly change this situation and have a major impact on the LHC physics program.

Although the understanding of gluon jets is quite poor, there in fact exist a wide range of precision perturbative calculations of event shapes on $H \to gg$, which have never been compared to data. Two examples, the thrust event shape and the energy-energy correlator, are shown in Fig. 8.10. These predictions have never been compared with data. Since the perturbative features of gluon jets are well understood, and already available to high accuracies, comparison with data would enable detailed studies of the non-perturbative structure of gluon jets.

QCD for the Higgs

Although the primary focus of this section is on the use of ILC for learning about QCD, due to its close relation to the other topics in this section, it is also interesting to briefly mention how newly developed jet substructure tools, in particular quark vs. gluon tagging just discussed, can be used to provide new handles on the Higgs boson at the ILC. One of the interesting questions about the Higgs boson that is difficult to study directly at the LHC are its couplings to light (u,d,s) quarks. While these couplings can be probed at the LHC by precise measurements of the p_T spectrum of the Higgs, potentially enabling measurements at the level of $y_s \leq 0.5 y_b$, this requires a precise

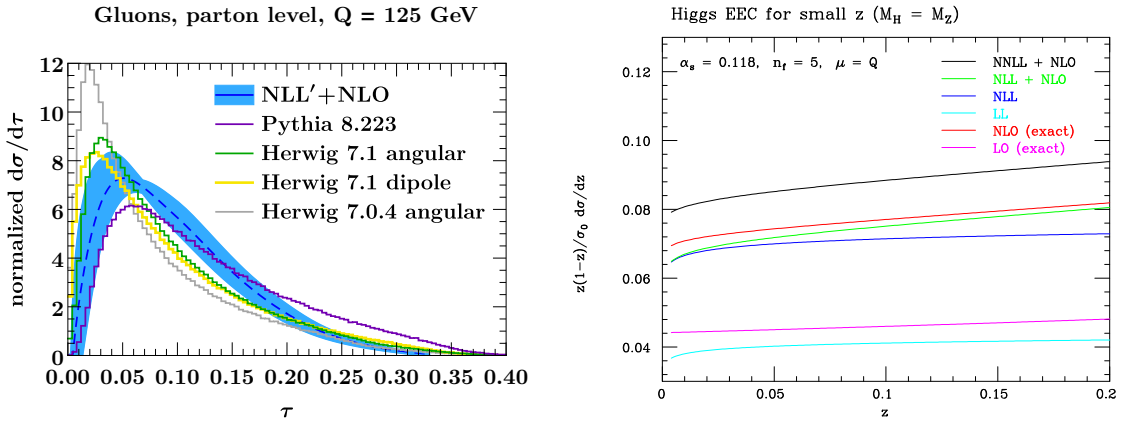

Figure 8.10: Precision perturbative calculations in $H \to gg$. In (a) we show a double logarithmic Sudakov event shape observable, and in (b) and single logarithmic collinear observable.

understanding of the gluon/quark luminosities.

At the ILC, precision measurements of event shapes on Higgs decays can provide much more precise handles on the light quark Yukawas due to the differing radiation patterns of quark and gluons. In particular, [] was able to achieve $y_{u,d,s} \leq 0.091 y_b$ and 95% confidence. This was using a fairly conservative approach of a single event shape, thrust. This is shown in Fig. 8.11. Almost certainly with more sophisticated event shapes, this bound could be significantly improved, and would provide an interesting example of the interplay between precision QCD measurements and the Higgs program at the ILC.

New Non-Perturbative Inputs

Another important part of the legacy of LEP is the measurement of universal non-perturbative functions of QCD. Although there are currently no methods for first principles calculations of non-perturbative Lorentzian observables in QCD, much of the predictivity of QCD comes from factorization theorems which express cross sections in terms of universal non-perturbative functions. Famous examples measured at LEP include fragmentation functions. These can then be used in other colliders, such as at the LHC, and have had a large impact on the collider physics program. While it is clear that measurements at the ILC would improve our understanding of fragmentation functions, since these functions have been discussed extensively in the literature, here we focus on universal non-perturbative inputs that were not defined at the time of LEP, which could be measured precisely at ILC, and would have a significant impact on the LHC physics program.

Measurements at the LHC rely strongly on the use of tracking information. This is both due to the fact that it suppresses pile-up, which will become increasingly important in the high-luminosity era, and because it enables the remarkable angular precision of the tracker to be used, which is particularly important for many jet substructure measurements. However, only observables that are completely inclusive over the spectrum of final states can be computed purely from perturba-

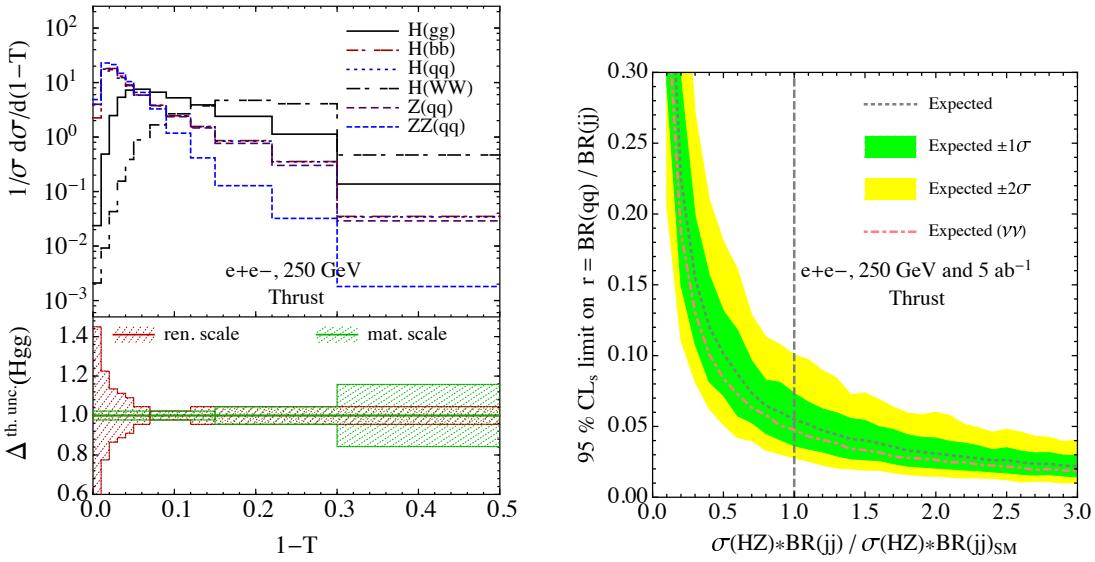

Figure 8.11: Precision measurements of event shapes on Higgs decays used to bound the light quark Yukawas.

tion theory, and therefore the calculation of track based observables (which distinguish final state particles based on their charge) requires some non-perturbative input. However, the situation is not hopeless, since this non-perturbative information is universal, and is described by so called "track functions", which describe the fraction of energy carried by charged particles from from a fragmenting quark or gluon. These can be viewed as generalizations of fragmentation functions, since they encode correlations in the final state hadrons due to the fact that a single fragmenting quark or gluon can decay into multiple charged hadrons.

Recently it has been shown how to compute jet substructure observables at high precision incorporating track functions, which gives promise for precision jet substructure measurements at the LHC. However, despite this new found theoretical understanding, track functions have never been experimentally measured. Furthermore, such measurements in archived LEP data are difficult due to the lack of gluon jets.

The ILC would provide very clean sources of quark and gluon jets on which one could precisely measure the quark and gluon track functions. This would be synergistic with the high luminosity LHC physics program, and would be a particularly valuable contribution with many applications.

Boosted Top Quarks

If the ILC were to operate at an energy of 1 TeV, this would provide a particularly exciting scenario for a precision measurement of the top quark mass from hadronic event shapes. Being the heaviest particle of the SM, the top quark mass is an important parameter for electroweak vacuum stability,

and for precision electroweak fits. At e^+e^- colliders there are two different approaches to measure the top quark mass, one being a threshold scan, and the other being a measurement using an event shape observable measured on boosted decaying top quarks. This second approach allows in addition for a calibration of the top quark mass as implemented in parton shower Monte Carlo programs, which are used in all current top quark mass measurements at the LHC. Furthermore, it would provide significant insight into the dynamics of top quark jets, which would also be applicable in the LHC environment, improving our understanding of measurements of the top quark mass at the LHC.

Here we highlight two distinct approaches to measuring the top quark mass using boosted top quark jets in e^+e^-. The first is a measurement using the two-jettiness observable, and the second is a measurement using the three-point energy correlator.

The most well established program to measure the top quark mass using event shapes in e^+e^- is to use the two-jettiness (thrust) observable. In the limit of boosted top quarks, the two-jettiness observable effectively measures the sum of the masses of the two jets arising from the decay products of the boosted top quarks. It thus exhibits strong sensitivity to the value of the top quark mass. Since it is an inclusive event shape observable, one can derive a rigorous factorization theorem for the observed distribution using a combination of SCET and HQET, which factorizes the dynamics at different scales, allowing in particular for a rigorous field theoretic treatment of the top quark mass in a short distance scheme. This distribution has been computed at next-to-next-to-next-to leading logarithmic accuracy, and suggests that perturbative uncertainties at the order of 100 MeV can be achieved for the top quark mass. A plot of the distribution is shown in Fig. 8.12.

More recently, an alternative approach to measuring the top quark mass was put forward, particularly motivated by developing a clean understanding in the complex LHC environment. One of the issues with measurements based on the jet mass is that the mass is sensitive to soft contamination and non-perturbative effects. Instead of measuring the mass directly, one can flip the measurement of the mass into a measurement of the angular scale of the top decay products as measured by a three-point correlation function. Unlike the behavior in a conformal theory, these correlators will exhibit a sharp peaked structure at the angular scale $\zeta \sim m_t^2/Q^2$. The location of the peak therefore provides direct sensitivity to the top quark mass. However, unlike the jet mass, the location of the peak is unaffected by soft contamination and hadronization. This is seen in Fig. 8.13. Furthermore, this measurement is quite interesting in general, since it probes the structure of multipoint correlators on top decays.

Precision measurements of the top quark mass using energy flow observables in e^+e^- are therefore particularly interesting both because they provide competitive measurements of this important SM parameter, and because they generalize to the more complicated case of hadron colliders.

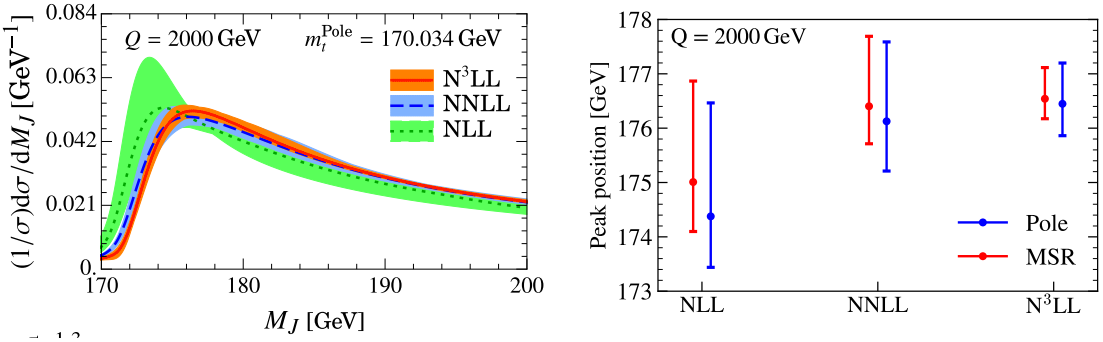

Figure 8.12: (a) The jet mass distribution on boosted top quark jets. (b) The peak position extracted using Pole mass or MSR mass schemes.

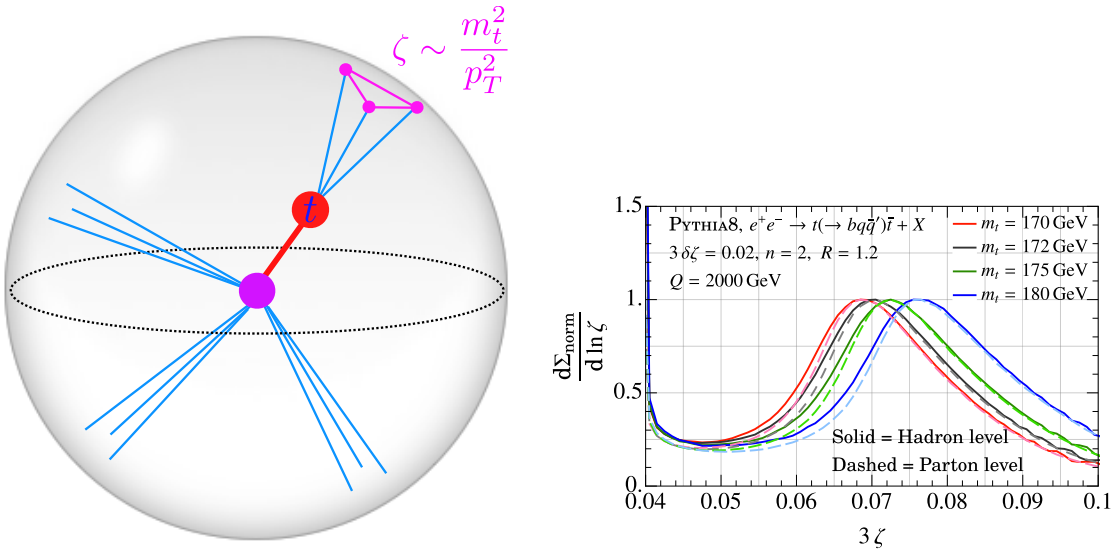

Figure 8.13: (a) The angular scale of the top quark as probed by a three point correlation function. (b) The angular distribution for different top masses. Hadronization has an extremely minor impact on the peak position, leading to a clean probe of the top quark mass with perturbative physics.

Chapter 9

ILC Precision Electroweak Measurements

[5 pages; corresponding editors: Graham Wilson (gwwilson@ku.edu), Roman Pöschl (poeschl@lal.in2p3.fr)]

9.1 Introduction

The ILC facility with thousand-fold larger accumulated data-sets than prior e^+e^- experiments, polarized beams, and the potential to take data at a wide range of center-of-mass energies will provide the opportunity to advance greatly knowledge of the precision electroweak (PEW) sector. The measurement precision will far exceed the precision achieved in the legacy measurements from LEP/SLC near the Z-pole [268] and from LEP at higher center-of-mass-energies up to 208 GeV [253]. The underlying assets are much higher statistics, really precise modern detectors with much improved reconstruction of particle and jet momenta, polarized beams, and improved theoretical modeling.

An important aspect for fully exploiting the potential is adequate control of systematic uncertainties. This includes aspects such as detector calibration and alignment, control of reconstruction efficiencies and geometrical acceptance, determination of the center-of-mass energy, differential luminosity, integrated luminosity, and the polarization of the beams. These need to be maintained over years of accelerator operation and are a critical pre-requisite for extracting the most physics out of potential dedicated physics runs at special center-of-mass energies such as the WW threshold and especially at the Z-pole. Such running is already feasible with the initial 250 GeV ILC accelerator described in Chapter 4 as discussed in [269].

It is obviously not feasible to run the ILC in the single configuration best adapted to measuring each individual PEW observable with the highest precision while still delivering on aspects such as the Higgs, top, and Higgs self-coupling programs. The various ILC data-taking configurations will impact the knowledge gained for each PEW observable in different ways. Having several measurement methods for the same observable with complementary systematic uncertainties should lead to improved knowledge. An important goal for the next years is to further explore these

possibilities to better understand their relative merit and inform accelerator and detector design work.

Examples of the configurations under consideration are:

- Running synergistic with the core physics program. A good example is a LEP2-style measurement of the W mass that is well suited to exploiting data collected at the center-of-mass energy of 250 GeV.

- Complementary methods enabled by high energy running such as measurement of Z properties using radiative return events.

- A dedicated physics run using a polarized scan near the Z-pole accumulating a data sample of $100\,\mathrm{fb}^{-1}$ and up to 4 BZs.

- Short few day pilot runs near the Z-pole accumulating at least 10M hadronic Zs at a time for detector calibration and alignment, and for physics; each such sample would be roughly comparable to the whole LEP-1 program, and would permit calibration of the tracker momentum-scale to a statistical uncertainty of 2.5 ppm.

- A dedicated physics run with a polarized scan near the WW threshold.

After describing some of the measurement techniques and prospects, we will revisit these issues more quantitatively. For now let us summarize our current thinking:

1. An accelerator built for running above ZH threshold should be exploited as much as possible using Higgs production compatible data. So a clear case needs to be made for the added benefit of dedicated extensive runs at lower energies.

2. The opportunities to make large improvements in the Z observables with a dedicated scan are obvious and warrant dedicated exploitation once the accelerator has been upgraded. In order to evaluate better the eventual reach and required running time, the Z pilot runs should be used early in the ILC program to gain valuable experience. They will also serve as a rich physics sample, a valuable resource for calibration and alignment for the higher energy running, and a high statistics benchmark for the tuning of hadronization models.

3. The W mass can already be measured rather well with the standard ILC program likely obviating the need for substantial time investment in a dedicated run near threshold. Nevertheless, the potential for such a dedicated run with as high as possible beam polarizations should be retained given the perceived uniqueness of the threshold-based observable.

9.2 Radiative Return to the Z

9.3 Measurement of Di-fermion cross sections

In general electroweak di-fermion production in the process $e^+e^- \to f\overline{f}$, with $f \neq e$, i.e s-channel production in the following, is driven by the coupling $Q_\gamma^{e,f}$ of the initial and final state particles to the photons and the by the couplings $Q_{L,Z}^{e,f}$, $Q_{R,Z}^{e,f}$ of fermions with left-handed and right-handed helicity to the Z boson and a potential Z' Boson of new physics. In a general form the couplings can be expressed as.

$$Q_{e_i f_j} = Q_e^\gamma Q_f^\gamma + \frac{g_{e_i}^Z g_{f_j}^Z}{\sin^2\theta_W \cos^2\theta_W} \frac{s}{s - M_Z^2 + i\Gamma_Z M_Z} + \sum \frac{g_{e_i}^{Z'} g_{f_j}^{Z'}}{\sin^2\theta_W \cos^2\theta_W} \frac{s}{s - M_{Z'}^2 + i\Gamma_{Z'} M_{Z'}} \tag{9.1}$$

with $i, j = L, R$, $Q_{e,f}^\gamma$ the electromagnetic charges and θ_W being the weak mixing angle at Born level. The first part of the equation describes the electromagnetic couplings to the photon. The second part describes the couplings of the fermions to the Z boson. This second term may be affected by $Z - Z'$ mixing as for example suggested in [270]. The third term takes into account couplings to new vector bosons of e.g. type Z' as for example heavy Kaluza-Klein recurrences included in Randall Sundrum Models with warped extra dimensions. The relative importance of the contributions is determined by the Breit-Wigner functions.

In a general form the differential cross section of the process $e^+e^- \to f\overline{f}$ for relativistic polarised electron, with polarisation $\mathcal{P}_{e^-}$ and positron beams, with polarisation $\mathcal{P}_{e^+}$, can be written as [268, 271, 272].

$$\begin{aligned}\frac{d\sigma}{d\cos\theta} =& \frac{3}{4}(1 + |\mathcal{P}_{e^-}||\mathcal{P}_{e^+}|)(1 - \mathcal{P}_{\text{eff}} A_{LR}) \left(\frac{1}{2}\sigma_{0,HC}(1 + \cos^2\theta) + (\sigma_{0,HV}/\gamma_f)\sin^2\theta\right) \\ &+ [\sigma_0(1 + |\mathcal{P}_{e^-}||\mathcal{P}_{e^+}|)((A_{FB})_0 - \mathcal{P}_{\text{eff}} A_{LRFB})]\cos\theta\end{aligned} \tag{9.2}$$

with $\cos\theta$ or $\sin\theta$ being the cosine and sine of the polar angle of the final state fermions, $\mathcal{P}_{\text{eff}} = (\mathcal{P}_{e^-} - \mathcal{P}_{e^+})/(1 + |\mathcal{P}_{e^-}||\mathcal{P}_{e^+}|)$ being the effective polarisation and γ_f being the boost of the final state fermions.

The differential cross section contains four linearly independent quantities.

- The total unpolarised cross section σ_0 split into a helicity-conserving, $\sigma_{0,HC}$, and a helicity-violating part $\sigma_{0,HV}$. In the Standard Model the helicity violating part vanishes at relativistic energies of the final state fermion. In practice the actual cross-section for a given fermion is often normalised to the total hadronic cross section σ_{had} yielding $R_q = \sigma_q/\sigma_{had}$ and $1/R_\ell = \sigma_\ell/\sigma_{had}$ in case of final state quarks and leptons, respectively;
- The unpolarised forward backward asymmetry $(A_{FB})_0$;
- The left-right asymmetry A_{LR};

- The left-right-forward-backward asymmetry A_{LRFB}.

The quantities depend on the combinations $Q_{e_i f_j}$ defined in Eq. 9.1. These or similar quantities derived from Eq. 9.2 can be used to determine independently four different individual couplings or the four combinations. In all observables the couplings to the Z enter linearly for centre-of-mass energies away from the Z-Pole due to the γ/Z interference, which allows for determining the actual sign of the couplings. The two asymmetries A_{LR} and A_{LRFB} are only available with polarised beams. In the Standard Model these are of the form $(g^Z_{e_L} - g^Z_{e_R}) \times A(Q^\gamma_e,\, Q^\gamma_f, g^Z_{e_{L,R}},\, g^Z_{f_{L,R}})$ in case of A_{LR} and $\beta_f(g^Z_{f_L} - g^Z_{f_R}) \times A'(Q^\gamma_e,\, Q^\gamma_f,\, g^Z_{f_{L,R}},\, g^Z_{e_{L,R}})$, with $\beta_f = \sqrt{(\gamma_f^2 - 1)/\gamma_f^2}$, in case of A_{LRFB}. In addition $(A_{FB})_0$ is of the form $\beta_f(g^Z_{f_L} - g^Z_{f_R})(g^Z_{e_L} - g^Z_{e_R})\hat{A}(Q^\gamma_e,\, Q^\gamma_f,\, g^Z_{f_{L,R}},\, g^Z_{e_{L,R}})$. All asymmetries thus vanish close to the production threshold of the fermions yielding reduced sensitivity to the weak part of the interaction. On the Z-Pole (A_{LR}) depends only on the couplings of the electrons while A_{LRFB} depends only of the final state fermion (A_{LRFB}) to the Z. On the Z-Pole this separation allows for a model independent determination of the initial and final state couplings or, equivalently, of the weak mixing angle. The argumentation before relies heavily on the availability of initial state beam polarisation. In principle the electroweak couplings can also be extracted by analysing the final state polarisation. This is readily possible for τ leptons and t quarks for which the polarisation can be derived from the decay particles. At the ILC the analysis of the final state polarisation could be useful as an independent cross-check.

9.3.1 Strategy

The ILC program will comprise a running on the Z-Pole (GigaZ). Supposing that the couplings to the photon are fixed by QED, this program can be used to fix the couplings to the Z boson eventually discovering the presence of a Z' that mixes with the Z. The figure 9.1 shows the precision that can be expected for key quantities at the ILC at the Z-pole.

This translates into precision on the couplings at the Z pole.

In recent years the community has carried detailed studies of the processes $e^+e^- \to b\bar{b}$ and $e^+e^- \to c\bar{c}$ at $\sqrt{s} = 250\,\text{GeV}$. The polar angle distribution for $e^+e^- \to b\bar{b}$ is given in Fig. 9.2 [273]. It illustrates very clearly that the two combinations of beam polarisation yield different sensitivities for the underlying electroweak couplings.

The result makes use of the correct determination of the charge of the final state quark and is therefore an important benchmark for detector optimisation in terms of measuring secondary vertices and particle ID. A careful analysis of systematic errors has been carried out that includes systematic errors on the hadronic 2-jet cross section as the normalisation in R_q, the beam polarisation and the influence of initial state radiation. The latter implies the detection of the ISR photon among the two jet final state, which advocates the availability of highly granular calorimeters that allow for efficient particle separation. Overall the statistical and systematic errors on key are of the order of 1-3 per mil. This precision would yield high sensitivity to new physics as for example proposed in Grand Higgs Unification models, see Fig. 9.3.

As is pointed out in Ref. [276] it is important to measure di-fermion production for all fermions

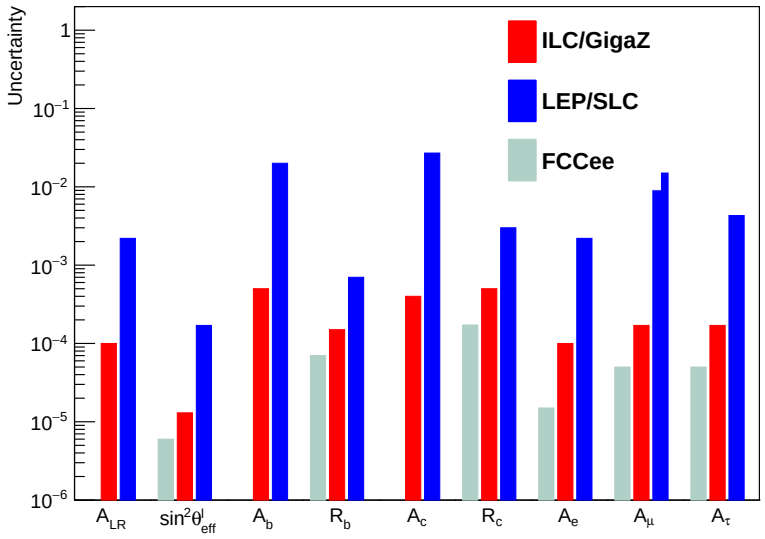

Figure 9.1: *Summary of the precision achievable for ILC Z-Pole running compared with LEP/SLC results [268] and FCCee projections [?] for observables and derived quantities that are described in the text.*

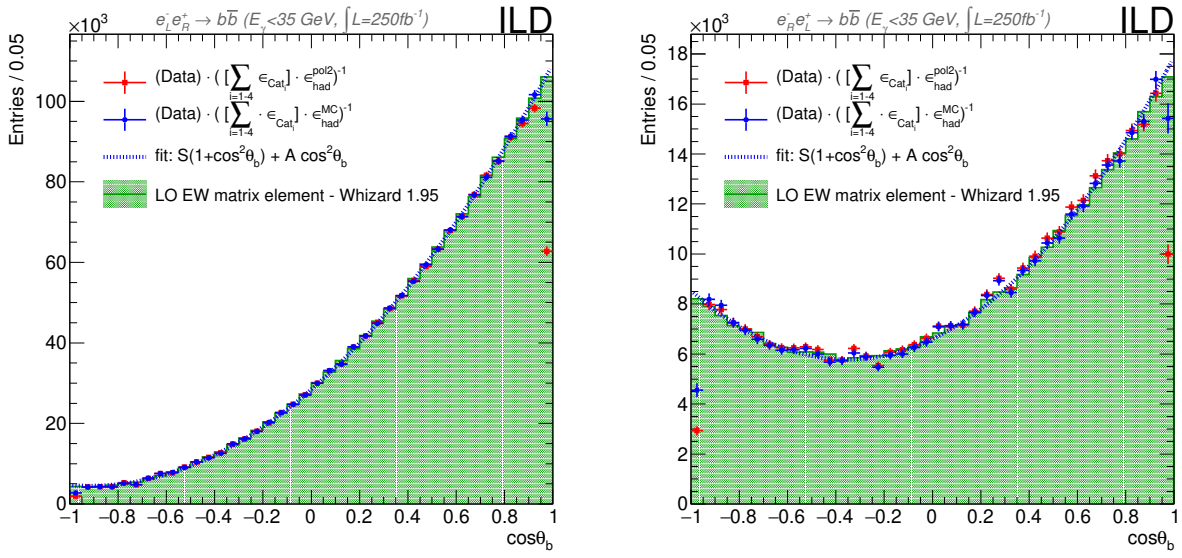

Figure 9.2: $\cos\theta_b$ distributions obtained for $e^-_L e^+_R$ (left) and $e^-_R e^+_L$ (right). The generator distribution is the green histogram and the red and blue dots show the reconstructed distributions after correction charge for charge migration and two different methods for the correction for efficiency and acceptance.

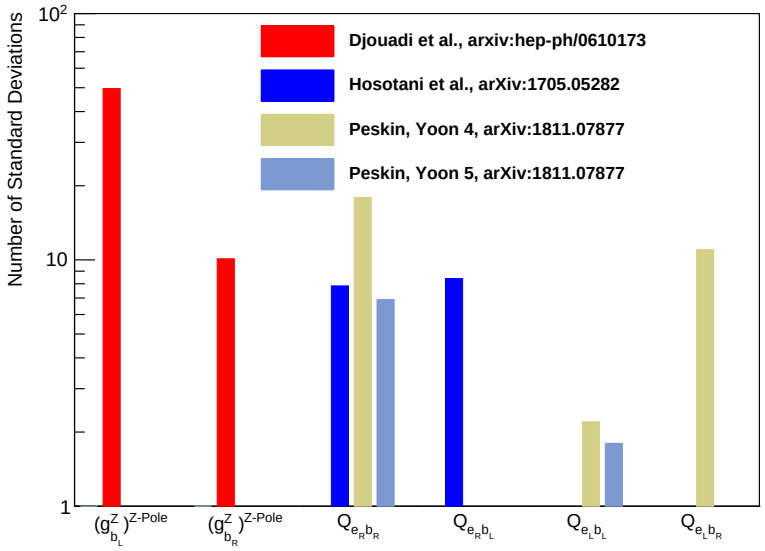

Figure 9.3: Visibility of deviations from the SM predictions in $g^Z_{b_j}$, $g^Z_{b_j}$ (to do: still missing in this plot) and the helicity amplitudes $Q_{e_i b_j}$, in standard deviations, from combined ILC250/Z-Pole running, expected from new physics models with Randall-Sundrum extra dimensions [270, 274, 275].

and different centre-of-mass energies since the effect of new Z' bosons will increase with increasing beam energy.

9.3.2 Outlook

The previous paragraphs focused on results obtained for the production of bottom of charm quark pairs. These studies will be complemented during the Snowmass process by a study of the process $e^+e^- \to s\bar{s}$. The set of results for bottom, charm and strange-quark pair production may then allow for estimating also the precision on the measurement of electroweak for the lightest quarks u, d. For a complete picture of di-fermion production the precision on electroweak couplings for final state leptons will have to evaluated. For this, studies presented in [277] will have to be carried out in more detail or existing results would have to be extended [278]. The precision expected for the Z-Pole running are based on extrapolations from full simulation studies at a centre of mass energy of 250 GeV. Given the high precision it will be very important to carry out the studies for Z pole running with full simulation.

9.4 W and Z Boson Masses

9.5 W Boson Branching Fractions

Chapter 10

ILC Physics Measurements at 350, 500, and 1000 GeV

[15 pages; general corresponding editors: Daniel Jeans (daniel.jeans@kek.jp), Jenny List (jenny.list@desy.de), Michael Peskin (mpeskin@slac.stanford.edu)]

10.1 Top Quark

[corresponding editors: Roman Pöschl (poeschl@lal.in2p3.fr), Frank Simon (fsimon@mpp.mpg.de), Marcel Vos (vos@ific.uv.es)]

10.1.1 Top Quark Mass

The top quark mass is one of the fundamental parameters of the Standard Model that must be determined experimentally. Direct measurements at hadron colliders based on Monte Carlo template fits to the reconstructed top quark decay products reach a precision down to 600 MeV at the LHC [279, 280] and the Tevatron [281]. Combinations can further improve [282, 280]. Extractions of the top quark pole mass from measured cross sections using first-principle, fixed-order calculations have reached GeV precision [283, **?**].

Top quark mass measurements at the HL-LHC [284] are expected to reach an experimental precision of a few hundred MeV [259], while work is ongoing to improve Monte Carlo generators [285, 286] and to provide a robust interpretation of the Monte Carlo mass parameter in a field-theoretical mass scheme [287, 288, 289]. A complete and recent review can be found in Ref. [290].

An electron-positron collider with sufficient energy to produce top quark pairs has excellent potential to measure the top quark mass with even better precision and a rigorous interpretation. It was realized even before the discovery of the top quark that a scan of the center-of-mass energy of the collider through the top quark pair production threshold yields a very precise top quark mass

measurement [291, 292, 293, 294], with a rigorous interpretation. Since then, the theory predictions for the threshold scan have reached NNNLO precision [295] and an NNLL resummation [296] has been performed. The threshold mass that is most naturally extracted from a comparison to the theory can be converted to the $\bar{M}S$ scheme (or any other scheme) at four-loop accuracy [297], with an intrinsic uncertainty due to missing higher orders of $\mathcal{O}(10$ MeV) and a parametric uncertainty of $\mathcal{O}(50$ MeV) with the currrent α_s world average [282].

Phenomenological studies of the threshold scan in realistic conditions have been performed by several groups [298, 299, 300, 301]. Fits are performed on pseudo-experiments with an integrated luminosity of 100-200 fb^{-1} divided over up to 10 center-of-mass energies. Apart from the top quark mass, the threshold scan is sensitive to the strong coupling, the top quark Yukawa coupling and the top quark width. Typically, several parameters are floated simultaneously in the fits[1]. Importantly, recent studies take into account the theory uncertainty [302, 303], that is expected to be the dominant source of uncertainty for a top quark mass measurement in a threshold scan at an e^+e^- collider. The statistical uncertainty can be reduced to approximately 20 MeV, depending on the number of free parameters and the number and range of the energy points [304]. The systematic uncertainty from missing higher orders in the prediction and the parametric uncertainty due to the strong coupling constant add up to approximately 50 MeV, with the current state-of-the-art calculations and world average for α_s.

While the threshold is generally considered to be the "golden" top quark mass determination, alternative methods have been studied by several groups. A direct mass measurement can be performed at any center-of-mass energy above the top quark pair production threshold and may provide important information on the interpretation of the MC mass parameter. A statistical uncertainty of 30 MeV (40 MeV) is expected in the l+jets (all-hadronic) channel after the CLIC run that collects 500 fb^{-1} at $\sqrt{s} = 380$ GeV [298].

A measurement of the differential cross section of radiative $e^+e^- \to t\bar{t}\gamma$ events, where the top quark pair is produced in association with a hard photon from Initial State Radiation (ISR) can yield a top quark mass determination [305]. The measurement of the photon energy gives an event-by-event determination of the effective center-of-mass energy and allows to map out the $t\bar{t}$ threshold with data collected at any center-of-mass energy below ~ 1 TeV. The expected precision is approximately 110 MeV for CLIC380 (1 ab^{-1} at $\sqrt{s} = 380$ GeV and approximately 150 MeV for ILC500 (4 ab^{-1} at $\sqrt{s} = 500$ GeV), including theoretical and experimental systematic uncertainties. This approach is competitive compared to HL-LHC expectation, and the method maintains flexibility in and control over the field-theoretical mass scheme. A combination with the mass obtained from the threshold scan moreover enables a study of the scale dependence ("running") of the top quark mass, testing the evolution predicted by the Renormalization Group Equation (RGE).

Operation of the ILC at the top mass threshold and beyond can hence provide a top quark mass with a precision well beyond what is achievable at hadron colliders and a rigorous interpretation in terms of a field-theoretical mass scheme.

[1] These studies are valid within the SM, releasing only the relation between the width and the mass. The interplay between the top-quark mass extraction and electroweak coupling uncertainties (parameterized in an effective field theory) has not been studied yet.

10.1.2 Top Quark Electroweak Couplings

In many extensions of the Standard Model, the top quark plays a special role. Composite Higgs models, for instance, generally predict sizeable deviations for the top quark electro-weak couplings [306]. Precise measurements of top electro-weak couplings can therefore constrain broad classes of composite Higgs scenarios [251].

As the top quark escaped scrutiny at the previous generation of electron-positron colliders, its interactions with the neutral gauge bosons of the Standard Model are relatively poorly constrained. Studies of top quark pair production at hadron colliders have characterized the strong interaction of the top quark in detail, and single top quark production and top quark decay are a sensitive probe of the charged-current interaction. The interactions with the photon and Z-boson have only become accessible with the observation of rare associated production processes, such as $pp \to t\bar{t}X$ and $pp \to tXq$, with $X = \gamma, Z$ (and H, of course; a discussion of the interaction of the top quark with the Higgs boson is left for **??**). Recent comparisons of cross section measurements to SM predictions have reached a precision of 10-15%, with statistical, experimental and theoretical uncertainties contributing with roughly equal weight [307]. Top quark EW operators can also be constrained through loop-level effects of off-shell degrees-of-freedom in the top quark pair production rate [308], which could provide complementary bounds of competitive precision for some Wilson coeffients.

The potential of LHC run 3 and the HL-LHC stage to improve these measurements has been studied in Ref. [259] for $t\bar{t}V$ production and EW single top production. A complete set of prospects is obtained by adopting the S2 scenario also used for the Higgs sector [309] that extrapolate run 2 results, by scaling the statistical and experimental sytematics uncertainties with the inverse square root of the luminosity, while assuming that the uncertainties in the theoretical SM predictions and uncertainties due to Monte Carlo modelling are reduced by a factor 2 with respect to today's state of the art (here, we use the results documented in Ref. [310], refining earlier results of Ref. [311]).

The ILC offers a unique opportunity to measure the electro-weak couplings of the top quark [312, 313], and these measurements are among the prime targets of the ILC top physics programme. The pair-production process in e^+e^- collisions probes the $t\bar{t}Z$ and $t\bar{t}\gamma$ vertices directly. The contributions from the photon and Z-boson are disentangled by using the two polarization configurations. The ILC prospects to constrain the D6 EFT operator coefficients that shift the top and bottom quark EW couplings are compared to current bounds from the LHC and LEP and an extrapolation to HL-LHC in Figure 10.1. The measurements of top quark production rates at the ILC improve the measurement of the EW couplings and the corresponding bounds on the relevant EFT operator coefficients by two orders of magnitude with respect to the current LHC results, and by well over an order of magnitude with respect to HL-LHC expectations. Data above the top quark pair production threshold are clearly required to provide tight bounds on the operator coefficients that affect the top quark couplings.

Measurements at two center-of-mass energies above the $t\bar{t}$ threshold allow to disentangle contributions of the relevant two-fermion and four-fermion operators in the SMEFT [314]. The prospects for constraints on the $e^+e^-t\bar{t}$ four-fermion operators with the 1 TeV run envisaged at the ILC yield 68% CL bounds of order $C/\Lambda^2 \sim 10^{-3} TeV^{-2}$ [314] and form a powerful test for scenarios with composite (right-handed) top quarks [251] for compositeness scales well beyond the center-of-mass

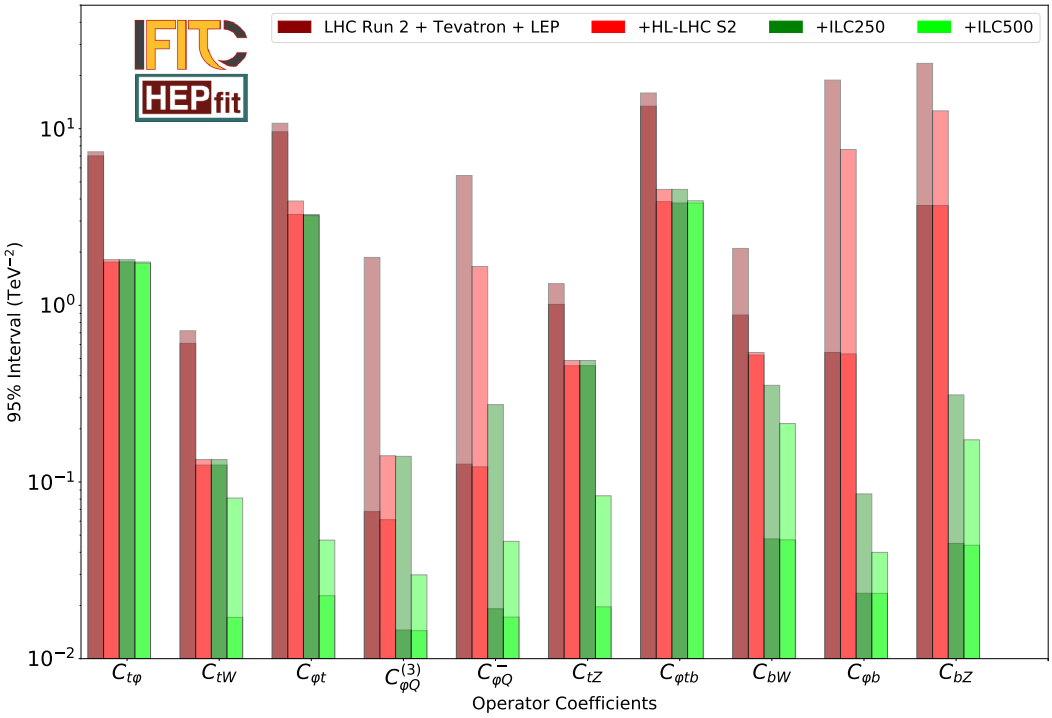

Figure 10.1: Comparison of current 95% CL bounds on the two-fermion Wilson coefficients of the SMEFT that affect the top and bottom quark EW couplings. The LHC bounds correspond to the results of Ref. [307], the HL-LHC S2 projection follows Ref. [311] and the HL-LHC Higgs report [309], while the ILC prospects are based on Ref. [314].

energy.

Dedicated CP-odd observables yield powerful constraints on CP violation in the top sector [315]. Other processes, such as single top quark production and vector-boson-fusion production at high energy provide complementary information [298].

There is a subtle interplay between the Higgs and top physics programmes, as top quark couplings affect the loop diagrams for $gg \to H$ production at the LHC and $H \to \gamma\gamma$ and $H \to Z\gamma$ decays at the LHC and ILC [316]. Precision measurements of tree-level processes, such as *Higgs-strahlung* $e^+e^- \to ZH$ production, gain a sensitivity to top EW couplings through loop corrections. Precise measurements of top quark couplings are required to fully constrain all degrees of freedom of the Higgs EFT [317]. A further discussion is presented in section 12.1.

10.1.3 Searches for FCNC interactions of the top quark

Processes with flavour-changing neutral currents (FCNC) are forbidden at tree level in the SM and are strongly suppressed at higher orders by the Glashow-Iliopoulos-Maiani (GIM) mechanism. The branching fractions for top quark FCNC decays $t \to qX$, where $q = u, c$ and $X = \gamma, g, Z, H$, are of the order of 10^{-12}–10^{-16}. Some extensions of the SM predict a strong enhancement of the FCNC top quark decay rates, increasing the branching fraction up to 10^{-4}.

The search for FCNC interactions of the top quark at the LHC has reached excellent sensitivity for the tqX vertex. The current 95% CL bounds based on searches for top decays and single top production with the partial run 2 data are equivalent to branching fractions of $10^{-3} - 10^{-5}$ and are expected to improve significantly with the HL-LHC data [259, 318, 319].

An e^+e^- collider has a very specific role in the search programme for FCNC couplings. The LEP bounds from searches for $e^+e^- \to t\bar{q}, \bar{t}q$ remain competitive for tqZ and $tq\gamma$ and in particular the $tqll$ operators [320]. The 250 GeV phase of a Higgs factory is expected to improve the LEP bounds by one to two orders of magnitude [321], yielding competitive results in comparison with the full HL-LHC prospects. The higher-energy stages of the ILC are particularly relevant for the bounds on four-fermion operators e^+e^-tq. The sensitivity to these operators increases very strongly with the higher-energy operation [322].

The current 95% CL bounds on the EFT operator coefficients are compared to the prospects of the HL-LHC (3 ab^{-1} at 14 TeV), and three energy stages of the ILC (2 ab^{-1} at 250 GeV, 4 ab^{-1} at 500 GeV and 8 ab^{-1} at 1 TeV) in Fig. 10.2. The current LHC bounds and HL-LHC projections from [] are indicated as dark red and purple arrows, respectively, where the upper arrow corresponds to up quarks and the lower one to charm quarks. The expected bounds for the several ILC energy stages, shown as solid bars, are extrapolated from the study of Ref. [323, **?**]. More details of the procedure are given in Ref. [322]. The increase in sensitivity is particularly pronounced for the e^+e^-tq operators, that are found to scale roughly as $s^{-3/2}$.

10.1.4 Unexplored areas

10.2 Higgs

10.2.1 WW fusion

[corresponding editor: Daniel Jeans (daniel.jeans@kek.jp)]

As well as providing additional Higgs-strahlung events, ILC collisions at 500 GeV will provide a large sample of Higgs bosons produced via the WW fusion process. While the resulting set of Higgs bosons cannot be identified using the unbiased recoil mass method applicable to Higgs-strahlung, they none the less provide an important sample to further probe the Higgs sector. The number of Higgs bosons produced at ILC500 will be similar to the number at ILC250, providing additional statistical power to many measurements. The experimental techniques and background composition are different at the different energies, production methods and beam polarisations,

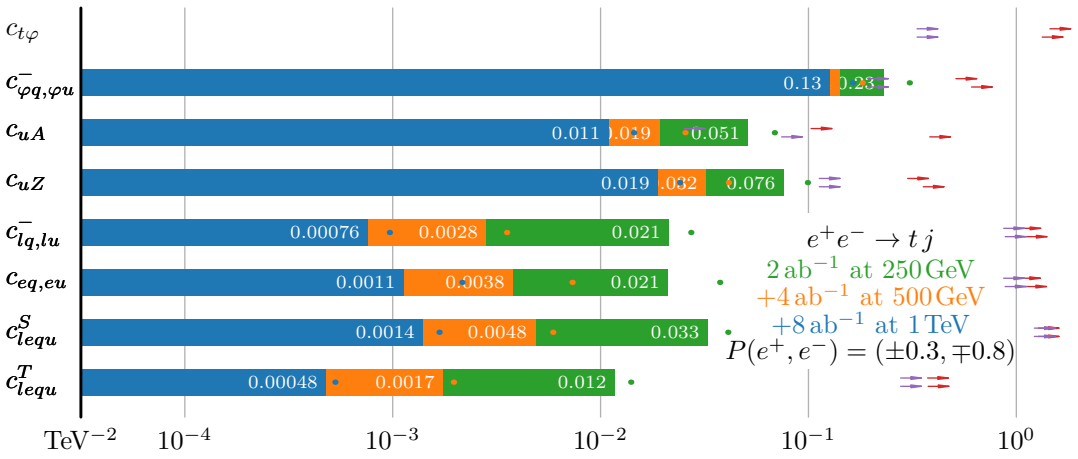

Figure 10.2: The projected 95% C.L. bounds on the EFT operator coefficients that give rise to the FCNC $e^+e^- \to tq$ production process. The bounds are given in units of TeV^{-2} for the LHC run 2 (dark red arrows), for the HL-LHC (purple arrows) and for the three nominal ILC stages: 250 GeV (green bars), 500 GeV (orange bars) and 1 TeV (blue bars). The round markers of the same color represent the expected bounds without beam polarization.

providing for a range of systematic checks by comparing measurements of related observables made under different conditions, before combining the measurements to achieve optimal sensitivity.

The comparison of Higgs production in the Zh and WW-fusion processes, enabled respectively by the hZZ and hWW coupling, with the measured decay branching ratio to WW^* and ZZ^* will allow independent checks of the Higgs couplings to $V(= W/Z)$, while the experimental sensitivity to anomalous HVV couplings, which typically grow with energy, will be enhanced at ILC-500.

10.2.2 Higgs Self-Coupling

[corresponding editor: Jenny List (jenny.list@desy.de) — do we need some more general motivation here, or will this be given in the overall introduction? Where will the possibility of large deviations be introduced?]

At center-of-mass energies of at least 500 GeV, the self-interaction of the Higgs boson, in particular the triple-Higgs coupling λ, can be probed directly by studying the production of Higgs boson pairs. The SM cross-sections of the two relevant di-Higgs production processes double Higgs-strahlung, $e^+e^- \to ZHH$, and di-Higgs production in WW fusion, $e^+e^- \to \nu\bar{\nu}HH$, are shown as a function of the center-of-mass energy in Fig. 10.3. While the WW fusion becomes important at and above 1 TeV, the cross-section for double Higgs-strahlung reaches a maximum around $500 - 600$ GeV, rendering this energy range, which among the future colliders only the ILC proposes to study, quite special. The importance of studying double Higgs-strahlung becomes evident when considering the effect of deviations of the self-coupling from the value predicted by the SM. Models with BSM Higgs-boson sectors naturally predict Higgs self-couplings with $\lambda_{\text{BSM}} \neq \lambda_{\text{SM}}$ (as well as additional diagrams contributing to double Higgs production), as will be discussed below.

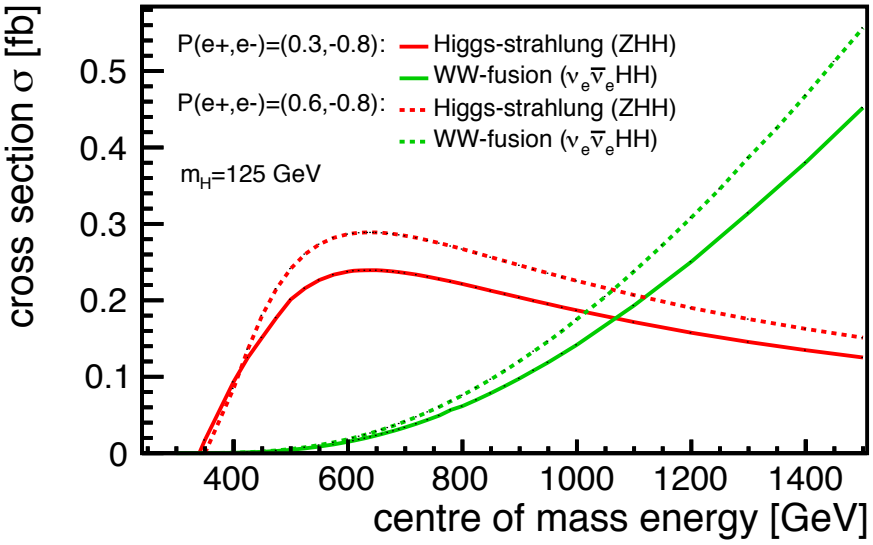

Figure 10.3: Cross-sections for double Higgs production in the SM via Higgs-strahlung and WW fusion as a function of the center-of-mass energy [324].

In Fig. 10.4 one can see that the cross-sections of the different di-Higgs production mechanisms show a non-trivial dependence on λ (here normalised to its SM value λ_{SM}). This is due to the fact that several Feynman diagrams contribute to di-Higgs production, and only some of them actually contain the triple-Higgs vertex. In particular in all boson-fusion processes, the amplitude of the triple-Higgs diagram enters with a minus sign, meaning that a larger value of the self-coupling reduces the cross-section by negative interference — until the quadratic term wins for large values of λ above $\sim 1.7\lambda_{\mathrm{SM}}$. For double Higgs-strahlung, the cross-section rises with λ in the range where boson fusion dives into a minimum, thus giving unique complementary information on the Higgs self-interaction. For the ILC, the prospects for measuring double Higgs production have been studied at the time of the ILC TDR in full, Geant4-based simulation of the ILD detector, using the state-of-the-art reconstruction tools at the time [5], both at $\sqrt{s} = 500\,\mathrm{GeV}$ [324, 326] and 1 TeV [326]. These studies found that at 500 GeV, double Higgs-strahlung can be observed with a significance of $8\,\sigma$ if $\lambda = \lambda_{\mathrm{SM}}$. This would translate into a measurement precision on λ of 27% for the H20 running scenario, combining the $HH \to b\bar{b}b\bar{b}$ and $HH \to b\bar{b}WW^*$ channels. It has been shown that all other SMEFT parameters can be constrained so well from other measurements at the ILC that they do not any further uncertainty to this number [327]. Combined with the measurements of double Higgs production from WW fusion at $\sqrt{s} = 1\,TeV$, the precision expected in case of $\lambda = \lambda_{\mathrm{SM}}$ improves to 10%. Since the TDR, the b-tagging efficiency in ILD has been improved by 5% at the same level of purity [221]. This improvement and the inclusion of $HH \to \tau^+\tau^- b\bar{b}$ have been estimated to improve the ILC500 precision on λ from the 27% mentioned above to about $21 - 22\%$ [324]. Another limiting factor for the double Higgs-strahlung analysis is the invariant di-jet mass reconstruction, important for separating ZHH from ZZH and ZZZ backgrounds. New developments in correcting for missing energy from neutrinos in semi-leptonic heavy quark decays and kinematic fitting show striking improvements on the di-jet mass reconstruction [328]. Further

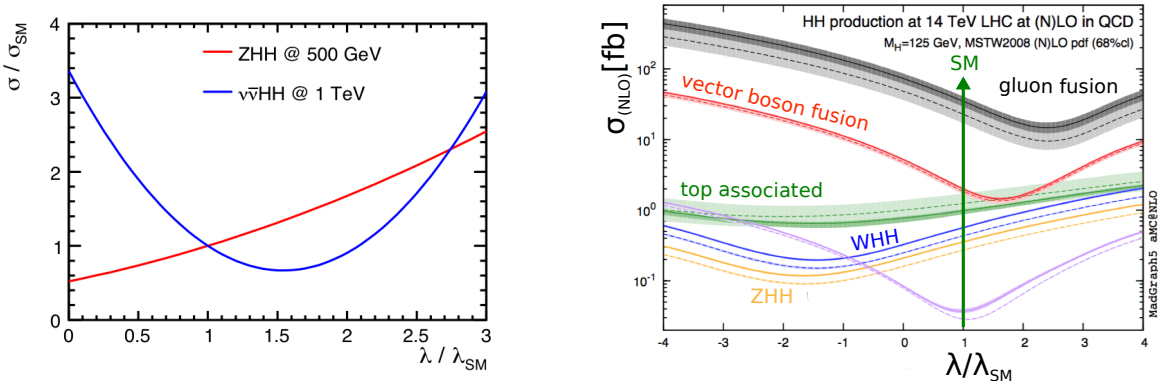

(a) (b)

Figure 10.4: (a)Cross-sections for double Higgs production via Higgs-strahlung (at $\sqrt{s} = 500\,\text{GeV}$) and WW fusion (at 1 TeV) as a function of the triple-Higgs coupling (normalised to its SM value) [324]. (b) Analogous graphs for double-Higgs production modes at the LHC [325]. Fusion-type processes exhibit qualitatively the same behaviour in pp as in e^+e^- collisions, and the same similarity between pp and e^+e^- can be observed for the Higgs-strahlungs-like processes. Note that at LHC, double-Higgs-strahlung is burried by many orders of magnitude below fusion-type processes.

improvements on the jet clustering and on the flavor tag are being expected from deep learning approaches [329] as well as from a full exploitation of the charged hadron identification capabilities of ILD [330]. Propagation of all these improvements of the high-level reconstruction to the full double Higgs-strahlung analysis carries the potential to bring the ILC500 sensitivity to better than 20%.

All the above mentioned numbers apply only to the case $\lambda = \lambda_{\text{SM}}$. However, in models with extended Higgs sectors the self-coupling can deviate significantly from its SM value, even if other Higgs couplings are rather SM-like. As an example, in Refs. [331, 332] it was shown that, taking into account theoretical and experimental constraints, in a model with two Higgs doublets (2HDM) where all fermions couple only to one Higgs doublet ("Yukawa type I") values of $-0.5 \lesssim \lambda/\lambda_{\text{SM}} \lesssim 1.5$ are possible. [add more references... - or will this be discussed in "big questions"?]. Deviations in λ are particularly relevant in the context of electroweak baryogenesis, which typically requires $\lambda > \lambda_{\text{SM}}$ (see Ref. [333] for a review). The capability of a collider experiment to determine the triple Higgs self-coupling depends strongly on its value realised in nature. Figure 10.5 shows the extrapolation of the ILC results to a wide range of self-coupling values (covering, e.g., the full range allowed in the 2HDM type I). The self-coupling measurement at 500 GeV becomes more sensitive for $\lambda > \lambda_{\text{SM}}$, and especially provides sensitivity in the region around $\lambda = 1.5\lambda_{\text{SM}}$, where the fusion processes are nearly "blind", as can be seen in Fig. 10.5a. Fig. 10.5b compares the combination of ILC500 and ILC1000 (shown in red) to a BSM extrapolation of the ATLAS HL-LHC projection for the self-coupling [334] (black dashed). This figure clearly shows that only a combination of Higgs-strahlungs- and fusion-based measurement, e.g. from ILC500 and ILC1000, can guarantee

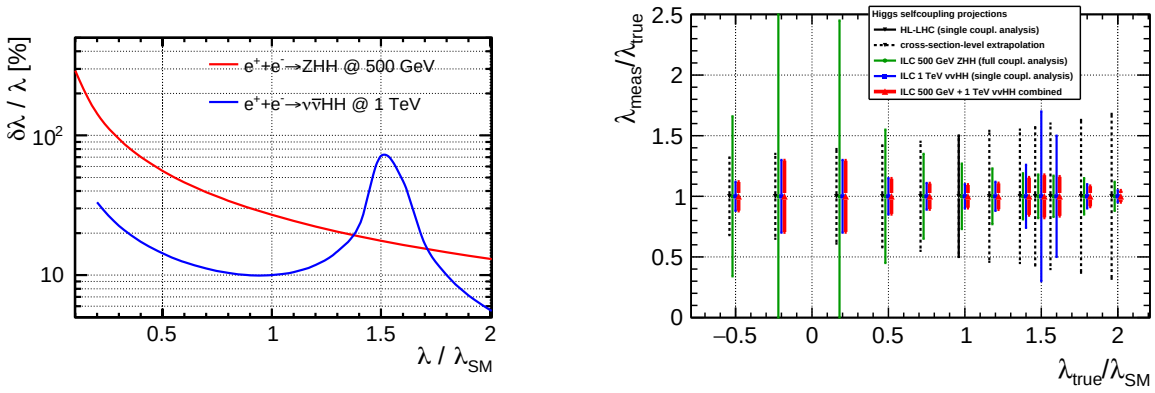

(a) (b)

Figure 10.5: (a)Expected precision on the self-coupling from Higgs-strahlung (at $\sqrt{s} = 500\,\text{GeV}$) and WW fusion (at 1 TeV) as a function of the triple-Higgs coupling (normalised to its SM value) [324]. (b) Same as (a), but drawn as "error bars" at fixed values of $\lambda/\lambda_{\text{SM}}$. Shown in addition are in black the HL-LHC projectiopn from ATLAS [334] for $\lambda = \lambda_{\text{SM}}$, and its extrapolation to other values of λ, and in red the combination of ILC500 and ILC1000.

a measurement of the self-coupling at the level of at least 30% *for any value of the self-coupling nature might have chosen.*

10.2.3 Top Quark Yukawa Coupling

[corresponding editor: Marcel Vos (vos@ific.uv.es)]

The top quark is the SM particle with the strongest coupling to the Higgs boson. The top quark Yukawa coupling, close to ∼1 in the SM, is therefore one of the key targets of high-energy physics. The Higgs boson discovery channels at the LHC are sensitive to this coupling indirectly, through Higgs production and decay channels such as $gg \to H$ and $H \to \gamma\gamma$ that proceed primarily through top quark loops. Under certain assumptions, the Higgs production and decay rates can yield a precise bound on the top quark Yukawa coupling. A more direct, and more robust, measurement is possible in the associated $pp \to t\bar{t}H$ production process, observed in 2018 [335, 336]. The projection for the HL-LHC envisages an uncertainty of approximately 3% on the signal multiplier κ_t dominated by theory uncertainties [309]. Several groups have studied the interplay between

At the ILC, indirect probes are available: the $H \to \gamma\gamma$, $H \to gg$ and $H \to Z\gamma$ channels provide sensitivity to the top Yukawa coupling already in 250 GeV data. These measurements can determine the top Yukawa coupling with ∼1% precision, under the assumption that no new particles enter in the loops. These measurements may therefore provide an early indication of new physics, but a deviation of the SM cannot be unambiguously pinpointed. In more general EFT fits, the constraint on the coefficient $C_t\phi$ of the operator that shifts the top Yukawa coupling obtained from these indirect probes is not robust, as its effect is degenerate with poorly bounded degrees of

freedom [317].

The $t\bar{t}$ threshold scan offers an indirect determination that is more specific for the top quark Yukawa coupling. The production rate close to threshold is sensitive to Higgs-exchange effects and can yield a competitive precision of 4% on the top-quark Yukawa coupling [337]. However, the current uncertainty in state-of-the-art calculation would add a 20% theory uncertainty [303] and there is no clear perspective to reduce or circumvent this uncertainty.

The direct measurement in $e^+e^- \to t\bar{t}H$ production requires a center-of-mass energy of at least 500 GeV. The cross section rises sharply around that energy; raising the center-of-mass energy to 550 GeV enhances the production rate by a factor or approximately four and the measurement of the $t\bar{t}H$ coupling by a factor two. Several groups have performed detailed full-simulation studies at center-of-mass energies ranging from 500 GeV to 1.4 TeV [338, 339, 337]. With 4 ab^{-1} at 550 GeV, a precision of 2.8% is expected on the top Yukawa coupling, which could improve to 1% with 8 ab^{-1} at 1 TeV. Measurements at multiple center-of-mass energies and with different beam polarizations can further characterize the $t\bar{t}H$ coupling [340].

10.3 Triple gauge couplings

[corresponding editor: Jenny List (jenny.list@desy.de)]

The ILC prospects for triple gauge coupling measurements at $\sqrt{s} = 250\,\text{GeV}$ have been introduced in Section 8.3. These have actually been extrapolated from previous studies at $\sqrt{s}500$ GeV and 1 TeV based on full simulation of the ILD detector concept [260, 341]. While the experimental conditions become slightly more challenging at higher center-of-mass energies (more forward-boosted event topologies, higher pile-up from beamstrahlung pairs and photoproduction of low-p_t hadrons), the fundamental gain in sensitivity with $1/s$ dominates by far. Figure 10.6 summarizes the current state of the expected precisions, as discussed in more detail in the following paragraphs.

The full simulation study at 500 GeV [260] was limited to a binned analysis of three (out of five) angles in the $WW \to \mu\nu qq$ and WW $toe\nu qq$ channels. For an integrated luminosity of $500\,\text{fb}^{-1}$, this study found statistical uncertainties of $(6.1, 6.4, 7.2) \times 10^{-4}$ for g_1^Z, κ_γ and λ_γ, respectively. An unbinned likelihood or optimal observable analysis of all five angles, including also fully hadronic WW events as well as single-W events has been estimated [342] to improve these numbers by a factor of 2.4 for g_1^Z and by a factor of 1.9 for κ_γ and λ_γ. Assuming the full integrated luminosity of ILC500 instead of only $500\,\text{fb}^{-1}$ gives another factor of 2 improvement to $(1.3, 1.7, 1.9) \times 10^{-4}$. At this level of precision, systematic uncertainties need to be considered. As shown in [266], the effects of a finite knowledge of the luminosity and the beam polarisations is negligible when including them as nuisance parameters in a global fit. The effect of different permille-level uncertainties on the selection efficiency and percent-level uncertainties on the residual background has been evaluated in [260] by propagation through the whole analysis chain, thereby treating them as fully uncorrelated between data sets and observables, obviously a very pessimistic assumption. Based on considerations of correlated uncertainties and nuisance parameters in global fits, more recent studies expect that systematic uncertainties of $(3, 3, 2) \times 10^{-4}$ can be reached [264]. In total, the

htb

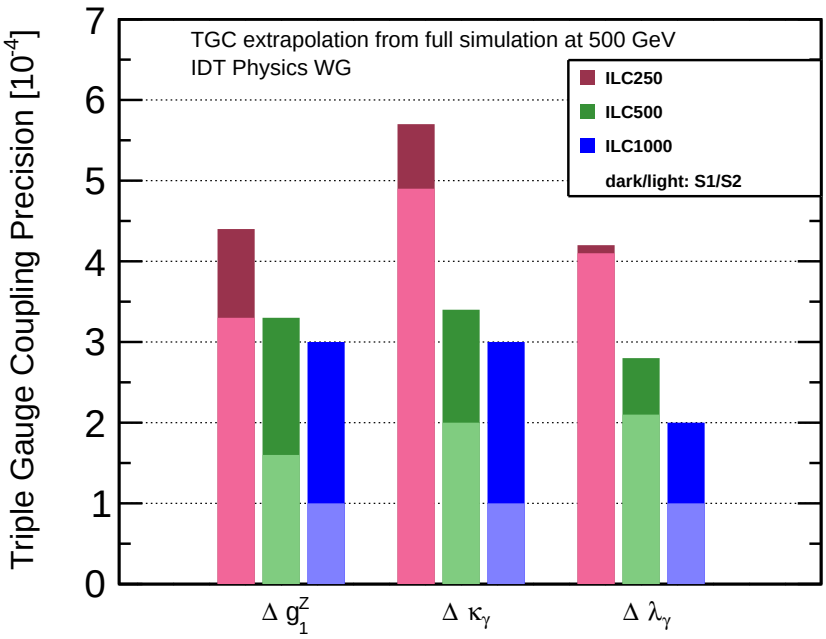

Figure 10.6: Expected precisions on anomalous charged triple gauge couplings at the three energy stages of ILC. The results at 500 GeV and at 1 TeV are based on the ILD full simulation analyses of semi-leptonic W pair production, extrapolated to include improvements from the fully hadronic channel and single-W production as well as for upgrading from a binned analysis of three angles to an optimal observable technique [264]. The S1 scenario assumes the systematic uncertainties from [264], the S2 illustrates the hypothetical reduction by a further factor 2-3 to the level of 1×10^{-4}.

expected precisions on the three couplings thus reach $(3.3, 3.4, 2.8) \times 10^{-4}$ for ILC500.

The full simulation study at 1 TeV [341] found statistical precisions of $(1.9, 1.7, 2.7) \times 10^{-4}$ for a luminosity of $1\,\mathrm{ab}^{-1}$ with the same analysis technique as at 500 GeV (semileptonic W pairs, binned analysis using three angles). Alone a scaling to the full luminosity of $8\,\mathrm{ab}^{-1}$, not even speaking of the previously discussed analysis improvements, renders the statistical uncertainty negligible with respect to the systematic uncertainties as given above. Thus, an adequate estimate of the 1 TeV prospects requires a thorough revision of the systematic effects. While it has already been shown that any global scaling as well as the variation of a simple angular cut-off can be determined from the data without any loss of precision on the TGCS [266], complete treatment in particular of the remaining backgrounds in such a nuisance-parameter-based approach remains future work.

10.4 Quark and Lepton Pair-Production

[corresponding editor: Taikan Suehara (suehara@phys.kyushu-u.ac.jp)]

10.5 New Particle Searches – TeV Scale

[corresponding editor: Mikael Berggren (mikael.berggren@desy.de)]

In this section, we will discuss the prospects at the ILC for the direct discovery of new particles. Our discussion will of course be given in the context in which the LHC experiments have carried out a large number of new particle searches, some reaching deeply into the mass region above 1 TeV. Still, we will explain, experiments at e^+e^- colliders can bring a complementary approach to new particle searches and open new and very interesting windows for discovery [343, 344].

In general, the new particle searches done at the LHC have focused on scenarios within each theory of new physics that give the *best* possible experimental prospects to observe new physics. This gives a chance to find such signs far out in a hitherto uncharted land. However, there is no guarantee that new physics would be discovered even if it is within the kinematic reach of the experiment. The actual parameters of the theory might be far from the ones giving the searched-for signature.

It is a rather different perspective to concentrate on the *worst* possible points in the theoretical parameter space. This clearly cannot reach as far out as in the previous case, but now a negative result would make it possible to claim that the new physics theory is ruled out at *all* possible parameter values below the kinematic reach of the experiment. It would also make discovery of the new physics *guaranteed* if it is indeed energetically reachable.

Lepton colliders have a lower reach in energy, but excel in fully exploiting all possible manifestations of new physics within reach. As the e^+e^- initial state implies electroweak production, the background rates will be quite low. This has consequences for the detector design and optimisation: The detectors can feature close to 4π coverage, and they do not need to be radiation hard, so that the tracking system in front of calorimeters can have a thickness as low as a few percent

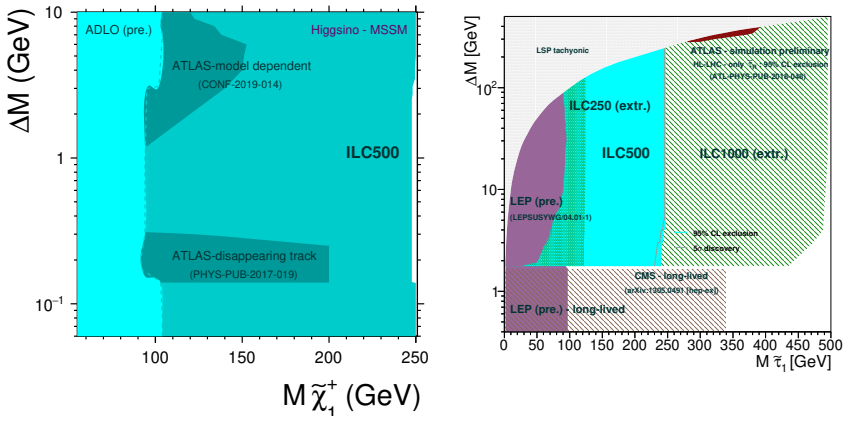

Figure 10.7: Exclusion and discovery reaches for a $\tilde{\chi}_1^{\pm}$ (left), or a $\tilde{\tau}_1$ (right).

of a radiation-length. In addition, the low rates means that the detectors needn't be triggered, so that *all* produced events will be available to analysis. Furthermore, at an e^+e^- machine, point-like objects are brought into collision, meaning that the initial state is fully known, and that the full beam energy is carried by the interacting objects. The beam-spot is sub-microscopic in size, allowing experimenters to find displaced vertices at much smaller distances, even in channels (like $\tilde{\tau}$ pair production), where there is no reconstructable primary vertex.

Many of these features also are relevant in exploiting the LHC's blind-spots, namely, any signal stemming from processes without QCD interactions, or with only soft final states. Here, trigger-less operation of almost fully hermetic detectors is a great advantage. Often, in reactions of this type, only kinematic reconstruction of the full event can reveal BSM physics. These reactions can be studied powerfully at a lepton collider.

10.5.1 SUSY

We start our exposee with supersymmetry (SUSY) [345, 346, 347, 348], for several reasons. Not only is SUSY the most complete theory of BSM, it can also serves as a boiler-plate for BSM in general, since almost any new topology can be obtained in some flavour of SUSY, in particular if also possible violation of R-parity and/or CP-symmetry, or non-minimal models are considered. In addition, it is the paradigm that has been most studied with detailed detector simulation. In most cases, studies were done with full simulation with all SM backgrounds, and all beam-induced backgrounds included. It is true that SUSY is under some stress by recent LHC results. However, ILC offers different angles to explore the properties of SUSY compared to LHC, e.g. loop-hole free searches, and complete coverage of compressed spectra.

Naturalness, the hierarchy problem, the nature of dark matter (DM), or the observed value of the magnetic moment of the muon [349], all prefer a light electroweak sector of SUSY. Except for the third generation squarks, the coloured sector - where pp machines excel - does not provide any

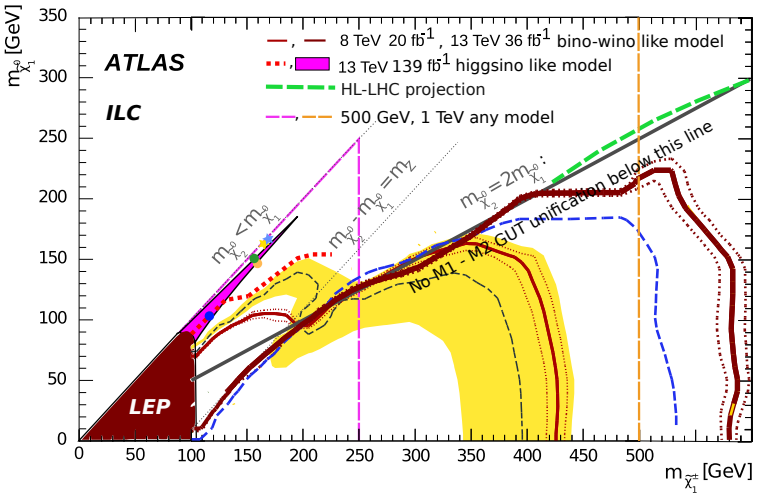

Figure 10.8: Observed or projected exclusion regions for $\tilde{\chi}_1^{\pm}$ NLSP, for LEPII, LHC, HL-LHC and for ILC-500 and ILC-1000 The symbols indicate where the higgsino LSP models shown in Fig. 10.9 are located.

insight into any of these issues. In addition, many models point into this direction: If the Lightest SUSY Particle (the LSP) is Higgsino or Wino, there must be other bosinos close in mass to the LSP, since the $\tilde{H}$ and $\tilde{W}$ fields have several components, leading to a close relation between the physical bosino states; only a Bino-LSP can have large difference, $\Delta(M)$, between the LSP and the Next to Lightest SUSY Particle (the NLSP). However, in the case of a Bino LSP, an overabundance of DM is expected [350], and to avoid such a situation, a balance between early universe LSP production and decay is needed. One compelling option is $\tilde{\tau}$ co-annihilation, and for this process to contribute enough, the early universe density of $\tilde{\tau}$ and $\tilde{\chi}_1^0$ should be similar, which implies that their mass must be quite similar.

Furthermore, if the LSP is Higgsino, one can obtain *Natural SUSY* [351]: In such models one finds

$$m_Z^2 \;=\; 2\frac{m_{H_u}^2 \tan^2\beta - m_{H_d}^2}{1-\tan^2\beta} - 2\,|\mu|^2$$

which implies that requiring low fine-tuning leads to the condition that the Higgsino mass-parameter μ must be $\mathcal{O}(m_Z)$, i.e. an LSP at the weak scale.

In the case of such compressed, low $\Delta(M)$, spectra, most sparticle-decays are via cascades, where the last decay in the cascade - that to SM particles and the LSP - features small $\Delta(M)$. For such decays, current LHC limits are for specific models, and only the limits from LEPII [352, 353, 354, 355, 200, 356, 357] are model-independent. In fact, current observations from LHC13, LEP, g-2, DM (assumed to be 100% LSP), and precision observables taken together also point to a compressed spectrum [358].

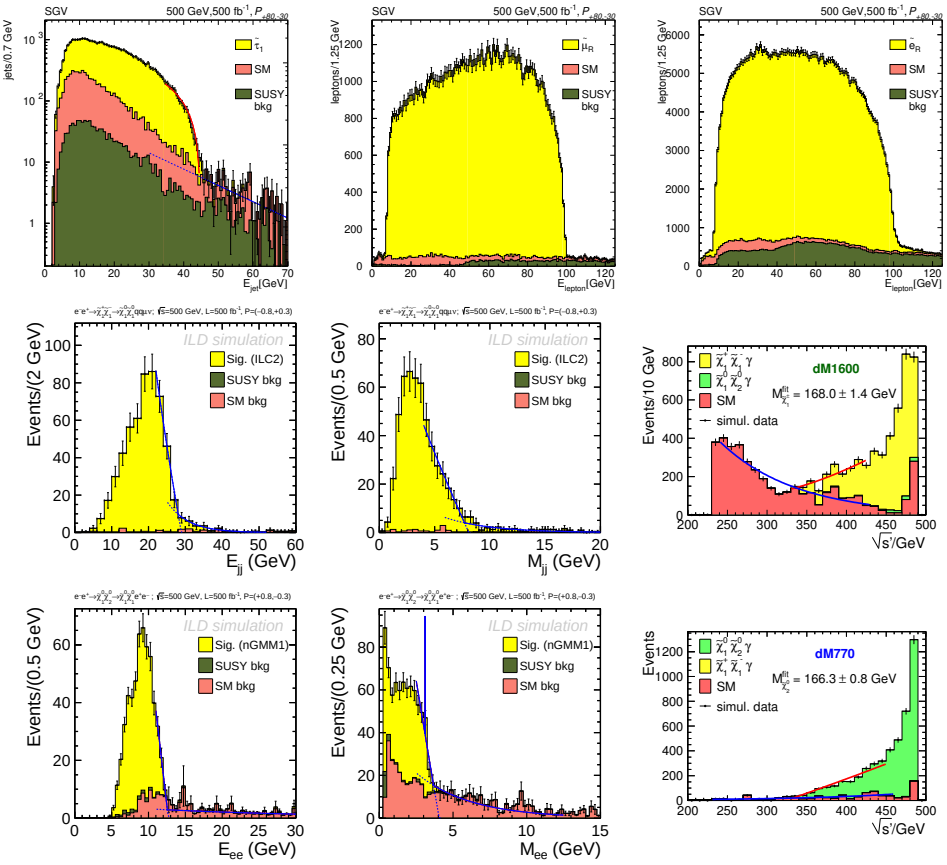

Figure 10.9: Top row: $\tilde{\tau}$, $\tilde{\mu}$ and $\tilde{e}$ spectra. Middle and bottom rows: Observables for three different Higgsino-LSP models. The middle row shows the case of $\tilde{\chi}_1^\pm$ production, the bottom one that of $\tilde{\chi}_2^0$ production.

At ILC one can perform a loophole free search for SUSY because in SUSY, the properties of NLSP production and decay are completely predicted for given LSP and NLSP masses, due to SUSY-principle: "sparticles couples as particles". Note that this does not depend on the (model dependent) SUSY breaking mechanism. By definition, there is only one NLSP, and it must have 100% BR to its (on- or off-shell) SM-partner and the (stable or unstable) LSP. [2] Also, there is only a handful of possible candidates to be the NLSP. Hence by performing searches for every possible NLSP, model independent exclusion and discovery reaches in the $M_{NLSP} - M_{LSP}$ plane, separately for each NLSP candidate, or globally, by determining which NLSP gives the weakest limit at any point. There will be no loopholes to the conclusion. Examples of this procedure are shown in Fig. 10.7 for the cases of a $\tilde{\chi}_1^\pm$ [359] or a $\tilde{\tau}_1$ [360] NLSP. The $\tilde{\chi}_1^\pm$ is a conservative extrapolation from the LEP results, while the $\tilde{\tau}_1$ one is obtained with detailed fast detector simulation, where the $\tilde{\tau}$ and LSP properties were chosen such that the limit is the weakest possible one, i.e. the experimentally

[2] In RPV-SUSY, the LSP could decay, but experience from LEP indicates that this leads to *more* stringent limits.

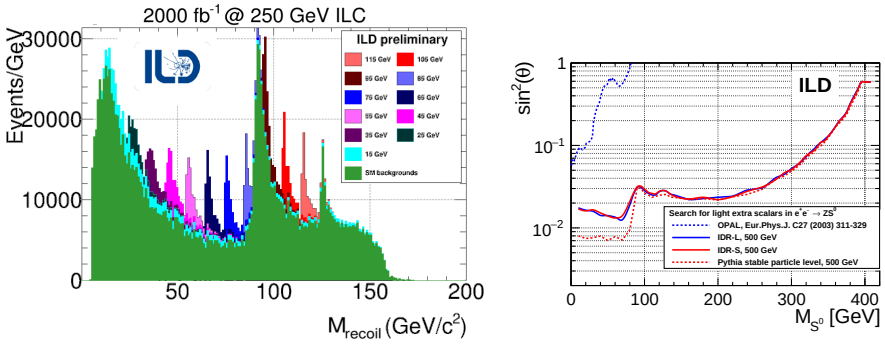

(a) (b)

Figure 10.10: (a) Recoil mass distributions for several new scalars and the SM background. (b) Projected exclusion limit for new scalars, in terms of the coupling compared to the coupling an SM Higgs at the same mass would have.

"worst possible" case. In the figure, it can be seen that the discovery and exclusion reaches are almost the same, and reach quite close to the kinematic limit $2M_{NLSP} = E_{CMS}$. It should also be noted that the HL-LHC projection from ATLAS is exclusion only, and is for specific assumptions on the $\tilde{\tau}$ properties, assumptions that are not the most pessimistic. In Fig. 10.8, the various current or projected limits are shown in a single plot [359, 361, 362, 363, 364, 365]. It should be noted that below the heavy black line, GUT unification of the Bino and Wino mass-parameters M_1 and M_2 is not possible: The difference between $M_{\tilde{\chi}_1^0}$ and $M_{\tilde{\chi}_1^\pm}$ cannot be larger than what the line indicates, if such a unification is realised.

In fact, at the ILC, SUSY discovery would happen quite quickly. The situation that a interesting SUSY signal will be at the intermediate significance (neither excluded, nor discovered) for years will never occur: Either the process is not in reach and there is no sign of it, or it will be discovered immediately. This means that studies of SUSY at ILC would almost directly enter into the realm of precision studies. The plots in Fig. 10.9 shows a number of examples of the kind of signals that would be expected, obtained by detector simulation studies: Typical slepton signal ($\tilde{\tau}$, $\tilde{\mu}$ and $\tilde{e}$) in the top row, in a $\tilde{\tau}$ co-annihilation model [366]. Typical chargino and neutralino signals in different Higgsino LSP models are shown in the following rows. The left-hand two plots are models with moderate (a few to some tens GeV) ΔM [367], while the right-hand ones is for a model with very low (sub-GeV) ΔM [368]. In all the illustrated cases, it was found that the SUSY masses could be determined at the sub-percent level, the polarised production cross-sections to the level of a few percent. Many other properties could also be obtained from the same data, such as decay branching fractions, mixing angles, and sparticle spin.

10.5.2 BSM at ILC: New scalars, WIMPS, Dark photons, Right-handed neutrinos

Many BSM models predict the existence of a *new Higgs-like scalar* (S), produced in $e^+e^- \to Z^* \to ZS$ with unknown decays of S. Such a state could have escaped detection at LEP if its production cross-section is much lower than that of a SM Higgs at the same mass. Hence, a search for such a state should be done at all accessible masses, and without any assumption on the decay modes. At an e^+e^- collider this can be done using the recoil-mass, i.e. the mass of the system recoiling against the measured Z. In [369], a full detector simulation study was performed, and it was found that couplings down to a few percent of the SM-Higgs equivalent can be excluded, see Fig. 10.10(a).

The primary probe at the ILC for the direct production of *WIMP dark matter* are photons emitted as initial-state radiation in association with the pair production of dark matter. Such a Mono-photon search is analogous to Mono-X searches at the LHC. The main backgrounds to this search are the radiative neutrino production, which is irreducible, and the radiative Bhabha scattering process, in which the outgoing electron and positron escape undetected in the beam pipe. At LEP, searches for photon events with missing energy were performed [370, 371], and were later re-analysed within the effective operator framework [372][3]. The prospects to detect WIMPs with

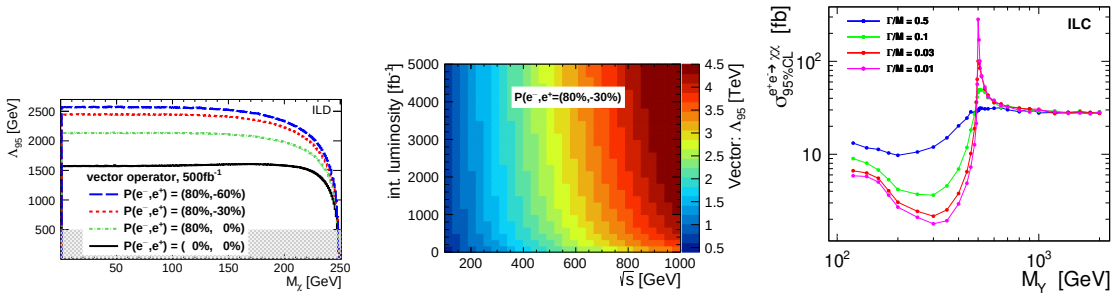

(a) (b) (c)

Figure 10.11: (a): Observational reach (3σ) of the ILC for a Spin-1 WIMP in terms of WIMP mass and κ_e for three different chiralities of the WIMP-fermion couplings. (b): Expected sensitivity for a vector operator in an EFT-based interpretation as a function of integrated luminosity and centre-of-mass energy [373]. (c): Expected excludable cross-section as a function of the mass of the mediator, for different mediator widths.

such methods at the ILC and to determine their properties have been studied for a centre-of-mass energy of 500 GeV in detailed detector simulation [374, 373]. Also at the ILC, the experimental sensitivity have been interpreted in the framework of effective operators. Figure 10.11a shows the exclusion reach found, and Figure 10.11b shows the extrapolation of these results to a wide range of integrated luminosities and centre-of-mass energies [373]. For the full 500 GeV-program of the ILC, scales of new physics (Λ) of up to 3 TeV can be probed, while the 1 TeV-energy-upgrade of the ILC would extend this even to 4.5 TeV or more, depending on the integrated luminosity. At

[3] Note that under LEP or ILC conditions the effective field theory approximation is accurate, while it is questionable in similar analyses at hadron colliders.

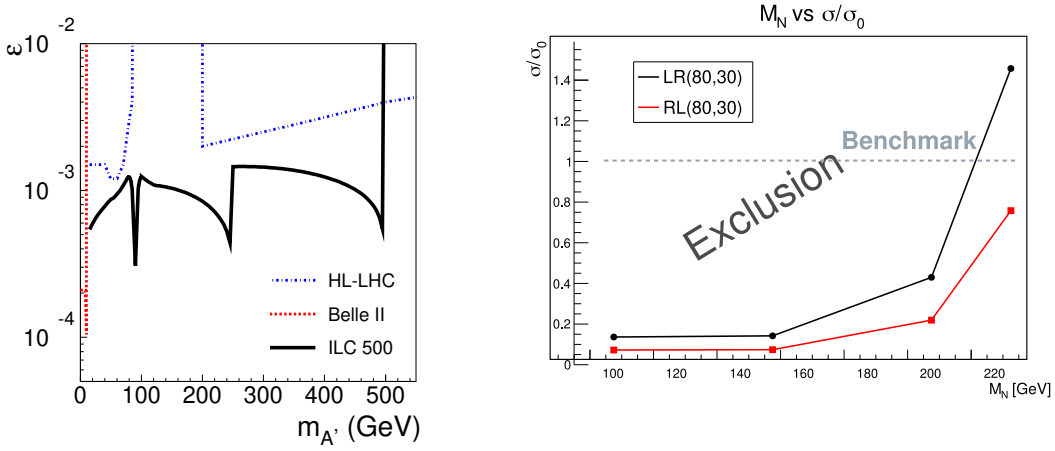

(a) (b)

Figure 10.12: (a) Exclusion limit projections for dark photons, for ILC (solid), BelleII (dash) and HL-LHC (dot-dash). (b) Exclusion reach for Right-handed Heavy Neutrinos.

250 GeV, the full reach will be attained already at a modest integrated luminosity. Also in the case that the mediator is in fact well below the centre of mass energy of ILC, such searches can be performed, this time without assuming that an EFT can correctly model the process [375]. It follows from what is said above that in this case, the search cannot be model independent, but still only modest model assumptions would be needed. One can study the process by only determining the effect of the width of the mediator. The reach in coupling will depend on the assumed width, and the result will be a set of exclusion reaches, labelled by the assumed width. The result of such an analysis is shown in 10.11c. We see that, as expected, a more narrow mediator yields a stricter limit, and that once the mediator mass is above E_{CMS}, the width no longer plays a role.

10.5.3 Heavy neutrinos

10.6 New Particle Searches – Dark Sector

[corresponding editor: Maxim Perelstein (m.perelstein@cornell.edu)]

Many extensions of the Standard Model contain fields that do not carry any SM gauge charges. Such fields are said to belong to the "dark sector", and may include sterile neutrinos, additional gauge bosons, particles responsible for dark matter, *etc.* A brief review of the commonly used set of benchmark models for dark sectors and their interactions with the SM is contained in Section 11.1. The common feature of dark-sector particle candidates is their feeble couplings to the SM, typically orders of magnitude smaller than the SM gauge interactions. High luminosity and clean environment of the ILC offer unique opportunities to search for such particles, while the precisely

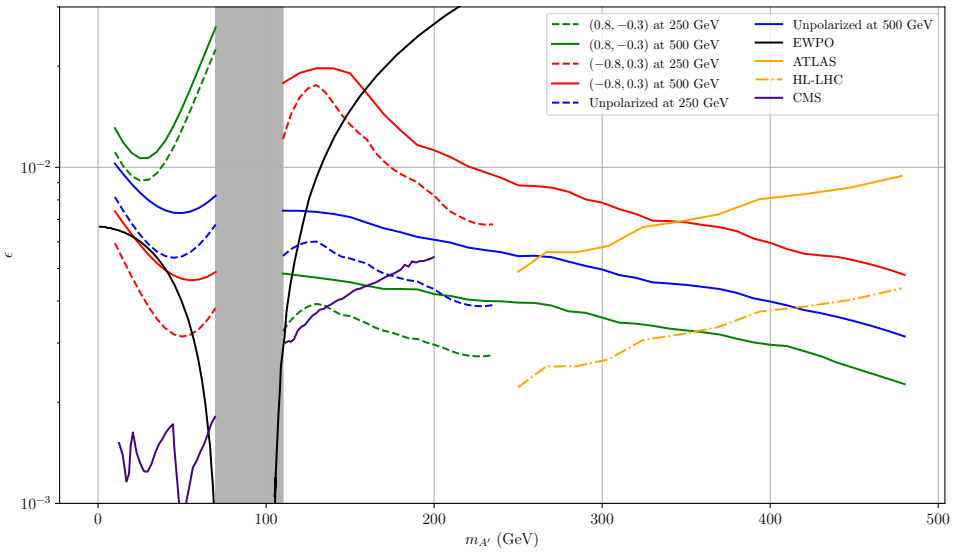

Figure 10.13: Current constraints and the projected reach of the HL-LHC, ILC-250 and ILC-500 for the dark Z gauge boson.

characterized initial state and beam polarization may be crucial to determine their nature in case of discovery.

The ILC will offer two complementary avenues to search for the dark sector particles. First, additional detectors mounted at the ILC beam dumps will provide unmatched sensitivity to dark sector particles with masses below 10 GeV or so. This will be covered in detail in Section 11.3. Second, the general-purpose detectors at the main IP have sensitivity to signals of the dark sector particles with masses up to the full ILC center-of-mass energy. Here, we focus on the latter case. As an example, consider a "dark Z", the gauge boson of an additional $U(1)_D$ gauge group. The interactions of the dark Z with the SM are induced by kinetic mixing of the $U(1)_D$ with the hypercharge, as well as possibly through mass mixing if there exist additional Higgs field(s) charged under both $U(1)_D$ and the SM gauge groups. Unlike the Z' bosons that have been extensively considered in the literature, the dark Z does not have direct gauge couplings to SM fermions, greatly weakening experimental constraints. The dark Z can be produced at the ILC through $e^+e^- \to A' + \gamma$. The current bounds on the dark Z, along with projected reach of the HL-LHC and the ILC-500, are shown in Fig. 10.13.[4] There exists a parameter range where the ILC would be the first experiment to discover this new physics. If the discovery is made, either at the HL-LHC or the ILC, the ILC will have a unique capability to precisely measure the dark Z couplings and determine their chiral structure. A relatively short dedicated ILC run with $\sqrt{s} \approx m_{A'}$ could provide this information, similar to the LEP-1 and SLD measurements of the SM Z properties.

[4]This analysis assumes that the dark Z decays back into SM. An alternative scenario is that dark Z decays invisibly to other dark sector states. In this case, the familiar γ+missing energy signature can be used to search for the dark Z at the ILC.

If the dark sector contains a scalar field S, couplings $S|H|^2$ or $S^2|H|^2$ are possible. If $m_S < m_h/2$, these couplings would induce exotic Higgs decays. The specific signatures depend on the details of the dark sector model. In models where S is stable or decays purely within the dark sector, such decays will appear as $h \to$ invisible. The ILC offers an exquisite sensitivity in this channel, extending the HL-LHC reach on the branching ratio by a factor of 20. On the other hand, in models where dark sector states can decay back to the SM, visible signatures may appear. A well-motivated example is $S \to b\bar{b}$, which is the dominant decay if $m_S > 2m_b$ and the flavor texture of its couplings is aligned with the SM Yukawas. This results in a $4b$ final state, which is notoriously difficult to discern at the LHC but will be accessible at the ILC (see Fig. 8.6). Another possibility is that $m_S > m_h/2$, so that no new Higgs decays are induced. This case is very challenging at hadron colliders, especially if the S field carries quantum numbers that forbid its mixing with the Higgs (as happens, for example, in models where S is the dark matter particle). The ILC will offer a unique window on this scenario through a very precise measurement of the $e^+e^- \to hZ$ cross section, sensitive to one-loop corrections induced by S loops [376].

Another well-motivated experimental target is a pseudo-Goldstone boson of a spontaneously broken global symmetry in the dark sector, with coupling structure motivated by the familiar QCD axion. Such "axion-like particle", or ALP, can be produced at the ILC in association with photons, Z, or Higgs, and detected through its decays to photons or e^+e^- pairs. ILC searches will be sensitive to ALPs in the 1–500 GeV mass range, with couplings 1–2 orders of magnitude below the current limits [377, 378].

Chapter 11

ILC Fixed-Target Program

[7 pages; corresponding editor: Stefania Gori (sgori@ucsc.edu)]

In addition to its central collider, the ILC accelerator can host a number of additional detectors, including detectors for fixed-target experiments and beam dump experiments. These can provide the setting for a multi-faceted program. The main purpose of these experiments will be to search for dark sector particles interacting only feebly with the Standard Model. The intense and high-energy electron and positron beams that the ILC makes available also have uses in nuclear and hadron physics and in studies of strong-field QED. They can also provide resources for developing advanced electron and positron accelerators.

In this chapter, we will present the variety of fixed-target and remote experiments that could be mounted at the ILC site and estimate their potential both for dark sector searches and for other physics questions.

11.1 The physics of light dark sectors

Many extensions of the Standard Model contain fields that do not carry SM gauge charges. Such fields are said to belong to the "dark sector". From the observational point of view, such singlet fields are motivated by the existence of dark matter, as well as by the baryon-anti baryon asymmetry. From a more theoretical side, they appear frequently in models of gauge unification, string theory compactifications, *etc.* Dark sectors can also address some of the anomalies in data as the anomaly in $(g-2)_\mu$. Dark sector particles with a mass at or below the GeV scale are particularly motivated since they can naturally lead to thermal dark matter scenarios. Dark sector fields may still have non-gauge couplings to the SM, allowing them to be produced and detected in collider experiments. Particularly, as we describe below, dark sector particles can communicate with SM particles through the so-called "portal interactions".

The field content of the dark sector and the structure of its interactions with the SM are not strongly constrained by theoretical considerations or by data, and a large variety of viable models are possible. Focusing on *renormalizable* couplings between dark sector and SM fields provides a

useful set of benchmark models to explore this physics scenario.

- **Dark Photon Portal:** If the dark sector contains an abelian gauge group, $U(1)_D$, its gauge field can couple to the SM via the "kinetic mixing" term $\mathcal{L} = \epsilon F_D^{\mu\nu} F_{Y\,\mu\nu}$, where F_Y and F_D are the $U(1)_D$ and the SM hypercharge field-strength tensors, respectively. The kinetic mixing induces a coupling of A', the gauge boson associated to $U(1)_D$, to the SM. If $m_{A'} \ll M_Z$, A' simply couples to the electromagnetic current, while a heavier A' acquires Z-like couplings (the latter scenario is often described as a "dark Z").

  A light dark photon ($m_{A'} < 10$ GeV) can be produced at the ILC beam dump through electron - positron pair-annihilation, and bremsstrahlung productions. Once produced, the dark photon can be long lived, propagate through the dump and then decay to SM particles like e^+e^- in the decay volume. The dark photon can also decay invisibly (e.g. to DM). As we will discuss in Sec. 11.3, in both cases, detectors placed behind the dump will offer new sensitivity to the dark photon parameter space.

- **Higgs Portal:** If the dark sector contains a dark scalar field S, the couplings $S|H|^2$ or $S^2|H|^2$ are possible, where H is the SM Higgs doublet. If $m_S < m_h/2$, the $S^2|H|^2$ coupling induces exotic Higgs decays of the type $H \to SS$. (the ILC sensitivity to exotic Higgs decays is discussed in Sec. 8.2.) **Connect also to the far detectors section, if we have one.** Furthermore, relatively light scalars, S, could be produced in the dump through electron - positron pair-annihilation, the Primakoff process, and bremsstrahlung, thanks to the S mixing with the SM Higgs possibly induced by the $S|H|^2$ and $S^2|H|^2$ operators. Because of this mixing, the dark scalar can decay back to SM particles.

- **Neutrino Portal:** A right-handed neutrino, N, is a SM singlet, and as such may be considered to belong to the dark sector, coupled to the SM through the neutrino portal interaction, HLN, where L is the SM lepton doublet. This operator induces the mixing of the sterile neutrino with the SM active neutrinos, leading to the production of sterile neutrinos in the dump and to its subsequent decay into SM particles.

It is customary to add another benchmark to this list, which involves dimension-5 couplings but is very well theoretically motivated: the "axion portal". Finally, new dark gauge bosons arising from gauging anomaly-free approximate symmetries of the SM are also well studied in the literature:

- **Axion Portal:** A pseudo-scalar singlet, a, can couple to the SM via $aF\tilde{F}$, where F is the EM (or other gauge) field strength tensor. This coupling is allowed if a is a Nambu-Goldstone boson, such as the axion. While the original motivation comes from the "QCD axion" solution to the strong CP problem, phenomenological studies also consider a more general possibility of "Axion-Like Particle" (ALP), whose mass and couplings are not constrained by the QCD axion model. If sufficiently light, ALPs can be produced in the ILC dump through Primakoff production and then decay to photons thanks to the $aF\tilde{F}$ coupling.

- $\boldsymbol{U(1)_{e-\mu}}$, $\boldsymbol{U(1)_{e-\tau}}$, $\boldsymbol{U(1)_{\mu-\tau}}$: The corresponding gauge bosons, Z', couple to some of the leptons of the SM. Because of these couplings, they will be produced in the dump from electron

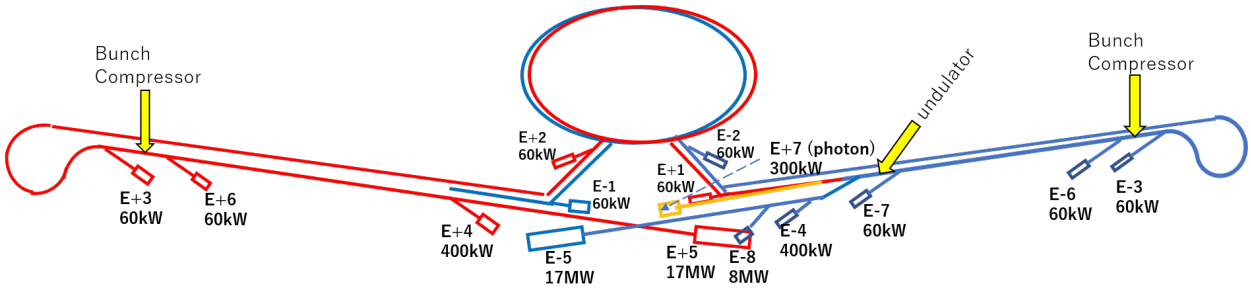

Figure 11.1: Distribution of beam dumps over the ILC facility. The electron, positron and photon beamlines are colored blue, red and yellow, respectively.

(or positron) scattering with the dump nuclei. Z' will decay back to either the charged leptons or the neutrinos of the SM, giving rise to either a visible or invisible signature to be searched for in a detector placed after the dump.

11.2 ILC Facilities for Fixed-Target Experiments

The ILC can provide very high energy, high intensity, low emittance electron and positron beams. The unique beams can also be used for purposes other than the collider experiments. The single-pass nature of ILC allows us to use the beams even destructively so long as the influence to the collider experiments is not significant.

The most appropriate locations of using the beams are the beam dumps. There are 15 beam dumps distributed over the entire facility. Their locations are schematically shown in Figure 11.1. In this section, we will briefly describe only those which may be useful for some of the fixed target experiments.

Main dumps (E−5,E+5)

The main dumps (E−5 and E+5) are located about 300 m downstream of the interaction point (IP). Each of them accepts the full power beam (125 GeV, 2.5 MW) of ILC250. The main body of the dump is a water tank of cylindrical shape, 1.8 m diameter, ∼10 m long, filled with high-pressure (∼10 atm for ILC500) water. This is followed by a shield of several tens of meter long in order to absorb muons created in the dump. This muon shield will be split into many pieces so that appropriate location can be chosen to insert the detector for fixed target experiment. The opposite beam which is going to the IP is running nearby. The beam-center distance is 0.014 (crossing angle) × 300-400 m = 4-6 m. This will limit the size of the area available for the fixed target experiment.

There have already been several proposals to make use of the secondary particles from these dumps. Experiments parasitic to the collider experiment are normally expected so that the beams come to the dumps after beam-beam interaction at the IP. It may also be possible to plan a dedicated machine time in principle but it is better to use the tune-up dumps (E−4, E+4) unless the full power beam is necessary. Also it must be noted that it is almost impossible to make use of

the beam between IP and the dump, by either placing a target or by extracting the beam, because of the safety problems.

Tune-up dumps (E−4,E+4)

Another location to make use of the full energy beam (but lower power) is the tune-up dumps E−4 and E+4. These dumps are used for the commissioning of the main linacs. The electron/positron beams are extracted from the main beam line so that they do not go to the experimental hall. Up to 400 kW (including 20% margin) can be accepted. These dumps will also be used in case of emergency. When an erroneous beam is detected (large off-energy), fast kickers are excited and eject the beam to these tune-up dumps. The field rise time is shorter than the bunch distance (554 ns) and the duration is more than 100 μm, corresponding to more than 200 bunches.

There can be two different modes of using these tune-up dumps, dedicated modes and parasitic modes. In the latter mode a part of the beam (some small number of bunches or pulses) is extracted during normal collider operation using fast kickers. However, in all modes to make use of the tune-up dumps, it must be noted the devices of the dumps (dump body, kickers, etc.) are not necessarily designed for routine operation at 5 Hz. Deliberate planning with the experiment and accelerator sides is mandatory.

One possible proposal to make use of E±4 is the QED experiment (Sec. 11.4). In this case the repetition rate of the laser is limited so that it suffices to extract the last one bunch in 1312 bunch train during the regular collider operation. The required kicker is simple (500 ns rise time, no flat-top necessary, no constraint of fall time, 5 Hz) and can be installed in the main beamline. The emergency kicker need not be used for this purpose. A major challenge for this proposal is how to transport the laser beam deep underground with the laser on the surface.

Photon dump (E+7)

The baseline design of ILC adopts a positron source using helical undulators. The 125 GeV electron beam emits photons which produce the positron beam. The energy of the photons is several MeV and the number of photons is $\sim 10^{17}$ per second. After producing positrons, these photons are dumped at ~ 2 km downstream. The total photon power is about 60 kW. (The design limit of the dump is 300 kW because of future upgrade.) This can be a unique source of gamma ray although the parameters are driven by the requirement of the collider operation.

Beams with low bunch charge

Colliders prefer high bunch charge because the luminosity is proportional to bunch charge square. However, some fixed target experiments may prefer a lower bunch charge with a shorter bunch distance. Obviously, CW operation is impossible because the klystrons accept only pulse operation (duty $\sim$1 %). What may be done at most is to fill all buckets of 1.3 GHz with weak bunches (population up to $\sim 2\times10^7$) with the pulse length kept ($\sim$ 0.7ms) by introducing a different electron gun. The damping ring is not compatible with this beam format, hence a beamline, a few hundred meter long, to bypass the damping ring is needed. There are several other problems expected (e.g., emergency issue) so that serious discussion with accelerator side is needed. A positron beam of such format seems to be very difficult due to the large emittance.

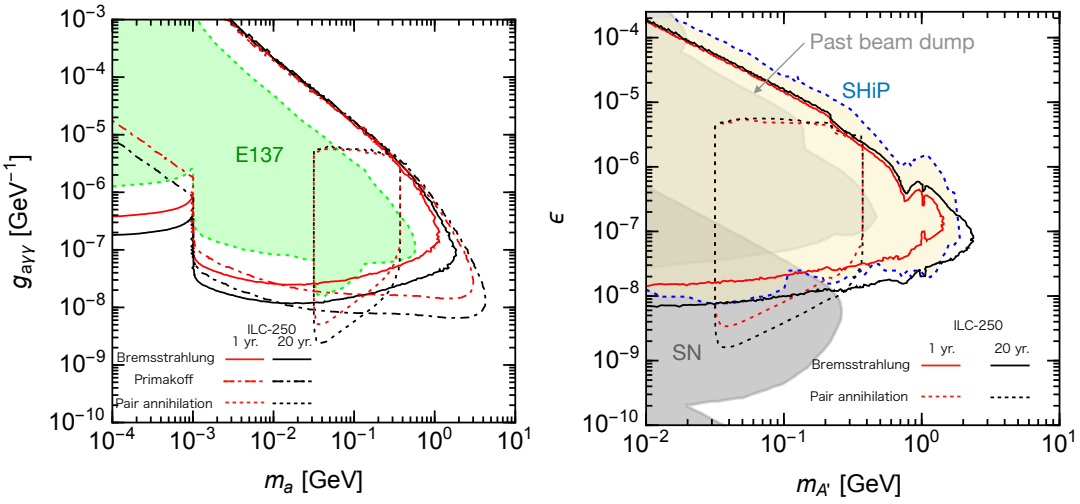

Figure 11.2: The reach of a beam-dump experiment at the ILC-250 for axion-like particles (left) and dark photons (right). Taken from Ref. [381]. See also [382] for another study of the reach on axion-like particles.

It is easy to reduce the bunch charge with the bunch distance fixed. Obviously this is possible only in dedicated modes. The only problem is whether the beam is visible by the monitors for orbit control. It may be possible to add a 'pilot bunch' with normal charge for orbit control. Another possiblity, depending on the nature of the experiment, is to scrape the halo particles by a movable target during the normal collider experiment. This is appropriate in the tune-up dump line. The safety issue must be carefully considered.

11.3 Dark Sector Particle Searches

Dark sector particles could be produced from the interactions of either the e^- or the e^+ beam with the corresponding beam dump. Since such particles are very weakly coupled to ordinary matter, they could propagate through the beam dump and the muon shield without interacting, and decay back to the SM after that. Such events could be probed by detectors located 50–100 m away from the beam dump and behind the muon shield, searching for visible decay products (e.g. signatures involving two or more leptons, or two or more photons) [379] . Alternatively, the dark sector particles could decay to other dark sector states, such as the stable DM particles. A detector could be mounted behind the muon shield to search for elastic scattering of DM particles on atomic electrons, similarly to what has been proposed for the BDX experiment at JLAB [380].

In this section, we discuss the discovery prospects of (both visible and invisible) dark particles at the ILC beam dump experiment. The ILC environment offers unique advantages for this type of physics: highest-energy lepton beams available at any existing or planned machine; very high integrated luminosity (about 4×10^{21} particles on target per year for the main beam dumps at ILC-250) and the availability of both electron and positron beams. These features will enable the

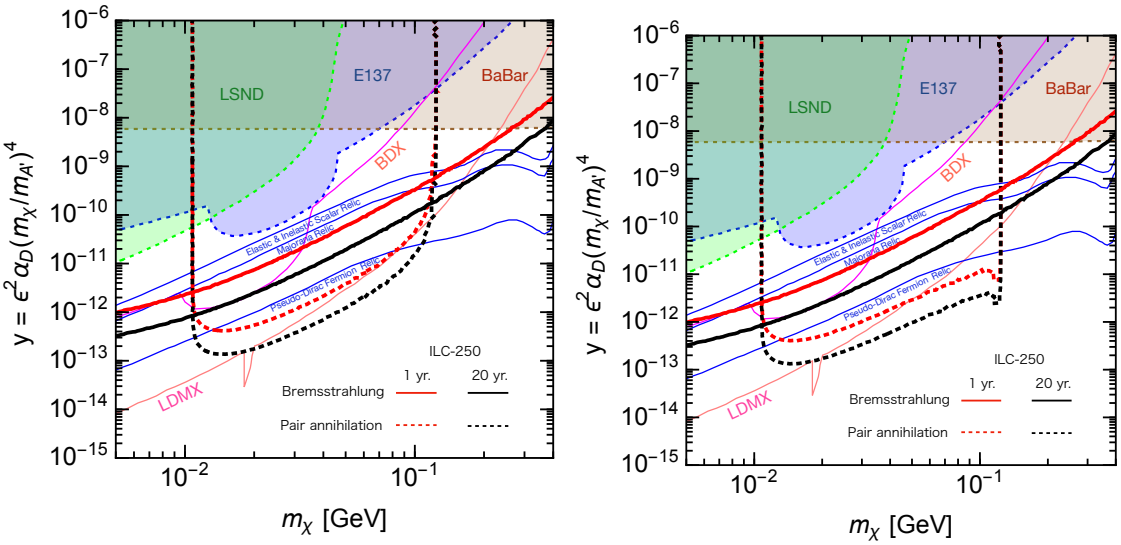

Figure 11.3: Reach of the ILC search for dark photon decaying invisibly to a pair of stable dark matter particles. For comparison, the current constraints (shaded) and reach of proposed BDX and LDMX experiments are also shown. Blue lines indicate the parameters where the DM thermal relic density matches the observed value. From [**?**].

ILC experiments to expand the reach of searches for dark particles to higher masses and smaller couplings.

As an example, the expected ILC reach for visibly-decaying ALPs and dark photons is shown in Fig. 11.2. In both cases, the ILC will greatly expand the reach of the currently available experiments, probing higher dark particle masses and smaller couplings. Similar improvements were demonstrated for leptophilic gauge bosons, such as $U(1)_{\mu-\tau}$ [383], or for dark scalars [382]. If a dark-sector particle is discovered, the ILC can probe its nature and discriminate among theoretical models. Uniquely among the proposed experiments, the ILC can measure and compare the production rates at electron and positron beam dumps, as well as study the dependence on the rates on beam polarization.

The reach of a search for a dark photon decaying invisibly to a pair of dark matter particles is shown in Fig. 11.3. This search relies on detection of elastic scattering of DM particles on an atomic electron in the detector placed 100 m downstream of the beam dump behind a muon shield, and is conceptually similar to the proposed BDX experiment [380]. The ILC experiment will probe the parameter space of this model far beyond the regions constrained by the current generation of searches. In particular, a broad range of parameters where the model can reproduce the observed DM relic density through thermal freeze-out can be probed (see the blue lines in the figure). Note that the experiment at the positron dump (right panel of Fig. 11.3) has a somewhat higher reach than the electron-dump counterpart, due mainly to the additional dark photon production channel $e^+e^- \to A'$ (with e^- being an atomic electron inside the dump). Once again, if a signal is discovered, the availability of e^- and e^+ beams with closely matched parameters, as well as beam polarization, will give the ILC the unique ability to discriminate among possible theoretical interpretations.

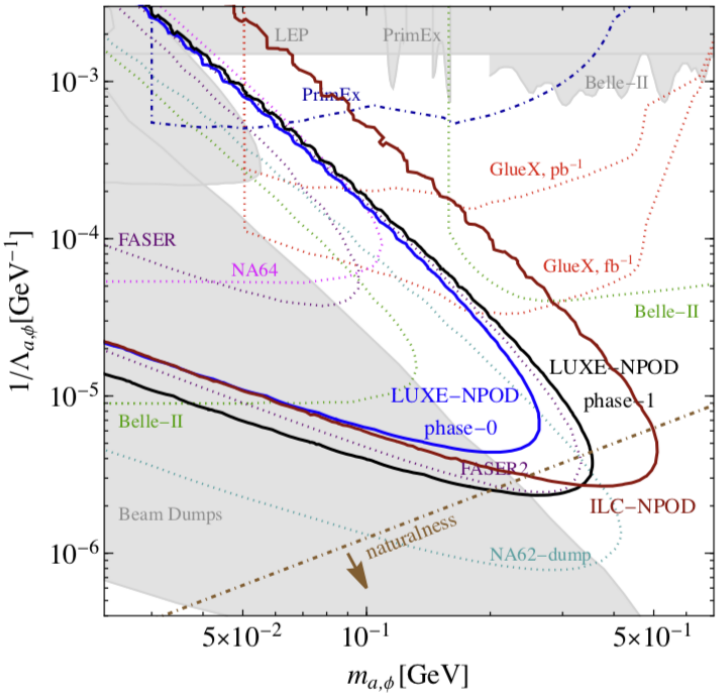

Figure 11.4: Sensitivity of the ILC version of the LUXE-NPOD experiment [384] searching for scalar and axion-like particles that couples to photons. The sensitivity is expressed in terms of parameters Λ_a and Λ_ϕ defined in eq. (11.1).

In addition to using the main beam dumps, the ILC offers other interesting opportunities for novel dark sector particle searches. For example, a high-powered laser can be mounted at one of the tune-up beam dumps. This setup will enable the exploration of strong-field QED, as discussed below. Interactions of the electron beam with the laser field will also produce a high-luminosity photon beam, which can in turn interact with a target to produce dark sector particles such as ALPs. An effective Lagrangian describing the coupling of an ALP a or a scalar ϕ to the photon field can be written

$$\mathcal{L} = \frac{a}{4\Lambda_a} F_{\mu\nu}\tilde{F}^{\mu\nu} + \frac{\phi}{4\Lambda_\phi} F_{\mu\nu}F^{\mu\nu} \ . \tag{11.1}$$

and the sensitivity of such experiments can be described as limits on the parameters Λ_a, Λ_ϕ.

This experimental concept was developed for the LUXE-NPOD experiment proposed at DESY [384]. The high energy and intensity of the ILC beams will greatly expand its sensitivity. The limits expected from the ILC fixed target program are shown in Fig. 11.4. Another interesting possibility is to use the photon beam produced by the positron source to search for ALPs based on the "light-shining-through-the-wall" concept. This and other schemes are currently being investigated.

11.4 Experiments on Strong-Field QED

The electron beam of 120 GeV available for fixed-target experiments will also provide another experimental program, one on QED in very strong fields. At the *Schwinger critical field* of

$$eE = m_e^2 \text{ or } E = 10^{18} \text{ V/m} \tag{11.2}$$

the QED vacuum becomes unstable with respect to spontaneous e^+e^- pair creation. This suggests a new regime of QED that has not yet been studied in the laboratory.

A figure of merit is defined by

$$\chi = eE/m_e^2 \tag{11.3}$$

Currently, the highest χ achieved in the laboratory is $\chi \sim 0.3$ at the SLAC experiment on nonlinear QED E-144 [385, 386, 387]. This experiment observed the nonlinear QED processes

$$e^- + n\gamma \to e^-\gamma \text{ and} e^-\gamma \to e^-e^+e^- \tag{11.4}$$

up to $n = 4$, with successively smaller rates for increasing n. At $\chi \sim 1$, these nonlinear QCD processes have rates comparable to the single-photon processes and require dedicated nonperturbative analysis.

Such large fields are not only of conceptual interest. The corresponding magnetic fields of

$$B = 10^{14} \text{ gauss} \tag{11.5}$$

are observed in magnetars, pulsars with large magnetic fields that are responsible for Fast Radio Bursts and other extreme astrophysical phenomena, and such large fields are also likely to be present in active galactic nuclei. These systems also host electron-positron plasmas that may have unique and surprising properties. Such high fields also occur in the bunch-bunch collisions at TeV e^+e^- colliders. In both cases, we need laboratory experiments to develop and calibrate the plasma evolution codes that are needed to model these systems.

To achieve fields above the Schwinger critical field in the laboratory, the best method is to interact a relativistic electron beam with an intense laser beam. In head-on collision, the intensity of the laser field is increased by $(E_e/m_e)^2$ when viewed in the frame of the electrons, boosting the laser fields to very high intensity. A 2 GeV electron beam on a focused pulse from a 10 PW laser can achieve $\chi \sim 1$ in the frame of the electrons, and we can imagine going higher both in the laser intensity and the in the electron beam energy. The E-144 experiment collided a 50 GeV electron beam with pulses from a 1 TW laser. Today, there are two new initiatives. The experiment E-320, at SLAC's FACET-II facility, now commissioning, will interact a 13 GeV electron beam with a 20 TW laser [388, 389]. The LUXE experiment, planned at DESY, will interact a 16.5 GeV electron beam with a 40 TW laser [390, 391] Both experiments should reach χ values above 1, with possible upgrades to reach $\chi \sim 5 - 10$.

In the mid-2030's, we should have available 100 PW lasers at wavelengths of 1μ. Such high-power lasers are mainly limited in repetition rate, so one might imagine 100 PW pulses at 1/sec

or 10 PW pulses at 10/sec. We estimate the pulse sizes at 2 μ in diameter, with a pulse length of 40 fsec or 120 μ. These conditions lead to

$$\chi \sim 250 \tag{11.6}$$

deep in the regime beyond the critical field. In this strong field, the radiation length is about 0.3 μ.

We envision three stages of strong QED experiments. First, in normal incidence, high energy single electrons would pass through the laser bunch with an optical depth of a few radiation lengths. With a tracker and calorimeter the interaction point to measure the final e^+, e^- and γ momenta and energies, this experiment would study the primary radiation processes at $\chi \sim 100 - 200$. Second, in head-on collisions, single electrons would initiate QED showers leading to the coherent production of an e^+e^- plasma. The features of this plasma have been simulated in [392]. It will be fascinating to observe the dynamics and modes of excitation of this plasma. Third, an electron beam with bunches of 10^7 particles or more would be collided head-on with the laser bunches. This would produce a dense, incoherent e^+e^- plasma of astrophysical interest. This three-stage program would enter and fully characterize this new regime of QED.

The requirements of the first stage of the program, for single- or few-electron collision and particle tracking and calorimetry, are very similar to the requirements for the LDMX-type dark matter experiment described in the previous subsection. Thus, these experiments could be located in the same experimental hall, swapping targets but keep much of the infrastructure in place.

Chapter 12

Precision Tests of the Standard Model

[12 pages; corresponding editors: Junping Tian (tian@icepp.s.u-tokyo.ac.jp), Christophe Grojean (christophe.grojean@desy.de), Michael Peskin (mpeskin@slac.stanford.edu)]

12.1 Precision Standard Model Theory for ILC

[corresponding editor: Ayres Freitas (afreitas@pitt.edu)

To achieve the goals described in sections 8 and 9, precise predictions for the Standard Model (SM) expectations of the relevant observables are needed. A detailed discussion of the required theory work for studies at $\sqrt{s} \approx 91$ GeV, 160 GeV and 250 GeV can be found in Ref. [393] and references therein. The necessary improvement can be split into three categories:

- Fixed-order calculations: For the Z-pole program, electroweak N^{3}LO corrections as well as leading N^{4}LO corrections for the effective Z-fermion vertices are needed. Here "leading" refers to corrections enhanced by powers of the top Yukawa coupling and/or QCD strong coupling. For the 250-GeV program and physics at the WW threshold, NNLO electroweak corrections for $2 \to 2$ scattering processes are mandatory. In addition, calculations of Higgs decay amplitudes must be completed to NNLO order, in particular, for the Higgs decay $H \to 4f$. Higher-order QCD corrections to $H \to gg$ and $H \to b\bar{b}$ are also needed.
- To study effects of detector acceptance and background subtraction, Monte-Carlo tools need to be created with the precision of the expected measurements. This requires an accurate treatment of multi-photon initial state radiation and awareness of beam polarization. Furthermore, the Monte-Carlo programs must be matched to the fixed-order calculations discussed in the previous bullet point. Beyond the leading order QCD and electroweak corrections must be merged in an appropriate way. For a more detailed discussion of QED effects, see Ref. [394].
- Theoretical predictions for the precision observables within the SM also require a range of SM parameters as inputs, most notably the top and bottom quark mass, $m_{t,b}$, the strong

coupling α_s, and the running electromagnetic coupling at the weak scale, $\alpha(M_Z)$. m_t can be measured with high precision at the ILC, but its extraction from the data required resummed higher-order QCD corrections computed in an effective field theory framework. More precise determinations of m_b, α_s and $\alpha(MZ)$ may be possible with improved lattice QCD calculations.

Instead of running on the Z-pole, ILC can also produce high-precision measurements of Z-boson properties by using the radiative return method at $\sqrt{s} = 250$ GeV, as described in section 9.2. A detailed study of the theoretical needs for this program is still lacking. It will require the evaluation of multiple emissions of collinear initial state photons, see e.g. Ref. [395], as well as full SM corrections to the process $e^+e^- \to \gamma Z$. A closer look at the required theory calculations and tools within the Snowmass process would be highly desirable.

12.2 Frameworks for Effective Field Theory

(This section will discuss the theoretical issues for the interpretation of ILC measurements using Effective Field Theory. In the ILC literature, global fits are done using SMEFT with dimension-6 operators only. There are alternative frameworks. What model-dependence does this choice bring in? Can invisible and exotic Higgs decays be included in these global fits? These issues will be discussed in some detail at Snowmass, and we hope to incorporate insights from that discussion.)

12.3 A practical SMEFT analysis for ILC

In discussing the ILC capabilities for the measurement of Higgs boson couplings, Effective Field Theory has another importance beyond providing a general theoretical framework. An important property of the Higgs boson is its total width Γ_H. The total width of the Higgs boson must be know to interpret the data. The most common observable is the rate of a Higgs boson process, which is given by

$$\sigma \cdot BR(e^+e^- \to A\bar{A}) = \sigma(e^+e^- \to H + X) \cdot \frac{\Gamma(H \to A\bar{A})}{\Gamma_H} \tag{12.1}$$

Theoretical predictions, both in the SM and in new physics models, are given for the absolutely normalized partial widths $\Gamma(H \to A\bar{A})$. To extract these, we need to know Γ_H. On the other hand, Γ_H has the SM value of 4.3 MeV for a 125 GeV Higgs boson mass. This value is so small that it cannot be extracted with high precision directly from experiment, either at e^+e^- or at hadron colliders. To determine Γ_H, we need a model.

The model used to extract Γ_H should on the one hand be general and model-independent, while on the other hand it should have few enough parameters that these can all be determined from data without degeneracies. Such a model must be a compromise, but hopefully we can use theory insight to choose a model that satisfies both requirements as well as possible.

It is quite remarkable that the ILC provides a sufficiently large number of measurements of sufficient specificity that we can use SMEFT as a model to reconstruct the Higgs width. General

SMEFT has of course an infinite number of parameters, and even truncating SMEFT to consider only dimension-6 baryon- and lepton-number conserving operators leads to 76 new coefficients for 1 generation and 2499 for three generations. However, the set of coefficients involved in ILC reactions at the tree level is much smaller. We will argue in a moment that 18 operators suffice. Adding to these 4 relevant SM parameters and 2 parameters representing the Higgs boson decay rates to invisible and unclassified exotic decay modes, we arrive at a practical SMEFT fitting scheme with 24 parameters [396, 327]. These parameters are constrained by information about Higgs decays, but, since the SMEFT Lagrangian is intended to be a complete low-energy representation of particle physics, we can add data from precision electroweak measurements, $e^+e^- \to W^+W^-$, fermion pair production, and other reactions that can be studied at the ILC. If we are careful about the treatment of systematic errors, we can also supplement the fit by quantities that are particularly well-measured at the LHC. This gives a robust framework to use in translating the ILC data to normalized values of the Higgs boson partial widths and the value of the total Higgs width Γ_H.

The model restrictions of this "model-independent" framework are:

1. Truncate the SMEFT to renormalizable and dimension-6 operators only. The fit is done strictly at the linear level in SMEFT operator coefficients

2. Calculate the new physics contributions to ILC processes at the tree level only, and drop all operators that do not contribute in the tree-level expressions. It is consistent to drop all 4-fermion operators except for the operator that corrects G_F and all operators that contain quark and gluon fields except for the operators that correct the W and Z total widths.

3. Assume lepton universality. That is, assign the same coefficients to corresponding operators with e, μ, and τ. We will relax this assumption in Sec. 12.6 and show that this has little effect on the global fit.

4. Drop all CP-violating operators. This is justified because CP-violating operators with coefficient C_i contribute to CP-conserving observables only in order C_i^2, while we keep new physics contributions in linear order only. We will show in Sec. 12.7 that this assumption is justified.

5. Include invisible and unclassified exotic decays of the Higgs boson with two parameters that give the total rates. We assume that the light states into which the Higgs boson could decay have no effect on precision electroweak observables. We will discuss models that give exceptions to this assumption in Sec. 12.9.

These assumptions do include the assumption of a clear separation in mass scale between the particles of the SM—including the Higgs boson—and particles mediating new interactions. However, there are no assumptions that the new physics model is of a specific type, for example, weak or strong coupling, leptophilic or leptophobic, *etc.* The use of SMEFT has a clear advantage over other modelling schemes for the Higgs width in that it allows us to use constraints from the well-established gauge symmetry $SU(2) \times U(1)$ to reduce the number of parameters.

In the ILC papers [396] and [218], two more assumptions were used. First, the 4-fermion operator correcting G_F was considered to be sufficiently well constrained by LEP 2 that it could be omitted. We will discuss this point further in Sec. 12.6. Second, possible corrections to the

Higgs self-coupling were ignored in fitting data from single-Higgs reactions. We will relax these assumptions in this discussion. We will discuss tits including the Higgs self-coupling in some detail in Sec. 12.5.

We then take the set of SMEFT operator coefficients used in the practical fit as a subset of the full set of dimension 6 operators in the Warsaw basis [397]. Our effective Lagrangian is

$$\mathcal{L} = \mathcal{L}_{SM} + \mathcal{L}_H + \mathcal{L}_{W,B} + \mathcal{L}_{\Phi\ell} + \mathcal{L}_{Phiq} + \mathcal{L}_{4\ell} \tag{12.2}$$

Here $\mathcal{L}_{SM}$ is the Standard Model Lagrangian, Φ is the scalar Higgs doublet field. For definitiveness, we take the defining mass scale of the dimension 6 operator coeffiicients to be $v = 246$ GeV. Then the dimension 6 terms are given by, for the terms depending only on the Higgs and vector boson fields,

$$\begin{aligned}
\mathcal{L}_H &= \frac{C_{\Phi D}}{v^2}(\Phi^\dagger D_\mu \Phi)((D_\mu Phi^\dagger)\Phi) + \frac{C_{\Phi\Box}}{v^2}(\Phi^\dagger\Phi)\Box(\Phi^\dagger\Phi) + \frac{C_\Phi}{v^2}(\Phi^\dagger\Phi)^3 \\
\mathcal{L}_{W,B} &= \frac{C_{\Phi W}}{v^2}(\Phi^\dagger\Phi)W^a_{\mu\nu}W^{a\mu\nu} + \frac{2C_{\Phi WB}}{v^2}(\Phi^\dagger t^a\Phi)W^a_{\mu\nu}B^{\mu\nu} + \frac{C_{\Phi B}}{v^2}(\Phi^\dagger\Phi)B_{\mu\nu}B^{\mu\nu} + \frac{C_W}{v^2}\epsilon_{abc}W^{a\nu}_\mu W^{b\rho}_\nu W^{c\mu}_\rho
\end{aligned} \tag{12.3}$$

and, for the terms depending on the Higgs fields and on lepton and quark fields,

$$\begin{aligned}
\mathcal{L}_{\Phi\ell} &= \sum_{j=e,\mu,\tau}\Bigg[\frac{C^{(1)}_{\Phi\ell jj}}{v^2}(\Phi^\dagger i\overleftrightarrow{D}_\mu\,\Phi)(\ell^\dagger_{jL}\gamma^\mu\ell_{jL}) + \frac{4C^{(3)}_{\Phi\ell jj}}{v^2}(\Phi^\dagger i\overleftrightarrow{D}^a_\mu\,\Phi)(\ell^\dagger_{jL}\gamma^\mu t^a\ell_{jL}) + \frac{C^{(R)}_{\Phi\ell jj}}{v^2}(\Phi^\dagger i\overleftrightarrow{D}_\mu\,\Phi)(\ell^\dagger_R\gamma^\mu\ell_R) \\
\mathcal{L}_{\Phi q} &= \sum_{j=u,c,t}\Bigg[\frac{C^{(1)}_{\Phi qjj}}{v^2}(\Phi^\dagger i\overleftrightarrow{D}_\mu\,\Phi)(q^\dagger_{jL}\gamma^\mu q_{jL}) + \frac{4C^{(3)}_{\Phi\ell jj}}{v^2}(\Phi^\dagger i\overleftrightarrow{D}^a_\mu\,\Phi)(q^\dagger_{jL}\gamma^\mu t^a q_{jL}) \\
&\qquad + \frac{C^{(R)}_{\Phi ujj}}{v^2}(\Phi^\dagger i\overleftrightarrow{D}_\mu\,\Phi)(u^\dagger_R\gamma^\mu u_R) + \frac{C^{(R)}_{\Phi djj}}{v^2}(\Phi^\dagger i\overleftrightarrow{D}_\mu\,\Phi)(d^\dagger_R\gamma^\mu d_R)\ .
\end{aligned} \tag{12.4}$$

Here $t^a = \sigma^a/2$, the weak isospin generator, and

$$\begin{aligned}
\Phi^d agger\overleftrightarrow{D}_\mu\,\Phi &= (\Phi^d aggerD_\mu\Phi - (D_\mu\Phi^d agger)\Phi) \\
\Phi^d agger\overleftrightarrow{D}^a_\mu\,\Phi &= (\Phi^d aggert^aD_\mu\Phi - (D_\mu\Phi^d aggert^a)\Phi)
\end{aligned} \tag{12.5}$$

Among the 4-lepton terms, only one is relevant to the analysis of Higgs couplings. This is

$$\mathcal{L}_{4\ell} = \frac{C^3_{\ell ell1122}}{v^2}(\ell^\dagger_{1L}\gamma_\mu t^a\ell_{1L})(\ell^\dagger_{2L}\gamma^\mu t^a\ell_{2L})\ , \tag{12.6}$$

the dimension 6 operator that renormalizes the G_F.

12.4 Expectations for the practical SMEFT fit

(This section will gather the information from the previous sections on uncertainties expected in cross section and reaction rate measurements and quote projected errors on Higgs boson couplings. As a placeholder, we put here the results from [218], shown in the Table 12.1 and in Fig. **??**. These will be updated for the submitted version of this report.)

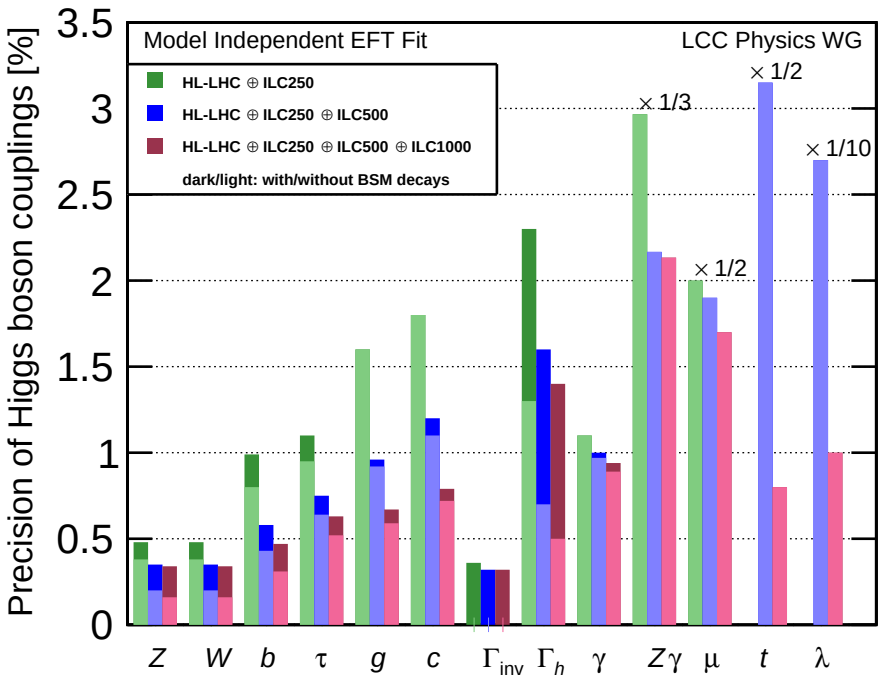

Figure 12.1: Projected Higgs boson coupling uncertainties for ILC250, ILC500, and ILC1000, also incorporating results expected from the HL-LHC, based on the SMEFT analysis described in the text. The darker bars show the results allowing invisible and exotic Higgs decay channels; the lighter bars assume that these BSM decays are not present. The column λ refers to the HHH coupling. In the last four columns, all bars are rescaled by the indicated factor.

12.5 Expectations for the Higgs self-coupling

(This section will discuss the determination of the expected uncertainty on the value of the Higgs boson self-coupling at the ILC from the point of view of SMEFT. The corrections to the SM value of the Higgs self-coupling are parametrized by the operator coefficient C_ϕ. We will discuss the extraction of C_ϕ from 1-loop corrections to the Higgs boson rates measured at 250 and 500 GeV and from the measurement of double Higgs production. In both cases, we will use the practical SMEFT fit to argue that both determinations are model-independent within the assumptions of that analysis.)

12.6 Constraints on violations of lepton universality

(In this section, we will extend the practical SMEFT fit by adding separate SMEFT coefficients for operators containing e , μ, and τ. We will show that the results of the previous sections are robust

	ILC250		ILC500		ILC1000	
coupling	full	no BSM	full	no BSM	full	no BSM
hZZ	0.48	0.38	0.35	0.20	0.34	0.16
hWW	0.48	0.38	0.35	0.20	0.34	0.16
hbb	0.99	0.80	0.58	0.43	0.47	0.31
$h\tau\tau$	1.1	0.95	0.75	0.64	0.63	0.52
hgg	1.6	1.6	0.96	0.92	0.67	0.59
hcc	1.8	1.8	1.2	1.1	0.79	0.72
$h\gamma\gamma$	1.1	1.1	1.0	0.97	0.94	0.89
$h\gamma Z$	8.9	8.9	6.5	6.5	6.4	6.4
$h\mu\mu$	4.0	4.0	3.8	3.8	3.4	3.4
htt	—	—	6.3	6.3	1.6	1.6
hhh	—	—	27	27	10	10
Γ_{tot}	2.3	1.3	1.6	0.70	1.4	0.50
Γ_{inv}	0.36	—	0.32	—	0.32	—

Table 12.1: Projected uncertainties in the Higgs boson couplings for the ILC250, ILC500, and ILC1000, with precision LHC input. All values are *relative* errors, given in percent (%). The columns labelled "full" refer to a 22-parameter fit including the possibility of invisible and exotic Higgs boson decays. The columns labelled "no BSM" refer to a 20-parameter fit including only decays modes present in the SM. Please see the text of Appendix A for further explanation of this table.

with respect to this extension.

12.7 Constraints on CP-violating operator coeffifients

(This section will discuss the inclusion of CP-violating operators within the context of SMEFT. We will show that the four CP-violating coefficients introduced in the natural extension of the practical SMEFT fit will be accurately determined by ILC and LHC data.)

12.8 Constraints on heavy-quark operators

(The list of dimension-6 SMEFT operators expands greatly when operators that specifically involve heavy-quark fields are included. This section will discuss the relation more standard form-factor descriptions of BSM corrections to top quark properties to a full SMEFT analysis. What experiments are required to resolve all of the ambiguities?)

12.9 Tests of more general Effective Field Theory frameworks

(This section will discuss the relaxation of SMEFT assumptions toward more general Effective Field Theories, and how to test the need for this generalizations at the ILC.)

Chapter 13

Big Physics Questions Addressed by ILC

[10 pages; corresponding editors: Nathaniel Craig (ncraig@physics.ucsb.edu), Mihoko Nojiri (mihoko.nojiri@kek.jp), Maxim Perelstein (m.perelstein@cornell.edu), Michael Peskin (mpeskin@slac.stanford.edu)]

The discovery of the 125 GeV Higgs boson poses even more questions that it answers. Within the SM, the Higgs boson explains the the origin of all particle masses through the Higgs mechanism. The 125 GeV boson seems to fulfill this role, but still there remain many questions both about this boson and about the SM itself. Is this boson solely responsible for the breaking of electroweak symmetry and the generation of mass? Is it a singleton, or is it merely the first of several Higgs bosons? What sets the mass parameter for this boson? Can we explain electroweak symmetry breaking in physical terms, with a theory in which that mass is computable? If the SM is correct up to very high scales and the its parameters are equal to the current central values, the vacuum we see is unstable. Is this the true situation, and, either way, what is the true behavior of the vacuum of the universe far in the future? In addition, the discovery of the Higgs boson sharpens questions that have been asked since the SM was first formulated. What is the origin of flavor and the fermion generations? Why is there more matter than antimatter? What is the nature of dark matter? What other types of new matter exist in nature?

Through its comprehensive set of precision measurements of the couplings of the 125 GeV Higgs boson, and through its larger program of measurements of electroweak reactions at the weak-interaction scale, the ILC has the power to give insight into all of these questions. In this chapter, we will outline these questions in more detail and describe their relation to ILC measurements. In the next chapter, we will illustrate the insights from the ILC in a complementary way, through quantitative comparison of the ILC projected measurements with the predictions of models of physics beyond the SM.

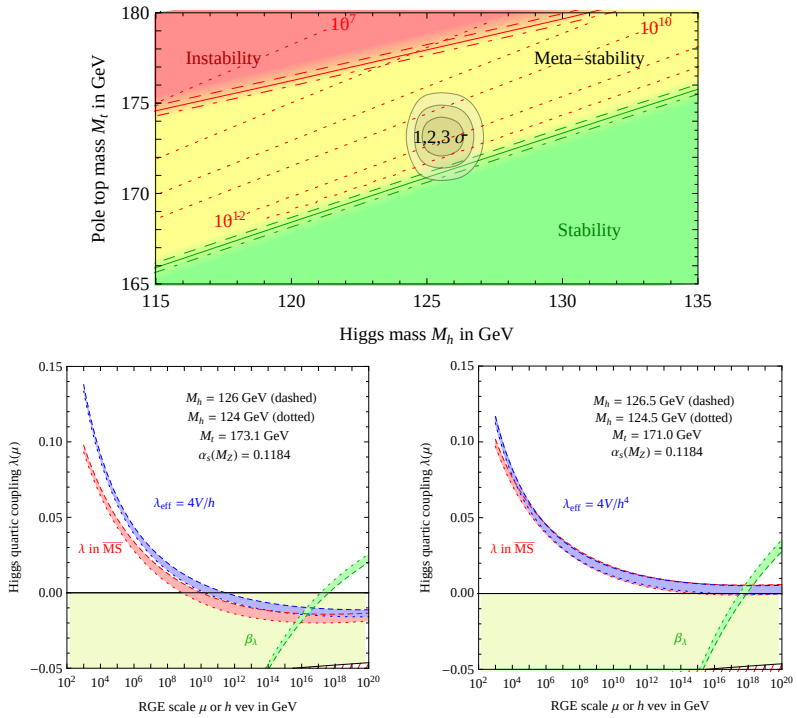

Figure 13.1: top: Regions of stability, metastability, and instability of the SM vacuum, shown as a function of m_H and m_t,showing the current best values in the region of metastability. bottom: Renormalization-group evolution of the Higgs quartic coupling to large Q assuming $m_t = 173.1$ GeV (left) and $m_t = 171.0$ GeV (right). From DeGrassi, *et al.* [398].

13.1 Can the Standard Model be exact to very high energies?

At TeV energies, the Higgs field quartic coupling increases with energy due to renormalization-group running. However, it is a prediction of the SM that this coupling turns over and begins to decrease at very high energies. For the current central values of SM parameters, the Higgs quartic coupling becomes negative at about $!0^{11}$ GeV, leading to a vacuum instability, assuming that the SM is still exact at those energies. Within the SM, the outcome depends sensitively on the values of the Higgs boson mass and the top quark mass. We do not know today what the SM predicts for our universe.

Precision measurements of these two quantities to the accuracy projected for the ILC will resolve this. The nature of the SM vacuum state as a function of the top quarks and Higgs boson masses is shown in Fig. 13.1 [398]. As is shown in the bottom graphs in this figure, a change of 2 GeV in the central value of the top quark mass brings us from eventual instability to stability. Since the calculation uses the short-distance value of the top quark mass, the uncertainty must include the error in converting the top quark mass as measured in experiment (*e.g.*, the pole mass) to a short-distance value (*e.g.*, the $\bar{M}S$ mass). Thus, this calculation, within the SM, requires very precisely understood inputs at the energy of the electroweak scale. We have seen above that the

ILC will determine the Higgs boson mass to a precision of 15 MeV and the short-distance top quark mass to a precision of 40 MeV, well within the requirements for a definitive statement.

If the future experiment proves the SM vacuum metastable, two possibilities arise. On the one hand, the SM could be exactly correct up to the scale of the instability. In that case, we will need to understand how the universe before the electroweak phase transition settled down to the metastable vacuum of today. Alternatively, new physics may arise below the energy scale of 10^10 GeV, where the value of the four-point interaction of the Higgs boson becomes negative, and this could change the physics of the Higgs potential in such a way as to make the vacuum state stable. Such new physics may exist above the scale of 1 TeV or so, which is directly or indirectly explored in current particle experiments, but it may also occur at lower scales, since the nature of the Higgs boson remains largely unexplored.

Another intriguing possiblity is that the Higgs boson and top quark masses are such that the balance point toward instability is moved just to Planck scale, as indicated in the right-hand graph in Fig. 13.1. In this case, it is possible to arrange that the Higgs field is the inflaton which is responsible for generating cosmic structure [399, 400].

We do not know whether the Standard Model is correct up to high energy scales. If we relax this assumption, there are relatively straightforward extensions of the Standard Model that can make the vacuum stable. For example, in a model where singlet scalar fields interact with the Higgs boson, the vacuum can be stable for some parameter regions of the model. It is even possible that such extension of the SM l can accommodate dark matter by requiring Z_2 symmetry. The Higgs boson couplings can be different from the standard model ones, and such deviations may be detected by the precision measurement of the Higgs bosons. These models can contain additional first-order phase transitions. In this case, significant gravitational waves may be produced by a phase transition in the early universe and observed as a background in low-frequence gravitational wave observations.

It is also possible that the Higgs sector is stabilized by high symmetry. Such a symmetry would require many new particles to completely change the Higgs boson interaction and its high-energy behavior. An example of such a scenario is the supersymmetric model. In the supersymmetric model, all bosons have partner fermions and vice versa due to the symmetry of the theory. The model also relates Higgs four-point couplings to the fourth power of gauge couplings so that the scalar potential is bounded from below. The supersymmetic models have at least two Higgs doublets, namely, five Higgs bosons. In addition, the down-type quarks leptons can have large Yukawa coupling. The Higgs boson decay can receive significant corrections detectable by the Higgs factories if the masses of the additional Higgs bosons are around TeV. In addition to that, the predicted partners can be directly searched at linear collider or though the measurement of oblique corrections.

The other new physics possibility between the Planck scale to the weak scale is the change of space-time. In the warped extra-dimensional model, the Higgs boson can be the field in the IR brane. Yukawa coupling to the fermions is determined by the overlap of the fermion wave function in 5 dim to the Higgs boson on the brane. The effective field theory involving Higgs boson higher-order terms can express the physics picture, and the precision study of Higgs interaction can provide crucial information.

It is quite generally true that the high-precision measurement of Higgs boson and top quark masses can give profound insight into all of these possibilities. The measurement must be carried out with a high degree of confidence and control of experimental and theoretical systematic errors. That is possible uniquely at an e^+e^- collider such as the ILC.

13.2 Why is there more matter than antimatter?

The origin of matter is no less compelling a mystery than the origin of mass. Assuming inflationary cosmology, the universe began in a state with equal amounts of matter and antimatter. From this starting point, the abundance of matter over anti-matter can be explained starting from symmetric initial conditions if some epoch in the early universe satisfies the Sakharov conditions—B violation, C and CP violation, and loss of thermal equilibrium. These ingredients seem suggestively present in the quark sector of the SM itself, but, quantitatively, the asymmetry generated is too small by 10 orders of magnitude. The problem is that the quarks that are sensitive to the CP-violating CKM angles are very light compared to the Higgs vacuum expectation value. So it is possible to generate the observed baryon asymmetry in simple extensions of the Standard Model in which there are new particles and new sources of CP violation at or above the weak interaction scale. These models must also include a mechanism for taking the universe out of thermal equilibrium, such as a first-order phase transition or late-decaying particles. Models in which the out-of-equilibrium events take place at or below the TeV scale can be directly tested at the ILC. A prominent class of models is that in which the electroweak transition itself becomes first-order due to the coupling of the Higgs boson to other new particles. Another interesting class of model involves dark sector particles or heavy neutrinos that would be revealed at the ILC.

In the SM, the electroweak phase transition (EWPT) is predicted to be a second-order, or nearly so. A first-order phase transition, necessary for electroweak baryogenesis, requires a substantial modification of the SM Higgs potential at finite temperature. Generically, this is only possible if new particles with substantial couplings to the Higgs boson, and with masses below the TeV scale, are present. Such particles can be searched for directly at the LHC, and some possibilities (for example, top quark partners in supersymmetric models) are already strongly constrained. However, other options, such as new gauge-singlet scalar fields coupled to the Higgs, remain wide open. Precision Higgs measurements at the ILC will be sensitive to such scenarios. In particular, the $e^+e^- \to Zh$ cross section will be measured at the level sensitive to generic one-loop corrections to the Higgs propagator. This measurement will probe a wide range of first-order EWPT models, including those with a gauge-singlet scalar. Likewise, models with a first-order EWPT typically predict significant deviations in the Higgs cubic coupling, which can be discovered at the 500 GeV or 1 TeV ILC upgrade.

An illustrative scan of the parameter space of a model with a single real scalar mixing with the SM Higgs boson is shown in Fig. 13.2 [401]. The blue points represented models with a strongly first-order electroweak phase transition. In this class of models, the Higgs self-coupling is enhanced almost by a factor of 2, and the Higgs couplings to ZZ is has a relatively large correction (about 5%) compared to the SM prediction. With the precisions explained in previous sections, uncertainties of 23% on the Higgs self-coupling and 0.4% on the HZZ coupling after the 500 GeV stage, the ILC

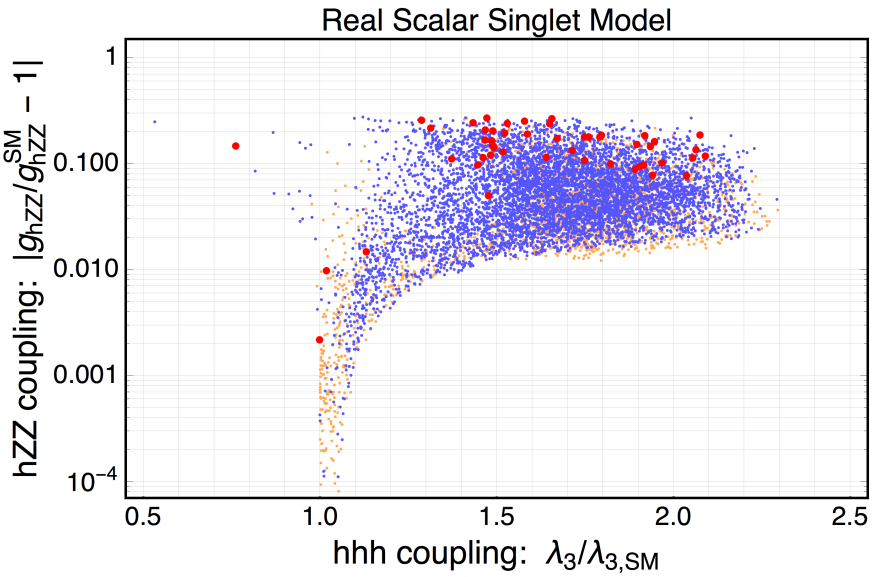

Figure 13.2: Scan of the parameter space for a model of baryogenesis at the electroweak scale with one new electroweak singlet Higgs field mixing with the SM Higgs doublet, from Huang, Long, and Wang [401]. Blue points represent models with a strong first-order electroweak phase transition, required for successful baryogenesis.

will be able to discover these effects with high confidence.

The exploration of models of electroweak baryogenesis will also include tests for CP violation in Higgs boson and top quark decays. There is an alternative class of baryogenesis models, called "leptogenesis", in which the CP violation and the out-of-equilibrium dynamics occurs in the neutrino sector. This can also be tested at the ILC if the relevant heavy neutrinos are at the weak scale. We will discuss both these issues in the following chapter.

13.3 What is the dark matter of the universe?

Perhaps the most compelling evidence for physics beyond the Standard Model comes from the sky, with a host of concordant observations indicating that baryons comprise only a fraction of the matter in the universe. Although viable dark matter candidates span many decades in mass, the near-coincidence of dark matter and baryon abundances suggests a non-gravitational mechanism to connect the two. This singles out dark matter candidates at or below the weak scale that interact with the Standard Model through one of several possible portals. We have discussed in Chapters 8, 10, and 11 that these models often have special difficulties for the discovery of new particles at hadron colliders, difficulties that can be overcome at the ILC.

Famously, a particle with a mass in the GeV-TeV range, coupled to the SM via weak-scale interactions, naturally has the right relic density to explain the observed DM. Such Weakly-Interacting

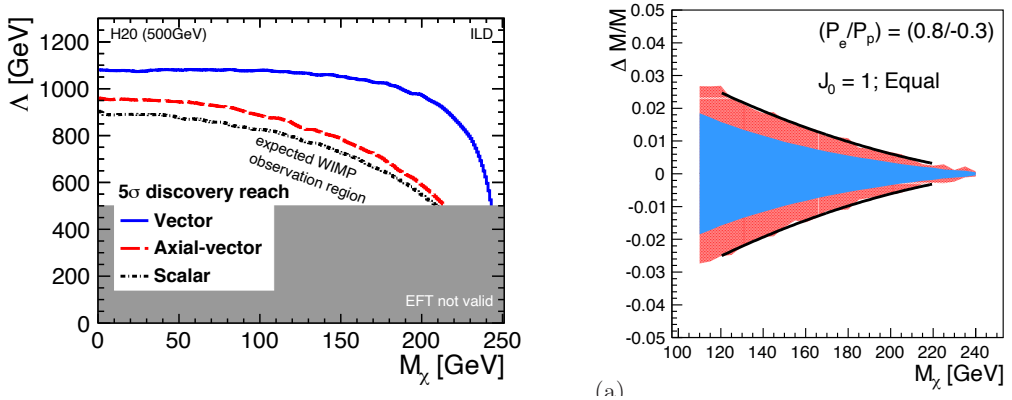

Figure 13.3: Left: ILC reach for dark matter particle coupled to electrons through an effective dim.-6 operator of various spin structures. Right: Fractional accuracy of WIMP mass determination at the ILC using the fit to a photon spectrum in the γ+inv. final state.

Massive Particles (WIMPs) can be pair-produced at colliders. Once produced, WIMPs escape the detector, leading to a missing energy signature. The reach of the ILC to WIMPs in the model-independent γ+MET channel is shown in Fig. 13.3. The ILC is sensitive to the lepton (specifically, electron) coupling of the WIMP, making the ILC search complementary to those at hardon colliders and nuclear-recoil direct detection searches which are primarily sensitive to WIMP coupling to quarks and gluons.

At the ILC, WIMPs can also be produced in decays of other, heavier BSM particles. A well-studied example of this production mechanism occurs in supersymmetric models, where the lightest supersymmetric particle (LSP) can play the role of WIMP dark matter. In many models, the LSP is nearly degenerate in mass with other electroweak-ino states, while strongly-interacting superpartners are much heavier. Such models pose difficulties for searches at hadron colliders due to small cross sections and soft visible energy deposits. The democratic production and clean environment in the ILC collisions allow for efficient searches for this physics. **(Make connection to SUSY section)**

While WIMP paradigm is attractive, there are many alternative scenarios for microscopic origin of dark matter. The ILC will be able to shed light on many of these alternatives. For example, the DM may reside in a "dark sector", a set of fields with no SM gauge interactions (but potentially rich structure of interactions among themselves). Such dark sectors are connected to the SM via a "portal" interaction. A simple and natural portal to DM can be provided by a dark photon, a new $U(1)$ gauge boson which couples both to the SM (via kinetic mixing with the SM $U(1)$ gauge group) and to the dark sector. The ILC will be able to search for the dark photon in two ways. First, it can be produced at the main interaction point, and detected either through its decays back to the SM or the missing-mass peak in the spectrum of the associated SM photon. **figure** Second, an additional detector placed 10-50 m downstream of the ILC beam dump can exploit the high current end energy of the ILC beams to extend the sensitivity to sub-GeV dark photons. **(Make connection to fixed-target section)**

Another natural candidate for a portal to the dark sector is the Higgs boson. Higgs decays into dark-sector states can provide a window into the dark sector. Such decays may result in an invisible Higgs decay signature, which can be accessed at the ILC with sensitivity a factor of 20 better than that expected at HL-LHC. Alternatively, some of the produced dark-sector states can decay back to SM particles, lead to exotic multi-particle final states in Higgs decays. For example, in models of asymmetric dark matter consisting of bound states of a confining gauge group (similar to QCD) in the dark sector, Higgs decays may produce events known as "dark showers", characterized by multiple displaced vertices. Thanks to the large sample of Higgs bosons that will be collected and clean environment with low track multiplicity, the ILC offers unparalleled opportunities to search for such phenomena.

If a signature of the dark matter particle (or an associated mediator particle) is discovered, either at the ILC or in another experiment, the ILC can play a crucial role in determining the properties of this particle such as its mass and spin, as well as strength and structure of its couplings to the SM. For example, the WIMP mass can be determined with a 1-2% accuracy by fitting the photon spectrum from the model-independent γ+invisible signature; see Fig. 13.3. Such measurements are challenging at hadron colliders. Further, the polarized beams at the ILC may help to disentangle the chiral structure of the couplings. (**Some examples: figure**) In some models, the ILC may even provide enough information to calculate the relic abundance of the discovered stable particle(s), and to test whether it is indeed responsible for the observed dark matter.

We will bring together all of the ILC approaches to the search for dark sector particles and summarize their sensitivity in the next chapter.

13.4 What is the energy scale of new physics?

The Higgs boson is an exquisitely sensitive barometer for new physics, with any deviation in its properties from the Standard Model prediction providing a smoking gun indication of new physics. If new physics enters at or above the weak scale, these deviations can be systematically captured in effective field theory extensions of the Standard Model that encode the energy scale of new physics. In this section we interpret the SMEFT projections of section 12 in terms of motivated scenarios for new physics, translating ILC precision into qualitative lessons about the nature of the Higgs boson, its potential, and its coupling to other Standard Model particles.

In the next chapter, we will describe the relation betwen the levels of precision that will be reached in the ILC experiments and the predictions of specific models of new physics. We will demonstrate that the ILC is robustly sensitive to the predictions of these models, and that the pattern of deviations of the Higgs couplings from the SM predictions gives insight into the nature of new physics responsible for those deviation. Here, we will discuss a higher-level issue: What does the high-precision study of the Higgs boson tell us in general about the scale of new physics? Can we use this information to make fundamental tests of the SMEFT framework and of the quantum field theory description of the Higgs boson more generally?

The scale of new physics: The observation of any deviation from Standard Model predictions would be an unambiguous indicator of new physics. As we have discussed in the previous chapter, this can then be interpreted within the SMEFT framework, in terms of nonzero Wilson coefficients c_i/Λ^2 for a set of irrelevant operators. If such deviations can be well-described by dimension-6 operators in SMEFT, their size would allow us to infer the ratio of the couplings and masses of new physics. At the ILC, the anticipated sensitivity to Wilson coefficients of dimension-6 operators ranges from the few percent to per-mil level, depending on both the nature and number of operators in question. If new particles interact with the Standard Model at tree level with generic $\mathcal{O}(1)$ couplings, this could provide indirect evidence for particles as heavy as tens of TeV. If new particles instead interact only at loop level, the ILC remains sensitive to new particles between the weak scale and the TeV scale. Such particles need not carry Standard Model quantum numbers, in which case they would have remained undetected at the LHC.

Constraints on Wilson coefficients coming from null results at the ILC would provide strong evidence for a mass gap between the weak scale and the TeV scale, though the strength of the inferred bounds varies from model to model. It should be noted that constraints on dimension-6 operators do not generally provide an unambiguous exclusion of new physics, since contributions from different UV degrees of freedom to a given Wilson coefficient may partially or wholly cancel. As we will discuss shortly, constraints on dimension-8 operators can provide an unambiguous exclusion of new physics up to the corresponding scale due to positivity bounds that forbid cancellations among different UV contributions.

The "size" of the Higgs: A key higher-dimension SMEFT operator of broad significance is

$$\mathcal{O}_H = \frac{1}{2\Lambda^2}\left(\partial_\mu |H|^2\right)^2 \ , \tag{13.1}$$

the leading nontrivial form factor for the Higgs field. The scale Λ associated with $\mathcal{O}_H$ encodes the effective "size" of the Higgs boson, which may arise due to quantum corrections from new particles or compositeness of the Higgs itself. The leading effect of $\mathcal{O}_H$ on Higgs properties is to generate a universal shift in Higgs couplings relative to their Standard Model values. This shift necessarily drops out of ratios of branching ratios typically measured at hadron colliders. We can sensitive to this parameter only if we can measure the Higgs partial width in absolute terms. Thus, the direct measurement of the Zh cross section at the ILC using the recoil Z boson as a tag allows the first unambiguous probe of $\mathcal{O}_H$.

Among other things, bounds on (or measurement of) $\mathcal{O}_H$ quantify the extent to which the observed Higgs boson is an elementary or composite scalar. A sharp target is provided by the ratio of the Higgs' size to its Compton wavelength. This ratio is of order unity for fully composite scalars, while smaller values correspond to increasingly elementary scalars. To date the neutral pion is the most elementary-seeming (pseudo)scalar yet observed in nature, with a ratio of size to Compton wavelength on the order of $\sim 1/6$. LHC measurements of Higgs properties do not yet probe pion-like levels of compositeness, and retain some degree of model-dependence. At the ILC, observation of $\mathcal{O}_H$ would provide compelling evidence for the compositeness of the Higgs, while sufficiently stringent bounds would ultimately indicate that the Higgs is the most elementary scalar observed to date.

The Higgs self-coupling: A second key operator at dimension 6 is $\mathcal{O}_6 = \frac{1}{\Lambda^2}|H|^6$, which gives the leading correction to the Higgs self-coupling in the SMEFT framework. The anticipated precision of the ILC's constraint on $\mathcal{O}_6$ is sufficient to unambiguously establish the non-zero self-interaction of the Higgs boson. This would, in turn, be the first observation of a self-interacting particle whose interaction preserves all of its internal quantum numbers. Conversely, if the ILC measures a nonzero value of $\mathcal{O}_6$, this would immediately indicate new physics below the TeV scale.

Positivity tests of analyticity and unitarity: In local, unitary quantum field theories, the basic assumption of relativistic causality implies that amplitudes are analytic functions of their kinematic variables. This analyticity in turn implies to positivity bounds in the space of SMEFT couplings [402]. On one hand, these may be viewed as theoretical constraints that sharpen the interpretation of experimental results by narrowing the space of allowed couplings and precluding cancellations between different UV contributions. On the other hand, they may be viewed as an opportunity for direct experimental tests of the axiomatic principles of quantum field theory such as analyticity, unitarity, and locality [403]. Experimental probes of positivity bounds are challenging because the vast majority apply to operators at dimension eight and higher on account of the energy growth required to impose UV-insensitive bounds. The effects of dimension-8 operators are typically subleading to those of dimension-6 operators, which are generally not subject to generic positivity bounds.

Nonetheless, there are a number of observables for which dimension-8 operators provide the leading contributions, enabling tests of positivity bounds at colliders. At the LHC, diboson production allows for sharp tests of positivity bounds on anomalous quartic gauge couplings [404, 405]. But the ILC is particularly well-positioned to test positivity bounds on account of its clean environment and the ability to make measurements at multiple well-defined center-of-mass energies, which can be used to disentangle contributions from operators with different scaling dimensions. Two particularly promising channels for testing positivity bounds at the ILC include $e^+e^- \to e^+e^-$ scattering [406] and $e^+e^- \to \gamma\gamma$ [407]. In both cases, ILC sensitivity to dimension-8 operators is sufficient to give unambiguous tests of positivity bounds, even in the presence of dimension-6 operators. In e^+e^- annihilation to vector bosons, the assumption that deviations from the SM arise from dimension-6 operators leads to specific predictions, such as relations between the γWW and ZWW trilinear couplings and the absence of corrections to $e^+e^- \to ZZ$, that can be tested with detailed measurements of the differential cross sections. Deviations from these predictions must be attributed to dimension-8 contributions. Through these analyses, the ILC can probe bedrock principles of quantum field theory, and, in the event of null results, can unambiguously exclude new physics in the relevant channels.

The linear realization of electroweak symmetry: Although the $SU(2)_L \times U(1)_Y$-symmetric Standard Model EFT (SMEFT) is currently the preferred effective field theory extension of the Standard Model, it is not the only possibility. As we have already described, it is an assumption in SMEFT that any additional sources of electroweak symmetry breaking beyound the observed Higgs boson are associated with large mass scales that can be cleanly integrated out. If there are additional sources of electroweak symmetry breaking below 1 TeV or if there are heavy particles

that still acquire most of their mass from the Higgs field, this would require using a different, more inclusive effective field theory. A logical candidate is the $U(1)_{\rm em}$-symmetric Higgs EFT (HEFT) [408], in which the Higgs field belongs to a nonlinear realization of weak-interaction $SU(2)$. At present, it is possible for either SMEFT or HEFT to describe deviations from the Standard Model, leaving unresolved whether electroweak symmetry is linearly or non-linearly realized by the known fundamental particles. This question is unlikely to be answered decisively at the LHC, leaving a compelling open question for the ILC.

If precision measurements of Higgs couplings at the ILC are not well-fit by SMEFT operators at dimension 6, HEFT may provide the more appropriate description. This would suggest that electroweak symmetry is not linearly realized by the particles of the Standard Model and signal the presence of non-decoupling new physics between the weak scale and a few TeV. On the other hand, consistency of ILC precision measurements with Standard Model predictions—and, in particular, verification of the Higgs coupling constant relations predicted by SMEFT—would significantly narrow the types of UV physics associated with HEFT. Future energy upgrades of the ILC could decisively determine whether electroweak symmetry is linearly realized by the known fundamental particles by probing scattering processes at the $\sim$ few TeV scale.

13.5 Why is electroweak symmetry broken?

Behind all of these questions, there is another very important one. All of the questions that we have discussed in this section eventually point back to mysteries about the Higgs boson.

The structure of the SM is such that the interactions of gauge bosons and fermions are specified completely by their quantum numbers and the values of the $SU(3) \times SU(2) \times U(1)$ gauge couplings. These couplings are dimensionless. For energies above a few GeV, all three of these couplings are weak. This part of the SM is easy to understand and has been tested in great detail through precision electroweak measurements and measurements of quark and gluon reactions at the LHC.

Any property of the SM that goes beyond this—including the basic mass scale of the model, the mass spectrum of quarks and leptons, and the origin of CP violation—necessarily involves the Higgs boson. The explanation that the SM gives for these aspects comes in the form of renormalizable parameters, the Higgs field mass and quartic terms and the Higgs-fermion Yukawa couplings. These are adjustable inputs to the quantum field theory. These input parameters are subject to some general phenomenological constraints, but attempt to compute these parameters from first principles have always led to paradoxes (such as the Gauge Hierarchy Problem). This is why the SM is often described as an effective theory that represents a more fundamental theory at higher energies. We are now at the point where we need to know how that more fundamental theory is constructed.

A basic physics question that we can ask about that more fundamental theory is, why is the $SU(2) \times U(1)$ symmetry of SM spontaneously broken? Like the values of the fermion masses, spontaneous symmetry breaking is an input to the SM. It comes in the assignment of a negative value to the Higgs field mass parameter μ^2. This value cannot be determined from first principles. The connection between the physical and the "bare" value of μ^2 is not well-defined and these

quantities can easily have different signs. This is a symptom of the fact that the SM is only a phenomenological theory. It cannot answer the why questions, not this one, not any of the others that we have listed above.

This situation stands in sharp contrast to our knowledge about spontaneous symmetry breaking acquired from the study of superconductivity, magnetism, and other condensed matter phenomena, pairing in nuclear physics, and even chiral symmetry breaking in low-energy QCD. In each case, there is a fascinating story that explains the why of the broken symmetry state. Some theorists are dismissive of similar explanations in "fundamental" physics. We disagree. It is true that any explanation of EWSB requires new physics beyond the SM. But, to us, this means that there is an opportunity to discover new fundamental forces now unknown. We ought to be grasping for it.

Model that explain the phenomenon of electroweak symmetry breaking (EWSB), require structure beyond the SM, but this can come in one of many forms. The theoretical literature contains a large number of different types of models that address this question. It is useful to divide these models roughly into categories. New theoretical ideas can give rise to new categories, but always with the imperative to explain the mass parameter of EWSB, the Higgs field vacuum expectation value $v = 246$ GeV. In the following, we will refer to physics at the "TeV scale", with new particles of mass from 100 GeV to a few TeV, the "10 TeV scale", with new particles in the range 5–50 TeV, and a "very high scale", with new particles above 10^9 GeV and possibly up to the Planck scale.

Here is a sampling of models found in the literature:

- **Models with a fundamental scalar field at the TeV scale**: Here the Higgs field is a fundamental field. To avoid the conceptual problems of the SM and to allow the Higgs potential to be computable, this the Higgs field must be supplemented by additional fields providing add structure. An example is the Minimal Supersymmetric Standard Model. Here, the Higgs potential can be computed in terms of the masses and couplings of supersymmetric particles, which in principle can be measured independently by experiments. The negative value of μ^2 can be generated by a loop diagram involving $\widetilde{t}_L$, $\widetilde{t}_R$, and the Higgs field Φ_u, and this mechanism is testable after observation of these particles.

- Models with a scalar field composite at the TeV scale: Here EWSB is due to new strong interactions at the TeV scale, as in the original Technicolor models. These models do not include a light Higgs boson doublet, but they may include a Higgs "imposter", for example, a light scalar dilaton. These models are allowed by the current LHC data only with considerable tuning [409] (recently updated to 2021 in v3).

- **Models with a scalar field composite at the 10 TeV scale**: Here EWSB is due to new strong interactions at a higher scale, with the Higgs field mass term protected by symmetry. For example, the Higgs doublet field can appear as a set of Goldstone bosons of the strong interaction theory. Little Higgs models are examples of models of this type. In these models, additional new TeV-scale particles such as vectorlike top quark partners are needed to build computable models of EWSB. These partners can be evade LHC constraints by being heavier than the limits or by being color-singlet, a class of models called "neutral naturalness".

- **Models with extra dimensions**: In such models, the Higgs doublet field can arise as

the 5th component of a 5- or higher-dimensional gauge field. Randall-Sundrum models fall into this class. The higher-dimensional field excitations ("Kaluza-Klein excitations") play an essential role in the computation of the Higgs potential and EWSB.

- **Models with fundamental scalar fields from very high scales**: Here the Higgs doublet is a fundamental scalar field arising at very high energy scales. For example, in the Relaxion model, the Higgs potential evolves on cosmological time scales along with the early expansion of the universe. Another example is Nnaturalness, in which the fundamental theory at the Planck scale contains a large number N of copies of the Higgs doublet with random μ^2 values, of which one has a mass at the TeV scale [246]. In these models, the presence of the fundamental scalar field is given and the mechanism only serves to solve the Gauge Hierarchy Problem. Often, extreme parameter values are needed. For example, in Nnaturalness, one requires $N \sim 10^{60}$.

The type of model dictates whether the model has the power to solve other questions about the SM such as the values of the fermion masses. In supersymmetry, these values are set by the values of Yukawa couplings at the scale of Grand Unification. In models in which the Higgs field is a Goldstone boson or an extra-dimensional vector field component, there is a possibility that the fermion Yukawa couplings can be generated dynamically at the TeV or 10 TeV mass scale.

Though some of these models, especially those of the last class, can be very difficult to test with colliders, all of the classes contain models with new particles at the TeV scale, plausibly within the reach or just beyond the reach of the LHC. These particles can also give tree-level or radiative corrections to the properties of the Higgs boson at the 5% level that can be discovered in a program of precision Higgs measurements. The very different physics origins of EWSB in these classes of models implies that the predictions for new particles and anomalous Higgs coupling are very different from one class of models to another. This gives the possibility that both direct and indirect effects of new particles can distiguish the classes and set us on the road to understanding correctly the origin of EWSB

In the next chapter, we will see how all of the issues described in this chapter can be addressed by measurements that the ILC will make possible.

Chapter 14

ILC Probes of the Big Questions

[8 pages; corresponding editors: Nathaniel Craig (ncraig@physics.ucsb.edu), Mihoko Nojiri (mihoko.nojiri@kek.jp), Maxim Perelstein (m.perelstein@cornell.edu), Michael Peskin (mpeskin@slac.stanford.edu)]

In this chapter, we will bring together the ILC capabilities for measurements and new particle searches discussed in Chapters 8–12 and the predictions of various models of new physics. This will allow us to discuss quantitatively the power of the ILC to access these models and address the issues they raise.

14.1 ILC and dark matter

In this section, we will review the probes available at ILC into the dark sector, including direct searches at the ILC CM energies, searches for exotic Higgs decays, and searches using the ILC beam dump and fixed target facilities.

14.2 ILC and supersymmetry

In this section, we will review the probes available at the ILC to investigate the predictions of models of supersymmetry, including direct searches and deviations in Higgs boson couplings. We will give attention to the parameter regions suggested by the possibility of light Higgsino missed by LHC and the parameter regions suggested by the muon $(g-2)$ deviation.

14.3 ILC and composite Higgs fields

In this section, we will review ILC probes for models with composite Higgs boson or extra dimensions, emphasizing especially the ability of precision top quark measurements to access this physics.

14.4 ILC and CP violation

In this section, we will review the various probes of new CP violation mechanisms available at the ILC, including measurements of Higgs decays, $e^+e^- \to W^+W^-$, and top quark production and decay.

14.5 ILC and flavor

In this section, we will review the ability of ILC to measure the Higgs Yukawa complings of the second generation of quarks and leptons and the implications of those measurements for models.

14.6 The Higgs Inverse Problem

In this section, we will discuss the relation of deviations from the SM Higgs coupling predictions to the space of possible underlying new physics models. Can we infer the model from the pattern of deviations?

Chapter 15

Long-Term Future of the ILC Laboratory

[general corresponding editor: Michael Peskin (mpeskin@slac.stanford.edu)]

The story of the ILC does not end at 500 GeV, or even at 1 TeV. For the studies that we have described in this report, the ILC will create new international laboratory with substantial capabilities and infrastructure. It will be a major world center for particle physics, especially supporting the rapid growth of particle physics research in the Asia-Pacific region.

Although we are now proposing only the first stages of this laboratory, it is important that the ILC laboratory should have a longer-term vision that continues the study of particle physics. Especially if the precision study of the Higgs boson and the top quark reveals the existence of new physics at higher energies, it will be imperative to use the resources of the ILC laboratory to go there and fully characterize the interactions that extend the current Standard Model. Any electron accelerator at energies above 500 GeV must be a linear collider. Thus, it is natural to consider extensions of the ILC to meet this goal.

The layout and geology of the ILC site allow the construction of linear accelerators as long as 50 km. However, still, to reach multi-TeV or higher energies, we will need to develop new accelerating technologies with much higher accelerating gradients. These can be based on superconducting RF, normal-conducting RF, or advanced concepts such as plasma wakefield acceleration.

In this Section, we will describe visions for the long-term future of the ILC Laboratory. Section 5.1 will discuss designs for superconducting RF accelerators based on technologies now being developed to achieve higher gradients. Section 5.2 will discuss designs based on normal conducting accelerators. Section 5.3 will discuss designs based on advanced acceleration ideas. Section 5.4 will present the physics motivation for extension of the ILC to multi-TeV energies. Section 5.5 will discuss the physics of multi-10-TeV energies and the physics of electron colliders at these energies.

All of these ideas point to a long-term future for the ILC Laboratory, in which this laboratory

remains at the forefront of discovery in particle physics.

15.1 Very High Gradient Superconducting RF

[5 pages; corresponding editor: Hasan Padamsee (hsp3@cornell.edu)]

In this section we consider ILC upgrade paths beyond 1 TeV using Superconducting RF cavities with improved performance. We will discuss extensions in energy (1) to 2 TeV and (2) to 3 TeV, depending on the needs of high energy physics. When costs are estimated, these are quoted in ILC currency units, 1 ILCU = $ 1 US using 2012 prices (see Sec. 4.1.6).

1. From 1 TeV to 2 TeV, the design will be based on:

   (a) Gradient advances of Nb cavities to 55 MV/m anticipated from on-going SRF R&D on Nb structures discussed in Sec. 4.3.

   (b) Radically new travelling wave (TW) superconducting structures [117, 118, 119] optimized for effective gradients of 70+ MV/m, along with a 100% increase in R/Q (discussed in more detail in Sec. 4.3.). The large gain in R/Q has a major beneficial impact on the refrigerator heat load, the RF power, and the AC operating power.

2. From 1 TeV to 3 TeV based on

   (a) Radically new travelling wave (TW) superconducting structures [117, 118, 119] optimized for effective gradients of 70+ MV/m, along with 100% increase in R/Q. The large gain in R/Q has a major beneficial impact on heat load, RF power, and the AC operating power.

   (b) 80 MV/m gradient potential for Nb_3Sn [121] with a Q of 1×10^{10}, based on extrapolations from high power pulsed measurements on single cell Nb_3Sn cavities. Further, the operating temperature is 4.2 K instead of 2 K.

All paths will require intense SRF R&D to realize the very high gradient and high Q performance. But there are several decades of R&D ahead to accomplish those goals before the time for a 2 TeV or 3 TeV upgrade is indicated by physics. We are optimistic that the Snowmass process will stimulate funding for these avenues for high energies.

Path 1a (for 2 TeV) requires the development of multi-cell structures of advanced shapes, for example the Low-Loss shape, and the translation of the best 1-cell results today to full-scale structures. Path 1b for 2 TeV and path 2a for 3 TeV require development of radically new Nb Travelling Wave (TW) structures with performance comparable to the best 1-cell Nb cavities of today. No new material development is required for paths 1a and b, or path 2a. Path 2b for 3 TeV require major improvement of Nb_3Sn performance for TESLA-like structures from 23 MV/m for the best 1-cells today to 80 MV/m in the future at a Q of 1×10^{10}, but operating at 4.2 K.

AC Power Demands for 2 TeV and 3 TeV

ILC Energy upgrades beyond 1 TeV (except path 2b) require 300–400 MW AC power for operation, which reflects the major advantage of the SRF technology. We can expect further reductions in AC power from on-going developments under the Green-ILC program [410] paramount in importance. Efforts under this umbrella are preparing to explore multiple paths to make ILC and its upgrades environmentally sustainable. Wind power is one avenue following the example of ESS in Sweden [411]. A 30–40 unit wind turbine farm is capable of providing 100 MW at a cost of 150 MEuro. Combined heat and power production using bioenergy or solar photovoltaic cells integrated in the buildings are other examples. New ways of recycling low heat water (below 50°C) would also enable agricultural use of recycled heat, such as greenhouse heating.

Anticipated Cost Reductions

The 1 TeV upgrade discussion in the TDR does not apply any learning curve cost reduction to cavity, cryomodules or klystrons. Between the baseline ILC at 0.25 TeV and the upgrade options to 2 TeV and 3 TeV the total number of cavities increases by a factor of 5 from 8000 to about 40,000, and the total number of klystrons increases by a factor of 5.6 from 250 to 1500. Accordingly, we apply a 25% cost reduction for cavities and klystrons for 2.5 doublings, using the 90% learning curve in the TDR. We further assume that due to RF power developments, the efficiency of klystrons will improve from 65% (TDR) to 85%. Taking into account modulator and distribution efficiencies of 90% each, we use 65% efficiency for newly installed RF systems for 1 TeV, 2 TeV and 3 TeV upgrades but continue to use 50% efficiency for RF systems installed for the first 0.5 TeV. We expect further cost reductions from several areas of R&D already started. Among the areas under exploration are niobium material cost reduction (25%) for sheet production directly from ingots (large grains), and/or from seamless cavity manufacturing from tubes with hydroforming or spinning to reduce the number of electron beam welds and weld preparations (15 - 20%). Based on the above ideas, we use an overall cost reduction of 50% in the cost of large productions of SW cavities. After including these reductions, we expect the cost of TW cavities will be 30% higher, leading to 15% increase in the cost of CM for TW structures.

Cost-reducing features for cryomodules [116] are to connect cryomodules in continuous, long strings similar to cryostats for long strings of superconducting magnets, saving the cost for the expensive ends. The elimination of the external cryogenic transfer line by placing all cryogenic supply and return services in the cryomodule also reduce costs, not only directly for the cryogenic components, but also by reducing tunnel space required. We estimate that by this method the filling factor from cavities to "linac tunnel length" will improve from 0.7 to 0.75.

Path 1a: 2 TeV Upgrade with 55 MV/m Nb

Scenario B of the ILC TDR [3] assumes a gradient/Q of 45 MV/m/2×10^{10} for the upgrade from 500 GeV to 1 TeV. Recall that the gradient/Q for the first 500 GeV is 31.5 MV/m/1×10^{10}. We expect that R&D in SRF technology will continue in parallel to both construction and operation

of the earlier ILC stages to reach 45 MV/m/2 $\times$ 10^{10}.

For the 2 TeV upgrade Option 1a we consider advances in SRF performance (as discussed in Sec. 4.3) to gradients/Q of 55 MV/m/2$\times 10^{10}$ based on the best new treatments applied to advanced shape structures such as the Re-entrant, Low-Loss, or Low-Surface-Field (LSF) candidates for which gradients of 52–59 MV/m have already been demonstrated with 1-cell cavities using the standard ILC recipe. New recipes under exploration over the last 5 years should give even higher gradients. The new shapes were developed to reduce H_{pk}/E_{acc} 15–20% below that of the TESLA shape. In addition, the R/Q for the advanced shapes is about 20% higher to help reduce the RF power, dynamic heat load and AC power.

Today the best result for a 1-cell cavity of standard TESLA shape given the best new treatment is 49 MV/m, confirmed by retesting at many labs, and by about 50 tests on many 1-cell cavities. Therefore, applying the best new treatments to the advanced shapes we can optimistically expect gradients from 56–59 MV/m with successful R&D.

The strategy adopted for path 1a is to replace the lowest gradient (31.5 MV/m) 0.5 TeV section of cavities/cryomodules, re-using the tunnel, RF and Refrigeration of this section, keep the 0.5 TeV section with 45 MV/m gradient (11,000 cavities), running with the slightly lower bunch charge (Table 15.2), and add 1.5 TeV with 55 MV/m and $Q = 2 \times 10^{10}$. With this approach it is possible to keep the total linac length to 52 km well below the currently expected 65 km site limit. Note: If we just add the full one TeV (24 km) to the existing 1 TeV (38km), the total linac length comes too close to 65 km.

Table 15.1 shows high level parameters for the 2 TeV upgrade as compared to 1 TeV in the ILC TDR. The luminosity is 7.9×10^{34} which is higher than the 3.75×10^{34} for CLIC 1.5 TeV [412]. Table 15.2 gives more detail parameters for beam and accelerator. The number of particles per bunch is slightly lower than for the 1 TeV case, but the number of bunches and rep rate are the same. The peak beam current is therefore slightly lower. The total beam power for two beams increases from 27 MW to 47 MW. Other beam parameters are adjusted so that the spot size at collision is reduced to 1.6 nm (from 2.7 nm).

As shown in Table 15.2, the total number of new cavities at 55 MV/m required for 1.5 TeV is 27,000, spanning a linac length of 36 km, of which 22 km can be installed into the empty tunnel (from the removed 0.5 TeV), leaving 14 km of new tunnel to be installed. Adding in the length (16 km) of the 0.5 TeV section remaining with 45 MV/m cavities, the total linac length will be 52 km, below the expected site limit of 65 km. There are savings from cryomodule parts if the tear down and replacement are staged so that some of the removed cryomodules parts are re-used. From 1600 CM removed from the 0.5 TeV section, we estimate the parts savings to be in the range of 0.5 B provided the removal and production of CMs are properly staged. For the new 1.5 TeV section, the cavity loaded Q is 6.7×10^6, the input power per cavity will be 365 kW, with RF pulse length 2.0 ms, similar to the RF pulse length for 1 TeV. The total number of klystrons required is 1150 of which 360 klystrons are re-used from the 0.5 TeV removed section, and 65 klystrons are available from the 0.5 TeV remaining section (which operates with the new, lower bunch charge), leaving 725 new klystrons to be added. We use 65% efficiency for RF systems installed for 1 TeV and above, and 50% efficiency for the RF system installed for the first 0.5 TeV, to give an average efficiency of 60%. The total 2 K refrigeration required will be 66 kW, of which 33 kW is re-used,

	units	ILC 1 TeV TDR	ILC 2 TeV path 1a	ILC 2 TeV path 1b	ILC 3 TeV path 2a	ILC 3 TeV path 2b	CLIC 3 TeV [412]
Energy	TeV	1	2	2	3	3	3
Luminosity	10^{34}	4.9	7.9	7.9	6.1	6.1	5.9
AC Power	MW	< 300	345	315	400	525	590
Cap. Cost	B ILCU	+ 5.5	+6.0	+4.9	+11.8	+11.0	
(total)		13.3	19.3	18.2	25.1	24.3	24.2 BCHF
Gradient	MV/m	45	55	70	70	80	72 / 100
(new linac)							
Q new linac	10^{10}	2	2	2	2	2 (4.2 K)	
CM unit cost	M ILCU	1.85	1.15	1.32	1.32	1.15	

Table 15.1: High level parameters for ILC energy upgrades. Costs (given in ILC currecy units) do not include Detector and Manpower.

leaving 33 kW new refrigeration to be installed. We assume a cryoload safety factor and RF power overhead of 20% each for the new installations. The damping ring and positron source will be same as for 1 TeV, due to the same number of bunches, but the beam dump cost will increase. Summing all the cost components outlined, the additional cost for the 2 TeV upgrade will be 6.0 B. The AC power to operate 2 TeV will be 345 MW, making ILC with SRF attractive for 2 TeV.

Path 1b: 2 TeV Upgrade from 1 TeV with 70 MV/m TW Nb structures

As discussed in Sec. 4.3, TW structures offer several advantages compared to standing wave (SW) structures: substantially lower peak magnetic (H_{pk}/E_{acc}) and lower peak electric field (E_{pk}/E_{acc}) ratios, together with substantially higher R/Q (for lower cryogenic losses, lower RF power and lower AC power). Instead of using the TESLA shape for the cells, the Low-Loss type shape further reduces the peak surface magnetic field. In addition, it becomes possible to lower the cavity aperture (from 70 mm to 50 mm) without incurring the penalty of higher wakefields since the beam bunch charge for the 2 TeV upgrade is lower than the bunch charge for 0.5 and 1 TeV stages (Table 15.1), while the luminosity for 2 TeV is still 2 times greater than for CLIC 1.5 TeV. By combining these steps, it becomes possible to obtain an overall 48% reduction in H_{pk}/E_{acc} and factor of 2 gain in R/Q over the TESLA standing wave structure. Sec. 4.3 discusses the challenges to develop the TW structures. The TW cavity development effort has started. We expect the cost of TW SRF cavities will be 30% higher, leading to 15% increase in the cost of CM for TW structures.

The first strategy adopted in this option is again to remove the lowest gradient (31.5 MV/m) 0.5 TeV section, re-use the tunnel, RF and Refrigeration of this section, keep the 0.5 TeV section (11,000 cavities) with 45 MV/m gradient (running with the slightly lower bunch charge for 2 TeV), and add 1.5 TeV with TW SRF cavities at 70 MV/m/$Q = 2 \times 10^{10}$ and R/Q 2 times higher than SW Nb cavities. With this approach it is possible to keep the total linac length to 44 km, well below the currently expected 65 km site limit.

	units	ILC 1 TeV TDR	ILC 2 TeV path 1a	ILC 2 TeV path 1b	ILC 3 TeV path 2a	ILC 3 TeV path 2b	CLIC 3 TeV [412]
Energy	TeV	1	2	2	3	3	3
particles/bunch	10^{10}	1.74	1.5	1.5	0.65	0.65	0.37
bunches/train		2450	2450	2450	4900	4900	312
bunch spacing	nsec	366	366	366	250	150	0.5
pulse current	mA	7.6	6.6	6.6	4.16	4.16	3
rep. rate	Hz	4	4	4	4	4	50
RF pulse length (added linac)	ms	1.94	2.0	1.76	2.6	2.6	0.00024
Beam power (2 beams)	MW	27.2	47	47	61	61	28
ϵ_x/ϵ_y	10^{-8} m	500/3	500/2	500/2	500/2	500/2	66/2
β_x/β_y (m)	10^{-3} m	22/0.23	22/0.23	22/0.23	16/0.15	16/0.15	
σ_x/σ_y (m)	10^{-9} m	335/2.7	237/1.6	237/1.6	165/1.0	165/1.0	40/1
σ_z	10^{-3} m	0.225	0.225	0.225	0.1	0.1	0.044
Ψ (beamstr. parameter)		0.21	0.5	0.5	1/045	1.045	5
δ (RMS energy spread)	%	10.5	20	20	16	16	35
Luminosity	10^{34}	4.9	7.9	7.9	6.1	6.1	5.9
photons/electron		1.95	2.1	2.1	1.2	1.2	2.2
coherent pairs @ IP		0	2×10^4	2×10^4	7.9×10^5	7.9×10^5	6.8×10^8
incoh. pairs @ IP		383	49	49	5	5	3×10^5
No. of klystrons (new + existing)	10^3	460 + 320 = 820	820 + 460 = 1280	755 + 425 = 1180	690 + 820 = 1500	1680 + 820 = 2500	
No. of cavities (new + existing)	10^3	11 + 16 = 27	27 + 11 = 38	21 + 11 = 32	43 + 0 = 43	37.5 + 0 = 37.5	160 (0.25 m)
Q_L (new cavities)	10^6	5.6	8	5	8	10	
input power (new cavities)	kW	350	365	460	300	550	
linac length (new + existing)	km	16 + 22 = 38	14 + 38 = 52	6 + 38 = 44	19 + 38 = 57	12 + 38 = 50	42

Table 15.2: Detailed parameters for the proposed ILC energy upgrades compared with CLIC 3 TeV.

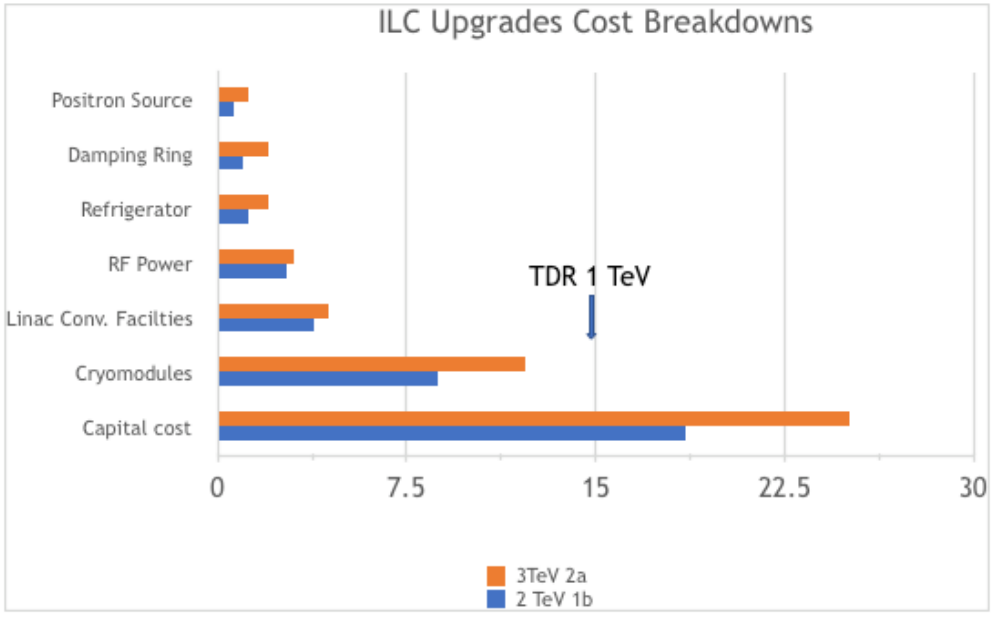

Figure 15.1: Cost breakdowns for some of the major systems for ILC 2 TeV (path 1b) and 3 TeV (path 2a) upgrades beyond 1 TeV. The bars show the TOTAL costs for (1 TeV +2 TeV) OR (1 TeV + 3 TeV). The added costs over 1 TeV are 4.9 B and 11.8 B. The ILC TDR estimates the capital cost for 0.5 TeV as 7.8 B and the added cost for upgrading from 500 GeV to 1000 GeV to be 5.5 B. All costs are given in ILC currency units ILCU, given by 1 ILCU = $ 1 US using 2012 prices.

As shown in Table 15.2, the total number of new TW cavities at 70 MV/m required is 21,000, spanning a linac length of 28 km, of which 22 km can be installed into the empty tunnel (from the removed 0.5 TeV), requiring 6 km of new tunnel to be installed. Adding in the length (16 km) of the 0.5 TeV section remaining, the total linac length will be 44 km, well below the expected site limit of 65 km. For 1600 CMs removed from the 0.5 TeV section, we estimate the savings in re-used parts to be in the range of 0.5B, provided the removal and production of CMs are properly staged. For the new 1.5 TeV section, the cavity loaded Q is 5×10^6, the input power per cavity will be 460 kW, with RF pulse length 1.76 ms. The total number of klystrons required is 1180, of which 360 klystrons are re-used from the 0.5 TeV removed section, and 65 klystrons are available from the 0.5 TeV remaining section (because it operates with the lower bunch charge than for 1 TeV), leaving 755 new klystrons to be added. The average RF power efficiency of new RF systems will be 65% and the existing RF systems from the first 0.5 TeV installation will be 0.5, giving an overall RF efficiency of 61%. The total 2 K refrigeration required will be 37 kW, of which 33 kW is re-used, leaving 4 kW new refrigeration to be installed. We assume a cryoload safety factor and RF power overhead of 20% each for the new installations. The damping ring and positron source will be same as for 1 TeV, due to the same number of bunches, but the beam dump cost will increase. Summing all the cost components outlined, the additional cost for the 2 TeV upgrade will be 4.9 B. The AC power to operate 2 TeV will be 315 MW, making this path attractive for the improved environmental impact. Note the substantial benefit to the AC power due to the 2 times higher R/Q of the TW cavities. If we follow the alternative path of removing the entire 1 TeV linac, keeping the RF, tunnel and Refrigerator, to install a brand new linac using 70 MV/m TW cavities, we will need to populate the existing 38 km of tunnel with 28,000 TW cavities (no new tunnel needed), and use the existing Refrigeration (no new refrigeration needed), adding 755 klystrons. Savings from re-using CM parts from $>$ 3000 CM from the 1 TeV section is estimated to be 1 B. The additional capital cost for this path will be 5.2 B, comparable to the path above, and the AC power will be 240 MW, less than the path above. The shorter tunnel and lower AC power may dominate the choice of this path.

Path 2a: 3 TeV Upgrade from 1 TeV with 70 MV/m TW Nb structures

The beam bunch charge for the 3 TeV upgrade is chosen to be 3 times lower than the bunch charge for 0.5 TeV stage to obtain a luminosity comparable to CLIC 3TeV [412]. The lower bunch charge helps with wakefields and with IP backgrounds. The number of bunches per RF pulse is doubled to 4900, and the bunch spacing is lowered due to the lower bunch charge (see Table 15.2).

The option adopted here is to remove ALL of the installed cryomodules for 1 TeV and replace them with new 70 MV/m TW cavities/cryomodules, plus add new linac sections to reach 3 TeV energy. We would re-use the existing RF and Refrigeration and CM parts from the removed 1 TeV section. As shown inTable 15.2, a total of 43,000 TW cavities will be required, so that with the (cavity to linac tunnel) filling factor of 0.75, the total length of the 3 TeV linac will be 57 km, under the expected site limit of 65 km. 38 km of tunnel would already be present from the 1 TeV removed, requiring 19 km of new linac tunnel. The total number of klystrons required will be 1500, of which 820 are available from the 1 TeV installation. The RF system cost will be higher due to the longer RF pulse length. Also, the existing 820 klystrons and RF system will have to be upgraded

to provide longer RF pulses, which will incur a cost of about 0.4 B. The efficiency of the first RF system installed with 360 klystrons for 0.5 TeV is 50%, and for the later installed RF system for the next 0.5 TeV with 460 klystrons it is 65%. Hence the average RF system efficiency used is 61%. The input power per cavity will be 300 kW due to the high gradient. The loaded Q will be 8×10^6. The total 2 K refrigeration requirement will be 95 kW of which 51 kW is already present, leaving a balance of 44 kW to be installed. Add in the cost of needed damping rings, positron source and beam dump for increasing the number of bunches from 2450 to 4900. The total additional capital cost for 3 TeV (from 1 TeV) will be 11.8 B, shown in Table 15.1 The total AC power to run 3 TeV will be 400 MW, with substantial benefit from the 100% higher R/Q of TW structures.

A lower cost alternative is to only replace the cavities/cryomodules in the first 0.5 TeV of the baseline stage which has relatively low performance (31.5 MV/m), as for the 2 TeV case above. The total number of new cavities installed will be 36,000, to require a tunnel length of 48 km plus 16 km of existing 0.5 TeV to make the total tunnel length of 64 km which is too close to the expected site limit. Therefore, this option is not preferred. Table 15.2 gives detailed parameters (for beam and accelerator) for ILC 3 TeV (Option 2a) with 70 MV/m TW structures as compared to CLIC 3 TeV. Note that the backgrounds at the IP for the ILC 3 TeV are much lower than for CLIC, and final beamstrahlung energy spread is 16% compared to 35% for CLIC. To reach the desired luminosity, the beam power is 61 MW with twice the number of bunches (4900) spaced closer together in the linac (250ns instead of 366 for 1 TeV) as allowed by the lower bunch charge. The peak beam current is 4.16 mA. The final vertical spot size is 1 nm, comparable to the CLIC case. Figure 15.1 shows the rough breakdowns for the costs of various systems: Cryomodules, RF, Refrigeration, Conventional Facilities, Damping Rings and Positron Sources for the two upgrade paths (1b and 2a) from 1 TeV (TDR) to 2 TeV and from 1 TeV to 3 TeV.

Path 2b: 3 TeV Upgrade with 80 MV/m Nb_3Sn structures at 4.2 K

Option 2b for 3 TeV is to consider 80 MV/m Standing Wave Nb_3Sn TESLA-like structures at 4.2 K with Q values of 1×10^{10}. In this case the challenge is to develop high performance Nb_3Sn. Due to the combined improvement of Carnot and technical efficiency at 4.2 K over 2 K, the ratio: AC power/cryo power improves from 730 to 230. We assume that the capital cost of 4.2 K refrigeration will be a factor 3 lower than for 2 K, and that the refrigerator units installed for 1 TeV are designed so that 1 watt of cooling at 2 K would be later equivalent to 3 watts of cooling at 4.2 K when the conversion is made for the 3 TeV upgrade at 4.2 K.

Our plan would be to install Nb_3Sn cavities for 3 TeV, removing all of the cryomodules for 1 TeV and replacing them with new 80 MV/m/$Q = 1 \times 10^{10}$ cavities/cryomodules, plus install new linac sections to reach 3 TeV energy. We will re-use the RF, Refrigeration and CM parts of the removed 1 TeV section, converting the 2 K refrigeration to remove heat load at 4.2 K. A total of 37,500 Nb_3Sn cavities will be required, so that with the filling factor (cavity to tunnel length) of 0.75, and the total length of the 3 TeV linac will be 50 km, well under the expected Japan site constraint of 65 km. 38 km of tunnel has already been installed for 1 TeV, so that 12 km of new linac will be required. The total number of klystrons required will be 2500, of which 820 are available from the removed 1 TeV installation. The existing klystrons and RF system will have

to be upgraded to provide longer RF pulses (2.6 ms), which will incur a cost of about 0.4 B. The number of new klystrons required is 1680. The average efficiency of old and new RF systems will be 63%. The input power per cavity will be 550 kW, at a loaded Q of 1×10^7, so couplers will need to be improved. The total 4.2 K refrigeration required will be 352 kW of which 51 kW (at 2 K) is already present for 1 TeV, equivalent to 150 kW at 4.2 K. The balance of 200 kW at 4.2 K needs to be installed. Add in the cost of needed damping rings, positron source and beam dump for increasing the number of bunches from 2450 to 4900. The total additional capital cost for 3 TeV will be 11.0 B, as shown in Table 15.1. The total AC power to run 3 TeV will 525 MW.

An alternative path is to install 2.5 TeV with Nb_3Sn cavities, keep the 0.5 TeV upgrade section (at 45 MV/m) and remove the 0.5 TeV section (at 31.5 MV/m). In this case, the total length of the 3 TeV linac will be 58 km, much closer to the expected 65 km limit. The capital cost will be smaller, 10.5 B, and the AC power will be larger, 560 MW. Operating the remaining 0.5 TeV section with Q_L of 1.6×10^7, and RF pulse length of 3.7 ms will be very challenging.

Incidentally, if the path considered is to install Nb_3Sn cavities for 2.5 TeV, leaving 16 km of the 0.5 TeV linac with 45 MV/m gradient in place, the total number of new cavities installed will be 31,000, to require a tunnel length of 41 km. Of this, 22 km is available and 19 km will be new tunnel. Therefore the total linac length will become 16 + 41 = 57 km, quite close to the expected site limit of 65 km. Thus, this path not preferred—despite the 0.5 B cost savings due to fewer cavities.

15.2 Very High Gradient Copper Accelerators

[corresponding editor: Emilio Nanni (nanni@slac.stanford.edu)]

The infrastructure provided by the construction of the ILC...

15.3 Plasma, Laser, and Structure Wakefield Accelerators

[5 pages; corresponding editor: Spencer Gessner (sgess@slac.stanford.edu)]

As a long-term goal, we envision upgrading the ILC with advanced accelerator technologies that not only deliver extremely high-energy beams, but do so in a highly-efficient manner to achieve high luminosities.

There are many challenges on the path to a PLC. May be able to solve some, but not all challenges. Develop notion of an Upgrade Matrix:

Beam-Driven Plasma Linear Collider

Research on beam-driven plasma wakefield acceleration is motivated by the ultimate goal of creating a linear collider that is affordable, highly-efficient, and operates at the highest possible energies.

Status	e^- Source	Positron acceleration	Drive complex	Interstage coupling	Plasm mediu
Conventional	Damping Ring	posi	Pulsed RF	Warm magnets	Laser-ioniz
Upgraded	Photoinjector	posi	CW RF	Warm magnets and plasma lenses	Laser-ionized
Advanced	Plasma injector	posi	CW High-Q	Combined function plasma	Beam-ionized

Table 15.3: Upgrade table for plasma-based linear collider.

There are many challenges on the path to a plasma-based upgrade to the ILC, but the field has shown steady progress on multiple fronts since the last Snowmass in 2013. Amongst many highlights are the first demonstration of highly-efficient plasma acceleration of electron beams [**?**], acceleration of positron beams in the non-linear regime [**?**], proton beam-driven acceleration [**?**], staged laser-plasma acceleration [**?**], plasma photocathodes for generating ultralow-emittance beams [**?**], and emittance preservation in an active plasma lens [**?**].

The remaining challenges associated with the development of a PLC have been identified in a variety of papers, workshops, and strategy sessions [**?**, **?**, **?**, **?**, **?**, **?**, **?**, **?**]. We enumerate some of them here:

1. High-efficiency, high-quality acceleration in a single plasma stage.
2. Coupling between plasma stages.
3. Positron acceleration in plasma.
4. Preservation of beam polarization.
5. High repetition-rate plasma acceleration and energy deposition in the plasma source.
6. Final focusing and alignment of beams at the collision point.

Experiments to demonstrate high-efficiency, high-quality electron acceleration in plasma are currently underway at FLASHForward at DESY and preparing to start at FACET-II at SLAC. These experiments will demonstrate the viability of PWFA technology and establish the tolerances for producing high-quality beams. Experiments at FLASHForward will also study high-repetition rate PWFA, while experiments at FACET-II will cover positron acceleration in plasma and beam focusing based on thin plasma lenses. Both FLASHForward and FACET-II need to be modified in order to demonstrate staged PWFA, which is a high priority for the field.

ILC Upgrade to multi-TeV using Laser Wakefield Accelerators

[1 page; corresponding authors: C. Schroeder, C. Geddes, E. Esarey (LBNL)]

Laser wakefield accelerators (LWFAs) [413] rely on an intense, ultrashort laser pulses to resonantly excite large amplitude electron plasma waves with relativistic phase velocities. The acceler-

ating fields of the plasma wave, or wakefields, are 1-10 GV/m, orders of magnitude larger than conventional accelerating structures, enabling compact acceleration of charged particle beams. LWFA technology provides an opportunity to upgrade the ILC to higher beam energy using the planned ILC main linac tunnel, site power, and infrastructure. An LWFA-based linac arm would consist of multiple plasma stages, each stage yielding a few GeV/stage energy gain, driven by a multi-J, short pulse laser [414, 415]. Laser drivers are highly flexible, and plasma mirror technology enables compact coupling of the laser driver into the plasma accelerating cells. The multi-Joule-class laser systems, potentially based on fiber laser combination, occupy an area of a few m2 and both the drive lasers and plasma accelerating stages may be placed in the ILC Main Linac tunnel. LWFAs accelerate short bunches, of order 10 micron, and the resulting beamstrahulung reduction at the IP yields significant power savings for a given target luminosity. To reach $E_{CM} = 1$ TeV, an LWFA-based linac requires potentially only 0.2 km in each linac arm, and 100 MW of power for both beams to reach a luminosity of 10^{34} cm^{-2}s^{-1}. This could be upgraded to $E_{CM} = 3$ TeV with luminosity of 10^{35} cm^{-2}s^{-1}, requiring a 0.65 km LWFA linac in each linac arm and 300 MW of power for both beams. The LWFA beam power for 1 TeV and 3 TeV would be 4 MW and 12 MW, respectively, and are within the power rating of the planned ILC beam dump. The unused main linac tunnel length could be employed to extend the BDS system to accommodate $E_{CM} = 3$ TeV, as well as space for linear cooling sections to further reduce the beam emittance. The bunch structure employed is one bunch each 20 μs, and additional bunch compressors would be required to achieve the short, 10-micron-scale, bunch length. Furthermore, achieving high beam energies (E_{CM} >3 TeV) is straightforward by adding additional LWFA stages, although the required increased luminosity would require site power beyond the planned ILC design. This provides a long-term upgrade path to continue realizing new physics reach in realistic stages using the infrastructure of a linear collider. Significant R&D is required to realize an LWFA-based linac, and, in particular, further development of high average power, short-pulse laser systems operating at tens of kHz repetition rates [416].

Structure Wakefield Accelerators

John Power (ANL), Chunguang Jing (ANL, Euclid) and Philippe Piot (ANL, NIU):

Structure Wakefield Acceleration (SWFA) has been proposed as the backbone for a high-gradient and high-efficiency accelerator for a multi-TeV linear collider [417]. Two separate SWFA schemes, two-beam acceleration (TBA) and collinear wakefield acceleration (CWA) are under consideration. This contribution will explore the application of the relatively mature SWFA schemes (both in the TBA and CWA implementations) as a possible upgrade path to the ILC. The ILC beam format (a train of 3.2 nC single-bunch with an O(MHz) micropulse repetition rate) is comparable to the 182-GHz CWA-based XFEL design that is being pursued at Argonne. The challenge for the CWA based linear collider would be to raise the overall efficiency due to its single pulse nature. Alternatively, the TBA technology currently under development at Argonne is a 26 GHz accelerator based on a high charge drive beam. Therefore, a TBA contribution to the ILC application would explore two avenues: either operating ILC with higher charge or raising the TBA operating frequency to operate at lower drive charge. Critical to both the TBA and CWA approaches would

be continued development of the SWFA bunch control R&D program. This program develops the bunch shaping technology critical for the main and drive beams. For example, we will explore the possibility of shaping the ILC 3.2nC Gaussian bunch for the CWA scheme with a transformer ratio of 5 to produce a 5TeV LC in the ILC tunnel at high efficiency. Note that bunch control is critical to both beam-driven wakefield acceleration methods: SWFA and plasma wakefield acceleration (PWFA).

15.4 Physics Opportunities for a Multi-TeV Collider

[7 pages; corresponding editors: Zhen Liu (zliuphys@umn.edu), James Wells (jwells@umich.edu)]

With the forward-looking multi-TeV collider in mind, consider the physics reach up to 3 TeV center-of-mass energy, leaving discussion on a higher energy collider to the following subsection. Multi-TeV collider options open the gates to access TeV new physics directly and explore new physics in a complementary way to the lower energy Higgs factory and high energy proton colliders. Multi-TeV lepton collider will shed light upon many-core puzzles of particle physics. We can probe Higgs self-coupling, Top Yukawas, electroweak precision observable in dibosons, testing EW symmetry breaking and universal theories, the SM precision measurement, etc. One can also access flavor physics through flavor-changing-neutral current measurement, lepton-flavor-universality-violation measurements, various Higgs Yukawas, and Top quark exotic decays. The multi-TeV collider enables us to directly produce and probe new particles, such as top partners, dark matter, and hidden sector new physics. In this section, we will select a few representative physics potentials of the Multi-TeV lepton collider, with many recent updates from CLIC [322, 418].

Higgs Trilinear

One can more directly access Higgs trilinear self-coupling at high-energy lepton colliders through the exploitation of Higgs pair production processes, which is affected by the Higgs self-coupling at tree level. An multi-TeV lepton collider like CLIC offers two main di-Higgs production modes [338], namely double Higgsstrahlung ($e^+e^- \to Zhh$) and vector boson fusion ($e^+e^- \to \nu\bar{\nu}hh$). The cross section for the two channels has different scaling as a function of the center of mass energy of the collider, see left panel of Fig. 15.2. Double Higgsstrahlung reaches a maximum not far above threshold (at $\sqrt{s} \sim 500\,\text{GeV}$) and then decreases due to the s-channel Z boson propagator. The vector boson fusion cross-section benefits from a logarithmic enhancement at higher collider energy. We consider multi-TeV collider with $\sqrt{s} = 1.4$ and 3 TeV 1.5 and $2\,\text{ab}^{-1}$ of integrated luminosity, respecitvely, with unpolarized beams [338].

In the right panel in Fig. 15.2 we show how the the trilinear Higgs self coupling changes the total cross-section in the two leading diHiggs channels. The result is shown as a function of $\delta\kappa_\lambda$, the correction to the Higgs self coupling normalized to its SM value:

$$\delta\kappa_\lambda = \kappa_\lambda - 1 = \hat{c}_6 - \frac{3}{2}\hat{c}_H. \tag{15.1}$$

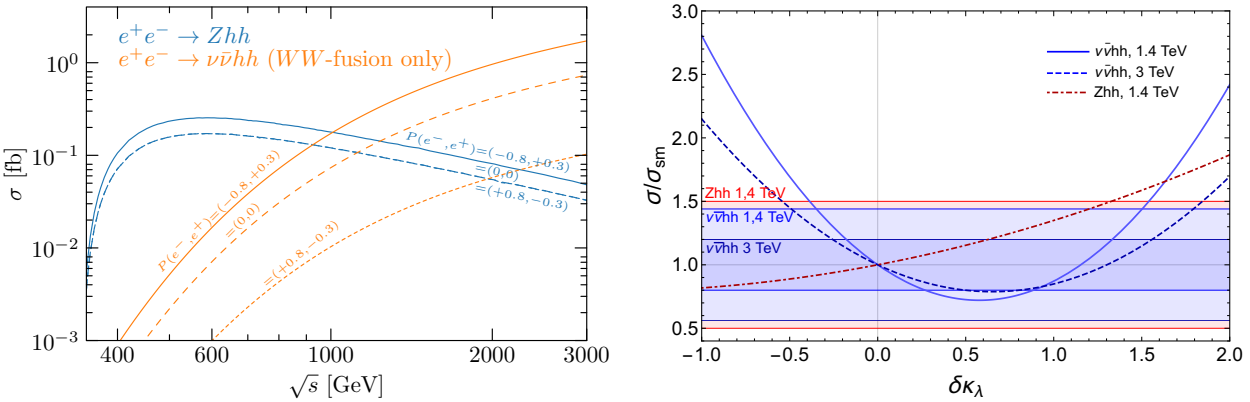

Figure 15.2: **Left:** Cross section of the two leading diHiggs production modes in a lepton collider as a function of the center-of-mass energy. **Right:** Dependence of the signal strengths on the trilinear coupling of the Higgs with the horizontal bands showing the estimated sensitivities.

We can see an interesting complementarity between these two leading diHiggs production channels. The Zhh cross-section grows for $\delta\kappa_\lambda > 0$ through constructive interference, more sensitive to positive deviations in the trilinear Higgs self coupling. The $\nu\bar{\nu}hh$ production, instead, is more sensitive to negative shifts of the trilinear coupling.

After combining both vector boson fusion and double Higgsstrahlung channels, the two runs at 1.4 TeV and 3 TeV are sufficient to exclude the second fit minimum at $\delta\kappa_\lambda \sim 1$ at 95%CL. We show the results in Table 15.4.

	$\Delta\chi^2 = 1$	$\Delta\chi^2 = 4$
1.4 TeV	$[-0.22,\ 0.48]$	$[-0.40,\ 1.05]$
3 TeV	$[-0.13,\ 0.16] \cup [1.13,\ 1.42]$	$[-0.24,\ 0.42] \cup [0.87,\ 1.53]$
combined	$[-0.12,\ 0.14]$	$[-0.21,\ 0.35]$
5 bins in $\nu\bar{\nu}hh$	$[-0.11,\ 0.13]$	$[-0.21,\ 0.29]$

Table 15.4: Single operator constraints on $\delta\kappa_\lambda$ deriving from the measurements of Zhh and $\nu\bar{\nu}hh$ cross sections, with all other parameters fixed to their standard-model values. In the lower two rows, a differential m_{hh} measurement in weak boson fusion di-Higgs production at $\sqrt{s} = 3$ TeV is further included.

The diHiggs production are also affected by modifications in other Higgs couplings. To consistently and reduce the model-dependence, we performed a study comparing single-operator constraints to that of a global fit, show in Table 15.5. The $\nu\bar{\nu}hh$ production with a differential analysis including 4 bins in the m_{hh} distribution, and the inclusive Zhh cross-section and the $\delta\kappa_\lambda$ dependence of the single-Higgs processes are included in this fit. The 3 TeV run will drastically increase the Higgs self-coupling sensitivity to the 1.4 TeV one, due to the increase in statistics to get access to detailed differential distributions.

	68 %CL	95%CL
1.4 TeV, exclusive	$[-0.21,\ 0.34]$	$[-0.38,\ 0.89]$
1.4 TeV, global	$[-0.22,\ 0.40]$	$[-0.39,\ 1.00]$
$1.4+3$ TeV, exclusive	$[-0.11,\ 0.12]$	$[-0.20,\ 0.27]$
$1.4+3$ TeV, global	$[-0.11,\ 0.13]$	$[-0.21,\ 0.29]$

Table 15.5: Single and global constraints on $\delta\kappa_\lambda$ after the 1.4 and 3 TeV runs of CLIC. We also show the combined results with the HL-LHC.

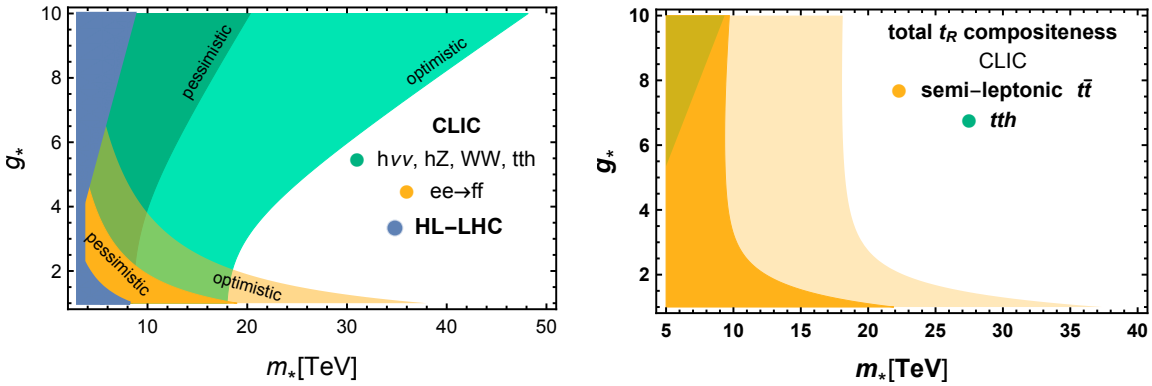

(a) 5σ discovery contours for Higgs compositeness in the (m_*, g_*) plane, overlaid with the 2σ projected exclusions from HL-LHC. Shaded areas are labeled as "pessimistic" and "optimistic" depending if operators coefficients were taken a factor 2 larger or smaller than the base estimates from the (m_*, g_*) value.

(b) The 5σ top quark compositeness discovery contours in the (m_*, g_*) planes from studies of $t\bar{t}$ and $t\bar{t}h$ final states. Darker and lighter shaded areas corresponds to the variations of the size of the operators coefficients by a multiplicative factor of 2 or 1/2 on top of the baseline expectation form the values of m_* and g_*.

Figure 15.3: Composite Higgs reach from Higgs boson, top quark and Drell-Yan studies taken from Refs. [322] and [298].

Higgs and Top Compositness

The Higgs precision program at a Multi-TeV lepton collider not only reveals the Higgs trilinear coupling but, more importantly, provides a holistic understanding of the dynamics of the Higgs boson. Typically we can see such comprehensive measurements through a global fit. Here, we highlight holistic physics through the important BSM paradigm of compositeness. We show the corresponding physics in terms of the composite Higgs geometric size l_H. A composite Higgs would manifest at CLIC through dimension-six SMEFT operators. The operator coefficients are enhanced or suppressed by positive or negative powers of the composite coupling parameter g^* [419]. We translate the CLIC sensitivity to the SMEFT into the discovery reach on Higgs compositeness, as displayed in Figure 15.3a from Ref. [322]. The projected HL-LHC exclusion reach (as opposed to discovery lines shown for CLIC) is also shown in the figure for unit c-coefficients. The improvement achieved by CLIC at small and intermediate g_* is due to the high-energy stages that allow for a

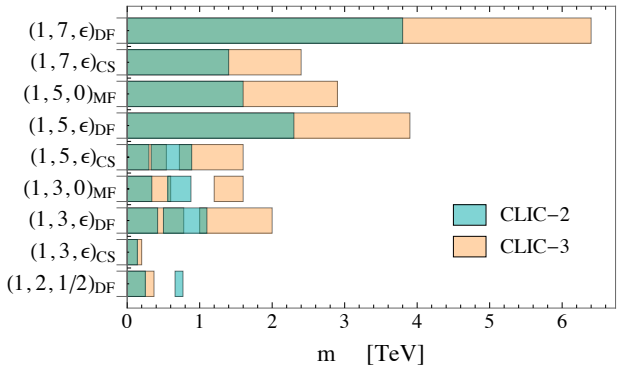

(a) 95% excluded masses for new electroweak n-plet states with hypercharge Y. The exclusion for each state denoted by (1,n,Y) at CLIC Stage2 and Stage3 is presented in green and yellow bar [421].

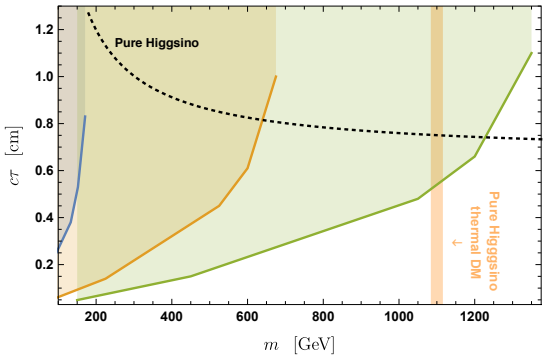

(b) 95% excluded region for a new physics signal from a pure Higgsino in the mass-lifetime plane. The black dashed line denotes the theory prediction for a the lifetime of a pure Higgsino doublet. Green, Yellow and Blue areas correspond to 3 TeV, 1.5 TeV and 380 GeV CLIC runs expected exclusions.

Figure 15.4: Reach of direct searches for Dark Matter.

very precise determination of the c_{HW}, c_{HB}, c_{2W} and c_{2B} SMEFT Wilson coefficients. Single Higgs boson couplings measurements are instead provide the most stringent constraints at large g_*.

The complementarity between precision and high mass searches can be seen in this plot. Measurements from high-intensity studies, from the Higgs precision, probe one combination of the two characteristic parameters of this scenario, while less copiously produced events probe the other combination at high invariant mass in the later stages of CLIC. We can also consider top quark compositeness in connection with the Naturalness puzzle. SMEFT operators in the top sector can be probed by measuring the top Yukawa coupling and as well as $t\bar{t}$ production at high-energy CLIC [420]. The reach in the "total t_R compositeness" scenario is displayed on Figure 15.3b. For further details, and for a similar result in the case of "partial top compositeness", see Sec. 2.1 of Ref. [322] and Sec. 10.2 of Refs. [298].

Dark Matter

The nature of dark matter in the Universe is a great mystery. Very little is known about the particle properties of dark matter and a large host of models provide viable dark matter candidates. A particularly compelling candidate is the so-called Weakly Interacting Massive Particles (WIMP) that naturally emerge from the standard cosmological history of the Universe as possible thermal relics that stop being in equilibrium with the plasma of the early Universe at a temperature roughly one order of magnitude below their mass and from that moment onward remain as relics in the Universe, interacting with the SM particles only through gravity, ultimately shaping the formation of galaxies and other cosmic structures. Thermal production of WIMPs can yield the observed abundance of dark matter for masses $M_{\rm WIMP} \simeq \text{TeV} \left(\frac{g_{\rm SM,DM}}{g_{\rm weak}}\right)^2$ where $g_{\rm DM,SM}$ roughly denotes the

strength of the couplings of processes that keep the dark matter in equilibrium, and g_{weak} is the coupling strength of the SM weak interactions.

Despite these requirements on the particle nature of the Dark Matter a large set of possibilities exists even if one restricts to consider weakly interacting massive particles. In Sec. 5 of Ref. [322] a comprehensive strategy is outlined to test a wide range of possible situations in which the Standard Model is extended by a WIMP and by other states possibly members of the same weak interactions multiplet or as independent state.

The approach we follow to study Dark Matter phenomenology by simply specifying masses and quantum numbers of new states has been called "Minimal DM" [422]. This approach has shown that new particles that can live also in very large (up to the 7-plet) representations of the SM $SU(2)$ group can give viable Dark Matter candidates. All this variety of weakly charged states are a target for future colliders. CLIC can probe them in several ways. First, one can perform model-independent indirect searches for new EW states by studying their radiative effects on the EW pair-production of SM particles, obtaining the 95% CL sensitivities reported in Figure 15.4a taken from results of Ref. [421]. The sensitivity reaches the thermal mass (i.e., the one which is needed in order to produce the observed thermal abundance) in the case of the Dirac fermion triplet candidate $(1, 3, \epsilon)_{\text{DF}}$. Second, one can exploit the fact that the charged component of the Minimal DM multiplet is long-lived, with a macroscopic decay length. Its distinctive signature is thus a "stub" track, which can be long enough to be seen if the particle is light enough to be sufficiently boosted. Figure 15.4b shows that CLIC can discover the thermal Higgsino at 1.1 TeV with this strategy.

In addition, it should be noted that CLIC is also sensitive to DM models that fall outside the Minimal DM paradigm, such as co-annihilation scenarios, in which two almost degenerate states can scatter into Standard Model states with a much stronger interaction than each of them singly. Models that exploit the presence of multiple states, such as the Inert Doublet model, can also be thoroughly explored at CLIC, extending significantly the domain of the parameters space probed in comparison to the HL-LHC capabilities [423, 424]. Details on these and other models are presented in Ref. [322, 425]. Here we content with stating that in general CLIC can effectively probe DM models with a sufficient mass-splitting to produce signals featuring prompt jets, leptons and photons plus missing momentum.

Hidden Sector

Hidden sector dynamics represents a large class of well-motivated BSM that are illusive at colliders and specialize search strategy are often needed for them. Here we chose two examples, RPV electroweakino in connection to baryogenesis, and Higgs decaying into Long-Lived hadronic particles in connection to neutral naturalness. For first example represents the reach for heavy new stables and the second example represents the reach for light stable through Higgs decays.

R-Parity Violating Long-Lived Wino and Higgsino

We consider a weak scale particle X that decays after its thermal freeze-out and triggers baryogenesis. A particle freezes out when its annihilation rate falls below the Hubble expansion rate. The temperature at freeze out, $T_{\rm fo}$, depends only logarithmically on the annihilation cross section, such that $T_{\rm fo} \sim M_X/20$ for annihilation cross sections $\sim$ fb.

The cosmological condition that X decay out of equilibrium requires that

$$c\tau_X \gtrsim 1 \text{ cm} \left(\frac{100 \text{ GeV}}{M_X}\right)^2. \tag{15.2}$$

Scattering with the SM may keep X in thermal equilibrium down to $T_{\rm fo}$, in which case the decay length should be somewhat longer. If X decays after freeze out, then the final baryon asymmetry is proportional to its would-be relic abundance if it does not decay (details see [426]). In any case, it is clear that WIMP baryogenesis models predict new particles that can decay in various components of a detector at the LHC (e.g. ATLAS or CMS) or CLIC, but typically in the displaced vertex regime (or out of detector as missing energy) due to the above cosmological condition.

If the decay temperature is less than the freeze-out temperature, $T_{\rm fo} > T_{\rm d} > T_{\rm BBN}$, and assuming that we can neglect washout processes, the baryon asymmetry is given by

$$\Delta_B = \epsilon_{\rm CP} n_X(T_{\rm fo}), \tag{15.3}$$

where $\epsilon_{\rm CP} < 1$ is a measure of CP violation in the decays that can be generated by interference between tree-level and loop-level decay diagrams. Directly measuring such a CP violation effect tied to baryogenesis at collider experiments is exciting yet generally challenging. So here we will focus on displaced decay signals tied to the other Sakharov condition for baryogenesis.

It is important to note that the lifetime of the parent particle X can be naturally very different from the couplings that lead to its production at the LHC. For example, if an approximately conserved Z_2 symmetry is responsible for the long lifetime, X particles can still be produced in pairs via Z_2 conserving interactions but decay slowly through interactions that violate the symmetry. These particles could be copiously produced at the LHC and CLIC. An earlier study proposed simplified models for WIMP baryogenesis mechanisms along with studies of sensitivity to these models in some searches at ATLAS and CMS [427].

The coverage extends to long and short lifetime as well, covering 0.1 millimeter to 500 meter for 500 GeV Wino. These pair-produced wino have low boost factors and therefore move slowly. Further development in using the precision timing for LLPs at the LHC, similar to the GMSB Higgsino benchmark study in Ref. [243], could improve the HL-LHC sensitivity significantly, especially for the long lifetime regime.

The advantage of high collision energy enables the LHC to cover wino mass up to 1650 GeV in the most sensitive $c\tau$ range ($\sim$ 10 cm). 3 TeV CLIC thus cannot compete with LHC in terms of the mass reach of wino in general. There is ample parameter space in $c\tau$ at masses below 1.5 TeV that HL-LHC are not sensitive to. This is due to both the large QCD background at the LHC and the current limit in vertex reconstruction efficiency. In contrast, CLIC, as a e^+e^- collider, provides a

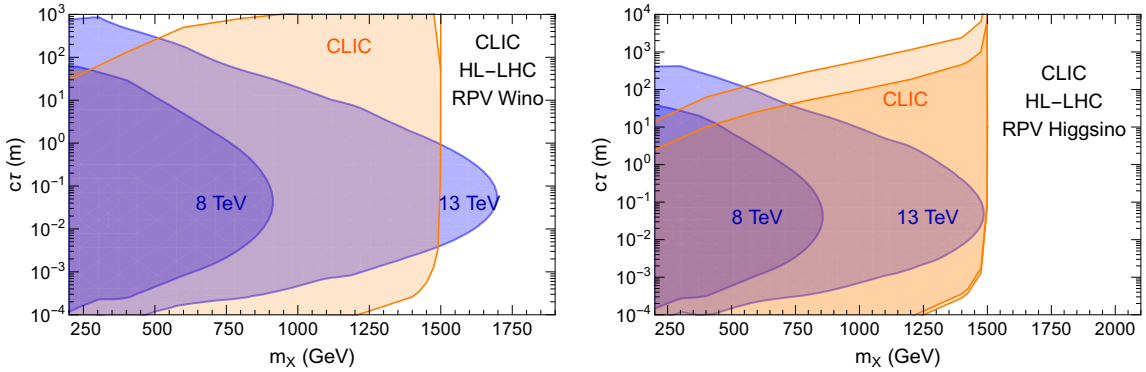

Figure 15.5: Event rates and exclusions for the wino and higgsino signal in the lifetime vs. mass plane. Orange: darker region corresponds to $N > 30$ events in the CLIC acceptance, lighter orange regions corresponds to $N > 3$ events and correspond to a projected 95% C.L. exclusion limit for zero expected background. The left (right) panel refers to the RPV wino (higgsino) signal. Blue region: the recasted current and HL-LHC (3 ab^{-1}) projected 95% C.L. exclusion limit as the function of Wino mass and its lifetime.

much cleaner environment for these searches, with almost full coverage for electroweak states below 1.5 TeV mass. With much lower background (in particular for hadronic channel) and improved vertex reconstruction techniques, CLIC has the great potential to close up the region that HL-LHC is not capable of effectively probing, which is illustrated in Fig. 15.5.

In Fig. 15.5, the projected exclusion limit for 3 TeV CLIC at 95% C.L. for the luminocity of $3\,\text{ab}^{-1}$ is indicated by the orange region in the wino mass and $c\tau$ parameter space, overlaid on the blue regions showing the LHC sensitivity. Here we simulated pair production of wino-like charginos at 3 TeV. The charginos almost exclusively decay to wino-like neutralino and a soft pion, since the couplings to bino-like neutralino states are heavily suppressed by large μ term. The wino-like neutralino decays hadronically via RPV couplings. We make simplified assumption for charginos: $c\tau_{\chi^\pm\to\chi^0} << c\tau_{\chi^\pm(\text{RPV})}$, so that tracks contributing to DVs come entirely from wino-like neutralinos and the track coming from the soft pion emitted by chargino decay is not associated with any vertex. For the analysis we assume a nearly perfect vertex reconstruction efficiency in the $c\tau$ range of $0.3 - 100$ mm. It is evident that CLIC at 3 TeV with $3\,\text{ab}^{-1}$ luminosity is sensitive to the large parts of parameter space that LHC is not, below the wino mass of 1500 GeV. It almost entirely covers the open parameter space for $c\tau > 1$ cm and $m_\chi < 1500$ GeV. For lower $c\tau$, CLIC can offer up to an order of magnitude improvement in terms of the reach in $c\tau$.

Higgs-portal singlet model The possibility that sets of particles secluded from our view exist in "mirror world" is an open question. These particles may be secluded to us because of a tiny coupling between Standard Model states and the new physics states in question. Such feeble interactions may be useful in a number of contexts to address open issues of the Standard Model, see e.g. Ref. [428] for a discussion, hence their search is very motivated. These searches are very challenging because the properties of the new physics states can only be vaguely guessed, hence a

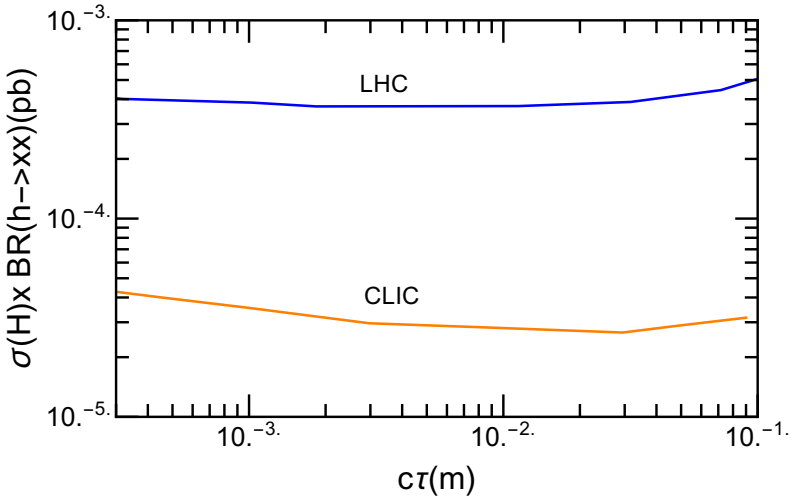

Figure 15.6: Blue line: HL-LHC projected 95% C.L. exclusion limit for the Higgs portal singlet model as the function of $c\tau_\chi$ for $m_\chi = 30$ GeV. Orange line: projection for CLIC with the same model.

broad program of searches needs to put in place to effectively explore this idea. In this context it is possible that new physics manifests itself with light new particles, which we have not yet seen because of their tiny couplings with SM particles. CLIC can make progress on the experimental exploration of this scenario in unique corners of its vast parameter space. For example, the clean environment and the absence of trigger allows CLIC to improve significantly over the HL-LHC in the search for Higgs or Higgs-like bosons decay to long-lived particles.

In Fig. 15.6, we compare the 95% C.L. reach of HL-LHC with CLIC for this class of models. LHC sensitivity of various classes of Higgs portal models is studied in [241]. These include Twin Higgs models, Folded SUSY models, quirky little Higgs models etc. Similar LHC sensitivity is obtained for the Higgs portal singlet model embedded in RPV-NMSSM that decays to SM quarks via RPV couplings as shown by the blue line in the Fig. 15.6 for $m_\chi = 30$ GeV.

At CLIC, the dominant mode of production is via W fusion, which has the cross section an order of magnitude lower than that at the LHC. Since we are dealing with on-shell production of light states, the cleaner environments and vertex reconstruction efficiencies can enable CLIC to have better $c\tau_\chi$ coverage than HL-LHC for a given mass of the exotic particle similar to the heavier case of RPV wino discussed before. This can be observed in Fig. 15.6. CLIC sensitivity to $h \to \chi\chi$ at 3 TeV for 95% C.L. is projected as indicated by the orange line using the sensitivity given for the Hidden valley models. CLIC will clearly have an order of magnitude better reach in the $c\tau_\chi$ range favored by the WIMP baryogenesis models with light singlets ($< 100\,\text{GeV}$).

CLIC can also search for relatively heavy Axion-Like Particles, that may be part of a feebly interacting sector that extends the Standard Model. These sectors may find their origin in several theoretical contexts, hence they are a useful simplified model to express the reach of CLIC in general parameter space ruled by the mass of the ALP and its decay constant. As a high en-

ergy collider CLIC can probe ALPs that are obviously outside the reach of dedicated low-energy experiments [378]. We can see that for the photo-phobic ALP [429] case, that are in any case representative for other couplings structures involving photons as well, and we can see about one order of magnitude of improvement in the bound of the decay constant of the ALP. In particular it is remarkable that CLIC can improve on LHC bounds and is able to enter regions of parameters space for the model in which the ALP mass is less than or comparable with its decay constant, where the models are more motivated.

15.5 Physics Opportunities for a Multi-10 TeV Collider

[5 pages; corresponding editors: Nathaniel Craig (ncraig@physics.ucsb.edu), Zhen Liu (zliuphys@umn.edu), Michael Peskin (mpeskin@slac.stanford.edu)]

(This section will review new work to be done for Snowmass on physics at very high energy e^+e^- and $\gamma\gamma$ colliders.)

Chapter 16

Conclusions

[3 pages; corresponding editor: Michael Peskin (mpeskin@slac.stanford.edu)]

This is the conclusion.

total page count: 186 pages + bibliography

ACKNOWLEDGEMENTS

We are grateful to ...

Bibliography

[1] T. Behnke, J.E. Brau, B. Foster, J. Fuster, M. Harrison, J.M. Paterson et al., eds., *The International Linear Collider Technical Design Report - Volume 1: Executive Summary*, 1306.6327.

[2] H. Baer et al., eds., *The International Linear Collider Technical Design Report - Volume 2: Physics*, 1306.6352.

[3] C. Adolphsen et al., eds., *The International Linear Collider Technical Design Report - Volume 3.I: Accelerator \& in the Technical Design Phase*, 1306.6353.

[4] C. Adolphsen et al., eds., *The International Linear Collider Technical Design Report - Volume 3.II: Accelerator Baseline Design*, 1306.6328.

[5] H. Abramowicz et al., *The International Linear Collider Technical Design Report - Volume 4: Detectors*, 1306.6329.

[6] P. Bambade et al., *The International Linear Collider: A Global Project*, 1903.01629.

[7] LCC Physics Working Group collaboration, *Tests of the Standard Model at the International Linear Collider*, 1908.11299.

[8] K. Fujii et al., *ILC Study Questions for Snowmass 2021*, 2007.03650.

[9] Linear Collider Collaboration collaboration, *The International Linear Collider Machine Staging Report 2017*, 1711.00568.

[10] M. Harrison, M. Ross and N. Walker, *Luminosity Upgrades for ILC*, 1308.3726.

[11] CERN, "Environment report." http://cds.cern.ch/record/2737239, 2020.

[12] JAHEP Subcommittee on Future Projects of High Energy Physics collaboration, S. Asai et al., "The final report of the subcommittee on future projects of high energy physics." http://www.jahep.org/office/doc/201202_hecsubc_report.pdf, 2012.

[13] Japan Association of High Energy Physicists (JAHEP), "A proposal for a phased execution of the international linear collider project." http://www.jahep.org/office/doc/201210_ILC_staging_e.pdf, 2012.

[14] T. Sanuki, "Overview of the topography and geology of the Kitakami site for the ILC." Presentation at DESY, Feb. 14, 2017, 2017.

[15] R.D. Heuer et al., "Parameters for the linear collider." https://icfa.fnal.gov/wp-content/uploads/para-Nov20-final.pdf, 2006.

[16] M. Dugan, G.and Harrison, B. List and N. Walker, "Implications of an energy-phased approach to the realization of the ILC." http://edmsdirect.desy.de/item/D00000001046475, 2014.

[17] G. White, "Change request ILC-CR-0002: Baseline optics to provide for a single $L*$." http://edmsdirect.desy.de/item/D00000001119175, 2014.

[18] K. Buesser, "Change request ILC-CR-0003: Detector hall with vertical shaft access." http://edmsdirect.desy.de/item/D00000001084745, 2014.

[19] E. Paterson, V. Kuchler, N. Solyak and T. Sanami, "Change request ILC-CR-0012: Reduction of width of linac shield wall and tunnel cross–section." http://edmsdirect.desy.de/item/D00000001127835, 2015.

[20] K. Yokoya, B. List and E. Paterson, "Change request ILC-CR-0013: Update of the ILC beam dump specifications." http://edmsdirect.desy.de/item/D00000001145035, 2016.

[21] K. Yokoya, "Change request ILC-CR-0016: Luminosity improvement at 250 GeV." http://edmsdirect.desy.de/item/D00000001159725, 2017.

[22] Positron Working Group, "Report on the ILC positron source." http://edmsdirect.desy.de/item/D00000001165115, 2018.

[23] International Committee for Future Accelerators (ICFA), "ICFA statement on the ILC operating at 250 GeV as a Higgs boson factory." https://icfa.fnal.gov/wp-content/uploads/ICFA-Statement-Nov2017.pdf, 2017.

[24] "TESLA Technology Collaboration." http://tesla-new.desy.de/.

[25] S. Schreiber and B. Faatz, *The free-electron laser flash*, *High Power Laser Science and Engineering* **3** (2015) E20.

[26] M. Vogt et al., *Status of the Superconducting Soft X-Ray Free-Electron Laser FLASH at DESY*, in *Proceedings, 9th International Particle Accelerator Conference (IPAC 2018), Vancouver, BC, Apr 29–May 4, 2018*, pp. 1481–1484 (TUPMF090), 2018, DOI.

[27] "European XFEL." https://www.xfel.eu/.

[28] "LCLS-II: A world-class discovery machine." https://lcls.slac.stanford.edu/lcls-ii.

[29] Z. Zhao, D. Wang, Z.-H. Yang and L. Yin, *SCLF: An 8-GeV CW SCRF Linac-Based X-Ray FEL Facility in Shanghai*, in *Proceedings, 38th International Free Electron Laser Conference, FEL2017*, pp. 182–184 (MOP055), 2018, DOI.

[30] N. Huang et al., *Features and futures of X-ray free-electron lasers*, *The innovation* **2** (2021) 100097.

[31] C. Adolphsen, "Optimum ML cavity performance: gradient, $Q0$, and other ML parameters." Presentation at 2011 Linear Collider Workshop of the Americas (ALCPG11), Eugene, OR, Mar 19–23, 2011, https://agenda.linearcollider.org/event/4572/, 2011.

[32] W. Singer et al., *Production of superconducting 1.3 GHz cavities for the European X-ray Free Electron Laser*, *Phys. Rev. Accel. Beams* **19** (2016) 092001.

[33] D. Reschke et al., *Performance in the vertical test of the 832 nine-cell 1.3 GHz cavities for the European X-ray Free Electron Laser*, *Phys. Rev. Accel. Beams* **20** (2017) 042004.

[34] N.J. Walker and D. Kostin, "The European XFEL – experience and lessons learned." Presentation, International Workshop on Future Linear Colliders (LCWS2017), Strasbourg, France, Oct 22–27, 2017, https://agenda.linearcollider.org/event/7645/, 2017.

[35] W. Kaabi et al., *Power couplers for XFEL*, in *Proceedings, 4th International Particle Accelerator Conference (IPAC 2013), Shanghai, China, May 12-17, 2013*, pp. 2310–2312 (WEPWO001), 2013, http://JACoW.org/IPAC2013/papers/wepwo001.pdf.

[36] S. Sierra et al., *Status and lesson learned from manufacturing of FPC couplers for the XFEL program*, in *Proceedings, 28th International Linear Accelerator Conference (LINAC16), East Lansing, MI, Sep 25–30, 2016*, pp. 572–574 (TUPLR048), 2017, DOI.

[37] D. Reschke, W. Decking, N. Walker and H. Weise, *The commissioning of the European XFEL Linac and its performance*, in *Proceedings, 18th International Conference on RF Superconductivity (SRF2017): Lanzhou, China, Jul 17–21, 2017*, pp. 1–5 (MOXA02), 2018, DOI.

[38] S. Berry and O. Napoly, *Assembly of XFEL cryomodules: lessons and results*, in *Proceedings, 28th International Linear Accelerator Conference (LINAC16): East Lansing, Michigan, September 25-30, 2016*, pp. 646–650 (WE1A02), 2017, DOI.

[39] T.J. Peterson et al., *A Survey of Pressure Vessel Code Compliance for Superconducting RF Cryomodules*, *AIP Conf. Proc.* **1434** (2011) 1575 [1209.2405].

[40] H. Weise, *How To Produce 100 Superconducting Modules for the European XFEL in Collaboration and with Industry*, in *Proceedings, 5th International Particle Accelerator Conference (IPAC 2014): Dresden, Germany, Jun 15–20, 2014*, pp. 1923–1928 (WEIB03), 2014, DOI.

[41] D. Kostin, W.-D. Moeller, A. Goessel and K. Jensch, *Superconducting accelerating module tests at DESY*, in *Proceedings,14th International Conference on RF Superconductivity (SRF2009), Berlin, Sep 20–25, 2009*, pp. 180–184 (TUPPO005), 2009, http://accelconf.web.cern.ch/AccelConf/SRF2009/papers/TUPPO005.PDF.

[42] D. Broemmelsiek et al., *Record High-Gradient SRF Beam Acceleration at Fermilab*, *New J. Phys.* **20** (2018) 113018 [1808.03208].

[43] Y. Yamamoto et al., *Achievement of Stable Pulsed Operation at 36 MV/m in STF-2 Cryomodule at KEK*, in *Proceedings, 18th International Conference on RF Superconductivity (SRF2017), Lanzhou, China, Jul 17–21, 2017*, pp. 722–728 (THYA02), 2018, DOI.

[44] K. Kasprzak et al., *Test Results of the European XFEL Serial-production Accelerator Modules*, in *Proceedings, 18th International Conference on RF Superconductivity (SRF2017), Lanzhou, China, July 17-21, 2017*, pp. 312–316 (MOPB106), 2018, DOI.

[45] S1Global collaboration, "S1Global report." http://edmsdirect.desy.de/item/D00000001005135, 2012.

[46] M.A. Kemp et al., *Final design of the SLAC P2 Marx klystron modulator*, in *Proceedings, 18th IEEE International Pulsed Power Conference (PPC11), Chicago, IL, Jun 19-23, 2011*, pp. 1582–1589, 2011, DOI.

[47] M.P.J. Gaudreau, N. Silverman, B. Simpson and J. Casey, *ILC-class Marx modulator at KEK*, in *Proceedings, 5th International Particle Accelerator Conference (IPAC 2014), Dresden, Germany, Jun 15-20, 2014*, pp. 562–563 (MOPME082), 2014, http://jacow.org/IPAC2014/papers/mopme082.pdf.

[48] I. Syratchev, "Introduction to the High Efficiency International Klystron Activity HEIKA." Presentation, CLIC workshop 2015, Geneva, Switzerland, Jan 26–30, 2015, https://indico.cern.ch/event/336335/, 2015.

[49] F. Gerigk, *Status and future strategy for advanced high power microwave sources for accelerators*, in *Proceedings, 9th International Particle Accelerator Conference (IPAC 2018), Vancouver, BC, Canada, Apr 29–May 4, 2018*, pp. 12–17 (MOYGB1), 2018, DOI.

[50] I.A. Guzilov, *Bac method of increasing the efficiency in klystrons*, in *Proceedings, 10th International Vacuum Electron Sources Conference (IVESC), Jun 30–Jul 4, 2014*, p. 6891996, 2013, DOI.

[51] D. Constable et al., *High efficiency klystron development for particle accelerators*, in *Proceedings, 58th ICFA Advanced Beam Dynamics Workshop on High Luminosity Circular e^+e^- Colliders (eeFACT2016), Daresbury, UK, Oct 24–27, 2016*, pp. 185–187 (WET3AH2), 2017, DOI.

[52] A.Y. Baikov, C. Marrelli and I. Syratchev, *Toward high-power klystrons with RF power conversion efficiency on the order of* 90 %, *IEEE Trans. Electron. Dev.* **62** (2015) 3406.

[53] E. Jensen, "Recent developments towards very high efficiency klystrons." Presentation, 9th CW and high average RF power workshop, Grenoble, France, Jun 20–24, 2016, https://indico.cern.ch/event/472685/, 2016.

[54] H. Nakai, "Change request ILC-CR-0014: Cryogenic layout." http://edmsdirect.desy.de/item/D00000001146525, 2016.

[55] R. Alley et al., *The Stanford Linear Accelerator polarized electron source*, *Nucl. Instrum. Meth.* **A365** (1995) 1.

[56] G. Alexander et al., *Undulator-based production of polarized positrons*, *Nucl. Instrum. Meth.* **A610** (2009) 451 [0905.3066].

[57] K. Moffeit et al., "Spin rotation schemes at the ILC for two interaction regions and positron polarization with both helicities." SLAC-TN-05-045, 2005.

[58] L.I. Malysheva et al., *Design of Pre-Dumping Ring Spin Rotator with a Possibility of Helicity Switching for Polarized Positrons at the ILC*, 1602.09050.

[59] M.G. Billing et al., *Status of Low Emittance Tuning at CesrTA*, in *Proceedings, 24th Particle accelerator Conference (PAC'11), New York, NY, Mar 28–Apr 1, 2011*, pp. 1540–1542 (WEP022), 2011, http://accelconf.web.cern.ch/AccelConf/PAC2011/papers/WEP022.PDF.

[60] J.V. Conway, Y. Li and M.A. Palmer, *The conceptual design of a vacuum system for the ilc damping rings incorporating electron cloud mitigation techniques*, in *Proceedings, 3rd International Conference on Particle accelerator (IPAC 2012), New Orleans, LA, May 2-25, 2012*, pp. 1960–1962 (TUPPR062), 2012, http://accelconf.web.cern.ch/AccelConf/IPAC2012/papers/TUPPR062.PDF.

[61] T. Naito et al., *Multi-bunch beam extraction using strip-line kicker at KEK-ATF*, in *Proceedings, 1st International Particle Accelerator Conference (IPAC'10), Kyoto, Japan, May 23–28, 2010*, pp. 2386–2388 (WEOBMH02), 2010, http://accelconf.web.cern.ch/AccelConf/IPAC10/papers/weobmh02.pdf.

[62] P. Emma, T. Raubenheimer and F. Zimmermann, *A bunch compressor for the next linear collider*, in *Proceedings, 16th Particle Accelerator Conference and International Conference on High-Energy Accelerators, (HEACC 1995), Dallas, TX, May 1-5, 1995*, pp. 704–706 (RPC03), 1996, http://accelconf.web.cern.ch/AccelConf/p95/ARTICLES/RPC/RPC03.PDF.

[63] N. Walker, "Change request ILC-CR-0010: Proposal to include bunch compressor sections into main linac accelerator system." http://edmsdirect.desy.de/item/D00000001119175, 2015.

[64] P. Raimondi and A. Seryi, *A Novel final focus design for future linear colliders*, *Phys. Rev. Lett.* **86** (2001) 3779.

[65] ATF2 collaboration, B.I. Grishanov et al., "ATF2 Proposal." SLAC-R-771, CERN-AB-2005-035, DESY-05-148, KEK-REPORT-2005-2, 2005.

[66] B.I. Grishanov et al., *ATF2 proposal, Vol. 2*, physics/0606194.

[67] T. Okugi, *Achievement of small beam size at ATF2 beamline*, in *Proceedings, 28th International Linear Accelerator Conference (LINAC16), East Lansing, MI, Sep 25-30, 2016*, pp. 27–31 (MO3A02), 2017, DOI.

[68] ATF2 collaboration, *Experimental validation of a novel compact focusing scheme for future energy-frontier linear lepton colliders*, *Phys. Rev. Lett.* **112** (2014) 034802.

[69] R.J. Apsimon et al., *Design and operation of a prototype interaction point beam collision feedback system for the International Linear Collider*, *Phys. Rev. Accel. Beams* **21** (2018) 122802 [1812.08432].

[70] R. Ramjiawan et al., *Development of a Low-Latency, High-Precision, Beam-Based Feedback System Based on Cavity BPMs at the KEK ATF2*, in *Proceedings, 9th International Particle Accelerator Conference (IPAC 2018): Vancouver, BC, Ap 29–May 4, 2018*, pp. 2212–2215 (WEPAL025), 2018, DOI.

[71] A. Latina and A. Faus-Golfe, "ATF2." Input paper for European Strategy for Particle Physics Update, 2018.

[72] D.R. Walz, L.R. Lucas, H.A. Weidner, R.J. Vetterlein and E.J. Seppi, *Beam Dumps, Energy Slits and Collimators at SLAC - - Their Final Versions and First Performance Data*, *IEEE Trans. Nucl. Sci.* **14** (1967) 923.

[73] S. Boogert et al., *Polarimeters and Energy Spectrometers for the ILC Beam Delivery System*, *JINST* **4** (2009) P10015 [0904.0122].

[74] B. Vormwald, J. List and A. Vauth, *A calibration system for Compton polarimetry at e^+e^- linear colliders*, *JINST* **11** (2016) P01014 [1509.03178].

[75] K. Yokoya, K. Kubo and T. Okugi, *Operation of ilc250 at the z-pole*, *arXiv preprint arXiv:1908.08212* (2019) .

[76] ILC Strategy Council, "Announcement of the results of the ILC candidate site evaluation in Japan." Press release 28.8.2014, http://ilc-str.jp/topics/2013/08281826/, 2014.

[77] B. Warmbein, "The road to Kitakami." ILC Newsline Feb. 20, 2014, http://newsline.linearcollider.org/2014/02/20/the-road-to-kitakami/, 2014.

[78] T. Sanuki, "New developments at the Kitakami site." Presentation at Linear Collider Workshop 2015 (LCWS15), Whistler, BC, Canada, Nov 1–7, 2015, https://agenda.linearcollider.org/event/6662/, 2015.

[79] T. Sanuki and I. Sekine, "Seismic base isolation for detectors and accelerator." Presentation at International Workshop on Future Linear Colliders, LCWS2018, Arlington, TX, Oct 22-26, 2018, https://agenda.linearcollider.org/event/7889/, 2018.

[80] T. Sanuki, "Tunnel floor vibration issue." Presentation at Asian Linear Collider Workshop (ALCW 2018), Fukuoka, Japan, May 28–Jun 2, 2018, https://agenda.linearcollider.org/event/7826/, 2018.

[81] OECD, "Prices and purchasing power parities (PPP)." http://www.oecd.org/sdd/prices-ppp/, 2018.

[82] Eurostat, *Eurostat-OECD methodological manual on Purchasing Power Parities*, Luxembourg: Publications Office of the European Union, 2012 ed. (2012).

[83] ILC Advisory Panel, "Summary of the ILC advisory panel's discussions to date after revision." Report, Jul 4, 2018, http://www.mext.go.jp/component/b_menu/shingi/toushin/__icsFiles/afieldfile/2018/09/20/1409220_2_1.pdf, 2018.

[84] P. Bambade, T. Barklow, T. Behnke, M. Berggren, J. Brau, P. Burrows et al., *The international linear collider: a global project*, *arXiv preprint arXiv:1903.01629* (2019) .

[85] S. Asai, J. Tanaka, Y. Ushiroda, M. Nakao, J. Tian, S. Kanemura et al., *Report by the committee on the scientific case of the ilc operating at 250 gev as a higgs factory*, *arXiv preprint arXiv:1710.08639* (2017) .

[86] A. Grassellino et al., *Accelerating fields up to 49 MV/m in TESLA-shape superconducting RF niobium cavities via 75C vacuum bake*, 1806.09824.

[87] A. Grassellino et al., *Unprecedented quality factors at accelerating gradients up to 45 MV/m in niobium superconducting resonators via low temperature nitrogen infusion*, *Supercond. Sci. Technol.* **30** (2017) 094004 [1701.06077].

[88] A. Gurevich, *Enhancement of rf breakdown field of superconductors by multilayer coating*, *Applied Physics Letters* **88** (2006) 012511.

[89] T. Kubo, *Superheating fields of semi-infinite superconductors and layered superconductors in the diffusive limit: structural optimization based on the microscopic theory*, *Superconductor Science and Technology* **34** (2021) 045006.

[90] M. Harrison, M. Ross and N. Walker, *Luminosity Upgrades for ILC*, in *Community Summer Study 2013: Snowmass on the Mississippi*, 8, 2013 [1308.3726].

[91] T. Sanuki, "Tunnel floor vibration issues." Presentation, Asian Linear Collider Workshop (ALCW2018), Fukuoka, Japan, May 28–Jun 2, 2018. https://agenda.linearcollider.org/event/7826/, 2018.

[92] K. Yokoya, *Beam-beam interaction in linear collider*, in *AIP Conference Proceedings*, vol. 592, pp. 185–204, American Institute of Physics, 2001.

[93] L. Evans and S. Michizono, *The international linear collider machine staging report 2017*, *arXiv preprint arXiv:1711.00568* (2017) .

[94] A. Ushakov, G. Moortgat-Pick, S. Riemann, W. Liu and W. Gai, *Positron source simulations for ilc 1 tev upgrade*, *arXiv preprint arXiv:1301.1222* (2013) .

[95] J. Jones and D. Angal-Kalinin, *Beam delivery system dogleg design and integration for the international linear collider*, *EuCARD-CON-2010-032* (2010) .

[96] A. Yamamoto in *ESPP Symposium 2019*, 2019.

[97] M. Pekeler, *Superconducting RF Cavity System Production for Particle Accelerators in Scientific and Industrial Applications*, in *Proceedings of ICHEP 2016*, 2016.

[98] W. Singer et al., *Development of large grain cavities*, *Phys. Rev. ST Accel. Beams* **16** (2013) 012003.

[99] A. Grassellino, *N Doping: Progress in Development and Understanding*, in *17th International Conference on RF Superconductivity*, p. MOBA06, 2015, DOI.

[100] A. Romanenko and C. Edwardson, *The effect of vacancies on the microwave surface resistance of niobium revealed by positron annihilation spectroscopy*, *Appl. Phys. Lett.* **102** (2013) 232601.

[101] S. Posen, A. Romanenko, A. Grassellino, O. Melnychuk and D. Sergatskov, *Ultralow Surface Resistance via Vacuum Heat Treatment of Superconducting Radio-Frequency Cavities*, *Phys. Rev. Applied* **13** (2020) 014024 [1907.00147].

[102] F. He et al., *Medium-temperature furnace bake of Superconducting Radio-Frequency cavities at IHEP*, 2012.04817.

[103] P. Dhakal, *Nitrogen Doping and Infusion in SRF Cavities: A Review*, *Phys. Open* **5** (2020) 100034 [2005.03149].

[104] K. Umemori, E. Kako, T. Konomi, S. Michizono, T. Okada, H. Sakai et al., *Study on Nitrogen Infusion using KEK New Furnace*, in *19th International Conference on RF Superconductivity (SRF 2019)*, p. MOP027, 2019, DOI.

[105] M. Wenskat, C. Bate, A. Jeromin, T. Keller, J. Knobloch, F. Kramer et al., *Cavity Cut-out Studies of a 1.3 GHz Single-cell Cavity After a Failed Nitrogen Infusion Process*, in *19th International Conference on RF Superconductivity (SRF 2019)*, p. MOP025, 2019, DOI.

[106] V. Shemelin and H. Padamsee, *The optimal shape of cells of a superconducting accelerating section*, .

[107] V. Shemelin, H. Padamsee and R. Geng, *Optimal cells for TESLA accelerating structure*, *Nucl. Instrum. Meth. A* **496** (2003) 1.

[108] J. Sekutowicz et al., *Low Loss Cavity for the 12 GeV CEBAF Upgrade*, .

[109] K. Saito, *"Strategy for 50 MV/m*, .

[110] Z. Li and C. Adolphsen, *A New SRF Cavity Shape with Minimized Surface Electric and Magnetic Fields for the ILC*, .

[111] F. Furuta et al., *Experimental comparison at KEK of high gradient performance of different single cell superconducting cavity designs*, *Conf. Proc. C* **060626** (2006) 750.

[112] G. Eremeev, R. Geng, H. Padamsee and V. Shemelin, *High Gradient Studies for ILC with Single Cell Re entrant Shape and Elliptical Shape Cavities made of Fine grain and Large grain Niobium*, *Conf. Proc. C* **070625** (2007) 2337.

[113] R. Geng, A. Seaman, V. Shemelin and H. Padamsee, *World record accelerating gradient achieved in a superconducting niobium RF cavity*, *Conf. Proc. C* **0505161** (2005) 653.

[114] C.E. Reece and G. Ciovati, *Superconducting Radio-Frequency Technology R& D for Future Accelerator Applications*, *Rev. Accel. Sci. Tech.* **5** (2012) 285 [1208.1978].

[115] R.L.e. Geng, *LSF Shape Cavity Development: Recent Results and Future Plan*, in *LCWS 2018*, 2018.

[116] T. Peterson and J. Weisend II, *TESLA & ILC Cryomodules*, in *Cryostat Design*, pp. 117–145 (2016), DOI.

[117] A. Avrakhov, P. Kanareykin and N. Solyak, *Traveling wave accelerating structure for a superconducting accelerator*, *Conf. Proc. C* **0505161** (2005) 4296.

[118] R. Kostin, P. Avrakhov, A. Kanareykin, N. Solyak, V. Yakovlev, S. Kazakov et al., *A high gradient test of a single-cell superconducting radio frequency cavity with a feedback waveguide*, *Supercond. Sci. Technol.* **28** (2015) 095007.

[119] V. Shemelin*PRSTAB, to be submitted* (2021) .

[120] S. Posen and D. Hall, *Nb_3Sn superconducting radiofrequency cavities: fabrication, results, properties, and prospects*, *Supercond. Sci. Technol.* **30** (2017) 033004.

[121] S. Posen, J. Lee, O. Melnychuk, Y. Pischalnikov, D. Seidman, D. Sergatskov et al., *Nb_3Sn at Fermilab: Exploring Performance*, in *19th International Conference on RF Superconductivity (SRF 2019)*, p. THFUB1, 2019, DOI.

[122] S. Posen in *TTC2019*, 2019.

[123] e. Godeke, A.*Supercond. Sci. Technol.* **19** (2006) R68.

[124] e. Becker, C.*Appl. Phys. Lett.* **106** (2015) 082602.

[125] I.L.C.I.A. Panel, *Summary of the ilc advisory panel's discussions to date after revision*, 2018.

[126] S.C. of Japan, *Assessment of the revised plan of international linear collider project*, 2018.

[127] I.I.D.T.W.G. 2, *Technical preparation and work packages during ilc pre-lab*, 2021. 10.5281/zenodo.4742018.

[128] R. Hori.

[129] F. Furuta, D. Bice, A.C. Crawford and T. Ring, *Fermilab EP Facility Improvement*, in *19th International Conference on RF Superconductivity (SRF 2019)*, pp. 453–455, 2019, DOI.

[130] Y. Pischalnikov, B. Hartman, J. Holzbauer, W. Schappert, S. Smith and J.-C. Yun, *Reliability of the LCLS II SRF Cavity Tuner*, in *17th International Conference on RF Superconductivity*, p. THPB065, 2015, DOI.

[131] V. Kashikhin, S. Cheban, J. DiMarco, E. Harms, A. Makarov, T. Strauss et al., *Superconducting Magnet Performance in LCLS-II Cryomodules*, in *9th International Particle Accelerator Conference*, p. WEPML009, 2018, DOI.

[132] M. Doleans, *Ignition and monitoring technique for plasma processing of multicell superconducting radio-frequency cavities*, *J. Appl. Phys.* **120** (2016) 243301.

[133] P. Berrutti, B. Giaccone, M. Martinello, A. Grassellino, T. Khabiboulline, M. Doleans et al., *Plasma ignition and detection for in-situ cleaning of 1.3 GHz 9-cell cavities*, *J. Appl. Phys.* **126** (2019) 023302 [1902.03172].

[134] S. Posen, J. Lee, D. Seidman, A. Romanenko, B. Tennis, O. Melnychuk et al., *Advances in Nb_3Sn superconducting radiofrequency cavities towards first practical accelerator applications*, 2008.00599.

[135] T. Barklow, J. Brau, K. Fujii, J. Gao, J. List, N. Walker et al., *ILC Operating Scenarios*, 1506.07830.

[136] M. Woods, *The Polarized electron beam for the SLAC linear collider*, in *12th International Symposium on High-energy Spin Physics (SPIN 96)*, pp. 623–627, 10, 1996 [hep-ex/9611006].

[137] M. Habermehl, *Dark Matter at the International Linear Collider*, Ph.D. thesis, Hamburg U., Hamburg, 2018. 10.3204/PUBDB-2018-05723.

[138] J. Strube and M. Titov, *Detector Liaison Report v2021.2.2*, *Zenodo* (2021) .

[139] M. Thomson, *Particle Flow Calorimetry and the PandoraPFA Algorithm*, *Nucl.Instrum.Meth.* **A611** (2009) 25 [0907.3577].

[140] K. Fujii et al., *Physics Case for the 250 GeV Stage of the International Linear Collider*, 1710.07621.

[141] J. Brau and *et.al.*, "The international linear collider: A global project." http://ilchome.web.cern.ch/sites/ilchome.web.cern.ch/files/ILC_Global_Project_Final.pdf, 2018.

[142] Strube, Jan and Titov, Maxim, "Linear Collider R&D liaison report." http://linearcollider.org/physics-detectors/working-group-detector-rd-liaison, 2018.

[143] L. Greiner, E. Anderssen, H. Matis, H. Ritter, J. Schambach et al., *A MAPS based vertex detector for the STAR experiment at RHIC*, *Nucl.Instrum.Meth.* **A650** (2011) 68.

[144] DEPFET collaboration, *The ultralight DEPFET pixel detector of the Belle II experiment*, *Nucl. Instrum. Meth.* **A845** (2017) 118.

[145] S. Murai, A. Ishikawa, T. Sanuki, A. Miyamoto, Y. Sugimoto, C. Constantino et al., *Recent status of FPCCD vertex detector R&D*, in *Proceedings, International Workshop on Future Linear Colliders (LCWS15): Whistler, B.C., Canada, November 02-06, 2015*, 2016 [1603.00009].

[146] T.a.t.L..c. Frank Gaede, "Linear Collider Workshop 2018 in Arlington, USA." https://agenda.linearcollider.org/event/7889/, 2018.

[147] LCTPC collaboration, *Development of a TPC for an ILC Detector*, *Phys. Procedia* **37** (2012) 456 [1203.2074].

[148] M. Hauschild, *Particle ID with dE/dx at the TESLA-TPC*, *AIP Conf. Proc.* **578** (2001) 878.

[149] LCTPC collaboration, *A Time Projection Chamber with GEM-Based Readout*, *Nucl. Instrum. Meth.* **A856** (2017) 109 [1604.00935].

[150] J. Bouchez et al., *Bulk micromegas detectors for large TPC applications*, *Nucl. Instrum. Meth.* **A574** (2007) 425.

[151] F. Sefkow, A. White, K. Kawagoe, R. Pöschl and J. Repond, *Experimental Tests of Particle Flow Calorimetry*, *Rev. Mod. Phys.* **88** (2016) 015003 [1507.05893].

[152] CALICE collaboration, *Technological Prototypes and Result Highlights of Highly Granular Calorimeters*, *PoS* **EPS-HEP2017** (2017) 497.

[153] CALICE collaboration, *Beam Test Results with Highly Granular Hadron Calorimeters for the ILC*, *Conf. Proc.* **C0908171** (2009) 539 [1002.1012].

[154] CALICE collaboration, *Construction of a technological semi-digital Hadronic calorimeter prototype for ILC*, in *Proceedings, 2010 IEEE Nuclear Science Symposium and Medical Imaging Conference (NSS/MIC 2010): Knoxville, Tennessee, October 30-November 6, 2010*, pp. 1800–1803, 2010, DOI.

[155] H. Abramowicz et al., *Forward Instrumentation for ILC Detectors*, *JINST* **5** (2010) P12002 [1009.2433].

[156] I. Bozovic-Jelisavcic, S. Lukic, M. Pandurovic and I. Smiljanic, *Precision luminosity measurement at ILC*, in *International Workshop on Future Linear Colliders (LCWS13) Tokyo, Japan, November 11-15, 2013*, 2014 [1403.7348].

[157] I. technical coordination, "ILD technical documentation." http://edmsdirect.desy.de/ildtdr.

[158] H. Abramowicz et al., *The International Linear Collider Technical Design Report - Volume 4: Detectors*, 1306.6329.

[159] T.B. *et.al.*, "The ILD Design Report." to be published.

[160] N. Sinev, J. Brau, D. Strom, C. Baltay, W. Emmet and D. Rabinowitz, *Chronopixel project status*, *PoS* **VERTEX2015** (2015) 038.

[161] J. Brau et al., *KPiX - A 1,024 Channel Readout ASIC for the ILC*, in *2012 IEEE Nuclear Science Symposium and Medical Imaging Conference and 19th Workshop on Room-Temperature Semiconductor X-ray and Gamma-ray Detectors*, pp. 1857–1860, 2012, DOI.

[162] A. Steinhebel and J. Brau, *Studies of the Response of the SiD Silicon-Tungsten ECal*, in *International Workshop on Future Linear Colliders*, 3, 2017 [1703.08605].

[163] B. Parker, A. Mikhailichenko, K. Buesser, J. Hauptman, T. Tauchi, P. Burrows et al., *Functional Requirements on the Design of the Detectors and the Interaction Region of an e^+e^- Linear Collider with a Push-Pull Arrangement of Detectors*, in *Particle Accelerator Conference (PAC 09)*, p. WE6PFP078, 2010.

[164] K. Buesser, *ILD Machine-Detector Interface and Experimental Hall Issues*, in *International Workshop on Future Linear Colliders (LCWS11)*, 1, 2012 [1201.5807].

[165] J. Brau, "The SiD Digital ECal based on Monolithic Active Pixel Sensors." ILCX2021, (2021).

[166] G. Aglieri, M. Aleksa, D.A. Feito, M. Angeletti, P. Antoszczuk, R. Ballabriga et al., *Strategic R&D Programme on Technologies for Future Experiments*, .

[167] E.D.R.R.P. Group, *The 2021 ECFA detector research and development roadmap*, *European Strategy report* **CERN-ESU-017** (2020) .

[168] *AIDA Innova, European Union's Horizon 2020 Research and Innovation programme* **under Grant Agreement No 101004761** (2021) .

[169] B. Fleming, I. Shipsey, M. Demarteau, J. Fast, S. Golwala, Y.-K. Kim et al., *Basic research needs for high energy physics detector research & development: Report of the office of science workshop on basic research needs for hep detector research and development: December 11-14, 2019*, .

[170] DEPFET collaboration, *DEPFET active pixel detectors for a future linear e^+e^- collider*, *IEEE Trans. Nucl. Sci.* **60** (2013) 1457 [1212.2160].

[171] P. Fischer et al., *Progress towards a large area, thin DEPFET detector module*, *Nucl. Instrum. Meth. A* **582** (2007) 843.

[172] Belle-II collaboration, *Belle II Technical Design Report*, 1011.0352.

[173] ALICE collaboration, *Technical Design Report for the Upgrade of the ALICE Inner Tracking System*, *J. Phys. G* **41** (2014) 087002.

[174] STAR collaboration, *STAR detector overview*, *Nucl. Instrum. Meth. A* **499** (2003) 624.

[175] NA62 collaboration, *The Beam and detector of the NA62 experiment at CERN*, *JINST* **12** (2017) P05025 [1703.08501].

[176] O.A.D.A. Francisco et al., *Microchannel cooling for the LHCb VELO Upgrade I*, 2112.12763.

[177] L. Andricek, M. Boronat, I. Garcia, P. Gomis, C. Marinas, J. Ninkovic et al., *Integrated cooling channels in position-sensitive silicon detectors*, *JINST* **11** (2016) P06018 [1604.08776].

[178] A. Mapelli, P. Petagna and M. Vos, *Micro-channel cooling for collider experiments: review and recommandations*, *AIDA note* **AIDA-2020-NOTE-2020-003** (2020) .

[179] S. Lee, M. Livan and R. Wigmans, *Dual-readout calorimetry*, *Rev. Mod. Phys.* **90** (2018) 025002.

[180] N. Akchurin et al., *Detection of electron showers in dual-readout crystal calorimeters*, *Nucl. Instrum. Meth. A* **686** (2012) 125.

[181] N. Akchurin et al., *The electromagnetic performance of the RD52 fiber calorimeter*, *Nucl. Instrum. Meth. A* **686** (2012) 125.

[182] S. Lee et al., *Hadron detection with a dual-readout fiber calorimeter*, *Nucl. Instrum. Meth. A* **866** (2017) 76.

[183] N. Akchurin et al., *Lessons from monte carlo simulations of the performance of a dual-readout fiber calorimeter*, *Nucl. Instrum. Meth. A* **762** (2014) 100.

[184] N. Akchurin et al., *Particle identification in the longitudinally unsegmented RD52 calorimeter*, *Nucl. Instrum. Meth. A* **735** (2014) 120.

[185] M. Antonello et al., *Tests of a dual-readout fibre calorimeter with sipm light sensors*, *Nucl. Instrum. Meth. A* **899** (2018) 52.

[186] M. Antonello et al., *Development of a silicon photomultiplier based dual-readout calorimeter: The pathway beyond the proof-of-concept*, *Nucl. Instrum. Meth. A* **963** (2019) 127.

[187] R. Aly et al., *First test-beam results obtained with idea, a detector concept designed for future lepton colliders*, *Nucl. Instrum. Meth. A* **958** (2020) 162088.

[188] M. Lucchini, W. Chung, S.C. Eno, Y. Lai, L. Lucchini, M. Nguyen et al., *New perspectives on segmented crystal calorimeters for future colliders*, *Journal of Instrumentation* **15** (2020) P11005.

[189] M. Aleksa, F. Bedeschi, R. Ferrari, F. Sefkow and C.G. Tully, *Calorimetry at FCC-ee*, *Eur. Phys. J. Plus* **136** (2021) 1066 [2109.00391].

[190] M. Aleksa et al., *Calorimeters for the FCC-hh*, 1912.09962.

[191] DELPHES 3 collaboration, *DELPHES 3, A modular framework for fast simulation of a generic collider experiment*, *JHEP* **02** (2014) 057 [1307.6346].

[192] S. Ovyn, X. Rouby and V. Lemaitre, *DELPHES, a framework for fast simulation of a generic collider experiment*, 0903.2225.

[193] M. Cacciari, *FastJet: A Code for fast k_t clustering, and more*, in *Deep inelastic scattering. Proceedings, 14th International Workshop, DIS 2006, Tsukuba, Japan, April 20-24, 2006*, pp. 487–490, 2006 [hep-ph/0607071].

[194] Aleksander Filip Zarnecki, "The ILC DELPHES card (IDT-WG3 Software Tutorial)." https://agenda.linearcollider.org/event/9264/, 2020.

[195] Delphes authors, "Delphes Project Page." https://github.com/delphes/delphes, 2009.

[196] ILD Concept Group collaboration, *International Large Detector: Interim Design Report*, 2003.01116.

[197] R. Brun and F. Rademakers, *ROOT: An object oriented data analysis framework*, *Nucl. Instrum. Meth. A* **389** (1997) 81.

[198] Frank Gaede, "delphes2lcio." https://github.com/iLCSoft/LCIO/tree/master/examples/cpp/delphes2lcio, 2021.

[199] M. Berggren, *SGV 3.0 - a fast detector simulation*, in *International Workshop on Future Linear Colliders (LCWS11) Granada, Spain, September 26-30, 2011*, 2012 [1203.0217].

[200] DELPHI collaboration, *Searches for supersymmetric particles in e+ e- collisions up to 208-GeV and interpretation of the results within the MSSM*, *Eur. Phys. J.* **C31** (2003) 421 [hep-ex/0311019].

[201] iLCSoft authors, *iLCSoft Project Page*, .

[202] F. Gaede, T. Behnke, N. Graf and T. Johnson, *LCIO: A Persistency framework for linear collider simulation studies*, *eConf* **C0303241** (2003) TUKT001 [physics/0306114].

[203] F. Gaede, *Marlin and LCCD: Software tools for the ILC*, *Nucl. Instrum. Meth.* **A559** (2006) 177.

[204] M. Frank, F. Gaede, C. Grefe and P. Mato, *DD4hep: A Detector Description Toolkit for High Energy Physics Experiments*, *J. Phys. Conf. Ser.* **513** (2014) 022010.

[205] M. Frank, F. Gaede, N. Nikiforou, M. Petric and A. Sailer, *DDG4 A Simulation Framework based on the DD4hep Detector Description Toolkit*, *J. Phys. Conf. Ser.* **664** (2015) 072017.

[206] GEANT4 collaboration, *GEANT4: A Simulation toolkit*, *Nucl. Instrum. Meth.* **A506** (2003) 250.

[207] F. Gaede, S. Aplin, R. Glattauer, C. Rosemann and G. Voutsinas, *Track reconstruction at the ILC: the ILD tracking software*, *J. Phys. Conf. Ser.* **513** (2014) 022011.

[208] J.S. Marshall and M.A. Thomson, *The Pandora Software Development Kit for Pattern Recognition*, *Eur. Phys. J.* **C75** (2015) 439 [1506.05348].

[209] T. Suehara and T. Tanabe, *LCFIPlus: A Framework for Jet Analysis in Linear Collider Studies*, *Nucl. Instrum. Meth.* **A808** (2016) 109 [1506.08371].

[210] W. Kilian, T. Ohl and J. Reuter, *WHIZARD: Simulating Multi-Particle Processes at LHC and ILC*, *Eur. Phys. J.* **C71** (2011) 1742 [0708.4233].

[211] T. Sjostrand, S. Mrenna and P.Z. Skands, *PYTHIA 6.4 Physics and Manual*, *JHEP* **05** (2006) 026 [hep-ph/0603175].

[212] D. Schulte, *Beam-beam simulations with Guinea-Pig*, *eConf* **C980914** (1998) 127.

[213] P. Chen, T.L. Barklow and M.E. Peskin, *Hadron production in gamma gamma collisions as a background for e+ e- linear colliders*, *Phys. Rev.* **D49** (1994) 3209 [hep-ph/9305247].

[214] A. Schütz, *Pair Background Envelopes in the SiD Detector*, in *Proceedings, International Workshop on Future Linear Colliders 2016 (LCWS2016): Morioka, Iwate, Japan, December 05-09, 2016*, 2017 [1703.05737].

[215] Jim Brau et al., "ILC Simulation Resources for Snowmass 2021." http://ilcsnowmass.org/, 2021.

[216] B.L. Ioffe and V.A. Khoze, *What can be expected from experiments with e^+e^- colliding beams at energy ∼100 GeV*, *Sov. J. Part. Nucl.* **9** (1978) 50.

[217] J. Yan, S. Watanuki, K. Fujii, A. Ishikawa, D. Jeans, J. Strube et al., *Measurement of the Higgs boson mass and $e^+e^- \to ZH$ cross section using $Z \to \mu^+\mu^-$ and $Z \to e^+e^-$ at the ILC*, *Phys. Rev. D* **94** (2016) 113002 [1604.07524].

[218] LCC Physics Working Group collaboration, *Tests of the Standard Model at the International Linear Collider*, 1908.11299.

[219] J. Tian, *A new method for measuring the Higgs mass at the ILC*, *ILD-PHYS-PUB-2019-001* (2020) .

[220] G. Wilson, *Complementary Higgs mass measurements at ILC*, .

[221] ILD Concept Group collaboration, *International Large Detector: Interim Design Report*, 2003.01116.

[222] H. Ono and A. Miyamoto, *A study of measurement precision of the Higgs boson branching ratios at the International Linear Collider*, *Eur. Phys. J. C* **73** (2013) 2343 [1207.0300].

[223] M.J. Basso et al., *Strange Quark as a probe for new physics in the Higgs Sector*, .

[224] S.-i. Kawada, K. Fujii, T. Suehara, T. Takahashi and T. Tanabe, *A study of the measurement precision of the Higgs boson decaying into tau pairs at the ILC*, *Eur. Phys. J. C* **75** (2015) 617 [1509.01885].

[225] S.-i. Kawada, J. List and M. Berggren, *Prospects of measuring the branching fraction of the Higgs boson decaying into muon pairs at the International Linear Collider*, *Eur. Phys. J. C* **80** (2020) 1186 [2009.04340].

[226] E. Antonov and A. Drutskoy, *Measurement of $\sigma(e^+e^- \to HZ) \times \mathcal{B}r(H \to ZZ^*)$ at the 250 GeV ILC*, 2108.08867.

[227] Y. Aoki, K. Fujii and J. Tian, *Study of the $h\gamma Z$ coupling at the ILC*, in *International Workshop on Future Linear Colliders*, 5, 2021 [2105.06665].

[228] D. Jeans and G.W. Wilson, *Measuring the CP state of tau lepton pairs from Higgs decay at the ILC*, *Phys. Rev. D* **98** (2018) 013007 [1804.01241].

[229] T. Ogawa, J. Tian and K. Fujii, *Sensitivity to anomalous ZZH couplings at the ILC*, *PoS* **EPS-HEP2017** (2017) 322 [1712.09772].

[230] T. Ogawa, *Sensitivity to anomalous VVH couplings induced by dimension-6 operators at the ILC*, Ph.D. thesis, 2018.

[231] D. Curtin et al., *Exotic decays of the 125 GeV Higgs boson*, *Phys. Rev.* **D90** (2014) 075004 [1312.4992].

[232] Z. Liu, L.-T. Wang and H. Zhang, *Exotic decays of the 125 GeV Higgs boson at future e^+e^- lepton colliders*, *Chin. Phys.* **C41** (2017) 063102 [1612.09284].

[233] LHC Higgs Cross Section Working Group collaboration, *Handbook of LHC Higgs Cross Sections: 4. Deciphering the Nature of the Higgs Sector*, 1610.07922.

[234] J. Alwall, R. Frederix, S. Frixione, V. Hirschi, F. Maltoni et al., *The automated computation of tree-level and next-to-leading order differential cross sections, and their matching to parton shower simulations*, *JHEP* **1407** (2014) 079 [arXiv:1405.0301].

[235] Q. Xiu, H. Zhu, X. Lou and T. Yue, *Study of beamstrahlung effects at CEPC*, *Chin. Phys.* **C40** (2016) 053001 [1505.01270].

[236] M. Greco, T. Han and Z. Liu, *ISR effects for resonant Higgs production at future lepton colliders*, *Phys. Lett.* **B763** (2016) 409 [1607.03210].

[237] M. Carena, Z. Liu and Y. Wang, *Electroweak phase transition with spontaneous Z_2-breaking*, *JHEP* **08** (2020) 107 [1911.10206].

[238] M.J. Ramsey-Musolf, *The electroweak phase transition: a collider target*, *JHEP* **09** (2020) 179 [1912.07189].

[239] S. Alipour-Fard, N. Craig, S. Gori, S. Koren and D. Redigolo, *The second Higgs at the lifetime frontier*, *JHEP* **07** (2020) 029 [1812.09315].

[240] Z. Chacko, P.J. Fox, R. Harnik and Z. Liu, *Neutrino Masses from Low Scale Partial Compositeness*, 2012.01443.

[241] N. Craig, A. Katz, M. Strassler and R. Sundrum, *Naturalness in the Dark at the LHC*, *JHEP* **07** (2015) 105 [1501.05310].

[242] D. Curtin and C.B. Verhaaren, *Discovering Uncolored Naturalness in Exotic Higgs Decays*, *JHEP* **12** (2015) 072 [1506.06141].

[243] J. Liu, Z. Liu and L.-T. Wang, *Enhancing Long-Lived Particles Searches at the LHC with Precision Timing Information*, *Phys. Rev. Lett.* **122** (2019) 131801 [1805.05957].

[244] J. Liu, Z. Liu, L.-T. Wang and X.-P. Wang, *Enhancing Sensitivities to Long-lived Particles with High Granularity Calorimeters at the LHC*, *JHEP* **11** (2020) 066 [2005.10836].

[245] S. Jung, Z. Liu, L.-T. Wang and K.-P. Xie, *Probing Higgs exotic decay at the LHC with machine learning*, 2109.03294.

[246] N. Arkani-Hamed, T. Cohen, R.T. D'Agnolo, A. Hook, H.D. Kim and D. Pinner, *Solving the Hierarchy Problem at Reheating with a Large Number of Degrees of Freedom*, *Phys. Rev. Lett.* **117** (2016) 251801 [1607.06821].

[247] N. Arkani-Hamed, R. Tito D'agnolo and H.D. Kim, *The Weak Scale as a Trigger*, 2012.04652.

[248] P. Meade and H. Ramani, *Unrestored Electroweak Symmetry*, *Phys. Rev. Lett.* **122** (2019) 041802 [1807.07578].

[249] I. Baldes and G. Servant, *High scale electroweak phase transition: baryogenesis and symmetry non-restoration*, *JHEP* **10** (2018) 053 [1807.08770].

[250] A. Glioti, R. Rattazzi and L. Vecchi, *Electroweak Baryogenesis above the Electroweak Scale*, *JHEP* **04** (2019) 027 [1811.11740].

[251] O. Matsedonskyi and G. Servant, *High-Temperature Electroweak Symmetry Non-Restoration from New Fermions and Implications for Baryogenesis*, *JHEP* **09** (2020) 012 [2002.05174].

[252] C. Degrande, N. Greiner, W. Kilian, O. Mattelaer, H. Mebane, T. Stelzer et al., *Effective Field Theory: A Modern Approach to Anomalous Couplings*, *Annals Phys.* **335** (2013) 21 [1205.4231].

[253] ALEPH, DELPHI, L3, OPAL, LEP Electroweak collaboration, *Electroweak Measurements in Electron-Positron Collisions at W-Boson-Pair Energies at LEP*, *Phys. Rept.* **532** (2013) 119 [1302.3415].

[254] ALEPH collaboration, *Improved measurement of the triple gauge-boson couplings gamma W W and Z W W in e+ e- collisions*, *Phys. Lett. B* **614** (2005) 7.

[255] DELPHI collaboration, *Measurement of trilinear gauge boson couplings $WWV, (V \equiv Z, \gamma)$ in e^+e^- collisions at 189-GeV*, *Phys. Lett. B* **502** (2001) 9 [hep-ex/0102041].

[256] L3 collaboration, *Measurement of triple gauge boson couplings of the W boson at LEP*, *Phys. Lett. B* **586** (2004) 151 [hep-ex/0402036].

[257] OPAL collaboration, *Measurement of charged current triple gauge boson couplings using W pairs at LEP*, *Eur. Phys. J. C* **33** (2004) 463 [hep-ex/0308067].

[258] CMS collaboration, *Search for anomalous triple gauge couplings in WW and WZ production in lepton + jet events in proton-proton collisions at $\sqrt{s} = 13$ TeV*, *JHEP* **12** (2019) 062 [1907.08354].

[259] P. Azzi et al., *Report from Working Group 1: Standard Model Physics at the HL-LHC and HE-LHC*, *CERN Yellow Rep. Monogr.* **7** (2019) 1 [1902.04070].

[260] I. Marchesini, *Triple gauge couplings and polarization at the ILC and leakage in a highly granular calorimeter*, Ph.D. thesis, Hamburg U., 2011.

[261] M. Diehl, O. Nachtmann and F. Nagel, *Probing triple gauge couplings with transverse beam polarisation in e+ e- —> W+ W-*, *Eur. Phys. J. C* **32** (2003) 17 [hep-ph/0306247].

[262] M. Diehl, O. Nachtmann and F. Nagel, *Triple gauge couplings in polarized e- e+ —> W- W+ and their measurement using optimal observables*, *Eur. Phys. J. C* **27** (2003) 375 [hep-ph/0209229].

[263] M. Diehl and O. Nachtmann, *Anomalous three gauge couplings in e+ e- —> W+ W- and 'optimal' strategies for their measurement*, *Eur. Phys. J. C* **1** (1998) 177 [hep-ph/9702208].

[264] R. Karl, *From the Machine-Detector Interface to Electroweak Precision Measurements at the ILC — Beam-Gas Background, Beam Polarization and Triple Gauge Couplings*, Ph.D. thesis, Hamburg U., Hamburg, 2019. 10.3204/PUBDB-2019-03013.

[265] J. Beyer, R. Karl and J. List, *Precision measurements of Triple Gauge Couplings at future electron-positron colliders*, in *International Workshop on Future Linear Colliders*, 2, 2020 [2002.02777].

[266] J. Beyer, *Achieving Electroweak Precision at Future Electron-Positron Colliders*, Ph.D. thesis, Hamburg U. (in preparation), Hamburg, 2022. 10.xxxx/PUBDB-2022-xxxxx.

[267] J. Beyer and J. List, *Interplay of beam polarisation and systematic uncertainties in electroweak precision measurements at future e+e- colliders*, in *Proceedings of SPIN Conference*, 1, 2022 [2022.01xyz].

[268] ALEPH, DELPHI, L3, OPAL, SLD, LEP Electroweak Working Group, SLD Electroweak Group, SLD Heavy Flavour Group collaboration, *Precision electroweak measurements on the Z resonance*, *Phys. Rept.* **427** (2006) 257 [hep-ex/0509008].

[269] K. Yokoya, K. Kubo and T. Okugi, *Operation of ILC250 at the Z-pole*, 1908.08212.

[270] A. Djouadi, G. Moreau and F. Richard, *Resolving the A(FB)**b puzzle in an extra dimensional model with an extended gauge structure*, *Nucl.Phys.* **B773** (2007) 43 [hep-ph/0610173].

[271] G. Moortgat-Pick, T. Abe, G. Alexander, B. Ananthanarayan, A. Babich et al., *The Role of polarized positrons and electrons in revealing fundamental interactions at the linear collider*, *Phys.Rept.* **460** (2008) 131 [hep-ph/0507011].

[272] C.R. Schmidt, *Top quark production and decay at next-to-leading order in e+ e- annihilation*, *Phys.Rev.* **D54** (1996) 3250 [hep-ph/9504434].

[273] A. Irles, "Quark Pair Production at Lepton Colliders: Experimental challenges."

[274] S. Funatsu, H. Hatanaka, Y. Hosotani and Y. Orikasa, *Distinct signals of the gauge-Higgs unification in e^+e^- collider experiments*, *Phys. Lett.* **B775** (2017) 297 [1705.05282].

[275] J. Yoon and M.E. Peskin, *Fermion Pair Production in SO(5) x U(1) Gauge-Higgs Unification Models*, 1811.07877.

[276] S. Funatsu, H. Hatanaka, Y. Hosotani, Y. Orikasa and N. Yamatsu, *Fermion pair production at e^-e^+ linear collider experiments in GUT inspired gauge-Higgs unification*, *Phys. Rev. D* **102** (2020) 015029 [2006.02157].

[277] Y. Deguchi, H. Yamashiro, T. Suehara, T. Yoshioka, K. Fujii and K. Kawagoe, *Study of fermion pair events at the 250 GeV ILC*, in *International Workshop on Future Linear Colliders*, 2, 2019 [1902.05245].

[278] D. Jeans and K. Yumino, *ILD benchmark: a study of $e^-e^+ \to \tau^-\tau^+$ at 500 GeV*, 1912.08403.

[279] The ATLAS Collaboration, *Measurement of the top quark mass in the $t\bar{t} \to$ lepton+jets channel from $\sqrt{s} = 8$ TeV ATLAS data and combination with previous results*, *Eur. Phys. J. C* **79** (2019) 290 [1810.01772].

[280] ATLAS, CDF, CMS, D0 collaboration, *First combination of Tevatron and LHC measurements of the top-quark mass*, 1403.4427.

[281] Tevatron Electoweak Working Group (CDF and D0 Collaborations) collaboration, *Combination of CDF and D0 results on the mass of the top quark using up 9.7 fb^{-1} at the Tevatron*, 1608.01881.

[282] Particle Data Group collaboration, *Review of Particle Physics*, *PTEP* **2020** (2020) 083C01.

[283] ATLAS collaboration, *Measurement of the top-quark mass in $t\bar{t}+1$-jet events collected with the ATLAS detector in pp collisions at $\sqrt{s} = 8$ TeV*, *JHEP* **11** (2019) 150 [1905.02302].

[284] A. G., B.A. I., B. O., F. P., L. M., R. L. et al., *High-Luminosity Large Hadron Collider (HL-LHC): Technical Design Report V. 0.1*, CERN Yellow Reports: Monographs, CERN, Geneva (2017), 10.23731/CYRM-2017-004.

[285] T. Ježo, J.M. Lindert, P. Nason, C. Oleari and S. Pozzorini, *An NLO+PS generator for $t\bar{t}$ and Wt production and decay including non-resonant and interference effects*, *Eur. Phys. J. C* **76** (2016) 691 [1607.04538].

[286] S. Ferrario Ravasio, T. Ježo, P. Nason and C. Oleari, *A theoretical study of top-mass measurements at the LHC using NLO+PS generators of increasing accuracy*, *Eur. Phys. J. C* **78** (2018) 458 [1906.09166].

[287] The ATLAS collaboration, *A precise interpretation for the top quark mass parameter in ATLAS Monte Carlo simulation*, *ATL-PHYS-PUB-2021-034* .

[288] M. Butenschoen, B. Dehnadi, A.H. Hoang, V. Mateu, M. Preisser and I.W. Stewart, *Top Quark Mass Calibration for Monte Carlo Event Generators*, 1608.01318.

[289] J. Kieseler, K. Lipka and S.-O. Moch, *Calibration of the Top-Quark Monte Carlo Mass*, *Phys. Rev. Lett.* **116** (2016) 162001 [1511.00841].

[290] A.H. Hoang, *What is the Top Quark Mass?*, *Ann. Rev. Nucl. Part. Sci.* **70** (2020) 225 [2004.12915].

[291] S. Gusken, J.H. Kuhn and P.M. Zerwas, *Threshold Behavior of Top Production in e^+e^- Annihilation*, *Phys. Lett.* **B155** (1985) 185.

[292] V.S. Fadin and V.A. Khoze, *Threshold Behavior of Heavy Top Production in e+ e- Collisions*, *JETP Lett.* **46** (1987) 525.

[293] V.S. Fadin and V.A. Khoze, *Production of a pair of heavy quarks in e+ e- annihilation in the threshold region*, *Sov. J. Nucl. Phys.* **48** (1988) 309.

[294] M.J. Strassler and M.E. Peskin, *The Heavy top quark threshold: QCD and the Higgs*, *Phys. Rev. D* **43** (1991) 1500.

[295] M. Beneke, Y. Kiyo, P. Marquard, A. Penin, J. Piclum and M. Steinhauser, *Next-to-Next-to-Next-to-Leading Order QCD Prediction for the Top Antitop S-Wave Pair Production Cross Section Near Threshold in e^+e^- Annihilation*, *Phys. Rev. Lett.* **115** (2015) 192001 [1506.06864].

[296] A.H. Hoang, A.V. Manohar, I.W. Stewart and T. Teubn er, *The Threshold $t\bar{t}$ cross-section at NNLL order*, *Phys. Rev.* **D65** (2002) 014014 [hep-ph/0107144].

[297] P. Marquard, A.V. Smirnov, V.A. Smirnov and M. Steinhauser, *Quark Mass Relations to Four-Loop Order in Perturbative QCD*, *Phys. Rev. Lett.* **114** (2015) 142002 [1502.01030].

[298] CLICdp collaboration, *Top-Quark Physics at the CLIC Electron-Positron Linear Collider*, *JHEP* **11** (2019) 003 [1807.02441].

[299] K. Seidel, F. Simon, M. Tesar and S.p. Poss, *Top quark mass measurements at and above threshold at CLIC*, *Eur. Phys. J.* **C73** (2013) 2530 [1303.3758].

[300] T. Horiguchi, A. Ishikawa, T. Suehara, K. Fujii, Y. Sumino, Y. Kiyo et al., *Study of top quark pair production near threshold at the ILC*, 1310.0563.

[301] M. Martinez and R. Miquel, *Multiparameter fits to the $t\bar{t}$ threshold observables at a future e^+e^- linear collider*, *Eur. Phys. J.* **C27** (2003) 49 [hep-ph/0207315].

[302] F. Simon, *A First Look at the Impact of NNNLO Theory Uncertainties on Top Mass Measurements at the ILC*, in *International Workshop on Future Linear Colliders (LCWS15) Whistler, B.C., Canada, November 2-6, 2015*, 2016, https://inspirehep.net/record/1427722/files/arXiv:1603.04764.pdf [1603.04764].

[303] M. Vos et al., *Top physics at high-energy lepton colliders*, 1604.08122.

[304] K. Nowak and A.F. Zarnecki, *Optimising top-quark threshold scan at CLIC using genetic algorithm*, *JHEP* **07** (2021) 070 [2103.00522].

[305] M. Boronat, E. Fullana, J. Fuster, P. Gomis, A. Hoang, V. Mateu et al., *Top quark mass measurement in radiative events at electron-positron colliders*, *Phys. Lett. B* **804** (2020) 135353 [1912.01275].

[306] F. Richard, *Present and future constraints on top EW couplings*, 1403.2893.

[307] V. Miralles, M.M. López, M.M. Llácer, A. Peñuelas, M. Perelló and M. Vos, *The top quark electro-weak couplings after LHC Run 2*, 2107.13917.

[308] T. Martini and M. Schulze, *Electroweak loops as a probe of new physics in $t\bar{t}$ production at the LHC*, *JHEP* **04** (2020) 017 [1911.11244].

[309] M. Cepeda et al., *Report from Working Group 2: Higgs Physics at the HL-LHC and HE-LHC*, *CERN Yellow Rep. Monogr.* **7** (2019) 221 [1902.00134].

[310] V. Miralles and M. Vos, *Prospects at the HL-LHC and ILC for measurements of the top quark EW couplings*, *Snowmass white paper* **to be published** (2021) [2XXX.YYYYY].

[311] G. Durieux, A. Irles, V. Miralles, A. Peñuelas, R. Pöschl, M. Perelló et al., *The electro-weak couplings of the top and bottom quarks – Global fit and future prospects*, *JHEP* **12** (2019) 98 [1907.10619].

[312] M.S. Amjad et al., *A precise characterisation of the top quark electroweak vertices at the ILC*, *Eur. Phys. J. C* **75** (2015) 512 [1505.06020].

[313] M.S. Amjad, M. Boronat, T. Frisson, I. Garcia, R. Poschl, E. Ros et al., *A precise determination of top quark electroweak couplings at the ILC operating at $\sqrt{s} = 500$ GeV*, 1307.8102.

[314] G. Durieux, M. Perelló, M. Vos and C. Zhang, *Global and optimal probes for the top-quark effective field theory at future lepton colliders*, *JHEP* **10** (2018) 168 [1807.02121].

[315] W. Bernreuther, L. Chen, I. García, M. Perelló, R. Poeschl, F. Richard et al., *CP-violating top quark couplings at future linear e^+e^- colliders*, *Eur. Phys. J. C* **78** (2018) 155 [1710.06737].

[316] G. Durieux, J. Gu, E. Vryonidou and C. Zhang, *Probing top-quark couplings indirectly at Higgs factories*, *Chin. Phys. C* **42** (2018) 123107 [1809.03520].

[317] S. Jung, J. Lee, M. Perelló, J. Tian and M. Vos, *Higgs, top and electro-weak precision measurements at future e^+e^- colliders; a combined effective field theory analysis with renormalization mixing*, 2006.14631.

[318] The ATLAS collaboration, *Sensitivity of searches for the flavour-changing neutral current decay $t \to qZ$ using the upgraded ATLAS experiment at the High Luminosity LHC*, *ATL-PHYS-PUB-2019-001* .

[319] ATLAS Collaboration collaboration, *Expected sensitivity of ATLAS to FCNC top quark decays $t \to Zu$ and $t \to Hq$ at the High Luminosity LHC*, *ATL-PHYS-PUB-2016-019* .

[320] G. Durieux, F. Maltoni and C. Zhang, *Global approach to top-quark flavor-changing interactions*, *Phys. Rev. D* **91** (2015) 074017 [1412.7166].

[321] L. Shi and C. Zhang, *Probing the top quark flavor-changing couplings at CEPC*, *Chin. Phys. C* **43** (2019) 113104 [1906.04573].

[322] J. de Blas et al., *The CLIC Potential for New Physics*, 1812.02093.

[323] J.A. Aguilar-Saavedra and T. Riemann, *Probing top flavor changing neutral couplings at TESLA*, in *2nd Workshop of the 2nd Joint ECFA / DESY Study on Physics and Detectors for a Linear Electron Positron Collider*, pp. 2428–2450, 2, 2001 [hep-ph/0102197].

[324] C.F. Dürig, *Measuring the Higgs Self-coupling at the International Linear Collider*, Ph.D. thesis, Hamburg U., Hamburg, 2016. 10.3204/PUBDB-2016-04283.

[325] R. Frederix, S. Frixione, V. Hirschi, F. Maltoni, O. Mattelaer, P. Torrielli et al., *Higgs pair production at the LHC with NLO and parton-shower effects*, *Phys. Lett. B* **732** (2014) 142 [1401.7340].

[326] J. Tian, *Study of Higgs self-coupling at the ILC based on the full detector simulation at* $sqrts = 500\ GeV$ *and* $\sqrt{s} = 1\ TeV$, in *LC Notes*, LC-REP-2013-003, https://flc.desy.de/lcnotes/noteslist/.

[327] T. Barklow, K. Fujii, S. Jung, M.E. Peskin and J. Tian, *Model-Independent Determination of the Triple Higgs Coupling at e+e- Colliders*, *Phys. Rev. D* **97** (2018) 053004 [1708.09079].

[328] Y. Radkhorrami and J. List, *Kinematic Fitting for Particle Flow Detectors at Future Higgs Factories*, in *Particles and Nuclei International Conference* , 11, 2021 [2111.14775].

[329] K. Goto, T. Suehara, T. Yoshioka, M. Kurata, H. Nagahara, Y. Nakashima et al., *Development of a Vertex Finding Algorithm using Recurrent Neural Network*, 2101.11906.

[330] U. Einhaus, *Charged Hadron Identification with dE/dx and Time-of-Flight at Future Higgs Factories*, in *Particles and Nuclei International Conference* , 12, 2021 [2112.10009].

[331] F. Arco, S. Heinemeyer and M.J. Herrero, *Exploring sizable triple Higgs couplings in the 2HDM*, *Eur. Phys. J. C* **80** (2020) 884 [2005.10576].

[332] F. Arco, S. Heinemeyer and M.J. Herrero, *Sensitivity to triple Higgs couplings via di-Higgs production in the 2HDM at* e^+e^- *colliders*, *Eur. Phys. J. C* **81** (2021) 913 [2106.11105].

[333] D.E. Morrissey and M.J. Ramsey-Musolf, *Electroweak baryogenesis*, *New J. Phys.* **14** (2012) 125003 [1206.2942].

[334] ATLAS collaboration, *Measurement prospects of the pair production and self-coupling of the Higgs boson with the ATLAS experiment at the HL-LHC*, .

[335] ATLAS collaboration, *Observation of Higgs boson production in association with a top quark pair at the LHC with the ATLAS detector*, *Phys. Lett. B* **784** (2018) 173 [1806.00425].

[336] CMS collaboration, *Observation of $t\bar{t}H$ production*, *Phys. Rev. Lett.* **120** (2018) 231801 [1804.02610].

[337] R. Yonamine, K. Ikematsu, T. Tanabe, K. Fujii, Y. Kiyo, Y. Sumino et al., *Measuring the top Yukawa coupling at the ILC at $\sqrt{s} = 500$ GeV*, *Phys. Rev. D* **84** (2011) 014033 [1104.5132].

[338] H. Abramowicz et al., *Higgs physics at the CLIC electron–positron linear collider*, *Eur. Phys. J. C* **77** (2017) 475 [1608.07538].

[339] T. Price, P. Roloff, J. Strube and T. Tanabe, *Full simulation study of the top Yukawa coupling at the ILC at $\sqrt{s} = 1$ TeV*, *Eur. Phys. J. C* **75** (2015) 309 [1409.7157].

[340] T. Han, T. Huang, Z.H. Lin, J.X. Wang and X. Zhang, *e+ e- —> t anti-t H with nonstandard Higgs boson couplings*, *Phys. Rev. D* **61** (2000) 015006 [hep-ph/9908236].

[341] A. Rosca, *Measurement of the charged triple gauge boson couplings at the ILC*, *Nucl. Part. Phys. Proc.* **273-275** (2016) 2226.

[342] T. Barklow, *private communication to J. List*, 2018.

[343] K. Fujii et al., *The Potential of the ILC for Discovering New Particles*, 1702.05333.

[344] M. Berggren, *What pp SUSY limits mean for future e^+e^- colliders*, in *International Workshop on Future Linear Colliders*, 3, 2020 [2003.12391].

[345] J. Wess and B. Zumino, *Supergauge Transformations in Four-Dimensions*, *Nucl. Phys.* **B70** (1974) 39.

[346] H.P. Nilles, *Supersymmetry, Supergravity and Particle Physics*, *Phys. Rept.* **110** (1984) 1.

[347] H.E. Haber and G.L. Kane, *The Search for Supersymmetry: Probing Physics Beyond the Standard Model*, *Phys. Rept.* **117** (1985) 75.

[348] R. Barbieri, S. Ferrara and C.A. Savoy, *Gauge Models with Spontaneously Broken Local Supersymmetry*, *Phys. Lett.* **119B** (1982) 343.

[349] Muon g-2 collaboration, *Measurement of the Positive Muon Anomalous Magnetic Moment to 0.46 ppm*, *Phys. Rev. Lett.* **126** (2021) 141801 [2104.03281].

[350] D.P. Roy, *SUSY Search in Future Collider and Dark Matter Experiments*, *AIP Conf. Proc.* **939** (2007) 63 [0707.1949].

[351] H. Baer and X. Tata, *Weak scale supersymmetry: From superfields to scattering events*, Cambridge University Press (5, 2006).

[352] LEP SUSY Working Group, ALEPH, DELPHI, L3 and OPAL Collaborations collaboration, *Combined lep chargino results, up to 208 gev for large m_0*, Tech. Rep. LEPSUSYWG/01-03.1.

[353] ALEPH collaboration, *Search for scalar leptons in e+ e- collisions at center-of-mass energies up to 209-GeV*, *Phys. Lett.* **B526** (2002) 206 [hep-ex/0112011].

[354] ALEPH collaboration, *Absolute mass lower limit for the lightest neutralino of the MSSM from e+ e- data at s**(1/2) up to 209-GeV*, *Phys. Lett.* **B583** (2004) 247.

[355] ALEPH collaboration, *Search for charginos nearly mass degenerate with the lightest neutralino in e+ e- collisions at center-of-mass energies up to 209-GeV*, *Phys. Lett.* **B533** (2002) 223 [hep-ex/0203020].

[356] L3 collaboration, *Search for scalar leptons and scalar quarks at LEP*, *Phys. Lett.* **B580** (2004) 37 [hep-ex/0310007].

[357] OPAL collaboration, *Search for anomalous production of dilepton events with missing transverse momentum in e+ e- collisions at s**(1/2) = 183-Gev to 209-GeV*, *Eur. Phys. J.* **C32** (2004) 453 [hep-ex/0309014].

[358] E. Bagnaschi et al., *Likelihood Analysis of the pMSSM11 in Light of LHC 13-TeV Data*, *Eur. Phys. J.* **C78** (2018) 256 [1710.11091].

[359] M.T. Núñez Pardo de Vera, M. Berggren and J. List, *Chargino production at the ILC*, in *International Workshop on Future Linear Colliders*, 2, 2020 [2002.01239].

[360] M.T. Núñez Pardo de Vera, M. Berggren and J. List, $\widetilde{\tau}$ *searches at the ILC*, in *International Workshop on Future Linear Colliders*, 5, 2021 [2105.08616].

[361] ATLAS collaboration, *Search for electroweak production of supersymmetric particles in final states with two or three leptons at* $\sqrt{s} = 13$ *TeV with the ATLAS detector*, *Eur. Phys. J. C* **78** (2018) 995 [1803.02762].

[362] ATLAS collaboration, *Searches for electroweak production of supersymmetric particles with compressed mass spectra in* $\sqrt{s} = 13$ *TeV pp collisions with the ATLAS detector*, *Phys. Rev. D* **101** (2020) 052005 [1911.12606].

[363] ATLAS collaboration, *Search for chargino–neutralino pair production in final states with three leptons and missing transverse momentum in* $\sqrt{s} = 13$ *TeV pp collisions with the ATLAS detector*, *Eur. Phys. J. C* **81** (2021) 1118 [2106.01676].

[364] ATLAS Collaboration collaboration, *Prospects for searches for staus, charginos and neutralinos at the high luminosity LHC with the ATLAS Detector*, Tech. Rep. ATL-PHYS-PUB-2018-048, CERN, Geneva (Dec, 2018).

[365] LEP SUSY Working Group, ALEPH, DELPHI, L3 and OPAL Collaborations collaboration, *Combined lep chargino results, up to* 208 *gev for low dm*, Tech. Rep. LEPSUSYWG/02-04.1.

[366] M. Berggren, A. Cakir, D. Krücker, J. List, I.A. Melzer-Pellmann, B. Safarzadeh Samani et al., *Non-simplified SUSY:* $\widetilde{\tau}$ *-coannihilation at LHC and ILC*, *Eur. Phys. J.* **C76** (2016) 183 [1508.04383].

[367] H. Baer, M. Berggren, K. Fujii, J. List, S.-L. Lehtinen, T. Tanabe et al., *The ILC as a natural SUSY discovery machine and precision microscope: from light higgsinos to tests of unification*, 1912.06643.

[368] M. Berggren, F. Brümmer, J. List, G. Moortgat-Pick, T. Robens, K. Rolbiecki et al., *Tackling light higgsinos at the ILC*, *Eur. Phys. J.* **C73** (2013) 2660 [1307.3566].

[369] Y. Wang, M. Berggren and J. List, *ILD Benchmark: Search for Extra Scalars Produced in Association with a Z boson at* $\sqrt{s} = 500$ *GeV*, 2005.06265.

[370] DELPHI collaboration, *Photon events with missing energy in e+ e- collisions at s**(1/2) = 130-GeV to 209-GeV*, *Eur. Phys. J.* **C38** (2005) 395 [hep-ex/0406019].

[371] DELPHI collaboration, *Search for one large extra dimension with the DELPHI detector at LEP*, *Eur. Phys. J.* **C60** (2009) 17 [0901.4486].

[372] P.J. Fox, R. Harnik, J. Kopp and Y. Tsai, *LEP Shines Light on Dark Matter*, *Phys. Rev.* **D84** (2011) 014028 [1103.0240].

[373] M. Habermehl, *Dark Matter at the International Linear Collider*, dissertation, Universität Hamburg, Hamburg, 2018. 10.3204/PUBDB-2018-05723.

[374] C. Bartels, M. Berggren and J. List, *Characterising WIMPs at a future* e^+e^- *Linear Collider*, *Eur. Phys. J.* **C72** (2012) 2213 [1206.6639].

[375] J. Kalinowski, W. Kotlarski, K. Mekala, P. Sopicki and A.F. Zarnecki, *Sensitivity of future linear* e^+e^- *colliders to processes of dark matter production with light mediator exchange*, *Eur. Phys. J. C* **81** (2021) 955 [2107.11194].

[376] N. Craig, C. Englert and M. McCullough, *New Probe of Naturalness*, *Phys. Rev. Lett.* **111** (2013) 121803 [1305.5251].

[377] M. Bauer, M. Neubert and A. Thamm, *Collider Probes of Axion-Like Particles*, *JHEP* **12** (2017) 044 [1708.00443].

[378] M. Bauer, M. Heiles, M. Neubert and A. Thamm, *Axion-Like Particles at Future Colliders*, *Eur. Phys. J. C* **79** (2019) 74 [1808.10323].

[379] S. Kanemura, T. Moroi and T. Tanabe, *Beam dump experiment at future electron–positron colliders*, *Phys. Lett. B* **751** (2015) 25 [1507.02809].

[380] BDX collaboration, *Dark Matter Search in a Beam-Dump eXperiment (BDX) at Jefferson Lab*, 1607.01390.

[381] K. Asai, S. Iwamoto, Y. Sakaki and D. Ueda, *New physics searches at the ILC positron and electron beam dumps*, *JHEP* **09** (2021) 183 [2105.13768].

[382] Y. Sakaki and D. Ueda, *Searching for new light particles at the international linear collider main beam dump*, *Phys. Rev. D* **103** (2021) 035024 [2009.13790].

[383] K. Asai, T. Moroi and A. Niki, *Leptophilic Gauge Bosons at ILC Beam Dump Experiment*, *Phys. Lett. B* **818** (2021) 136374 [2104.00888].

[384] Z. Bai et al., *LUXE-NPOD: new physics searches with an optical dump at LUXE*, 2107.13554.

[385] E144 collaboration, *Observation of nonlinear effects in Compton scattering*, *Phys. Rev. Lett.* **76** (1996) 3116.

[386] D.L. Burke et al., *Positron production in multi - photon light by light scattering*, *Phys. Rev. Lett.* **79** (1997) 1626.

[387] C. Bamber et al., *Studies of nonlinear QED in collisions of 46.6-GeV electrons with intense laser pulses*, *Phys. Rev. D* **60** (1999) 092004.

[388]

[389] F.C. Salgado et al., *Single Particle Detection System for Strong-Field QED Experiments*, 2107.03697.

[390] H. Abramowicz et al., *Letter of Intent for the LUXE Experiment*, 1909.00860.

[391] H. Abramowicz et al., *Conceptual design report for the LUXE experiment*, *Eur. Phys. J. ST* **230** (2021) 2445 [2102.02032].

[392] K. Qu, S. Meuren and N.J. Fisch, *Signature of Collective Plasma Effects in Beam-Driven QED Cascades*, *Phys. Rev. Lett.* **127** (2021) 095001 [2001.02590].

[393] A. Freitas et al., *Theoretical uncertainties for electroweak and Higgs-boson precision measurements at FCC-ee*, 1906.05379.

[394] S. Jadach and M. Skrzypek, *QED challenges at FCC-ee precision measurements*, *Eur. Phys. J. C* **79** (2019) 756 [1903.09895].

[395] J. Ablinger, J. Blümlein, A. De Freitas and K. Schönwald, *Subleading Logarithmic QED Initial State Corrections to $e^+e^- \to \gamma^*/Z^{0*}$ to $O(\alpha^6 L^5)$*, *Nucl. Phys. B* **955** (2020) 115045 [2004.04287].

[396] T. Barklow, K. Fujii, S. Jung, R. Karl, J. List, T. Ogawa et al., *Improved Formalism for Precision Higgs Coupling Fits*, *Phys. Rev.* **D97** (2018) 053003 [1708.08912].

[397] B. Grzadkowski, M. Iskrzynski, M. Misiak and J. Rosiek, *Dimension-Six Terms in the Standard Model Lagrangian*, *JHEP* **10** (2010) 085 [1008.4884].

[398] G. Degrassi, S. Di Vita, J. Elias-Miro, J.R. Espinosa, G.F. Giudice, G. Isidori et al., *Higgs mass and vacuum stability in the Standard Model at NNLO*, *JHEP* **08** (2012) 098 [1205.6497].

[399] F.L. Bezrukov and M. Shaposhnikov, *The Standard Model Higgs boson as the inflaton*, *Phys. Lett. B* **659** (2008) 703 [0710.3755].

[400] F. Bezrukov and M. Shaposhnikov, *Standard Model Higgs boson mass from inflation: Two loop analysis*, *JHEP* **07** (2009) 089 [0904.1537].

[401] P. Huang, A.J. Long and L.-T. Wang, *Probing the Electroweak Phase Transition with Higgs Factories and Gravitational Waves*, *Phys. Rev. D* **94** (2016) 075008 [1608.06619].

[402] A. Adams, N. Arkani-Hamed, S. Dubovsky, A. Nicolis and R. Rattazzi, *Causality, analyticity and an IR obstruction to UV completion*, *JHEP* **10** (2006) 014 [hep-th/0602178].

[403] G.N. Remmen and N.L. Rodd, *Consistency of the Standard Model Effective Field Theory*, *JHEP* **12** (2019) 032 [1908.09845].

[404] B. Bellazzini and F. Riva, *New phenomenological and theoretical perspective on anomalous ZZ and Zγ processes*, *Phys. Rev. D* **98** (2018) 095021 [1806.09640].

[405] Q. Bi, C. Zhang and S.-Y. Zhou, *Positivity constraints on aQGC: carving out the physical parameter space*, *JHEP* **06** (2019) 137 [1902.08977].

[406] B. Fuks, Y. Liu, C. Zhang and S.-Y. Zhou, *Positivity in electron-positron scattering: testing the axiomatic quantum field theory principles and probing the existence of UV states*, *Chin. Phys. C* **45** (2021) 023108 [2009.02212].

[407] J. Gu, L.-T. Wang and C. Zhang, *An unambiguous test of positivity at lepton colliders*, 2011.03055.

[408] T. Cohen, N. Craig, X. Lu and D. Sutherland, *Is SMEFT Enough?*, *JHEP* **03** (2021) 237 [2008.08597].

[409] I. Low, J. Lykken and G. Shaughnessy, *Have We Observed the Higgs (Imposter)?*, *Phys. Rev. D* **86** (2012) 093012 [1207.1093].

[410] .A.G.-I.W.G. Advanced Accelerator Association, *Green-ilc report*, .

[411] *How ess will become sustainable*, .

[412] M. Aicheler, P. Burrows, M. Draper, T. Garvey, P. Lebrun, K. Peach et al., *A Multi-TeV Linear Collider Based on CLIC Technology*, .

[413] E. Esarey, C.B. Schroeder and W.P. Leemans, *Physics of laser-driven plasma-based electron accelerators*, *Rev. Mod. Phys.* **81** (2009) 1229.

[414] C.B. Schroeder, E. Esarey, C.G.R. Geddes, C. Benedetti and W.P. Leemans, *Physics considerations for laser-plasma linear colliders*, *Phys. Rev. ST Accel. Beams* **13** (2010) 101301.

[415] C.B. Schroeder, C. Benedetti, E. Esarey and W.P. Leemans, *Laser-plasma-based linear collider using hollow plasma channels*, *Nucl. Instrum. Meth. A* **829** (2016) 113.

[416] W. Leemans, ed., *Report of the Workshop on Laser Technology for k-BELLA and Beyond*, .

[417] W. Gai, J.G. Power and C. Jing, *Short-pulse dielectric two-beam acceleration*, *J. Plasma Phys.* **78** (2012) 339.

[418] R. Franceschini, *Beyond the Standard Model physics at CLIC*, *Int. J. Mod. Phys. A* **35** (2020) 2041015 [1902.10125].

[419] G.F. Giudice, C. Grojean, A. Pomarol and R. Rattazzi, *The Strongly-Interacting Light Higgs*, *JHEP* **06** (2007) 045 [hep-ph/0703164].

[420] H. Al Ali et al., *The Muon Smasher's Guide*, 2103.14043.

[421] L. Di Luzio, R. Gröber and G. Panico, *Probing new electroweak states via precision measurements at the LHC and future colliders*, *JHEP* **01** (2019) 011 [1810.10993].

[422] M. Cirelli, N. Fornengo and A. Strumia, *Minimal dark matter*, *Nucl. Phys. B* **753** (2006) 178 [hep-ph/0512090].

[423] J. Kalinowski, W. Kotlarski, T. Robens, D. Sokolowska and A.F. Zarnecki, *Exploring Inert Scalars at CLIC*, *JHEP* **07** (2019) 053 [1811.06952].

[424] J. Kalinowski, W. Kotlarski, T. Robens, D. Sokolowska and A.F. Zarnecki, *Benchmarking the Inert Doublet Model for e^+e^- colliders*, *JHEP* **12** (2018) 081 [1809.07712].

[425] T. Han, Z. Liu, L.-T. Wang and X. Wang, *WIMPs at High Energy Muon Colliders*, *Phys. Rev. D* **103** (2021) 075004 [2009.11287].

[426] Y. Cui and R. Sundrum, *Baryogenesis for weakly interacting massive particles*, *Phys. Rev. D* **87** (2013) 116013 [1212.2973].

[427] Y. Cui and B. Shuve, *Probing Baryogenesis with Displaced Vertices at the LHC*, *JHEP* **02** (2015) 049 [1409.6729].

[428] J. Alexander et al., *Dark Sectors 2016 Workshop: Community Report*, 8, 2016 [1608.08632].

[429] N. Craig, A. Hook and S. Kasko, *The Photophobic ALP*, *JHEP* **09** (2018) 028 [1805.06538].